A Data-Driven Design Process including Multiphysics for Synchronous AC Machines using High-Performance Computing

Mohammad Hossain Mohammadi

Department of Electrical & Computer Engineering
McGill University
Montreal, Canada

April 2019

A thesis submitted to McGill University in partial fulfillment of the requirements for the degree of Doctor of Philosophy.

2019/04/29

Abstract

Over the past century, electric machines have been used in many applications and sizes, ranging from washing machines and other home appliances to large pumps and fans within the industrial sector. Typical procedures for designing them have advanced from analytical formulations to the more recent finite element analysis for running physics simulations. This latter tool allowed motor designers to arrive at design solutions operating close to reality with minimal need of manufacturing hundreds if not thousands of electric machines.

Despite the simulation benefits, only the electromagnetic performances are generally considered during a design process. Other physics, such as structural, acoustic and thermal, are usually ignored and only verified for a selected design. This assumption could lead to suboptimal solutions due to the tradeoffs among physical phenomena. Another issue is the increase in simulation time while incorporating multiphysics simulations in the design process. Depending on the modeling complexity, each motor simulation could take minutes or even hours to solve which can be problematic when thousands of designs are to be analyzed for different physics and operating points. Also, previous works often neglect using the simulated data to understand the underlying relationships among design performances and variables. In an optimization problem, only the final set of optimal solutions are analyzed which does not necessarily provide information on how they were achieved for re-use.

To address these issues, this thesis proposes a multiphysics design process for synchronous AC machines using a data-driven approach. Each stage of the proposed process is explained using different case studies of a synchronous reluctance machine with a varying number of slots and rotor barriers. Upon setting the initial specifications, thousands of motor geometries are simulated using electromagnetics, structural, acoustics, and thermal analyses in days instead of months with the help of a high-performance computing system. A new methodology known as *barrier mapping* is then introduced which relates the design spaces of multiple-barrier rotors and systematically reduces their simulation time. Finally, the acquired multiphysics datasets are statistically analyzed for all their performances and variables before recommending various optimal designs for different priorities. Extracting design knowledge and guidelines can help a motor designer arrive at a more informed choice when analyzing results and selecting an optimal design. While this thesis focuses on electric machines, the presented multiphysics design process is applicable to any physical device.

Résumé

Au cours du siècle dernier, les machines électriques ont été utilisées dans de nombreuses applications et de nombreuses tailles, allant des machines à laver et autres appareils ménagers aux grandes pompes et ventilateurs du secteur industriel. Les procédures pour les concevoir sont évoluées des formulations analytiques à la plus récente analyse par éléments finis afin d'exécuter des simulations physiques. Ce dernier outil a permis aux concepteurs des moteurs de parvenir à des solutions de conception fonctionnant au plus près de la réalité avec un besoin minimal de fabrication des centaines, voire des milliers, des machines électriques.

Malgré les avantages de la simulation, seules les performances électromagnétiques sont généralement prises en compte lors du processus de conception. Les autres aspects physiques, tels que structurel, acoustique et thermique, sont généralement ignorés et vérifiés uniquement pour une conception sélectionnée. Cette pratique pourrait mener à des solutions sous-optimales en raison des compromis entre les phénomènes physiques. Un autre problème est la durée de simulation augmentée lors qu'on incorpore des simulations multi-physiques dans le processus de conception. Selon la complexité de la modélisation, la résolution de chaque simulation de moteur peut prendre quelques minutes, voire plusieurs heures, ce qui pourrait poser un problème lorsque des milliers de conceptions doivent être analysées pour différents aspects physiques et points de fonctionnement. En plus, les ouvrages précédents négligent souvent l'utilisation des données simulées pour comprendre les relations fondamentales entre les variables et les indices de performance de conception. Dans un problème d'optimisation, seulement les dernières solutions optimales sont analysées, ce qui ne fournit pas nécessairement d'informations sur la façon dont elles ont été réalisées.

Pour résoudre ces problèmes, cette thèse propose un processus de conception multi-physique pour les machines synchrones au courant alternatif en utilisant une approche pilotée par les données. Chaque étape du processus proposé est expliquée à l'aide de différentes études de cas d'une machine à réluctance synchrone avec un nombre variable d'emplacements et de barrières de rotor. Lors de la définition des spécifications initiales, des milliers des géométries proposées de moteur sont simulées à l'aide d'analyses électromagnétiques, structurelles, acoustiques et thermiques, en quelques jours au lieu de plusieurs mois, à l'aide d'un système informatique haute performance. Ensuite, une nouvelle méthodologie connue sous le nom de *cartographie de barrière* est introduite. Elle relie les domaines de conception des rotors à barrières multiples et réduit systématiquement leur temps de simulation. Finalement, les données multi-physiques acquises sont analysées statistiquement pour toutes leurs performances et variables avant de recommander divers modèles optimaux pour différentes priorités. Développer les connaissances et les directives de conception aiderait les concepteurs de moteur à faire un choix plus éclairé lors de l'analyse des résultats et de la sélection d'une conception optimale. Bien que cette thèse se concentre sur les machines électriques, le processus de conception multi-physique présenté sera applicable aux tous dispositifs physiques.

Acknowledgments

I dedicate my sincere gratitude to my research advisor, Prof. David A. Lowther, for his continuous supervision, constructive criticism and financial support over the past few years. I am honored to have had this period to learn from his patience and persistence. Also, I am thankful to Prof. François Bouffard and Prof. Benoit Boulet for their valuable suggestions and comments on my research project.

I wish to thank Mentor Infolytica for providing me with academic licenses to their commercial software and high-performance computing service. I appreciate having worked with Dr. Derek Dyck during my summer internships with whom I had the opportunity to learn more about modeling, analyzing and validating electric machines.

Moreover, I am grateful for having insightful discussions with my fellow colleagues at the Computational Electromagnetic Laboratory, in particular, Dr. Vahid Ghorbanian, Dr. Rodrigo César Pedrosa Silva, Dr. Tanvir Rahman, Dr. Sajid Hussain, and Mr. Issah Ibrahim. Their experiences in diverse research areas helped me pursue my thesis project from different perspectives. My fellow volunteers at the IEEE Montréal Section have also been supportive. I enjoyed planning and organizing different local events and activities with them.

Last but not least, I am forever indebted to my loving family, partner and dear friends for their unconditional support and guidance through good and stressful times.

> *Human beings are members of a whole, In creation of one essence and soul.*
> *If one member is afflicted with pain, Other members uneasy will remain.*
> *If you have no sympathy for human pain, The name of human you cannot retain!*
>
> *Les hommes sont membres les uns des autres, et tous crées de même matière.*
> *Si un membre est affligé, les autres s'en ressentent.*
> *Qui n'est pas touché du mal d'autrui, ne mérite pas d'être appelé homme!*
>
> Sheikh Moslehedin Sa'adi, Golestan, 1258 CE

Contents

List of Figures

List of Tables

List of Acronyms

A	Acoustic
AC	Alternating Current
ALA	Axially-Laminated Anisotropic
AN	Analytical
C	Control
CC	Central Composite *or* Cluster Creation
CPSR	Constant Power Speed Range
CR	Cluster Removal
CSE	Control Strategy Emulator
DC	Direct Current
DE	Differential Evolution
DP	Demagnetization Proximity
DR	Deploy and Run
E	Electromagnetic
Fe	Iron
FE/FEA	Finite Element / Finite Element Analysis
FF	Full Factorial
FOC	Field-Oriented Control
FW	Flux Weakening
GA	Genetic Algorithm
GM	Gradient Method
GSM	Golden Search Method with Parabolic Interpolation
HEV	Hybrid and Electric Vehicle
HPC	High-Performance Computing

I	Inverter
IC	Internal Combustion
LH	Latin Hypercube
LSF	Load Sharing Facility
IM	Induction Machine
IN	Inductor
IPM	Interior Permanent Magnet Machine
LP	Lumped Parameter
M	Machine *or* Motor
MOGA	Multi-Objective Genetic Algorithm
MEC	Magnetic Equivalent Circuit
MPDP	Multiphysics Design Process
MTPA	Maximum-Torque-Per-Ampere
MTPV	Maximum-Torque-Per-Volt
NdFeB	Neodymium Iron Boron
NN	Artificial Neural Network
PDE	Partial Differential Equation
PI	Proportional-Integral
PM	Permanent Magnet
PM-SynRM	Permanent Magnet assisted Synchronous Reluctance Machine
PoV	Point-of-View
PS	Particle Swarm Optimization
PU	Per-Unit
PWM	Pulse Width Modulation
R	Rotor
RS	Response Surface
RMS	Root Mean Square
RMSE	Root Mean Square Error
SA	Sensitivity Analysis
S	Stator
SLP	Sequential Linear Programming
SLS	Sequential Least Squares

St	Structural
SR	Switched Reluctance Machine
SynRM/SyR	Synchronous Reluctance Machine
T	Thermal
TLA	Transversally-Laminated Anisotropic
TO	Topology Optimization
VM	Virtual Machine
VSD	Variable Speed Drive
WF	Weighted Factor

Chapter 1

Introduction

1.1 Background

With the proliferation of electricity as a clean and reliable energy resource in the past century, many industrial and energy companies have turned their attention to individual devices such as electric motors. In a recent article published by the International Energy Agency, electric motors were found to be the biggest sole-user of electrical energy. They consume nearly 53% of the global electricity with the industrial and building sectors accounting for the most use.

Typically, electric motors are used to drive pumps, fans, compressors, and other systems with sizes ranging from less than 1 kW to beyond 1 MW for heavy-duty tasks. With the advent of power electronic devices in recent years, efficient control of electric motors in *variable-speed drives* (VSDs) has improved motor efficiencies and reduced operating costs through energy savings [Mohan and Undeland, 2007]. As explained in [International Energy Agency, 2016], system efficiencies can increase between 15% and 35% by replacing a mechanical throttle with a VSD, which can effectively change a motor's speed based on a given control strategy. To standardize minimum efficiency requirements on a global scale, the International Efficiency Commission has introduced different efficiency classes, or categories, for line-start and variable-speed motors in IEC 60034-30-1 and 60034-30-2 respectively. In short, these requirements increase for high-order class numbers (denoted by IE1, IE2, IE3, IE4) and larger motor sizes measured by their output power. Increasingly more countries are adopting these efficiency standards to overcome future energy crises [McCoy and Douglass, 2014; Dorrell, 2014] since the total consumption is expected to rise more than 40% by 2040.

Moreover, the automotive industry's consumption of about 28% (7825 TWh) of primary energy [US Department of Energy, 2011] has raised questions on the low efficiency levels of traditional vehicles. A chief concern is the inefficient operation of *internal combustion* (IC) engines typically used in hydrocarbon-based vehicles. Despite their benefit of providing a high mileage and range compared to using a battery supply (for 1 kg, gasoline holds about 12 kWh as opposed to 1 kWh of a lithium-ion battery), IC engines function at a maximum efficiency of 40% around a specific speed and torque point [Ehsani et al., 2009]. The remaining losses contribute to unwanted heat energy or harmful air pollutants like nitrogen oxides, carbon monoxides, and unburnt hydrocarbons. It is not surprising that research and development of electric motors for *hybrid and electric vehicles* (HEVs) has been given more attention in the past decade, as both traditional and new vehicle manufacturers aim to reduce carbon emissions and fuel consumption within the transportation industry. Electric motors can sustain high efficiency levels of up to 95% for urban and highway driving cycles while matching or improving upon the drive performances of IC engines. In fact, several technical targets have been set by the US Department of Energy for the year 2020 to further improve HEV performances. These include reducing the powertrain's initial cost as well as increasing its output power for a given mass and volume.

To meet these technical targets, HEV manufacturers typically employ rare-earth *permanent magnet* (PM) motors, such as surface-mounted or *interior permanent magnet* (IPM) types. Properly-designed PM machines have competitive advantages over other topologies including high torque-to-rotor-volume density, efficiency levels, constant power speed range, and power factor (helps reduce inverter's kVA sizing and overall system costs). However, recent fluctuations in the price and supply of rare-earth materials, such as high-grade *Neodymium Iron Boron* (NdFeB), has led to further research activity in alternative motor topologies with significantly less or no rare-earth material, while sustaining the targeted efficiency and performance requirements [Boldea et al., 2014; Boglietti et al., 2014]. One possible substitute is the *synchronous reluctance machine* (SynRM) which is comprised of the same stator as a typical AC machine but its rotor only consists of ferromagnetic iron laminations to create a magnetically-salient structure. By adding low-cost PMs into the rotor structure, this *PM-assisted SynRM* (PM-SynRM) can compete with the performances of IPM motors [Morimoto et al., 2001; Niazi, 2006; Vartanian and Toliyat, 2009].

Nevertheless, typical procedures to design electric machines in the early years relied on solving analytical models with approximations and individually manufacturing them before experimentally testing their real-time performances. In constructing each motor design with a specific geometry, sufficient volumes of iron laminations, copper windings, PMs and housing structures are required. These can subsequently add to the overall financial cost of the final optimized product if multiple designs are to be experimentally tested. To tackle this costly problem, researchers have developed numerical procedures to predict a given motor's performances, such as *finite element analysis* (FE/FEA) which accounts for complex geometries and material nonlinearities in solving the underlying physical and electromagnetic *partial differential equations* (PDEs) [Silvester and Ferrari, 1996]. Specifically, Maxwell's Equations of Electromagnetism are used to form the underlying PDEs, and FEA can solve them on a given domain (surface for 2-D or volume for 3-D) for a set of boundary conditions. A benefit of using an FEA tool is its domain discretization: it allows users to change the geometric shape, excitation currents, winding configurations, material properties and other parameters without altering the problem definition [Lowther and Silvester, 1986; Jin, 2015].

While detailed FEA solutions can accurately and reliably solve low-frequency electromagnetic problems for complex geometries, they are a computational bottleneck which presents time issues when many models are to be solved. Typical design optimization procedures may rely on direct-FEA function evaluations which quickly become costly for large problems with a high number of design variables and objectives as well as multiple operating points. Alternatively, selected regions of the design space could be sampled in advance and solved using FEA in order to build a surrogate model, such as an *artificial neural network* (NN), for interpolating data points [Giurgea et al., 2007; Salimi, 2018; Silva, 2018]. This approach allows the optimization procedure to quickly evaluate objective or performance values using a computationally cheaper model without having to solve the underlying PDEs again. The final set of optimal solutions may then be validated with FEA to compute their relative errors before reporting them to the designer. Fitting or training these surrogate models, however, may be problematic when objective values vary greatly in particular regions of the design space (i.e. multiple peaks and valleys). This may lead to prediction problems when following general trends or inaccurately evaluating function values. Another issue relates to the overfitting of data points which depends on the given problem and the surrogate model's hyperparameters (e.g. the number of hidden layer neurons in NNs).

On the other hand, electric machines are multiphysical by nature as they combine electromagnetic, structural, thermal and acoustic domains in real operation. Simulating the physical subsystems takes longer to reach steady-state due to the different timescales. For example, a coupled electromagnetic-thermal simulation must run for a couple of seconds to account for the relatively slow rise and fall of material temperatures [Ghorbanian, 2018]. Furthermore, automotive manufacturers normally require a motor's efficiency map to predict a vehicle's system losses and fuel economy in a dynamic simulation [Ehsani et al., 2009]. This map reports the motor's efficiency for all its feasible torque and speed points which means that many operating points need to be simulated. While a numerical method such as FEA can aid this detailed calculation, prior knowledge of the input excitation conditions is required to ensure optimal operation. Despite selecting only one design, the simulation of hundreds of operating points after a preprocessing stage can further delay the analysis phase and increase development time. Therefore, these problems may introduce an infeasible timeline when many multiphysics models are to be solved, and industrial motor designers may not be inclined to address the modeling complexity of surrogates when the accuracy of optimal solutions are of utmost importance.

From the perspective of a software package, two objectives need to be considered during the design and analysis of electric machines: reduce computational time while avoiding any substantial compromise on the solution accuracy, and automate the simulation process as much as possible. While the first issue is an ongoing investigation [Bramerdorfer et al., 2016; Baranyai et al., 2017], the latter point has become more desirable given the recent shift toward data-driven approaches (defined in Section 1.4). By replacing a single workstation with a *high-performance computing* (HPC) system, sequences of time-consuming FEA simulations can be significantly sped up by distributing the design variations onto parallel workstations. Also, there has not been enough research on incorporating multiphysics of electric machines within the design process. It is unknown whether the addition is required and whether the impact is significant toward arriving at optimal designs. Most designers rely on electromagnetic simulations and ignore the effect of other physical domains during the design phase. Novel ways of treating multiphysics problems for electric machines, whether they are design or analysis-oriented, have become a necessary research investigation area. Over time, these approaches may replace traditional methods that rely on many assumptions or require development time for setting up analytical or surrogate models. The sections below present a brief theory of synchronous AC machines before discussing ongoing research and challenges.

1.2 Theory of Synchronous AC Machines

In a synchronous AC machine, the stator consists of silicon steel laminations and polyphase distributed windings as shown in Fig. 1.1. The insulated laminations decrease the eddy currents induced by the varying magnetic field. Upon feeding AC excitation to the windings, the stator produces a rotating magnetic field that interacts with the rotor. Similar to the stator structure, the rotor is comprised of silicon steel laminations and could include *permanent magnets* (PMs), damper windings or a combination of them. During steady-state operation, the mechanical rotation speed of the rotor shaft, N_m, is synchronized with the supply or excitation electrical frequency, f_e, through (1.1) where n_p is the number of poles. For example, a mechanical rotor speed of 1800 RPM could be achieved in a 4-pole motor if the supply frequency is 60 Hz.

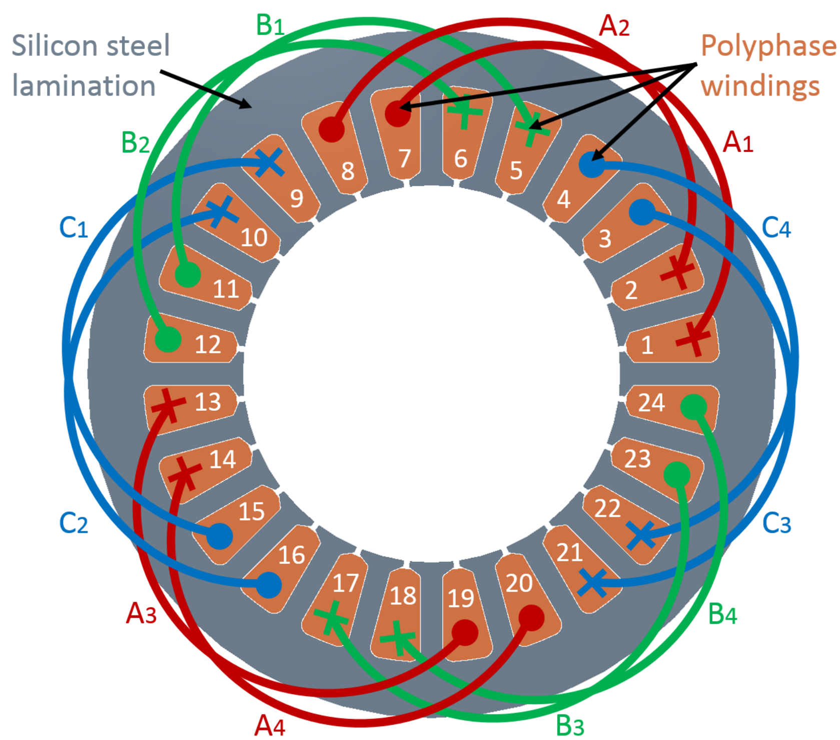

Fig. 1.1 Cross-section of a 24-slot 4-pole outer stator with 3-phase windings.

$$N_m = \frac{120 f_e}{n_p} \tag{1.1}$$

The AC excitation fed to the polyphase windings can be represented as balanced, sinusoidal signals given in (1.2). In practice, however, the sinusoidal quantities are mixed with higher order harmonics due to the machine geometry and switching effects in the inverter drive. Here, V_s is the stator RMS line voltage, I_s is the stator RMS line current, ω_e is the electrical angular speed, t is time, and ϕ is the power factor angle between V_s and I_s, commonly known as the displacement power factor. To better understand the relationship in the time domain, Fig. 1.2 (a) displays the voltage and current waveforms for an electrical period. Note that the current lags the voltage by the power factor angle ϕ. It is desired to keep ϕ close to zero in order to achieve unity power factor, i.e. $pf = \cos\phi \approx 1$. The implication of this condition is explained through (1.3) and Fig. 1.2 (b). For a given input active power P_{in}, a non-unity power factor increases the reactive power consumed, Q_{in}, as well as the required input apparent power, S_{in}, in VA.

$$\begin{aligned} v_a(t) &= \sqrt{2}V_s\cos(\omega_e t) & i_a(t) &= \sqrt{2}I_s\cos(\omega_e t - \phi) \\ v_b(t) &= \sqrt{2}V_s\cos(\omega_e t - 2\pi/3) & i_b(t) &= \sqrt{2}I_s\cos(\omega_e t - \phi - 2\pi/3) \\ v_c(t) &= \sqrt{2}V_s\cos(\omega_e t + 2\pi/3) & i_c(t) &= \sqrt{2}I_s\cos(\omega_e t - \phi + 2\pi/3) \end{aligned} \tag{1.2}$$

$$\begin{aligned} \boldsymbol{S}_{in} &= P_{in} + jQ_{in} \\ |\boldsymbol{S}_{in}| &= \frac{P_{in}}{\cos\phi} = \sqrt{3}V_s I_s \end{aligned} \tag{1.3}$$

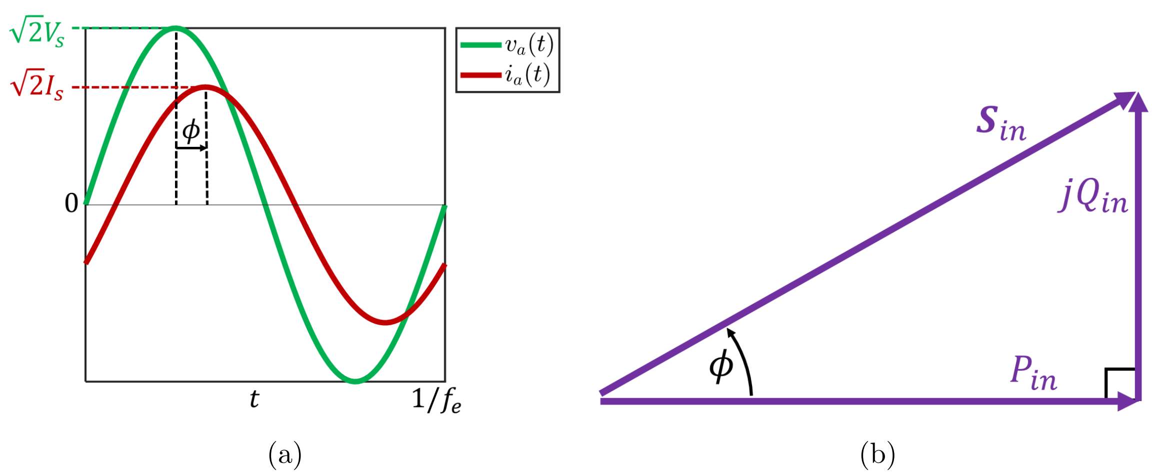

Fig. 1.2 (a) AC voltage and current waveforms. (b) Power vector triangle.

In motoring operation, the input electrical power, P_{in}, is fed by the polyphase stator winding excitation as in (1.4). This equation is similar to that of S_{in} in (1.3) except that the displacement power factor, $\cos\phi$, is included here.

$$P_{in} = \sqrt{3} V_s I_s \cos\phi \tag{1.4}$$

For a given N_m speed, the output mechanical power, P_{out}, in W produced on the rotor shaft relates through (1.5) to the mechanical torque, T_m, in Nm. This means that the output power is affected by varying either T_m, N_m or both.

$$P_{out} = T_m \omega_m = T_m \frac{N_m}{30/\pi} \tag{1.5}$$

Due to the inherent losses in an electric machine, the output power is always less than the input's. Hence, the power flow or conservation can be represented in (1.6), where P_{loss} corresponds to the motor losses, P_{Cu} is the conductor or copper loss in the stator windings, P_{Fe} is the iron loss in the silicon steel material, P_{mn} is the PM eddy current loss and P_{mech} is the mechanical loss on the shaft. In the initial electromagnetic design, P_{mech} is typically ignored since this loss component captures the mechanical coupling. It consists of the friction due to the bearings and between the moving parts and air, i.e. windage. These mechanical losses vary to the third power of the motor speed N_m [Chapman, 2005].

$$\begin{aligned} P_{in} &= P_{out} + P_{loss} \\ P_{loss} &= P_{Cu} + P_{Fe} + P_{mn} + P_{mech} \end{aligned} \tag{1.6}$$

In practice, it is desired to minimize P_{loss} so that less P_{in} is used to operate an electric motor. Lower losses result in a smaller temperature rise across the motor components which means that less heat is produced and dissipated. A lower motor temperature also places less strain on the required cooling system. Therefore, this loss information can be alternatively represented through the motor efficiency, η, given in (1.7) which ranges from 0% to 100%. A 100% efficiency signifies an ideal system with no losses.

$$\eta = \frac{P_{out}}{P_{in}} = \frac{P_{out}}{P_{out} + P_{loss}} \tag{1.7}$$

1.2.1 Material Characteristics

A synchronous AC machine consists of copper, silicon steel, PMs and possibly aluminum. Each material has different electrical and magnetic characteristics as explained below.

The conductor or copper windings are represented by an electrical resistance which contributes to the Ohmic or copper loss, P_{Cu}, in (1.8), given no dampers and a single harmonic are used. Here, R_s is assumed to be the AC phase resistance for a Y-connected winding, ρ is the electrical resistivity, l is the winding length, A is the conductor's cross-sectional area, α is the temperature coefficient, and T is the winding temperature. The 0 subscript corresponds to the ambient temperature condition. For copper, $\alpha = 0.00386$ and $\rho_0 = 1.733 \times 10^{-8}$ Ωm at 20°C [Giancoli, 2004]. A couple of observations can be made from (1.8). First, P_{Cu} exhibits a quadratic growth when the excitation is increased. Second, P_{Cu} linearly relates to R_s which itself is a linear function of T. If the copper windings operate at a higher temperature, R_s and P_{Cu} increase linearly.

$$
\begin{aligned}
P_{Cu} &= 3R_s I_s^2 \\
R_s &= \rho \frac{l}{A} \\
\rho &= \rho_0 \big(1 + \alpha(T - T_0)\big)
\end{aligned}
\tag{1.8}
$$

Fig. 1.3 (a) displays the ferromagnetic material characteristics of silicon steel for different operating temperatures. Here, B is the magnetic field density and H is the magnetic field intensity which depends on the supply current. For low excitation or small H values of silicon steel, B increases linearly as seen in Fig. 1.3 (a). Beyond the knee point, however, B begins to saturate which means that a much higher H is required to slightly boost B. This comes at an expense of further increasing the supply current I_s as well as the copper loss as seen in (1.8). In addition, increasing the temperature up to 180° for silicon steel does not significantly impact the iron magnetic characteristic.

The BH curves of NdFeB PM are shown in Fig. 1.3 (b). At no load, the remnant B is around 1.2 T for this PM material. During machine operation, the stator field could oppose that of the PM's which means that B decreases for negative H. Beyond a certain point known as the coercivity, the PM is completely demagnetized. This irreversible effect occurs earlier at higher temperatures. Also, increased temperatures decrease the remnant B resulting in less PM contribution to the machine [Hamidizadeh, 2016].

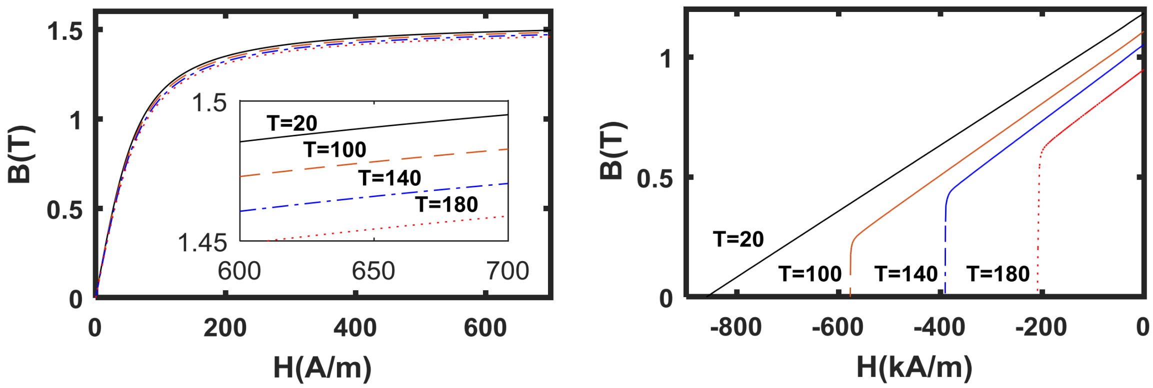

(a) (b)

Fig. 1.3 Magnetic material characteristics for temperatures up to 180°: (a) silicon steel, (b) NdFeB PM [Ghorbanian et al., 2018a].

From the ferromagnetic material characteristic, the iron loss P_{Fe} can mainly be broken down into two components given in (1.9): P_{hyst} is the hysteresis loss and P_{eddy} is the eddy current loss. The unknown coefficients, i.e. K_{hyst}, K_{eddy}, α and β, can be identified and fit experimentally. For example, M-19 29 Ga is represented by $K_{hyst} = 9.68569 \times 10^{-3}$, $K_{eddy} = 4.12318 \times 10^{-5}$, $\alpha = 1.19792$ and $\beta = 1.79564$. A detailed explanation of modeling and calculating iron losses is provided in [Hussain, 2017].

$$P_{Fe} = P_{hyst} + P_{eddy} = K_{hyst} f^{\alpha} B^{\beta} + K_{eddy} f^2 B^2 \tag{1.9}$$

Due to alternating currents and rotating fields in a synchronous AC machine, the BH curves of ferromagnetic cores follow different trajectories based on previous magnetic states as in Fig. 1.4 (a). This effect is responsible for the hysteresis loss which is a function of the peak induction level B and is represented by the BH loop's area. Also, eddy currents flow in closed loops on a plane perpendicular to the B field between the iron laminations as displayed in Fig. 1.4 (b). These currents produce a loss similar to the Ohmic loss in (1.8), where each lamination has a particular electrical resistance. The PM eddy current loss, P_{mn}, behaves in a similar manner. If a ferromagnetic core was manufactured as a solid block, the core's electrical resistance would be much lower due to a higher cross-sectional area causing an increase in the eddy currents and P_{eddy}. This is the reason why ferromagnetic cores are constructed and stacked using multiple insulated laminations of silicon steel.

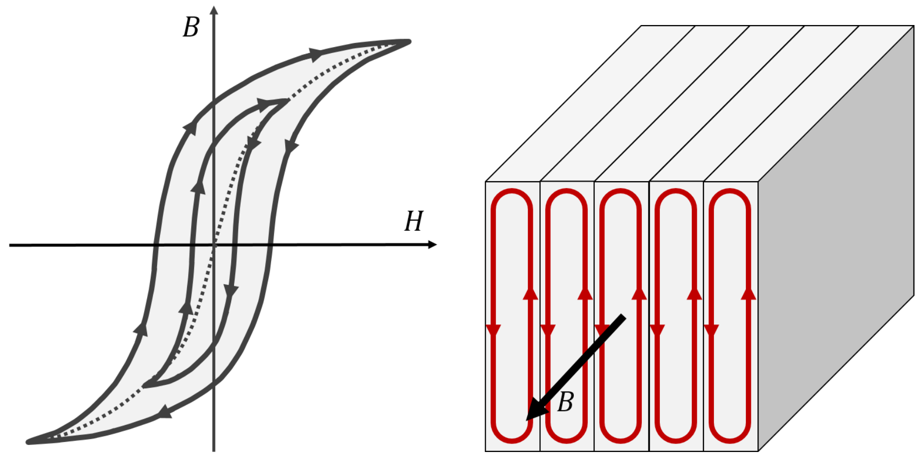

(a) (b)

Fig. 1.4 Iron loss components: (a) Hysteresis loops for different excitations. (b) Eddy current loops in stacked ferromagnetic laminations.

Fig. 1.5 shows that the iron power loss, P_{Fe}, increases for higher magnetic flux density or frequency. Also, the iron loss decreases for elevated temperatures due to the increased electrical resistance of the ferromagnetic material. It should be noted that material properties are generally uncertain in practice due to manufacturing processes of silicon steel laminations or magnetization of PMs [Saleem, 2018]. Stochastic material models could be used to obtain robust solutions in a design or optimization process [Li et al., 2017].

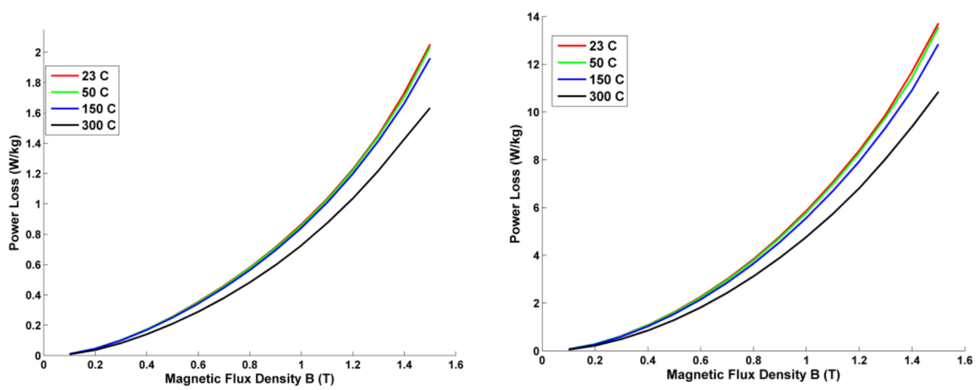

(a) (b)

Fig. 1.5 Iron power loss curves for different temperatures and frequencies: (a) 50 Hz, (b) 200 Hz [Hussain, 2017].

1.2.2 DQ Transformation

Given the polyphase nature of a synchronous AC machine, its electromagnetic quantities (currents, flux linkages, voltages) are time-varying which can complicate the machine's design, analysis, and control. To tackle this issue, the Park transformation is used to convert a time-varying 3-phase balanced system into 3-phase constants, namely the direct, quadrature and zero axes [Park, 1929]. The main requirement of this transformation is a rotating reference frame, i.e. the rotor, based on *field-oriented control* (FOC) [Krause et al., 2012]. This means that the rotor's mechanical position, θ_m, must be tracked at all times with the help of a rotor position sensor. Then, the electrical position, θ_e, and angular frequency, ω_e, can be calculated using (1.10).

$$\theta_e = \frac{n_p}{2}\theta_m = \omega_e t \rightarrow \omega_e = \frac{d\theta_e}{dt} \tag{1.10}$$

Assume that a 3-phase time-varying system or vector, $\boldsymbol{f}_{abc}(t)$, is given as in (1.11). Let the vector be composed of sinusoidal signals that are balanced with a peak value of F_s and a phase shift denoted the "advance angle", γ. In phasor form, $\boldsymbol{f}_{abc}(t)$ can be visualized as a vector rotating in a 2-D plane with a constant magnitude F_s at a fixed speed.

$$\boldsymbol{f}_{abc}(t) = \begin{bmatrix} f_a(t) \\ f_b(t) \\ f_c(t) \end{bmatrix} = \begin{bmatrix} F_s\cos(\omega_e t + \gamma) \\ F_s\cos(\omega_e t + \gamma - 2\pi/3) \\ F_s\cos(\omega_e t + \gamma + 2\pi/3) \end{bmatrix} \tag{1.11}$$

Then, the dq0 vector, $\boldsymbol{f}_{dq0}$, can be computed using $\boldsymbol{f}_{abc}(t)$ and the Park transformation matrix, $\boldsymbol{K}_s$, as given in (1.12). Due to the balanced, sinusoidal nature of $\boldsymbol{f}_{abc}(t)$ in (1.11), the 0^{th} component can be ignored. In steady-state, the direct and quadrature quantities are constants in time and depend only on the sinusoidal magnitude, F_s, and advance angle, γ.

$$\begin{gathered} \boldsymbol{K}_s = \frac{2}{3}\begin{bmatrix} \sin\theta_e & \sin(\theta_e - 2\pi/3) & \sin(\theta_e + 2\pi/3) \\ \cos\theta_e & \cos(\theta_e - 2\pi/3) & \cos(\theta_e + 2\pi/3) \\ 1/2 & 1/2 & 1/2 \end{bmatrix} \\ \boldsymbol{f}_{dq0} = \boldsymbol{K}_s\boldsymbol{f}_{abc}(t) = \begin{bmatrix} f_d \\ f_q \\ f_0 \end{bmatrix} = \begin{bmatrix} -F_s\sin(\gamma) \\ +F_s\cos(\gamma) \\ 0 \end{bmatrix} \end{gathered} \tag{1.12}$$

Fig. 1.6 illustrates an example of how the three time-varying ABC quantities in (1.11) correpond to two constant dq values using (1.12) for a given γ value and a motor speed N_m (or excitation frequency f_e). Knowing that f_d and f_q are constants in time, the $\boldsymbol{f}_{dq0}$ or simply the $\boldsymbol{f}_{dq}$ vector is normally represented as a fixed vector in the 2-D plane of (f_d, f_q) which is a rotating reference frame from the rotor's point-of-view.

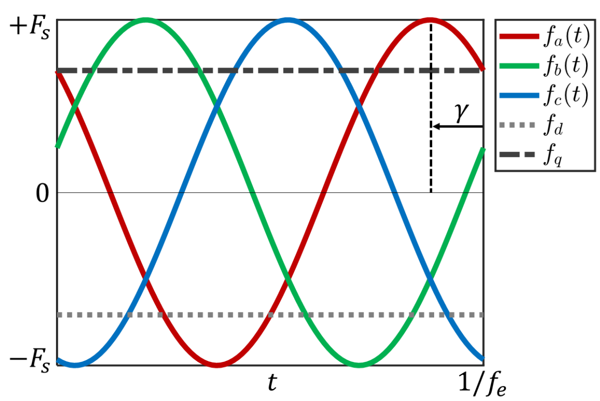

(a)

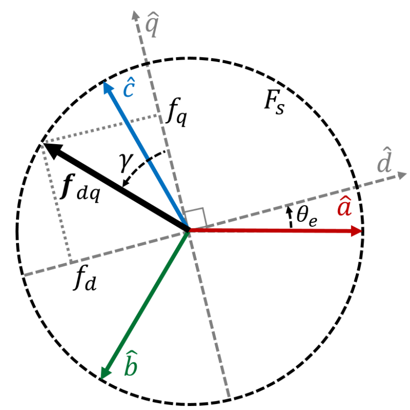

(b)

Fig. 1.6 ABC-to-DQ Park transformation: (a) time waveforms, (b) phasors.

DQ Vectors

The stator currents, flux linkages, and voltages can all be converted to their dq forms as given in (1.13). These dq quantities are all referred to the rotor's reference frame and provide a simplification of the electromechanical operation of a synchronous AC machine. Field and damper windings, core losses, and cross-coupling effects are all neglected in this section. From (1.13), it is observed that the stator current vector, $\boldsymbol{I}_s$, consists of the dq-axis components, I_d and I_d, where I_s is the current magnitude and γ is the advance angle measured counterclockwise from the q-axis. A similar representation holds for the stator flux linkage vector, $\boldsymbol{\lambda}_s$, and the stator voltage vector, $\boldsymbol{V}_s$. Other quantities include the load angle δ, the PM flux linkage λ_m, the dq-axis stator inductances L_d and L_q, and the stator winding resistance R_s. The steady-state vector diagram of $\boldsymbol{I}_s$, $\boldsymbol{\lambda}_s$ and $\boldsymbol{V}_s$ using (1.13) is represented in Fig. 1.7 for a synchronous AC machine. For a motoring operation, the stator current vector $\boldsymbol{I}_s$ lies in the second quadrant where a negative I_d value weakens the motor flux.

$$
\begin{aligned}
\boldsymbol{I}_s &= \begin{bmatrix} I_d \\ I_q \end{bmatrix} = \begin{bmatrix} -I_s \sin\gamma \\ +I_s \cos\gamma \end{bmatrix} \\
\boldsymbol{\lambda}_s &= \begin{bmatrix} \lambda_d \\ \lambda_q \end{bmatrix} = \begin{bmatrix} -\lambda_s \sin\delta \\ +\lambda_s \cos\delta \end{bmatrix} = \begin{bmatrix} L_d I_d + \lambda_m \\ L_q I_q \end{bmatrix} \\
\boldsymbol{V}_s &= R_s \boldsymbol{I}_s + j\omega_e \boldsymbol{\lambda}_s \\
&= \begin{bmatrix} V_d \\ V_q \end{bmatrix} = \begin{bmatrix} R_s & -\omega_e L_q \\ \omega_e L_d & R_s \end{bmatrix} \begin{bmatrix} I_d \\ I_q \end{bmatrix} + \begin{bmatrix} 0 \\ \omega_e \lambda_m \end{bmatrix}
\end{aligned}
\tag{1.13}
$$

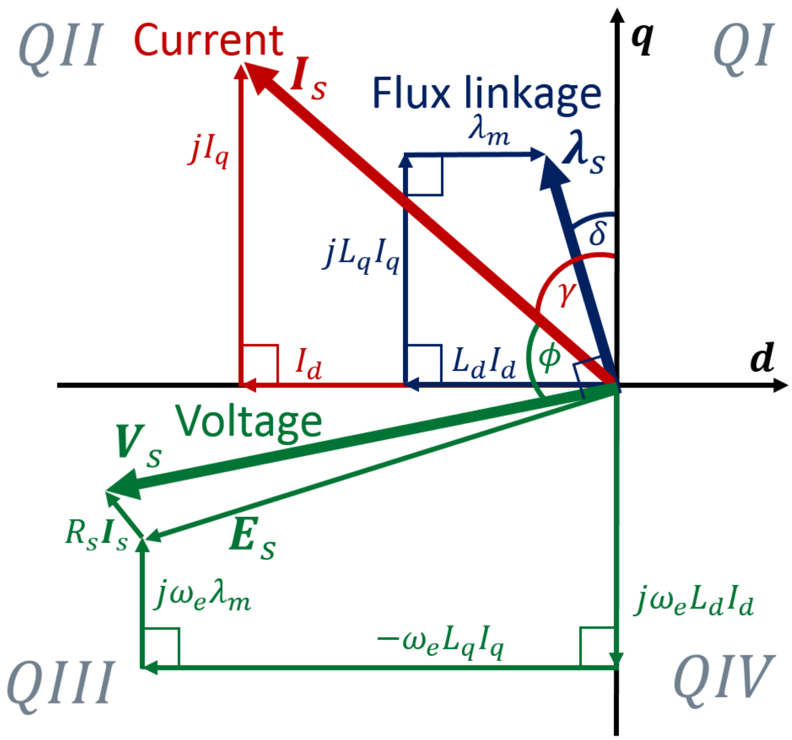

Fig. 1.7 Vector diagram of a synchronous AC machine in the dq plane.

This steady-state vector diagram provides a useful visual tool to analyze the relationships between the different electromagnetic vectors. It can be seen that the back EMF vector, $\boldsymbol{E}_s$, is comprised of the inductive and PM flux linkage components and is perpendicular to the $\boldsymbol{\lambda}_s$ vector. The power factor angle, ϕ, is measured between the current and voltage vectors, and the load angle, δ, is measured from the q-axis to $\boldsymbol{\lambda}_s$.

If the $\boldsymbol{I}_s$ vector is closer to $\boldsymbol{V}_s$, i.e. higher power factor or $\cos\phi$, the inverter kVA size can be reduced implying lower system costs. Also, the $j\omega_e L_d I_d$ component dictates how far $\boldsymbol{V}_s$ is vertically from $\boldsymbol{I}_s$ which can result in a low power factor. To compensate for this effect, L_d could be minimized since I_d is fixed for a given ω_e. Another approach to correct the power factor is to increase λ_m which brings $\boldsymbol{V}_s$ closer to $\boldsymbol{I}_s$ by affecting the vertical PM flux linkage component $j\omega_e\lambda_m$. This serves as the basis for PM-assisted motor designs that have a higher power factor and produce more electromagnetic torque.

DQ Rotor Representation

Fig. 1.8 displays a synchronous AC rotor labeled with its different components. Within each silicon steel lamination, air pockets known as *flux barriers* are used to control and guide the magnetic flux paths through the *flux carriers*. Permanent magnets could be inserted inside the rotor structure to assist the motor operation. The PM labels correspond to a radial magnetization direction, i.e. 'N' for outward and 'S' for inward. In other words, 'N' signifies that the outer radial end of the magnet is a North pole and the inner end is a South pole. The flux barriers are structurally held together with the help of tangential ribs on the outer periphery of the rotor. Also, the rotor d-axis is assumed to be oriented towards the minimum inductance path, while the rotor q-axis points to the path of maximum inductance. This dq convention follows that of [Park, 1929; Jahns, 1987; Soong and Miller, 1994]. As seen in Fig. 1.7, three parameters are required to characterize a synchronous AC motor: λ_m, L_d, L_q.

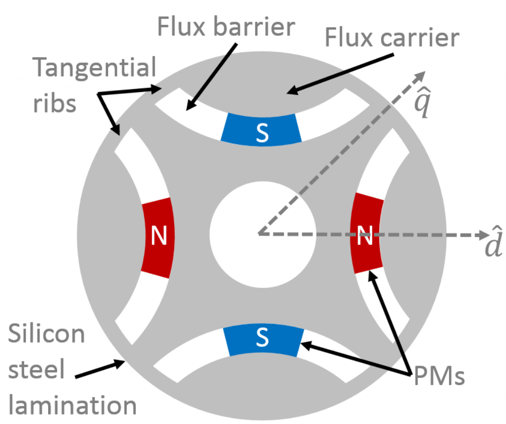

Fig. 1.8 Cross-section of a 4-pole inner rotor with permanent magnets.

To estimate the PM flux linkage, the stator windings are opened and the rotor with PMs is rotated at a given N_m speed corresponding to a ω_e value through (1.1) and (1.10). This rotating rotor field cuts the stator windings and produces a back EMF, $V_s = E_s$, across the motor terminals. Then, λ_m can be found using (1.14) with flux paths shown in Fig. 1.9 (a).

$$\lambda_m = \frac{E_s}{\omega_e} \tag{1.14}$$

For the d-axis inductance, the stator windings are fed with a current magnitude and an advance angle, γ, of 90°. This causes $\boldsymbol{I}_s = I_d$ and $I_q = 0$ from which the d-axis flux linkage, λ_d, can be measured using the winding voltage to find L_d using (1.15). The PM flux linkage, λ_m, is also needed. Notice in Fig. 1.9 (b) that these fluxes oppose and demagnetize the rotor field and also pass through the d-axis, along the flux barriers and the tangential ribs.

$$L_d = \frac{\lambda_d - \lambda_m}{I_d} \tag{1.15}$$

Estimating the q-axis inductance is similar to the L_d case. However, a γ value of 0° is used so that $\boldsymbol{I}_s = jI_q$ and $I_d = 0$. Then, the measured λ_q can be used to calculate L_q in (1.16). The fluxes pass through the q-axis, along the flux carriers as seen in Fig. 1.9 (c).

$$L_q = \frac{\lambda_q}{I_q} \tag{1.16}$$

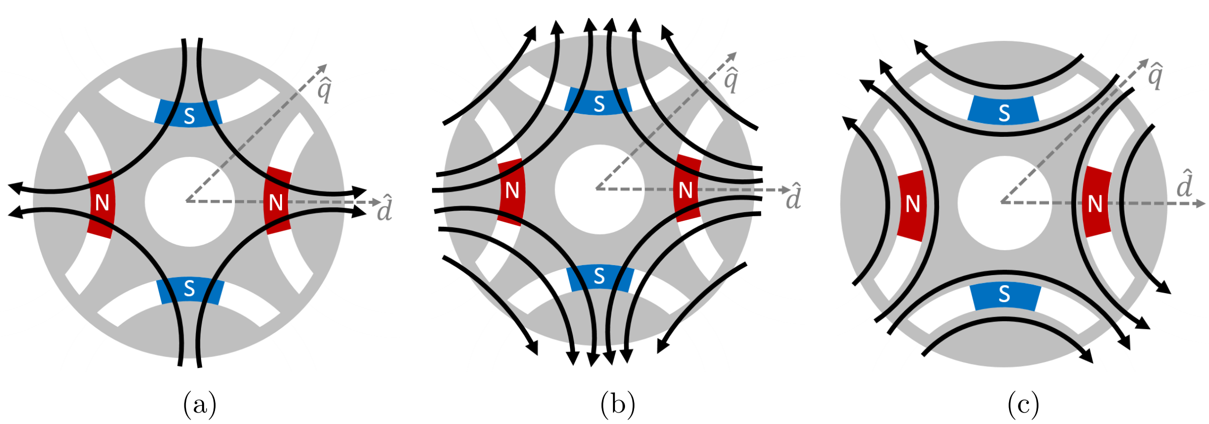

Fig. 1.9 Magnetic flux paths for estimating (a) λ_m, (b) L_d, (c) L_q.

1.2.3 Electromagnetic Torque

For a 3-phase motor with n_p poles, the electromagnetic torque, $\boldsymbol{T}_{em}$, along the $\hat{z}$-axis of the rotor shaft can be calculated through the cross product of the stator flux linkage vector $\boldsymbol{\lambda}_s$ with the stator current vector $\boldsymbol{I}_s$ from (1.13) to result in (1.17). This $\boldsymbol{T}_{em}$ equation can be expanded to isolate two components: PM torque, $\boldsymbol{T}_{pm}$, and reluctance torque, $\boldsymbol{T}_{rel}$.

$$\begin{aligned}\boldsymbol{T}_{em} &= \frac{3}{2}\frac{n_p}{2}\boldsymbol{\lambda}_s \times \boldsymbol{I}_s = \frac{3}{2}\frac{n_p}{2}\big(\lambda_d I_q - \lambda_q I_d\big)\hat{z} \\ &= \frac{3}{2}\frac{n_p}{2}\Big(\lambda_m I_q + (L_d - L_q) I_d I_q\Big)\hat{z} \\ &= \frac{3}{2}\frac{n_p}{2} L_d \Big(\underbrace{\frac{\lambda_m}{L_d} I_s \cos\gamma}_{\boldsymbol{T}_{pm}} + \underbrace{\frac{1}{2}(\xi - 1) I_s^2 \sin(2\gamma)}_{\boldsymbol{T}_{rel}}\Big)\hat{z}\end{aligned} \tag{1.17}$$

When analyzing a motor performance, it is convenient to quantify the dq inductances through the magnetic saliency ratio, ξ, given in (1.18). This ratio is normally greater than 1 for pure reluctance machines, but strictly equal to 1 for pure PM types. Also, the characteristic current, I_{ch}, in (1.18) should be close to the rated current for wide speed performance.

$$\begin{aligned}\xi &= \frac{L_q}{L_d} \\ I_{ch} &= \frac{\lambda_m}{L_d}\end{aligned} \tag{1.18}$$

Based on two conditions, different classes of synchronous AC machines can be created as summarized in Table 1.1. By setting $\xi = 1$ and a non-zero PM flux linkage, a pure PM machine is obtained with no rotor saliency. This means that no reluctance torque can be produced. In the other extreme, setting a zero PM flux linkage and $\xi \neq 1$ provides only a reluctance torque proportional to ξ. A hybrid scenario corresponds to an IPM or a PM-assisted machine producing both torque components.

Table 1.1 Different Classes of Synchronous AC Machines

Type	**Condition 1**	**Condition 2**	T_{em}
PM	$\lambda_m \neq 0$	$\xi = 1$	T_{pm}
Reluctance	$\lambda_m = 0$	$\xi \neq 1$	T_{rel}
IPM	$\lambda_m \neq 0$	$\xi \neq 1$	$T_{pm} + T_{rel}$

Fig. 1.10 (a) displays how the different torque components of an IPM machine vary against the advance angle, γ, for a fixed current magnitude, I_s, using (1.17). It is observed that the peak values of the PM and reluctance torques occur at 0° and 45° respectively. This means that depending on a motor geometry, the γ location of the maximum torque value can change. For the electromagnetic torque, its peak value is normally between 0° and 45° since it includes both torque components.

It should be noted that Fig. 1.10 (a) assumes fixed values for λ_m, L_d and L_q. In practice, λ_m is a function of temperature due to a lower remnant B in the magnet material seen in Fig. 1.3 (b). On the other hand, L_q decreases for a higher I_s value due to saturation as displayed in Fig. 1.3 (a). When the ferromagnetic core is saturated, a higher I_q value can no longer increase the machine flux along the q-axis shown in Fig. 1.9 (c). Hence, the growth of λ_q is limited which diminishes L_q through (1.16) and also decreases the saliency ratio, ξ. The d-axis inductance L_d is less affected by saturation when compared to L_q, since the d-axis paths mostly consist of flux barriers. Fig. 1.10 (b) demonstrates the variation of L_d and L_q against the stator current magnitude. This means that the γ location of the maximum torque changes for higher temperatures or I_s values. In some cases, cross-coupling effects can affect the dq inductances, i.e. L_d and L_q would depend on γ.

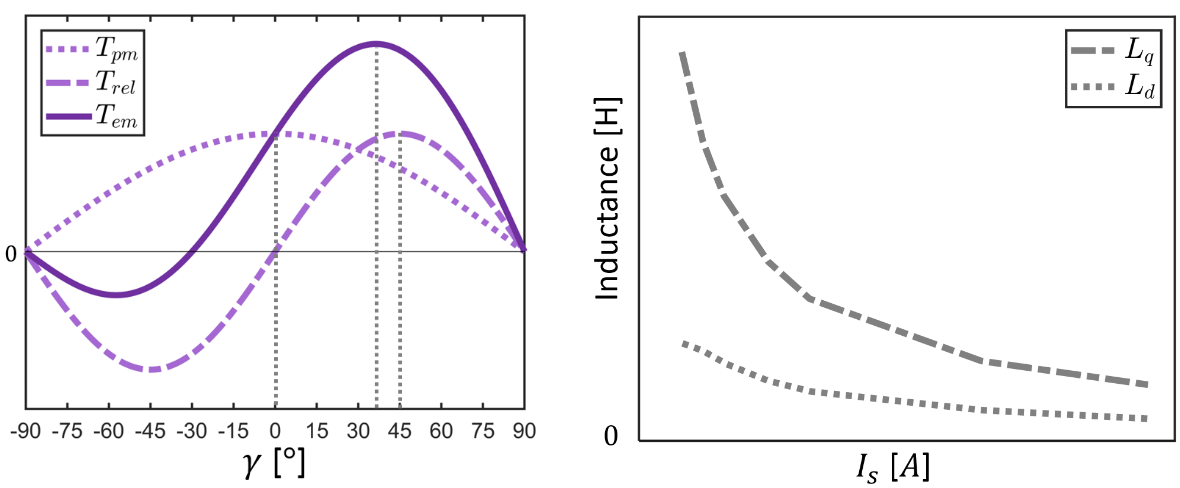

(a) (b)

Fig. 1.10 (a) Torque components vs. advance angle for a fixed current magnitude. (b) Variation of dq inductances against stator current magnitude.

1.2.4 Electric Drive System

In an electric drive, a voltage-driven source is required to operate an electric motor. A constant DC bus or link voltage, usually a battery supply, is connected directly to a closed-loop current-regulated, *pulse-width modulated* (PWM) inverter. By connecting each output phase of the PWM inverter between the DC link voltage and ground for different pulse widths or duty cycles, the output line voltage attempts to emulate a sinusoidal waveform in its fundamental component in order to excite the motor windings. The feedback signals include the line currents and the rotor position, usually measured through hall-effect sensors, encoders, resolvers, or sensorless position techniques. A current vector control algorithm accepts command signals such as torque or speed to produce the PWM inverter control signals. The inverter operation is demonstrated here through a Sine PWM method for a 3-phase, 2-level inverter as shown in Fig. 1.11.

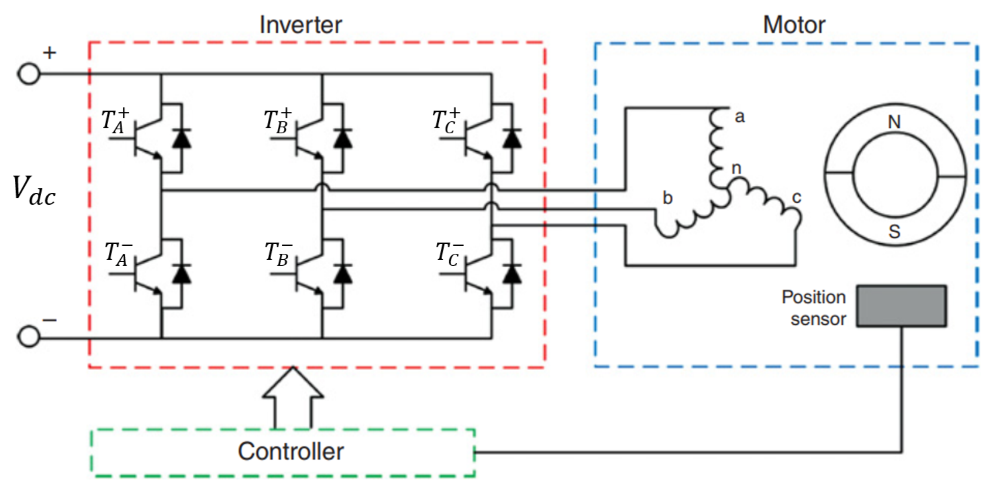

Fig. 1.11 Electric drive system: inverter, motor, controller [Rosu et al., 2017].

By converting a constant DC link voltage, V_{dc}, into balanced 3-phase PWM voltages, the inverter can drive the motor windings at a fundamental frequency, f_1. The voltage amplitude is modulated by comparing a triangular carrier waveform to a control sinusoidal voltage, while the switching frequency, f_{sw}, is varied by changing the carrier signal's frequency [Mohan and Undeland, 2007]. Every inverter leg of the 3-phase output consists of power transistors. For phase A, the upper transistor T_A^+ connects the phase output to V_{dc}, and the lower transistor T_A^- connects the phase output to ground. At any given time of the 2-level inverter operation, each phase output is either connected to V_{dc} or ground. For this inverter, a PWM line waveform V_{LL} similar to Fig. 1.12 is obtained. The fundamental component at a frequency of f_1 is buried within the PWM voltage and replicates a sinusoid. It is inevitable that the visible switching introduces unwanted harmonics into the terminal voltage supply.

For any modulation scheme, it is important to introduce metrics that quantify a PWM signal's quality: m_a is the amplitude modulation index in the linear region and m_f is the frequency modulation index given in (1.19). A higher m_f value ensures that more chops per electrical cycle represent the modulation signal. Increasing m_a increases the fundamental contribution of the PWM line voltage, $V_{LL_1}^{RMS}$, to the available DC bus voltage, V_{dc}. However, $V_{LL_1}^{RMS}$ cannot linearly increase for m_a values beyond 1 and instead begins to saturate outside the linear region. That is, $V_{LL_1}^{RMS}$ is a nonlinear function of m_a as explained below.

$$\begin{aligned} m_a &= \frac{2\sqrt{2}}{\sqrt{3}} \frac{V_{LL_1}^{RMS}}{V_{dc}} \\ m_f &= \frac{f_{sw}}{f_1} \end{aligned} \tag{1.19}$$

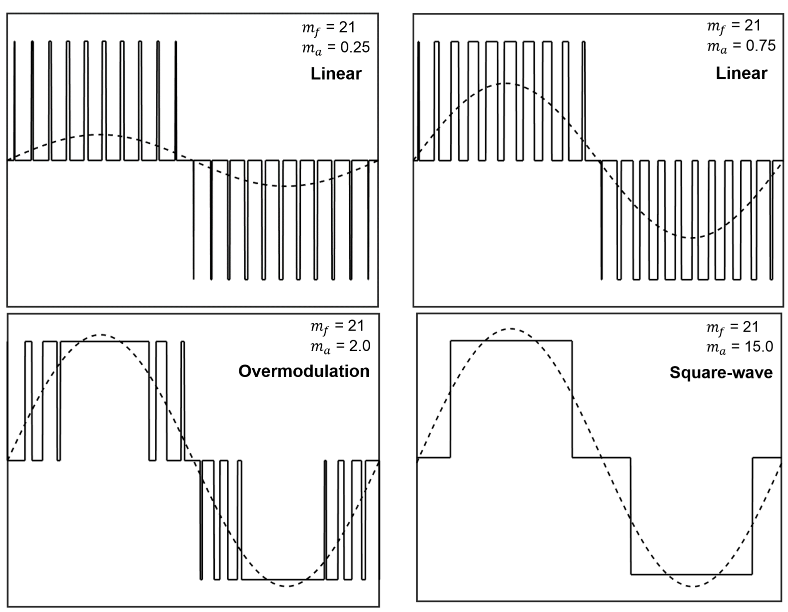

Fig. 1.12 Effect of varying m_a on the PWM line voltage, V_{LL}, for a fixed m_f. The fundamental component, V_{LL_1}, is shown as a dotted waveform.

Fig. 1.13 shows the effect of varying m_a on the PWM line voltage's fundamental. There are three distinct operation regions for any PWM scheme: linear, overmodulation and square-wave. In the linear region, $V_{LL_1}^{RMS}$ varies linearly from 0 to $0.612V_{dc}$ for m_a ranging from 0 to 1. This can be seen in the PWM waveforms of Fig. 1.12 for m_a values of 0.25 and 0.75. When the modulation signal's amplitude grows larger than V_{dc}, the PWM scheme enters the overmodulation region where m_a is greater than 1. For periods of time, the modulation signal is larger than V_{dc} causing the PWM line voltage to flatten with notches as shown in Fig. 1.12 for m_a of 2.0. Unfortunately, $V_{LL_1}^{RMS}$ can no longer increase linearly and enters the knee point of a saturation curve. High-order harmonics start to dominate when compared to the linear operation. For extremely high m_a beyond 3.24, the PWM line voltage resembles a square wave which sets a maximum limit of $0.78V_{dc}$ on $V_{LL_1}^{RMS}$ as displayed in Fig. 1.12. Typical fluctuations of a PWM signal are no longer visible with only 4 switches in a single period, i.e. each inverter switches only twice in one period. Low-order harmonics appear in the square-wave operation except for triplen harmonics (3, 6, 9, ...). A major disadvantage of the square-wave operation is that $V_{LL_1}^{RMS}$ can no longer vary for m_a, and only V_{dc} can be controlled. All these effects can be seen in the PWM waveforms of Fig. 1.12.

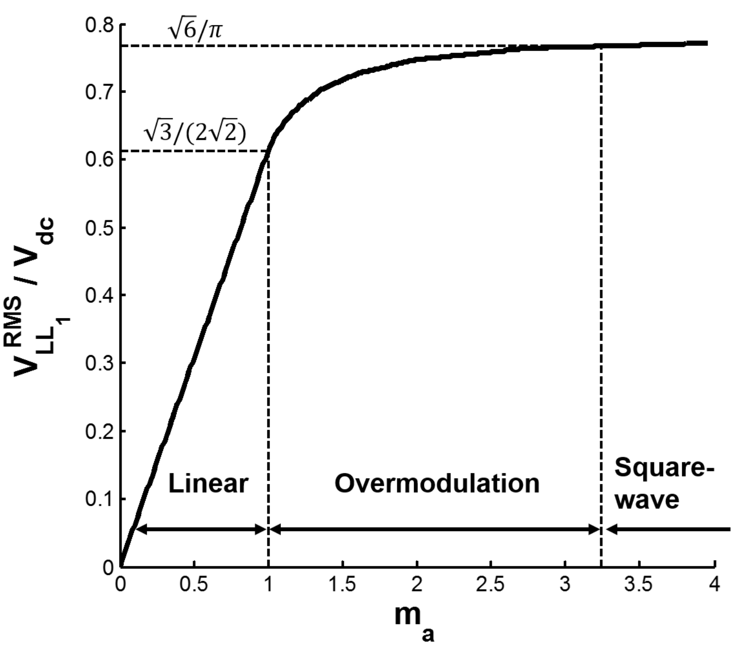

Fig. 1.13 Effect of varying m_a on the PWM line voltage (fundamental).

Fig. 1.14 illustrates a real-time control model for operating a synchronous AC motor when mechanically coupled to a load motor or dyno. At the first stage, the speed request, ω_m^*, is compared with the actual motor speed, ω_m, to produce the speed error, $\Delta\omega_m$. The actual speed is calculated using a speed observer and the rotor position, θ_m, that can be measured by a magnetic encoder. This $\Delta\omega_m$ error is then fed to a *proportional-integral* (PI) controller to generate the dq current references, $\boldsymbol{I}_{d,q}^*$. Next, these values are compared with the actual dq currents, $\boldsymbol{I}_{d,q}$, that are computed using the measured line currents, $I_{a,b,c}$, through current transducers and the ABC-to-DQ transformation block. Then, $\boldsymbol{\Delta I}_{d,q}$ is regulated by a second PI controller to produce the dq voltage references, $\boldsymbol{V}_{d,q}^*$, which are converted to ABC quantities, $V_{a,b,c}^*$, through an inverse Park transformation. These ABC voltages are mapped into time-varying duty cycles, $d_{a,b,c}^*$, using the DC bus voltage, V_{dc}. Finally, the inverter block generates PWM voltages to excite the motor's polyphase windings. This negative feedback transient loop is repeated until ω_m^* matches the actual speed, ω_m. Hence, the motor's field-oriented control consists of speed and current control loops, where the latter operates at a higher bandwidth. On the other hand, the dyno is torque-controlled using the torque sensor measurement, T, and a single current feedback loop. Note that the PI controllers can be tuned using the motor's lumped parameters. This real-time control model was used in [Hussain et al., 2017] for analyzing the effects of PWM excitation on the iron loss of a PM motor through experiment.

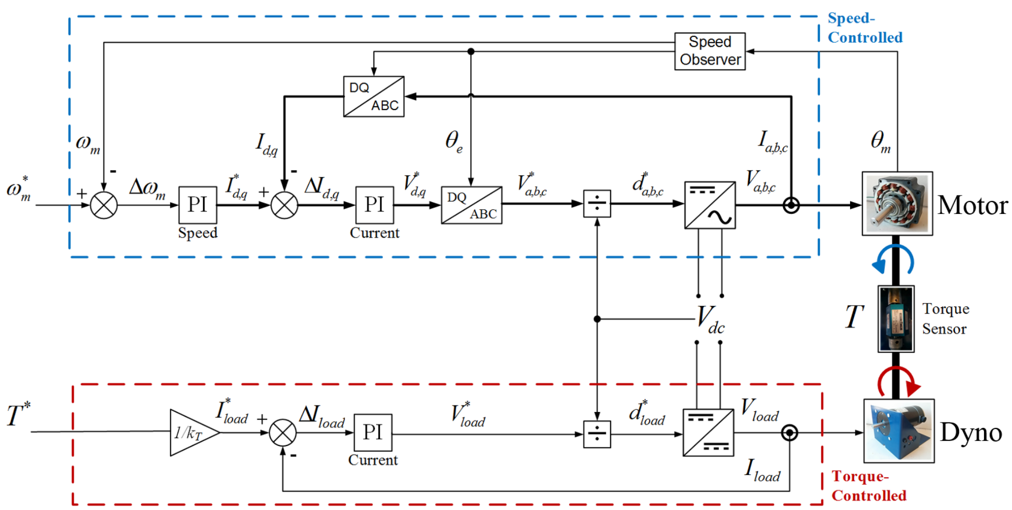

Fig. 1.14 Field-oriented speed control of a synchronous AC motor and torque control of a dyno acting as a load.

1.2.5 Modes of Operation

For an electric motor drive with limited inverter kVA capability, the motor characteristics against speed, N_m, are visually represented in Fig. 1.15. These include the electromagnetic torque, T_{em}, output power, P_{out}, stator voltage magnitude, V_s, stator current magnitude, I_s, advance angle, γ, and stator flux linkage magnitude λ_s. The corresponding mode diagram in the (I_d, I_q) plane is shown in Fig. 1.16. While the subsections below provide a brief summary with the help of both figures, a detailed explanation of variable-speed performances can be found in [Soong and Miller, 1994].

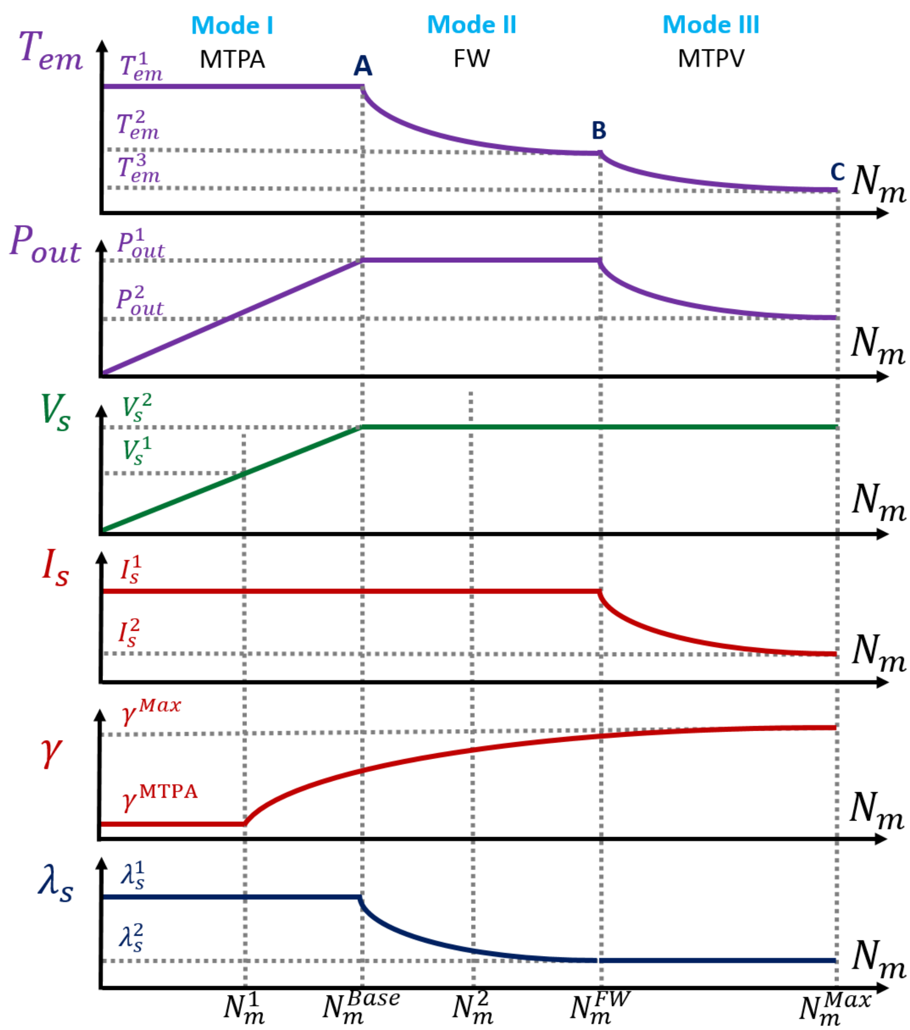

Fig. 1.15 Motor drive characteristics for different motor speeds.

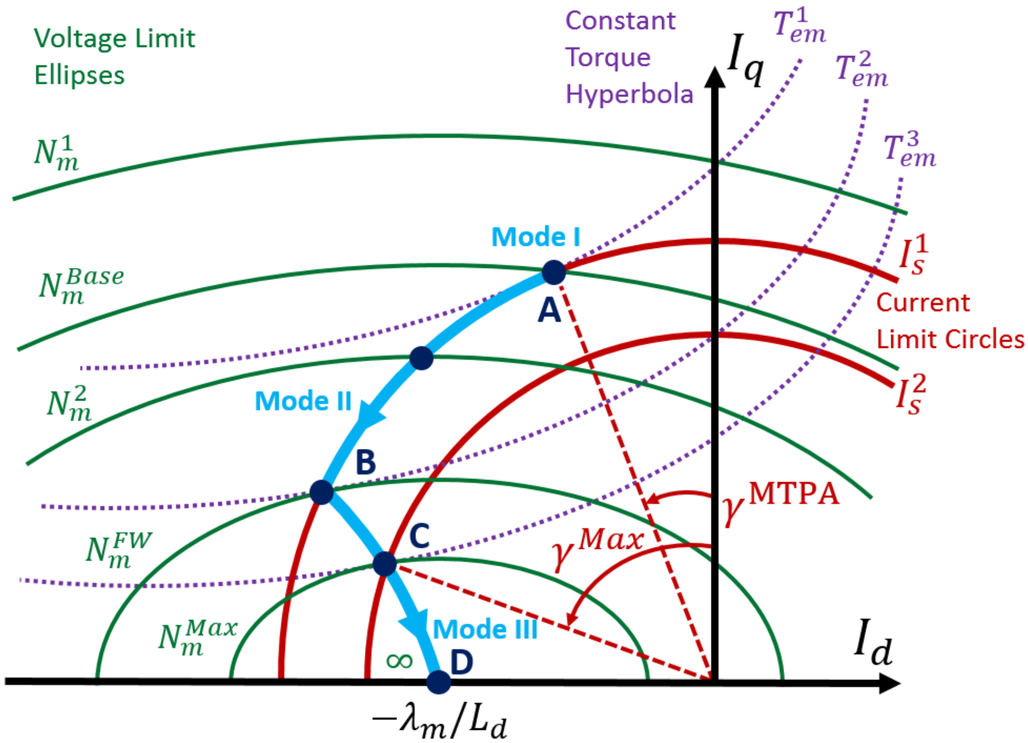

Fig. 1.16 Mode diagram including the maximum torque trajectory.

Mode I: Maximum Torque Per Ampere

From zero to base speed, N_m^{Base}, the electromagnetic torque, T_{em}, is kept constant under Mode I. In this operation, the stator current magnitude, I_s, and the stator flux linkage, λ_s, are also maintained. As the motor speed ramps up to N_m^{Base}, both the output power, P_{out}, and input voltage, V_s, increase linearly until the back EMF is equal to the terminal voltage.

The electromagnetic torque in (1.17) is a function of the motor's lumped parameters, λ_m, L_d and ξ, and the excitation conditions, I_s and γ. By fixing I_s for a given motor geometry, dq inductances from Fig. 1.10 (b) are chosen to calculate ξ. The λ_m parameter can be obtained in a similar way for a given temperature. This reduces the number of independent parameters to only I_s and γ for a fixed rotor structure. Fig. 1.10 (a) shows that for a constant current I_s, the torque-per-ampere curve follows a concave relationship with a local maximum with respect to the advance angle, γ. This implies that an optimal γ operating point exists, denoted as γ_{MTPA}, such that it maximizes the electromagnetic torque for a given current level

I_s, known as the *Maximum-Torque-Per-Ampere* (MTPA) control strategy. At high current magnitudes, the torque-per-ampere curves shear toward 90° due to the saturating q-axis inductance. The peak MTPA points require higher γ in order to demagnetize the saturated rotor iron paths and allow the motor to run at higher torque at the expense of additional rotor losses and decreased motor efficiency. Considering the maxima points for a range of stator currents, the MTPA-current trajectory follows a nonlinear relationship which requires knowledge of L_d and L_q for any I_s value.

Mode II: Flux Weakening

Above base speed, the stator voltage can no longer grow beyond the motor's back EMF, so it is kept constant by weakening the motor flux by increasing γ. If I_s is maintained at the same time, P_{out} is kept constant as well ensuring that T_{em} follows a speed-reciprocal relationship in Mode II. The phase voltage, V_s, known as the voltage-limit, can be represented in (1.20) using its dq-axis components. During steady-state, the maximum current-limit is similarly defined in (1.21). The voltage-limit is set by the battery supply voltage, while the current-limit is governed by the drive's thermal capacity. By expanding (1.20) using the stator voltage in (1.13) and ignoring the winding losses, the voltage-limit ellipse equation can be written in terms of ω_e, I_d and I_q. This means that for a fixed V_s, the radius of the voltage-limit ellipse shrinks at higher speeds. Note that the maximum V_s directly relates to the DC bus voltage, V_{dc}, through the inverter's operation, e.g. square-wave limit as in Fig. 1.13.

$$
\begin{gathered}
V_s^2 = V_d^2 + V_q^2 \\
\left(\frac{V_s}{\omega_e L_d}\right)^2 = \left(I_d + \frac{\lambda_m}{L_d}\right)^2 + \xi^2 I_q^2
\end{gathered}
\tag{1.20}
$$

$$
I_s^2 = I_d^2 + I_q^2 \tag{1.21}
$$

Referring to the (I_d, I_q) plane of the mode diagram in Fig. 1.16, a current-limit circle centered at the origin is plotted using (1.21) for a given I_s. The constant-torque hyperbolas are graphed using (1.17) to illustrate the feasible operational points for any rotor speed. Multiple voltage-limit ellipses are displayed using (1.20) for different rotor speeds. The voltage-limit ellipses are observed to be centered at -λ_m/L_d with its eccentricity governed by ξ. A higher saliency ratio value further stretches the voltage-limit ellipse along the d-axis.

Note that N_m grows by increasing the value of ω_e through the drive frequency.

Given that the size of the voltage-limit ellipse shrinks for increasing rotor speeds through (1.20), this smaller ellipse imposes fewer feasible dq current points. For producing the same torque at a higher speed, the operating dq current point should move along the constant-torque hyperbola outside the current-circle. However, the current-limit circle does not allow this current magnitude to increase. The output torque is then forced to decrease, while the dq current point shifts along the current-limit circle. This inherent tradeoff between the current-limit circle and voltage-limit ellipse becomes more apparent at higher speeds.

The operation discussion above can be summarized as follows using Figs. 1.15 and 1.16. Ranging from zero to rated motor speed, Mode I dictates a current-limited, constant-torque region where the maximum torque is obtained for a given operating current magnitude and MTPA advance angle γ_{MTPA}. The voltage-limit is still not violated, and point A in Fig. 1.16 corresponds to the boundary intersection of the constant-torque hyperbola with the current-limit circle. After the rated motor speed, Mode II is both current and voltage-limited. Since the voltage-limit ellipse has become smaller at a higher rotor speed, it is no longer possible to sustain the same constant torque at point A. For higher speeds, the torque produced is forced to decrease by moving along the feasible current-limit circle and maintaining constant power. The intersection between the current-limit circle and voltage-limit ellipse is illustrated by the bold trajectory line between points A and B: the current advance angle γ increases, while the current magnitude I_s is kept constant. Increasing γ demagnetizes the motor flux to maintain the same back EMF, hence naming this strategy as *Flux-Weakening* (FW) control.

Mode III: Maximum Torque Per Volt

Beyond a certain speed in the FW region, N_m^{FW}, the voltage-limit ellipse shrinks inside the current-limit circle. This means that I_s must be decreased, which affects T_{em} and P_{out}. Between points B and D, Mode III represents a voltage-limited region to provide the highest torque possible for a limited voltage supply. By intersecting the constant-torque hyperbolas with the voltage-limit ellipse along a tangent, it is theoretically possible to reach an infinite motor speed at point D. This voltage-limited strategy is known as *Maximum-Torque-per-Voltage* (MTPV) control. However, an infinite motor speed is never reached and a maximum mechanical speed, N_m^{Max}, at point C is selected based on the peak mechanical stress levels of the rotor structure.

1.3 Literature Review

This section reviews the current research and challenges related to machine design, multi-physics simulation, high-performance computing and efficiency maps while identifying gaps.

1.3.1 Synchronous Reluctance Machines

A synchronous reluctance machine produces reluctance torque through a magnetically salient rotor structure using flux barriers. Through an ideal set of sinusoidally-distributed coils excited by balanced sinewave currents, a smoothly-rotating stator field is produced in order to force the salient rotor to rotate and align its primary magnetic axis with the stator field. This helps to minimize the overall reluctance path between the stator and rotor structures thereby producing reluctance torque. Fig. 1.17 displays a SynRM from ABB typically used for fixed-speed applications such as fans, pumps, and compressors. The biggest difficulty with pure SynRMs, however, is geometrically designing their rotor structures. In fact, Kostko [1923] originally stated that a SynRM's poor performance is directly correlated to its poor geometric construction. By properly designing the stator and rotor lamination structures, the SynRM torque performance can be optimized by forcing the machine flux through the desired flux paths [Matsuo and Lipo, 1994; Soong et al., 1995].

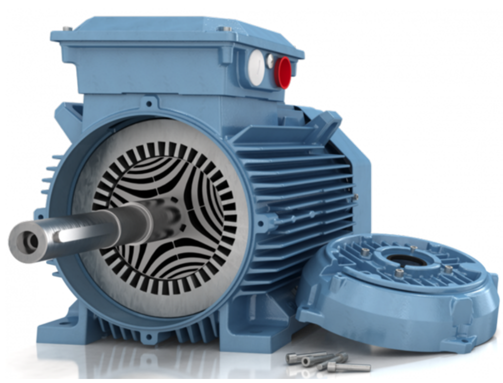

Fig. 1.17 Synchronous reluctance motor [ABB, 2012].

In general, there are two SynRM rotor structures which differ by their axis of stacking laminations: *axially-laminated anisotropic* (ALA) or *transversally-laminated anisotropic* (TLA) as illustrated in Fig. 1.18. The rotor d-axis is oriented towards the minimum inductance path, while the rotor q-axis is pointed to the maximum inductance path. ALA rotors are constructed by stacking multiple axially-laminated steel sheets in the radial direction, while TLA rotors employ regular rotor laminations in the transverse direction. The ferromagnetic layers with iron segments are known as *flux carriers*, while the air insulated layers are called *flux barriers* (or magnets in the case of PM-assisted rotors, as discussed later). The barriers in TLA rotors are held together using the tangential ribs shown in Fig. 1.8. The ALA rotor structure has a higher saliency ratio ξ than the TLA type as reported in [Staton et al., 1993] since the ALA's d-axis inductance is smaller. The lack of tangential ribs in ALA rotors reduce the leakage flux passing through the flux barriers as seen from Fig. 1.9 (b). Nowadays, the TLA structure is preferred because it employs standard iron lamination cutting similar to the manufacturing process of an *induction machine* (IM) stator.

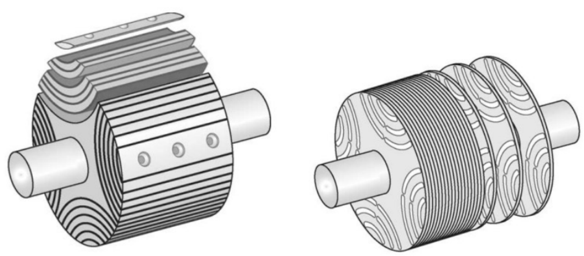

(a) (b)

Fig. 1.18 SynRM rotor laminations [Fukami et al., 2008]: (a) ALA, (b) TLA.

Generally, SynRMs can produce higher torque and efficiency levels compared with IMs for a constant power loss or operating temperature as presented in the theoretical and experimental results of [Lipo, 1991; Haataja, 2003; Boglietti et al., 2005]. At rated operation for the same motor volume and winding temperature, a SynRM performs better due to the elimination of the line-start cage which itself introduces rotor ohmic losses. This comparison has also been experimentally validated through ABB's recent SynRM production line ranging from 17 to 350 kW in output power. ABB [2012] has demonstrated that their SynRMs have smaller frame sizes and higher efficiency levels than their IM counterparts for supplying the same torque. Other advantages of SynRMs include faster dynamic performance due to smaller rotor sizes, synchronous speed behavior, simple rotor manufacturing using existing IM infrastructure, and low material cost due to the absence of expensive rare-earth magnets [Hendershot and Miller, 2010]. However, SynRMs generally suffer from significant torque ripple which has been addressed for different problems as discussed below.

Design Approaches

Moghaddam [2007] focused on the design of a 4-pole SynRM using a combination of FEA and analytical methods for improving the average torque and torque ripple. In his 15 kW application, Moghaddam found that increasing the number of flux barriers improved the electromagnetic performance in a saturating manner; there was no incremental benefit beyond 5 barriers. Also, he analyzed the sensitivity of the rib widths and airgap thickness on the output performances from which he concluded that the flux carrier and barrier widths play a prominent role in the rotor's structure. Similarly, [Pellegrino et al., 2013] studied round and angled-shaped flux barriers and reported that modeling two parameters per barrier (i.e. barrier's thickness and angular position at airgap) presents a good tradeoff between simulation results and computational time. Fig. 1.19 shows three typical barrier shapes used.

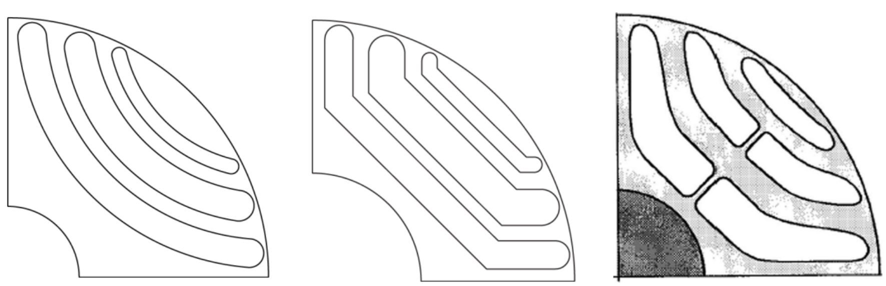

(a) (b) (c)

Fig. 1.19 Typical SynRM barrier shapes [Lu et al., 2017; Vagati et al., 1998]: (a) round, (b) angled, (c) fluid. Only a quarter rotor cross-section is shown.

In addition, a 2^{nd} order response surface methodology coupled with central composite sampling was used to diminish the torque ripple of a 6-slot 4-pole concentrated winding SynRM [Park et al., 2006]. This slot/pole combination was unsurprisingly prone to torque pulsation and a minimum torque ripple of 63.8% was achieved for a 5-barrier angled shape compared to 109.8% for the initial model. To achieve low torque ripple SynRMs, Vagati et al. [1998] have established a well-known analytical relationship between the number of stator slots and rotor flux barriers for a given pole number based on magnetic equivalent circuits. They stated and validated that per pole pair, the difference between the number of stator slots and rotor slots should be 4 apart from each other to inhibit dominating torque harmonics. From this relationship, the number of barriers can be chosen. Other combinations may or may not achieve lower torque ripple.

Furthermore, Howard et al. [2015] recently proposed an asymmetric flux barrier parameterization with more than 29 variables to model flux barrier shapes. The asymmetry can be either defined to be a different flux barrier arrangement for each rotor pole or the rotor's d-axis. They applied it to 24-slot and 36-slot SynRMs with torque ripples of 5.7% and 3.9% respectively while operating around 11 Nm and below 6000 RPM. Upon considering the same two objectives, the torque ripple was further reduced by skewing the rotor, as in common practice. Their results are not surprising since Sanada et al. [2004] have demonstrated earlier that asymmetric flux barrier arrangements yield significantly lower torque ripples. Sanada et al. compared symmetrical and asymmetrical structures of two IPM motors and a SynRM. They reported that the torque ripples reduced from 65%, 69%, and 50% to 10%, 12%, and 10% respectively while roughly maintaining average torque values of around 1.4 Nm, 1.9 Nm and 1.1 Nm for the three motors. Fig. 1.20 illustrates these employed asymmetric flux barriers. Likewise, Howard and Kamper [2016] extended their previous work by optimizing their asymmetrical rotor model using a weighted factor approach for three objectives (average torque, torque ripple, power factor). Interestingly, it was demonstrated that a Pareto optimal relationship exists between average torque and power factor in a per-unit objective space independent of power-level, pole number, and barrier number. In another work, Degano et al. [2016] automatically designed a fluid 3-barrier SynRM for three objectives (average torque, torque ripple, power losses) using a mixture of a stochastic optimization method coupled with electromagnetic FEA and a computationally efficient approach (10 seconds per sample). Upon finding the Pareto front (i.e. the set of optimal solutions), a design was selected with a low torque ripple of 8% and an average torque of around 117 Nm.

Another study of SynRM design methodology similarly kept the stator configuration fixed and a 3-barrier round-shaped rotor was designed (6 geometric variables) to both increase the average torque and decrease the torque ripple [Pellegrino et al., 2015]. Although the multi-objective optimization found designs matching well with experimental results, it may not be computationally efficient to explore across all 6 geometric design dimensions to find a set of Pareto front solutions. This problem becomes more prominent during the global search for optimal designs during the initial stage. To address this high dimensionality issue, [Mohammadi et al., 2017a] found optimal designs of a multiple-barrier SynRM rotor for a fixed stator using a computationally efficient approach (explained in detail in Chapter 3).

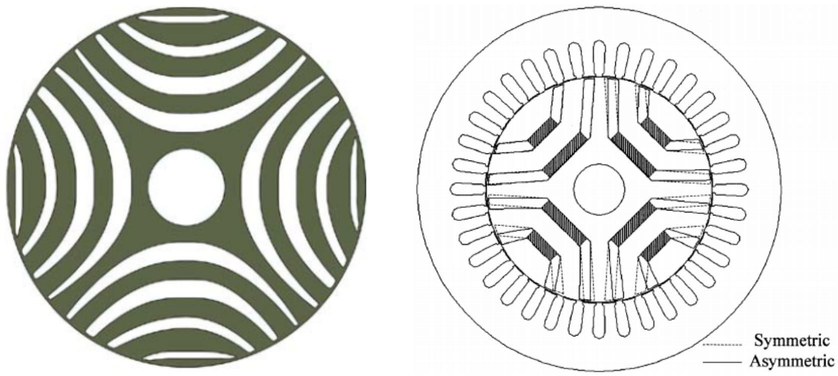

(a) (b)

Fig. 1.20 Asymmetric flux barriers in SynRM rotors: (a) [Howard et al., 2015], (b) [Sanada et al., 2004].

Optimal geometric relationships or constraints between different parameter spaces (single-barrier and multiple-barrier rotors) were extracted to reach highly accurate optimal solutions while saving computational time. An optimal region was first identified in the design space for a single-barrier rotor. Next, this optimal region was mapped to a multiple-barrier topology in order to constrain its sampling region during a multi-objective optimization. In addition to reducing the torque ripple, a benefit of this approach was to neglect suboptimal solutions and cluster optimal regions for the rotor optimization. A key difference with [Mohammadi et al., 2016] was that two SynRM case studies were considered with different rotor configurations (1, 2, 3, 4 flux barriers) for all possible variations in the feasible design space. Fig. 1.21 displays the two response surfaces of average torque and torque ripple as functions of the widths of the flux carrier and barrier for a round-shaped single-barrier SynRM. Both surfaces were characterized using NNs to map nonlinear relationships between the inputs and outputs in order to save computational time, instead of using direct FEA evaluations. Note that the average torque's map is unimodal where the optimal solutions cluster together around a single peak. This clustering provides useful information to motor designers on where to search for optimal structures. The analysis also extended the work of Hudák et al. [2006] which fixed the flux barrier ratio, otherwise known as the rotor insulation ratio, across all barriers. However, they employed round-shaped barriers and assumed that average torque is more desirable than torque ripple for the clustering of optimal solutions. It is worth considering how the location of the optimal regions would change for a multiphysics problem.

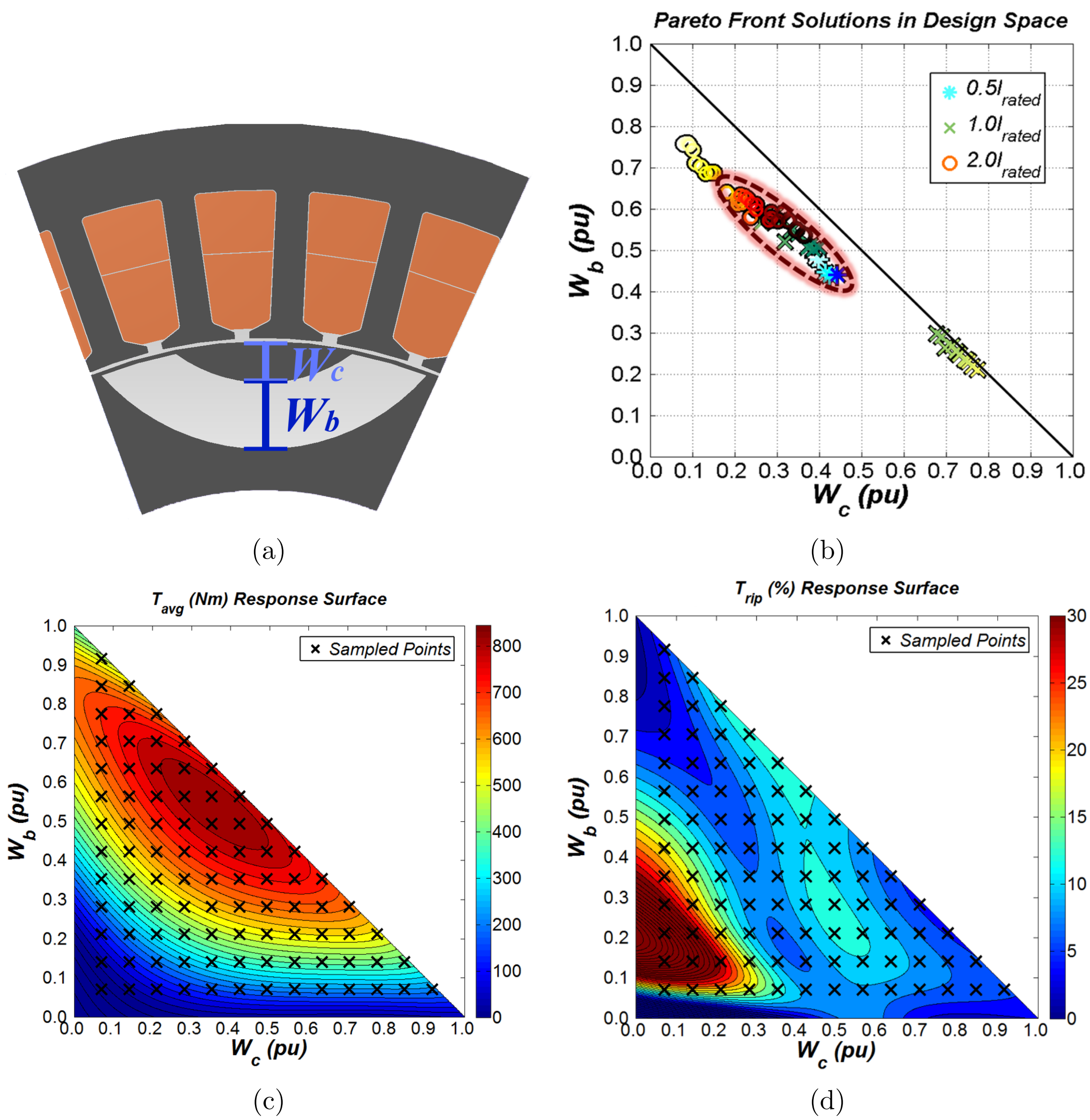

Fig. 1.21 [Mohammadi et al., 2016]: (a) Rotor variables of a round-shaped single-barrier SynRM, (b) elliptical cluster of optimal solutions in the design plane, (c-d) response surface maps of average torque and torque ripple.

Permanent Magnet Assist

Although SynRMs cannot maintain a constant power speed range and suffer from poor power factor, a slight addition of PMs in their rotor structures can help them compete directly with pure PM and IPM machines as demonstrated in [Bianchi et al., 2014] and in the second generation design of Chevrolet Volt's traction motor [Jurkovic et al., 2015]. For instance, Ooi et al. [2013] demonstrated a round-shaped flux barrier design entirely filled with low-cost ferrite magnets. Its efficiency levels exceeded 90% beyond base speed, while the PM demagnetization was controlled at high currents by tapering the barrier edges and including a center rib. The proposed motor could also meet the constant torque and power regions required for traction applications. In [Cai et al., 2016], a PM-SynRM under study (88% reluctance torque) was reported to have superior torque and flux weakening performances compared to a V-shaped IPM motor (78% PM torque) with similar ratings and ferrite magnets. Moreover, Vagati et al. [2014] presented general guidelines for the design of PM-SynRMs with ferrite magnets based on analytical derivations using magnetic circuits validated through FEA and experimental results. For example, one guideline states that small and medium-sized machines with natural ventilation would not suffer from demagnetization during transients. Due to their negative temperature coefficient, ferrite magnets may need to be warmed up to avoid demagnetization at lower temperatures.

Nevertheless, a PM-SynRM with superior characteristics can be designed by following a 3-step process as outlined in [Lu et al., 2017] and followed in [Mohammadi, 2015] for a 200 kW traction application. A flowchart for this PM-assisted SynRM design process is shown in Fig. 1.22. In Step 1, a SynRM's stator is sized based on its cooling and electrical constraints as described in [Pyrhonen et al., 2009; Hendershot and Miller, 2010]. For instance, the winding configuration and stator slot area are set to withstand the maximum current densities during normal and peak operations. Once the stator geometry and winding configuration are fixed, the SynRM rotor is geometrically designed to maximize its saliency ratio thereby increasing average torque while accounting for a low torque ripple. Next, all the rotor flux barriers are filled with equivalent PMs (i.e. PMs with variable remnant flux densities not available in the market) in order to meet the required power-speed characteristic in Step 2, especially in the flux weakening region. While these equivalent PMs with varying remnant flux density levels are not necessarily the final ones used during manufacturing, they are added to reach constant power operation at rated condition. Finally, in Step 3, the equivalent PMs are replaced with commercial ones concentrated in specific regions of the rotor barriers. Their locations may be influenced by possible demagnetizations and so must be carefully checked in advance. It is noticeable from the above procedure that the second and third steps are relatively straightforward once the baseline SynRM is readily available. Therefore, more effort is required to design the geometry of SynRM rotors in the first stage by varying the flux barrier shapes, widths, positions, etc. A further difficulty lies in accounting for multiphysics problems which impact the selection of optimal designs.

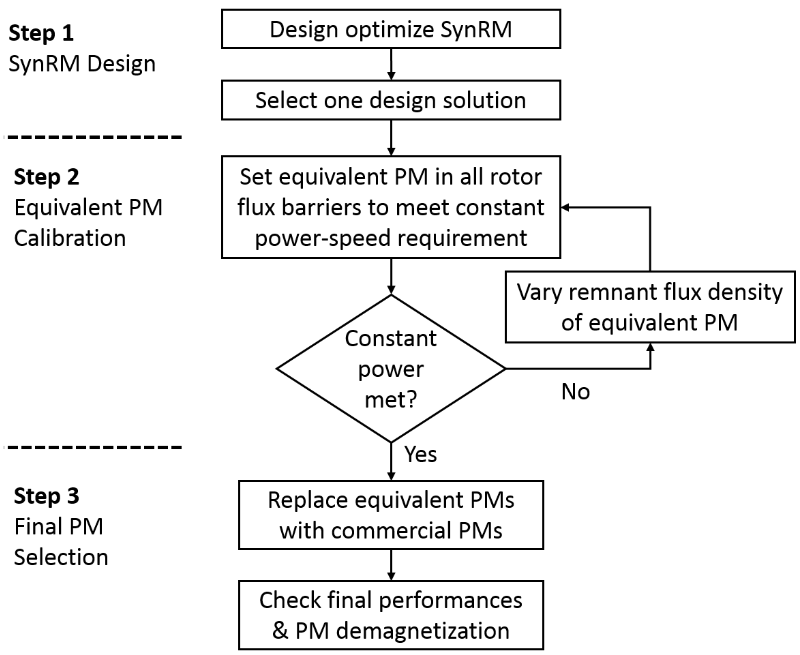

Fig. 1.22 3-step design process for a PM-assisted SynRM [Lu et al., 2017].

1.3.2 Multiphysics Challenges

With increasing computational power in recent years, multiphysics simulations have been a growing trend within industry and academia in order to model the different physical phenomena present in science and engineering systems [Keyes et al., 2013; Rosu et al., 2017]. This allows users to design optimized systems with more insight than just focusing on individual subsystems. In terms of electric machines, there are three main physics which influence their day-to-day operation: electromagnetic, mechanical and thermal.

Fig. 1.23 presented in [Bracikowski et al., 2012] describes the coupling among the different physical phenomena well. During startup, the machine's windings are fed with electrical voltage and current, V_s and i_s, which then produce magnetomotive force and flux, F and ϕ. Next, the interaction of the stator and rotor fluxes generate an electromagnetic torque, Γ_{em}, which rotates the shaft at a given speed, Ω. This increase in rotor speed limits the input current due to the increasing back electromotive force, E_g. At the same time, the winding resistance, R_s, the machine's flux density, B, and the converter's switching frequency, f_s, all introduce power losses which decrease the overall efficiency, η. These losses dissipate heat and increase the temperature, T, of different components over time, based on the cooling system used. This temperature rise affects the magnetic material characteristics and can degrade performance. Similarly, the increase in shaft speed subjects the rotor to high centrifugal forces that can expand and deform its structure. If not carefully designed, the rotor bridges or ribs could approach the material yield strength and break. Also, the harmonics of the airgap flux density, B_g, interact with the stator's natural frequency causing resonance and acoustic noise, L_p. Hence, it seems apparent how the different physical phenomena can impact the overall behavior of an electric machine. Focusing only on the electromagnetic performances during a SynRM's design process may not account for all these effects.

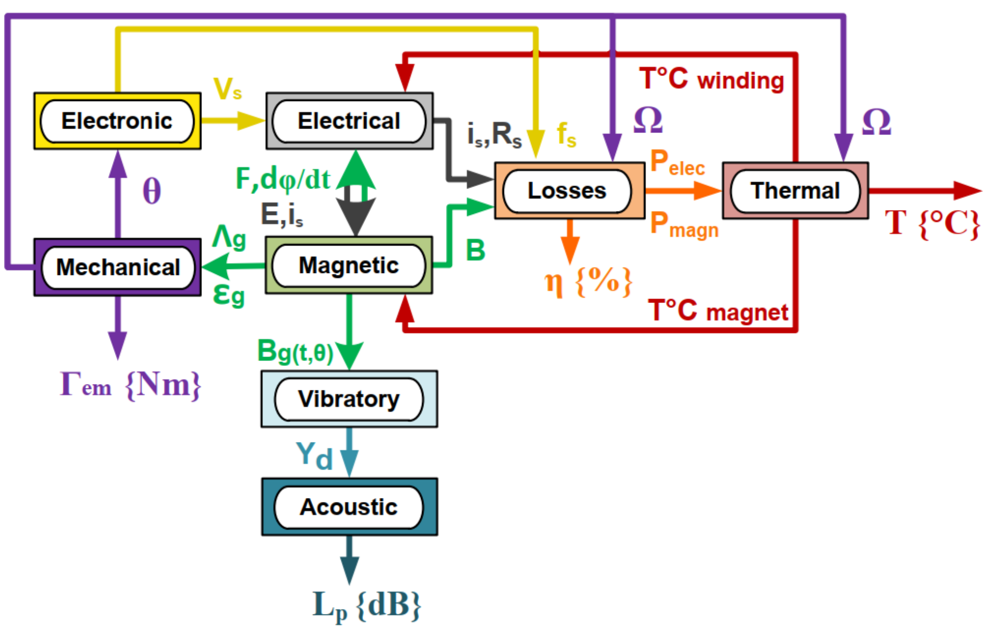

Fig. 1.23 Multiphysics coupling in machines [Bracikowski et al., 2012].

Mechanical Issues

The design of SynRMs poses significant challenges in terms of the machine's electromagnetic and mechanical performances as discussed in [Taghavi and Pillay, 2015]. For instance, one way to maximize the saliency ratio for a given SynRM is to reduce its pole number. This, however, degrades the machine's average torque and torque ripple, while smaller pole numbers introduce manufacturing and thermal problems due to longer stator end windings. On the other hand, increasing a SynRM's pole number can increase its torque-to-volume density, reduce its torque ripple, lower its converter ratings, and improve its mechanical robustness. However, the feasibility of manufacturing rotor laminations becomes questionable for high-pole small-sized motors. It is hard to geometrically fit all the flux carriers and barriers within a constrained rotor space. In addition, the tangential ribs are important parameters to consider in practical problems. Despite offering structural support to SynRM rotors operating at high speeds, fluxes circulating along these ribs and flowing through the barriers typically increase the d-axis inductance thereby reducing the electromagnetic torque. Ideally, they should be as small as possible to eliminate the contribution of leakage fluxes.

In fact, Taghavi and Pillay analytically showed that the electromagnetic torque diminishes in proportion to the tangential rib's width, lamination thickness, q-axis flux density, and the square of the pole number. From a mechanical perspective, these widths should be thick enough to withstand mechanical stress at different operating speeds and avoid radial deformation. Once the maximum stresses are computed using structural FEA or analytical methods, the maximum allowable rotor speed can be estimated as demonstrated in [Kolehmainen, 2010]. Compared to a traditional fixed bridge rotor with a large stress of 288 MPa along its bridges, Kolehmainen [2010] proposed a dovetail-type topology without any supporting bridges to achieve a maximum stress below 80 MPa at 3000 RPM permitting higher operating speeds (74% lower stress than steel's 305 MPa yield strength). Fig. 1.24 demonstrates the stress distributions for the two topologies. This mechanical benefit, however, compromised the electromagnetic performance since the average torque reduced by about 18% against the traditional design. Hence, electromagnetic and mechanical performances were in conflict with each other. Also, [Dziechciarz et al., 2016] similarly studied two 4-barrier SynRM rotors (round and fluid shapes) for their electromagnetic and structural aspects. They reported that fluid-shaped barriers perform better and adding ribs to the first barrier closest to the shaft is required to withstand maximum speed. In an alternative worst-case approach, Barcaro et al. [2014] performed analytical static stress analysis using the centrifugal and magnetic pressure forces on an IPM rotor to accordingly find the minimum widths of the tangential ribs. Despite the problem's simplification through algebraic equations, the calculated analytical values of the maximum von Mises stress were always found to overestimate the FEA solutions. This result suggests that static stress analysis can be a useful tool to effectively remove infeasible rotor designs when performing electromagnetic simulations without the need for time-consuming structural FEA simulations. A similar approach was also followed in [Lu et al., 2017].

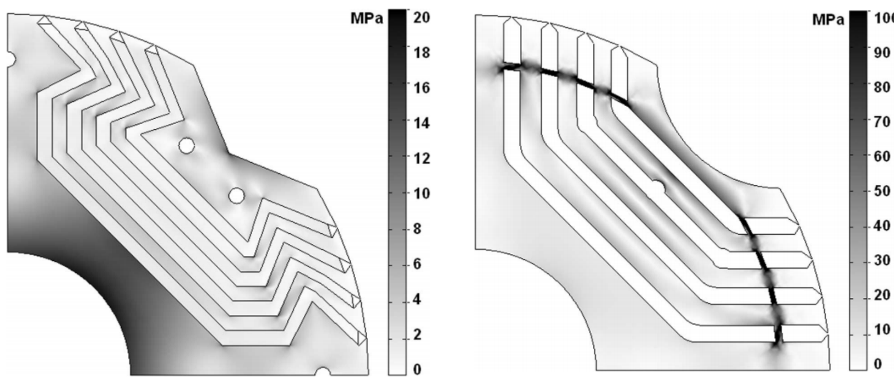

(a) (b)

Fig. 1.24 von Mises stress distributions for two SynRM rotor topologies in [Kolehmainen, 2010] at 3000 RPM: (a) dovetail, (b) fixed bridge.

Thermal Issues

Power losses in electric machines contribute to heat production which is typically accounted as part of the cooling requirements during an initial design stage. If a motor is not carefully designed to meet these requirements, certain regions inside its structure may heat up excessively and cause irreversible effects such as breaking the winding insulation, demagnetizing segments of PMs or even exceeding the material's Curie temperature. Most thermal variations are linked with winding resistances while iron losses (hysteresis and eddy current) contribute slightly as well. Accurately predicting an electric machine's temperature distribution can help in downsizing the machine and its cooling system. With respect to PM-assisted SynRMs, particular attention must be invested during the design process to avoid demagnetization in sensitive parts of PMs.

Different approaches are used to predict the thermal performance of an electric motor [Boglietti et al., 2009]: *lumped parameter* (LP) and FEA. A heat-transfer LP network is similar to an electrical circuit where conduction, convection and radiation are all accounted through thermal resistances (dependent on the geometric, material and cooling data). The power losses act as input "currents" from which the nodal temperatures are computed. An advantage of this thermal model is its computational speed which permits rapid thermal calculations as discussed in [Mellor et al., 1991; Staton and Cavagnino, 2008]. Commercial software such as Motor-CAD® allow users to model such networks considering different motor components, including the rotor and stator structures, windings, housing and cooling system [Staton, 2005]. Another approach to find a motor's thermal response is through FEA. The power losses calculated using electromagnetic FEA are used to set up the thermal FEA model that can handle complex geometries, 3-D end effects and individual winding strands in a stator slot. Several works have attempted to couple electromagnetic and thermal simulations together using different approaches as discussed below.

For example, Jiang and Jahns [2013] developed a two-way electromagnetic-thermal coupled FEA model of a 30 kW fractional-slot concentrated winding surface PM machine to check the machine's safe operation. After setting the initial temperatures, a 2-D transient electromagnetic simulation is run to feed the component losses to the 3-D thermal FEA. If the temperature convergence criteria is not met, the process repeats for more coupled iterations. Otherwise, the procedure stops and the final performances are reported after 2 to 6 coupled iterations. The same procedure is implemented in the MotorSolve® package of [Mentor-Infolytica Corporation, 2018] that relies on MagNet® and ThermNet®. While rated current densities are typically chosen in the initial stage of the classical design process, Jiang and Jahns demonstrated that these empirical values may not work in a practical setting due to the winding's insulation limit and PM demagnetization as shown in Fig. 1.25. Beyond these limits, an electromagnetic model overestimates the produced torque and may generate incorrect results. It may become necessary to perform a coupled simulation to find the maximum current density safe for operation. The authors even extended their previous analysis by reducing the PM motor's total mass using a surrogate-based approach in [Jiang and Jahns, 2014]. A NN was trained using 300 design samples to predict the maximum current density (6 inputs, 1 output, 1 hidden layer with 12 neurons). In a direct-FEA optimization approach, a single-objective problem was solved using differential evolution which evaluated

1500 designs including 7500+7500 transient electromagnetic and static thermal FEA simulations. All computations were reported to be completed in about 11 days on a single desktop computer. Upon using a NN with electromagnetic FEA, coupled simulations were no longer required and the optimization instead completed in about 4 days while reaching the same optimal solution as the direct-FEA optimization. Moreover, Sarikhani and Mohammed [2014] tackled the multiphysics design optimization of a PM motor using electromagnetic FEA and thermal lumped parameters. They formulated a multi-objective problem based on penalty functions to reduce the PM's temperature, copper and PM areas, torque and speed ripples, and total mass while considering several constraints. Similarly, Wang et al. [2015] employed a lumped parameter thermal model coupled with electromagnetic FEA for PM motors and SynRMs. A reduced dependence was reported between operating temperatures with core and rotor losses in both motor types thereby enabling partial decoupling of their problem. This information helped them reduce the number of simulation iterations necessary for convergence from six to two in order to reduce the total computation time. Lastly, Fatemi et al. [2016b] optimized an IPM motor design while considering different cooling systems and winding configurations (6 independent runs, 6600 designs each). For each configuration, a parallel sensitivity analysis was carried out to find which geometric variables influence the performance metrics.

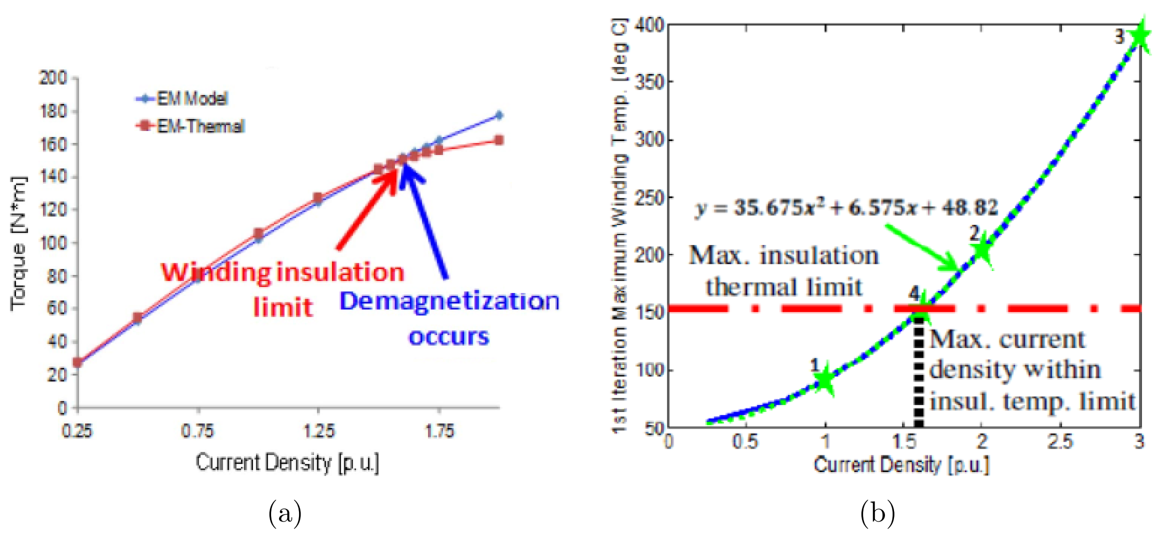

Fig. 1.25 Effects of coupled electromagnetic-thermal simulations [Jiang and Jahns, 2013]: (a) torque and (b) temperature vs. current density.

Acoustic Issues

Electric machines such as SynRMs may be prone to noise and vibration during normal use. If motors are not carefully designed to inhibit vibrational harmonics, their physical structure will emit undesirable acoustic noise in the surrounding environments. Some examples of possible noise sources include cogging torque (for PM-based motors), torque ripple, unbalanced rotors with eccentricity, worn bearings, and improper load coupling [Yang, 1981; Vijayraghavan and Krishnan, 1998].

In general, noise in electric machines arises from electromagnetic, mechanical, and aerodynamic sources [Gieras et al., 2005]. Also, magnetostrictive forces change the physical dimensions of a magnetic material in response to the magnetization. These forces inside the steel laminations of electric machines are insignificant, but cannot be ignored in transformers [Gieras et al., 2005]. Experimental results presented in [Le Besnerais, 2016] indicate that magnetostrictive effects do not need to be modeled when analyzing the acoustic noise in rotating machinery for different power ranges. Since this research focuses on electromagnetic calculations, only these sources are considered and primarily arise from the interaction of the airgap magnetic field with the stator structure. The term "sound pressure level", P_{SL}, is adopted instead of loudness to clarify the use of electromagnetic sources. Radial stresses along the airgap cause the stator teeth and back iron to vibrate resulting in audible noise as presented in Fig. 1.26. The rotor's vibrational behavior on acoustic noise is generally ignored for mechanical speeds below 100 kRPM as suggested in [Ede et al., 2002; Torregrossa et al., 2011]. To calculate P_{SL}, coupled FEA-based electromagnetic and structural simulations are required which could be computationally expensive during the design process.

Over the years, related research has demonstrated semi-analytical methods for predicting P_{SL} to avoid time-consuming co-simulations. For instance, recent studies have proposed simple, yet general approaches for different topologies of electric machines [Gieras et al., 2007; Islam and Husain, 2009; Islam et al., 2014; Chauvicourt, 2018]. The main drawback, however, was in modeling the stator core as a hollow, solid cylinder which neglects the slotting effect of practical stators. Although this approximation simplifies analytical expressions for computing the stator's natural frequencies, $\boldsymbol{f_s}$, approximation errors may lead to inaccurate predictions. In fact, Gieras et al. have identified this calculation as a significant challenge for the development of fast and accurate P_{SL} models. To address this problem and to represent stator variables such as the tooth width, tip thickness and tang angle, a new methodology

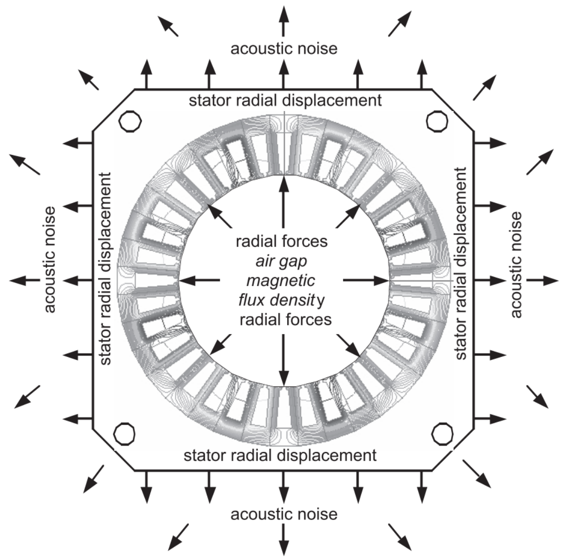

Fig. 1.26 Acoustic noise from electromagnetic sources [Gieras et al., 2005].

proposed in [Wang, 2017; Mohammadi et al., 2018b] and applied in [Rahman et al., 2017] were used. While this procedure is an approximation to detailed acoustic analysis, it can provide trends rather than accurate absolute values and identify low-noise regions while sampling several designs of electric machines.

The calculation procedure for P_{SL} which decouples the electromagnetic and structural FEA simulations is explained as follows using Fig. 1.27. In Step 1, the motor design parameters are set including the geometry and excitation. Next in Step 2, electromagnetic and structural analyses are performed using 2-D transient and 3-D modal FEA respectively. Once the electromagnetic simulation reaches its steady-state, the normal component of the flux densities in the airgap, $\boldsymbol{B_n}$, is extracted. The stator's modal analysis in the structural simulation produces $\boldsymbol{f_s}$. Then in Step 3, the magnetic stress or pressure wave, $\boldsymbol{P_n}$, is computed which in turn subjects the stator teeth to normal forces, $\boldsymbol{F_n}$. The dominant amplitudes are situated at 0, 1, and multiples of the number of poles and slots. During normal operation, tangential components of the airgap flux density are usually much smaller than $\boldsymbol{B}_n$ and so are generally neglected. Then at a given rotor speed, the harmonics of $\boldsymbol{F_n}$ interact with $\boldsymbol{f_s}$ causing physical deformations on the stator teeth through radial displacements, A_{mr}. Summing A_{mr} for all m vibration modes and r force harmonics leads to the sound pressure in Pa, P_S, and the sound pressure in dB, P_{SL}. More details are presented in Section 2.2.3.

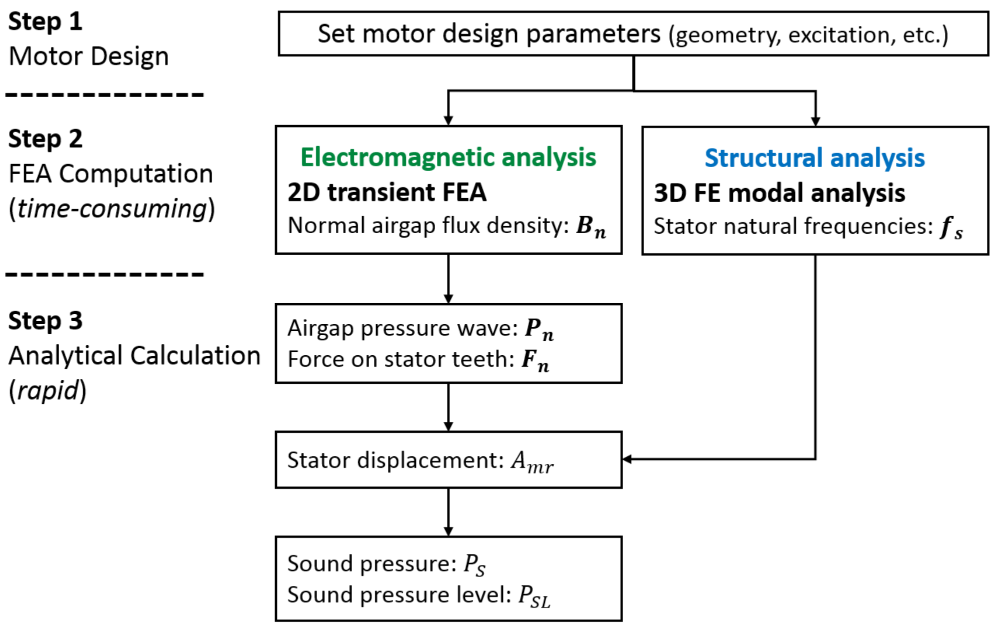

Fig. 1.27 Semi-analytical procedure for sound pressure level calculation.

While the simulation constants are known in advance and $\boldsymbol{B}_n$ can be retrieved from electromagnetic FEA, the difficulty lies in finding $\boldsymbol{f}_s$ for calculating P_{SL}. A structural FEA package like NX Nastran® of [Siemens PLM Software Inc., 2018] is required to accurately find the natural frequencies for different stator configurations and geometries. If such a specialized software is available, an accurate and effective way to quickly compute $\boldsymbol{f}_s$ for any stator geometry variation during the P_{SL} prediction is to build a surrogate model, such as a generalized regression NN [Specht, 1991], as suggested in [Wang, 2017]. A sampling technique, such as a full factorial [Jurecka, 2007] or a Latin hypercube [Park, 1994], can be used to systematically vary stator variables before fitting a NN model.

1.3.3 High-Performance Computing

Despite the benefit of using detailed FEA to predict a motor's electromagnetic performances, solving its nonlinear matrix equation for time-stepping problems introduces a computational burden when thousands of models are to be solved. Time-stepping becomes necessary for synchronous AC motors since the electromagnetic performances (e.g. torque, voltage, losses) are a function of rotor position which is synchronized to the winding currents in field-oriented control as explained in Section 1.2. At every time step and rotor position, a nonlinear matrix equation is solved (on the order of tens of thousands of degrees-of-freedom for typical 2-D FEA models) which increases the computational requirements for motor design problems.

Risticevic et al. [2016] attempted to solve a topology optimization problem for an IPM motor with a discretized 15×18 rotor grid (270 elements or variables, each containing either iron, air or PM). They ran 100 CPUs in parallel to evaluate 80,000 designs at base speed to solve their discrete optimization problem (time not reported). If more operation points or different stator combinations are considered, the computational time required to arrive at an optimal set of solutions or a Pareto front would be excessive (possibly requiring weeks of simulations), forcing the motor designer to compromise the model's complexity. An alternative approach to tackling such a computationally-intensive task is to employ a reduced-order model of an electric motor such as a *magnetic equivalent circuit* (MEC) or a surrogate-based approach that relies on FEA. For example, an FEA model can be evaluated in advance for different inputs (such as geometric or excitation) to train and build a surrogate model (e.g. low-order polynomial, kriging or NN) as a low-cost alternative for evaluating a motor's performances without additional FEA solutions [Silva, 2018].

While MECs provide analytical approximations for designing electric machines with simplified geometries [Tariq et al., 2010], accurate prediction of motor performances is not always possible. Nonlinear characteristics of magnetic materials including saturation play a prominent role in the operation of synchronous AC motors. Through past experiences, these nonlinearities can be taken into account through correction coefficients which may also introduce unwanted approximations [Niazi, 2006]. Likewise, there are many unknown variables in the early design stages which increase the computational expense of running FEA simulations. Hence, Bramerdorfer et al. [2016] discussed different ways of accelerating FE-based optimization for electric machines. Some of the proposed suggestions include: sampling using an effective design of experiments, setting up low-sized models for efficient data transfer, imposing geometrical symmetry (e.g. half-pole across a rotor), benefiting from circumferential and electrical periodicity, formulating proper optimization problems, employing state-of-the-art optimization algorithms, and quicker function evaluations such as those using surrogates. With increasing computational power to parallelize simulation tasks, more designs could be solved in less time especially using high-performance or cloud computing.

In summary, cloud computing allows users to access and use shared resources across the

Internet [Gai and Li, 2012]. The concept of a "cloud" is used to create an abstraction layer for users who may not necessarily know the intricate details of how their computationally intensive tasks are being deployed and solved in parallel but are interested to obtain results in less time. An interface between a novice user and the cloud service becomes important for a complete abstraction of the cloud's communication and distribution details. This new, on-demand computing paradigm offers experts in many fields, including electric machines, an unprecedented way to solve more complex problems (e.g. multiphysics design). It also helps shift the focus of acquiring and maintaining up-to-date hardware from the user's side to online platforms. Various names are associated and used in the literature to describe this concept with blurred differences among them, including high-performance, high-throughput or distributed computing. A key benefit of cloud computing is its modularity and expandability for solving computational tasks on a pay-as-you-go basis which provides cost-effective approaches for data-intensive applications. However, its possible risks consist of security breaches, lack of controllability, and openness with private data given which companies may be reluctant to share their internal sensitive information. To tackle this security problem, several enterprises are now building private cloud platforms using their resources and infrastructure to dedicate their computational needs with minimized security risk.

Moreover, the reduction of simulation times by decentralizing heavy computations has been tested in previous works. Chan and Chau [1991] first employed a local distributed computing platform to parallelize the design of electric machines. A graphics workstation was assigned for the automatic mesh generation, a minicomputer for FEA computation, another graphics workstation for visual evaluation, and several PCs for program editing, flexible data management and portable data storage. Different problems were solved using this approach, such as finding the Lorentz force in the end region of synchronous generators, calculating the dynamic loss density and 3-D thermal fields of induction motors during starting, and analyzing the electromagnetic performance of PM synchronous and DC brushless motors.

In a more recent study, General Motors developed their own HPC system as shown in Fig. 1.28 using a collection of recycled desktop computers [Smith, 2012a]. In this architecture, a remote laptop was connected to the internal network consisting of $N = 16$ compute nodes through a *load sharing facility* (LSF) master. The domain controller acted as the file server and stored all the user files with 2 TB of disk storage. The license servers were set up to work with Maxwell®, HFSS® and Q3D Extractor® software of ANSYS to enable the distribution of parametric variations, model extraction, characterization and optimization for a traction motor. Smith also reported a 16-times speedup using a 32-core HPC environment based on 16×2-core compute nodes. The benchmark system, i.e. a single-core desktop computer, took 72 hours to complete the same task as the HPC system which only used 4.5 hours. However, the actual speedup should be 8-times instead since the number of cores per node were not maintained in the performance comparison. Through the presented results, the author estimated that the HPC system can double engineering productivity, explore more design alternatives, reduce time to market, and improve motor performances. While these benefits may not be generalizable for all engineering projects, they demonstrate the power of relying on an HPC system for computationally-intensive and parallelizable tasks.

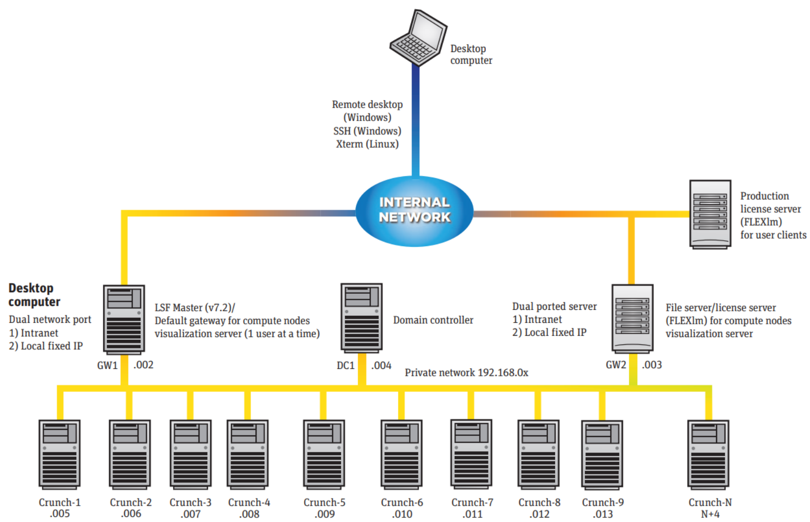

Fig. 1.28 HPC architecture of General Motors for distributed computing of electromagnetic simulation using ANSYS software [Smith, 2012b].

Furthermore, Gope et al. [2011] solved a 322×322 capacitance matrix of an integrated chip in an electromagnetic simulation using cloud computing and reported different speedups and costs as a function of the core count. For one single core, it was estimated that the total time taken would be 14.48 hours at US$ 28.56 whereas using eight cores would instead reduce the total time to only 2.42 hours at US$ 4.76. Using 640 cores decreased the simulation's time to 4 minutes while the cost increased to US$ 10.66, suggesting a tradeoff relationship between computational time and cost. An important issue to consider is that as the number of cores increase, the overall speedup can no longer increase linearly due to communication overheads among the cores. Similarly, Simpson and Mellor [2015] optimized an E-core power inductor for its multiphysics performances (2-D time-harmonic electromagnetic and 3-D steady-state thermal) using the distributed resources of cloud computing. With the help of 25 *virtual machines* (VMs), each one priced at US$ 0.43 per hour and consisting of 4 cores and 7.5 GB of RAM, a 3-objective problem (minimize inductance, maximize energy density and minimize peak operating temperature) was solved 150 independent times using particle swarm optimization with penalty functions (36 particles, 50 generations). For one optimized design, the computation time and cost were 0.45 hours (11.25 compute hours for 25 VMs) and US$ 4.84, while 150 sequential optimization runs cost about US$ 725 for 68 hours (1688 compute hours for 25 VMs). If only one VM was used for this problem, the total time would exceed 70 days and possibly impose an infeasible timeline for the research project. The authors also noted that alternative optimization methods could be researched to further reduce the total time and cost of using cloud computing resources. Nevertheless, a tradeoff relationship between computational time and cost still remains and a reasonable balance between the two must be selected based on the desired application.

Another study by Jiang et al. [2012] used high-throughput computing to optimize a 12-slot 10-pole PM machine rated at 30 kW continuous. More than 4200 designs were solved to reduce the motor's total mass from 27.80 kg to 20.65 kg while maintaining good electromagnetic performances. Differential evolution acted as the main optimizer with each generation simulated in parallel (6 variables, 85 individuals, 50 generations). The same problem was run twice to study the effect of parallelization on the solution's accuracy and total time, once using a single computer and then with 85 VMs. Although both approaches yielded similar solutions, it was observed that the parallelized approach sped up the optimization by 28.7 times as opposed to a theoretical limit of 85. Reported reasons for this deviation arose from the time required to perform the optimization procedure as well as communication overheads in the cloud, as expected. Jiang et al. also mentioned that a comprehensive optimization for electromagnetic, thermal and structural performances would become necessary in future works using a parallelized approach. Moreover, Sizov et al. [2013] as well as Wang et al. [2016] recently presented multi-objective optimization results for the large-scale design of PM machines and SynRMs respectively using differential evolution. The latter solved two problem formulations by simulating 10,200 designs (100 individuals, 51 generations) and reported improvements in the average torque, torque ripple, efficiency, and power factor.

Meanwhile, the previous work optimized the design of different PM motors on a single PC workstation using 30,000 FEA design evaluations. While the works summarized above have demonstrated the utility of cloud and high-performance computing of complex tasks, such as the design and optimization of electric machines, not many studies have incorporated the multiphysics evaluation of similar machines using an HPC platform for extracting knowledge or guidelines in a design process. It is also unclear how to choose the number of VMs and cost per VM, among other HPC parameters, for a given problem.

1.3.4 Efficiency Maps

In variable-speed traction applications, the electric drivetrain typically consists of a highly efficient synchronous AC motor in order to meet the low energy consumption targets set by the US Department of Energy [Yang et al., 2015]. Common examples include IPM motors and PM-SynRMs [Boldea et al., 2014].

After optimizing a motor's design for many objectives (e.g. average torque, torque ripple, efficiency, power factor, etc.) using FEA simulations, the vehicle's performance (e.g. total energy usage and range) within an urban setting is predicted using a dynamic simulator as in [Mahmoudi et al., 2015; Rahman et al., 2016]. A driving cycle with torque and speed points displayed in Fig. 1.29 is used to compute the total energy use for a given efficiency map. A prerequisite to this drive cycle analysis is the motor's efficiency map, whose speed and torque boundaries are imposed by the battery's peak voltage and the motor's thermal limit respectively. Calculating these maps, however, requires developing a detailed model of the electric motor before applying different motor control strategies at various operating points. These include the *Maximum-Torque-Per-Ampere*, *Flux Weakening* and *Maximum-Torque-Per-Volt* strategies explained in Section 1.2.5.

To characterize a synchronous AC motor, the dq-axis flux linkages need to be found. In a constant parameter or linear model, all three control strategies can be applied using approximate results at high current or speed operations [Soong and Miller, 1994; Goss et al., 2013]. Despite its quick solution, the constant parameter model overestimates the performance values and the lookup table method suggested in [Yang et al., 2015] is not flexible enough for any motor. A more realistic approach includes saturation and cross-coupling effects by modeling the dq flux linkage maps for different current magnitudes and advance angles. Using least-squares regression, a 2^{nd} order polynomial for two variables matched well

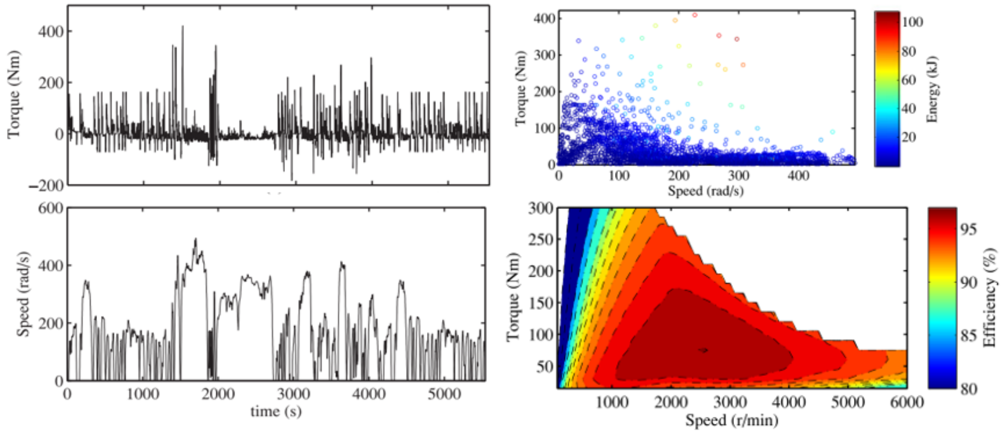

Fig. 1.29 Torque & speed points in a vehicle driving cycle used to compute energy use with the help of an efficiency map [Fatemi et al., 2016a].

with the current-driven FEA results in [Goss et al., 2013] and [Miao et al., 2016]. Moreover, ANSYS offers a fast approach to calculating efficiency maps by using an HPC system running 2-D FEA models [Dlala et al., 2013]. They managed to utilize 96 cores leading to a 90-times speedup for a parametric sweep of an IPM motor with 10,000 variations. In a similar manner, the effect of geometrically scaling motors for the calculation of efficiency maps was analyzed in [Stipetic and Goss, 2016], where the authors demonstrated simple relationships to reuse available data with minimal loss of information.

Once the optimal excitation conditions are set based on the control strategies, the efficiency or loss components (copper, iron, PM) at all operating points are either calculated via direct FEA simulations [Mahmoudi et al., 2015; Rahman et al., 2016] or estimated via inexpensive loss models [Goss et al., 2013]. However, it is currently unclear how the number of FEA evaluations impacts the accuracy and computational requirements of building an efficiency map. A reduced number of speed-torque points may be used to build an approximate map with the help of a surrogate model for problems requiring quicker evaluation rather than detailed analysis. It may be imperative to derive nonlinear motor control equations to consider the significant effects of saturation and cross-coupling. In addition, the computational aspects such as using different fitting functions need further investigation. By using such an approach and combining it with a cloud computing platform, automotive manufacturers and researchers could accurately compute the efficiency map of any synchronous AC motor drive with a reduction of computational time.

1.3.5 Summary of Literature Review

The literature review discussed above is summarized in table form as shown in Tables 1.2 and 1.3 from which several observations are made. First, there is no work which combines all multiphysics phenomena, i.e. electromagnetic, structural, thermal and acoustic, for the design or analysis of electric machines. It is widely known that these low-frequency devices are multiphysical in nature, and most designers generally ignore their non-electromagnetic performances due to increased modeling complexity and computational burden. This might explain why the number of performances or objectives is generally less than three in the cited literature (primarily average torque and torque ripple). At most, one more physical domain was previously used along with electromagnetics, whether it relied on a finite element, a lumped parameter or an analytical model. It is currently unknown how a multiphysics analysis impacts the selection of optimal designs, especially for synchronous AC machines.

Second, there is a lack of published knowledge on the parameters used to set up an HPC environment for motor design problems, with the exception of a few such as [Smith, 2012a; Ghorbanian, 2018]. These parameters include the number and specifications of virtual machines which directly impact the tradeoffs of computational time and financial cost for running HPC services. Given the recent increase in computing power and the ability to model more complex systems through multiphysics, an interface to an HPC system can provide potential users with more computational options based on their budget. There also seems to be less information present on the effort, especially total simulation time, required in solving such problems with only about half of the referenced works mentioning the number of FEA calls or evaluations (generally on the order of tens of thousands).

Furthermore, the number of rotor barriers related to the rotor topology in synchronous AC machines, such as IPM motors or SynRMs, was not varied in the studied optimization problems. Most works kept this number fixed, e.g. 3 or 4 barriers, which could possibly yield suboptimal designs. Increasing the number of barriers, subject to manufacturing and structural constraints, generally helps improve the electromagnetic performance which is a desired target for motor designers. Many works also neglect the relationship among different numbers of barriers when designing these machines, since most solutions are generally discarded and only the optimal designs are kept. It is unknown how different flux barriers correlate with each other in the multiphysics domain. Understanding their relationships can help provide insightful information to a motor design process.

The following acronyms are employed in the two tables displayed below:

- **Variable type**: C: control, I: inverter, M: motor, R: rotor, S: stator.
- **Objective type**: A: acoustic, E: electromagnetic, T: thermal.
- **Machine topology**: IM: induction, IN: inductor, IPM: interior permanent magnet, PM: permanent magnet, SR: switched reluctance, SyR: synchronous reluctance.
- **Multiphysics model**: AN: analytical, FE: finite element, LP: lumped parameter.
- **Sampling method**: CC: central composite, FF: full factorial, LH: Latin hypercube.
- **Optimization method**: DE: differential evolution, GA: genetic algorithm, GM: gradient method, NN: artificial neural network, PS: particle swarm optimization, RS: response surface, SA: sensitivity analysis, SLP: sequential linear programming, SLS: sequential least squares, TO: topology optimization, WF: weighted factor.

Table 1.2 Summary on efficiency map calculation. Full forms can be found above or in the List of Acronyms.

Reference	Overview				Optimal parameters				Control strategy			Efficiency calculation				Efficiency map plot		
	Motor type	Cross-coupling	Saturation	Efficiency map	Lumped parameter	Lookup table	Regression model	Optimization	MTPA	FW	MTPV	Analytical scaling	Direct FEA	Loss model	Use of HPC	Finite differences	Neural network	Exp. validation
Soong & M. (1994)	PM IPM SyR	-	✓	-	✓	-	-	-	✓	✓	✓	-	-	-	-	-	-	-
Goss et. al. (2013)	IPM PM	✓	✓	✓	-	-	✓		✓	✓	✓	-	-	✓	-	✓	-	✓
Dlala et. al. (2013)	IPM	✓	✓	✓	-	-	-	✓	✓	✓	-	-	✓	✓	✓	✓	-	✓
Yang et. al. (2015)	IPM IM SR	✓	✓	✓	-	✓	-		✓	-	✓	-	✓	-	-	✓	-	-
Mahmoudi et. al. (2015)	IPM IM PM	✓	✓	✓	-	-	✓	-	✓	✓	✓	-	✓	✓	-	✓	-	-
Stipetic et. al. (2016)	IPM PM	✓	✓	✓	-	-	✓	-	✓	✓	✓	✓	✓	✓	-	✓	-	-
Miao et. al. (2016)	IPM	✓	✓	-	-	-	✓	-	✓	✓	-	-	-	-	-	-	-	-
Mohammadi & L. (2017)	IPM PM-SyR	✓	✓	✓	-	-	✓	-	✓	✓	✓	-	✓	-	-	-	✓	✓

Table 1.3 Summary of literature review. Full forms are found above or in the List of Acronyms.

Reference	Simulation setup						Rotor flux barrier				Control		Objectives							Multiphysics				Optimization					HPC
	Num. of variables	Num. of objectives	Num. of slots	Num. of poles	Motor topology	Num. of barriers	Round	Angled	Fluid	Asymmetric	Direct	MTPA	Average torque	Torque ripple	Efficiency or losses	Power factor	Material cost	Total mass	Others	Electromagnetic	Structural	Thermal	Acoustic	Sampling method	Optimization method	Num. of FEA calls	Num. of parallel nodes	Total simulation time	Used?
Hudák et. al. (2006)	5R	-	36	4	SyR	15	✓	-	-	-	-	-	✓	✓	✓	✓	-	-	-	FE	-	-	-	-	SA	-	-	-	-
Park et. al. (2006)	4R	1E	6	4	SyR	5	-	✓	-	-	-	-	-	✓	-	-	-	-	-	FE	-	-	-	CC	RS	31	-	-	-
Degano et. al. (2016)	4R+1S	3E	36	4	SyR	3	-	-	✓	-	-	✓	✓	✓	✓	-	-	-	-	FE	-	-	-	-	GA	3.0K 2.4K	-	8.5h 6.5h	-
Pellegrino et. al. (2015)	7R+1C	2E	24	4	SyR	3	✓	✓	-	-	✓	-	✓	✓	-	-	-	-	-	FE	-	-	-	-	GA	5×3K	4	12.5h	-
Risticevic et. al. (2016)	15×18	4E	12	8	IPM	1	-	✓	-	-	-	-	✓	-	-	-	-	-	3✓	FE	-	-	-	-	TO	80K	100	-	✓
Sizov et. al. (2013)	4R+7S	2E	9	6	PM	1	-	✓	-	-	-	✓	✓	✓	-	-	-	-	-	FE	-	-	-	-	DE	10K 20K	1	1.8d 5.2d	-
Wang et. al. (2016b)	10R+1C	2E 3E	36	4	SyR	4	-	✓	-	-	✓	-	-	✓ ✓	✓ ✓	✓	-	-	-	FE	-	-	-	-	DE	5.1K 5.1K	-	-	-
Mohammadi et. al. (2016a)	2R 4R	2E	33	4 8 10	SyR	1 2	✓	-	-	-	-	✓	✓	✓	-	-	-	-	-	FE	-	-	-	FF	NN GA	3×90	4	16.3h	-
Mohammadi et. al. (2016b)	8R 6R	2E	33 12	8 4	SyR	4 3	✓	-	-	-	-	✓	✓	✓	-	-	-	-	-	FE	-	-	-	FF	-	9.3K 88K	1 10	7.0d 1.5d	- ✓
Howard et. al. (2015)	29R+1C	2E	24 36	4 4	SyR	4	-	-	✓	✓	✓	-	✓	✓	-	-	-	-	-	FE	FE	-	-	-	GM SLP	-	-	-	-
Howard & K. (2016)	29R+1C	3E	48	8	SyR	4	-	-	✓	✓	✓	-	✓	✓	-	✓	-	-	-	FE	FE	-	-	-	WF SLS	600	-	-	-
Taghavi & P. (2015)	Ribs	-	36	6	SyR	4	-	-	✓	-	-	-	✓	✓	-	-	-	-	✓	FE	FE	-	-	-	-	-	-	-	-
Barcaro et. al. (2014)	Ribs	-	48	4	IPM	3	-	✓	-	-	-	-	-	-	-	-	-	-	✓	FE	FE AN	-	-	-	-	-	-	-	-
Kolehmainen (2010)	-	-	72	4	SyR	4	-	?	-	-	-	-	✓	✓	✓	✓	-	-	✓	FE	FE	-	-	-	-	-	-	-	-
Dziechciarz et. al. (2016)	Ribs	-	27	4	SyR	4	✓	-	✓	-	-	-	✓	✓	-	-	-	-	-	FE	FE	-	-	-	-	-	-	-	-
Jiang et. al. (2012)	4R+2S	1E	12	10	PM	-	-	-	-	-	-	-	-	-	-	-	-	✓	-	FE	-	FE	-	-	DE	4.3K	85	25h	✓
Sarikhani & M. (2014)	7	4E+2T	12	10	PM	-	-	-	-	-	-	-	✓	✓	✓	-	-	✓	-	FE	-	LP	-	-	PS	-	-	-	-
Fatemi et. al. (2016)	5R+5S	2E	48 12	8 10	IPM	1	-	✓	-	-	-	✓	-	-	✓	-	✓	-	-	FE	-	LP	-	-	DE	6×6.6K	-	-	-
Simpson & M. (2015)	6	2E+1T	-	-	IN	-	-	-	-	-	-	-	-	-	-	-	-	-	3✓	FE	-	FE	-	-	PS	150×1.8K	25	2.8d	✓
Ghorbanian (2018)	6M+2I	8E+1T	24	4	IPM	1	-	✓	-	-	-	✓	✓	✓	✓	✓	✓	-	✓	FE	-	FE	-	LH	NN GA	(5+1)×3K	30	13.6d	✓
Wang et. al. (2014)	-	-	-	-	SyR PM	-	-	-	-	-	-	-	-	-	✓	-	-	-	✓	FE	-	LP	-	-	-	-	-	-	-
Islam et. al. (2010)	-	-	12	10	PM	-	-	-	-	-	-	-	-	-	-	-	-	-	✓	FE	-	-	AN	-	-	-	-	-	-
Wang et. al. (2016a)	2R+4S	2E+1A	33 12	8 10	SyR	1	✓	-	-	-	-	✓	✓	✓	-	-	-	-	✓	FE	-	-	AN	FF	-	2×90	-	-	-

1.4 Thesis Objective

Given the research gaps in the related works discussed above, the main goal of this thesis is to propose a *multiphysics design process* (MPDP) for synchronous AC machines using a data-driven approach. The term "data-driven" in this thesis is defined to be the concept of acquiring or gathering data from a device's simulation for the purpose of extracting knowledge and guidelines. Fig. 1.30 illustrates the flowchart of the proposed MPDP. This procedure is an alternative to that presented in [Ghorbanian et al., 2018b] by incorporating electromagnetic (E), structural (St), acoustic (A) and thermal (T) analyses in the performance evaluation. In brief, the MPDP consists of 6 stages which are either internally handled or require user interaction. Each stage is explained in the subsequent chapters with the help of a synchronous reluctance machine case study.

1.4.1 Contributions

The main contributions of this thesis are:

1. To incorporate multiphysics-based analysis of synchronous AC machines within the design process, such as electromagnetics, structural, acoustics, and thermal fields, in order to study their effects on the selection of optimal design solutions (selected publications: [Mohammadi et al., 2018a,b]);

2. To extract design knowledge of synchronous AC machines for different topologies with the help of FE-based simulations and statistical analysis for speeding up the design process (selected publications: [Mohammadi et al., 2017a, 2018a]);

3. To test the use of high-performance computing and report its associated parameters for the design and analysis of synchronous AC machines (e.g. number of VMs, total cost and time, VM size, overheads); and

4. To develop a computationally efficient algorithm for generating detailed efficiency maps of synchronous AC machines (selected publication: [Mohammadi and Lowther, 2017]).

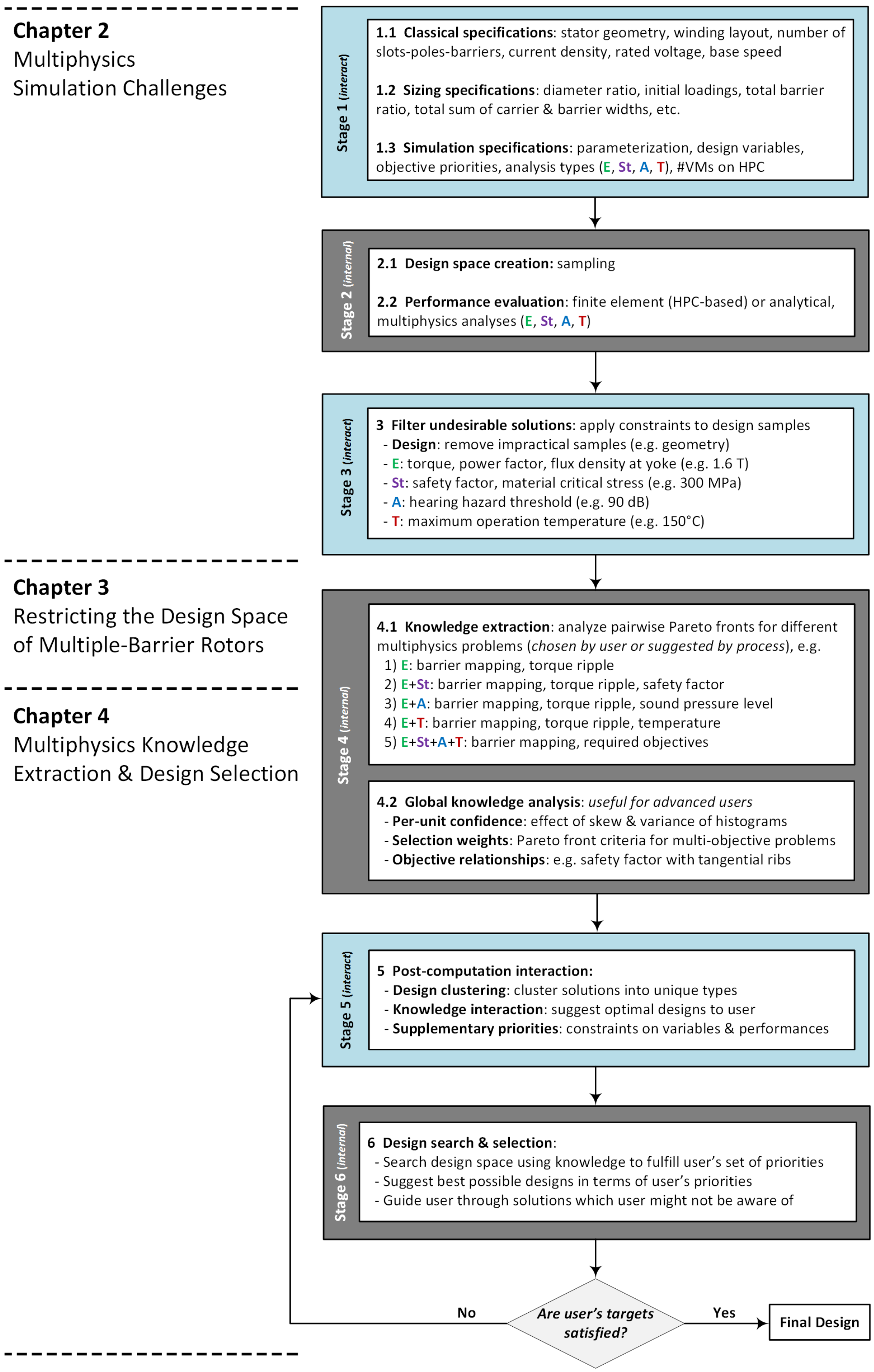

Fig. 1.30 Flowchart of the proposed multiphysics design process (MPDP).

1.4.2 Thesis Outline

The thesis is divided into the following chapters:

- **Chapter 2 Multiphysics Simulation Challenges**: The user interacts with the MPDP to set the initial specifications of a synchronous AC machine (classical, sizing, simulation) in Stage 1. The process then internally creates and samples the design space in Stage 2 before evaluating different multiphysics performances, i.e. electromagnetics, structural, acoustics, and thermal. The use of high-performance computing and its associated parameters for electromagnetic simulations are also discussed. Next, Stage 3 is presented for filtering undesirable solutions based on different constraints.

- **Chapter 3 Restricting the Design Space of Multiple-Barrier Rotors**: The explanation of the MPDP halts here in order to explain the *barrier mapping* methodology. This proposed method helps restrict the design space of multiple-barrier rotors through various motor models. Two different examples, i.e. only electromagnetic and electromagnetic with acoustic analyses, are demonstrated to show the computational effectiveness of the *barrier mapping* methodology based on statistical analysis for different-sized machines.

- **Chapter 4 Multiphysics Knowledge Extraction and Design Selection**: The MPDP continues from Chapter 2 to internally extract design knowledge and guidelines as well as perform *barrier mapping* in Stage 4. Then, the process interacts with the user to show how different solutions are clustered together in Stage 5, before selecting optimal designs based on the user requirements in Stage 6. Finally, a single optimal design selected for its weighted-best multiphysics performance is assisted with PMs. The variable-speed behavior of this PM-SynRM, including its efficiency map, torque/power versus speed characteristic and demagnetization plots, is also demonstrated.

- **Chapter 5 Conclusion**: A summary of this thesis and its findings are presented along with recommendations for future work.

- **Appendix A Correlation Coefficients**: Two different correlation coefficients, namely the Pearson and the Spearman, are briefly described and compared with the help of equations and visual examples. Throughout this thesis, the Spearman correlation coefficient is preferred to the Pearson.

- **Appendix B Incorporating Control Strategies within Design Optimization**: Two different methodologies to incorporate control parameters into the design optimization of synchronous AC machines are presented and compared. A metric is used to quantify the conflict level between the average torque and torque ripple for two case studies: an IPM and a SynRM. Using 2-D finite element analysis simulations, the results demonstrate that the traditional approach of lumping the control and design variables together can lead to poor designs, especially when the conflict is high.

- **Appendix C Efficiency Map Calculation for Synchronous AC Motors**: Nonlinear motor control equations are derived and used for the study of efficiency map calculation while accounting for both saturation and cross-coupling effects. Two synchronous AC motors are considered, including the 2010 Prius IPM and a PM-SynRM, with all procedure steps outlined in detail.

- **Appendix D Additional Results**: To further justify the use of the MPDP, additional results are presented for the two synchronous reluctance machine case studies. These results include histograms of components temperatures for different numbers of barriers, correlation plots of multiphysics performances for different numbers of slots and barriers, correlation plots of design metrics for different numbers of slots and barriers, and barrier mapping of multiphysics performances for different top percentiles.

Chapter 2

Multiphysics Simulation Challenges

In this chapter, the MPDP in Fig. 1.30 starts by interacting with the user to set the initial specifications. This first stage detailed in Section 2.1 defines the classical, sizing and simulation specifications which are all required prior to collecting results. These include selecting the slot-pole combination and parameterizing the machine geometry, among others. Next, the simulation process in Section 2.2 begins Stage 2 by creating and sampling the machine's design space. Different multiphysics performances are then evaluated using electromagnetic (E), structural (St), acoustic (A) and thermal (T) analyses. The use of a high-performance computing service and its associated parameters are discussed. Finally, the undesirable solutions are filtered in Stage 3 based on various constraints.

2.1 Stage 1: Initial Specifications (*interact*)

Stage 1 of the MPDP requires the user to interact with the software in order to set different specifications. The procedure for each substage is described in the subsections below.

2.1.1 Classical Specifications

First, the classical or general specifications must be selected which include the stator geometry, the winding layout, the numbers of slots and poles, the rated voltage and the base speed. In this thesis, two stators with different slot-pole combinations are considered as shown in Fig. 2.1: 24-slot 4-pole and 30-slot 4-pole. Each stator has a specific winding layout, a base speed of 2000 RPM and a supply DC bus voltage of 42V.

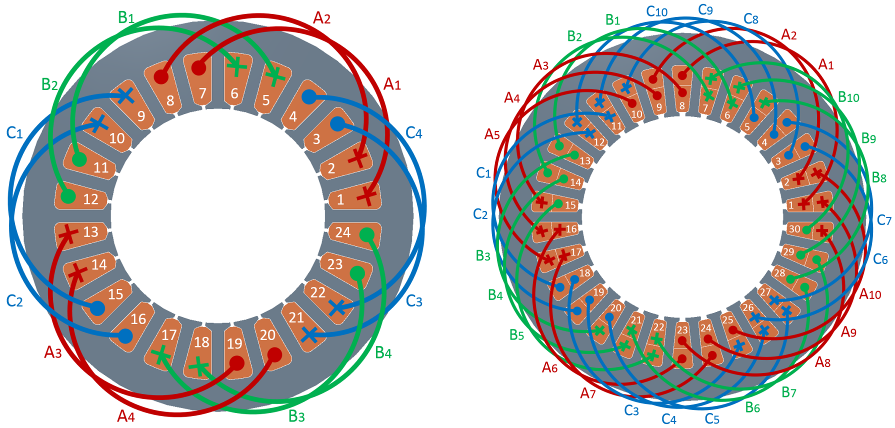

(a) (b)

Fig. 2.1 Cross-sections of the selected SynRM stators: (a) 24-slot, (b) 30-slot.

2.1.2 Sizing Specifications

After setting the classical specifications, a SynRM must be sized to obtain its first working design as discussed in [Hendershot and Miller, 2010; Taghavi and Pillay, 2014; Lu et al., 2017]. Sizing accounts for the electrical, magnetic and thermal loadings of the electric motor, particularly during transient operations. Different metrics such as the stator-to-rotor diameter ratio, torque-to-rotor volume and recommended flux density values in different components are typically used. This substage also considers the cooling requirements which are application-dependent. For example, the rated current density of the studied SynRMs is set based on natural cooling (less than 5 A/mm^2).

2.1.3 Simulation Specifications

Next, the simulation environment must be set up and starts with model parameterization. For an experienced user, it is possible to parameterize the stator or select alternative rotor topologies such as the ones displayed in Fig. 1.19 or 1.20. While the stator geometry and winding are assumed to be fixed here, a TLA rotor geometry with round-shaped barriers is varied to demonstrate how the MPDP functions. A visual example of the studied SynRM geometry is displayed in Fig. 2.2 and has fixed design parameters and information given in Table 2.1. For consistency among design variations, the rated current density is kept fixed.

Table 2.1 Fixed SynRM Design Parameters and Information

		24-slot	**30-slot**
Number of slots		24	30
Number of poles		4	4
Supply voltage	V_{dc}	42	42
Rated speed	RPM	2000	2000
Rated RMS current density	A/mm^2	4.5	4.5
Rated RMS current	A	10	10
Stack length	mm	76.0	76.0
Airgap thickness	mm	0.5	0.5
Stator outer diameter	mm	94.0	94.0
Stator inner diameter	mm	51.5	51.5
Back iron thickness	mm	7.55	8.25
Tooth width	mm	3.0	2.4
Tooth tip thickness	mm	0.8	0.8
Slot opening width	mm	0.8	1.5
Tooth tang angle	°	30	30
Rotor outer diameter	mm	50.5	50.5
Rotor yoke thickness	mm	5.0	5.0
Width of tangential ribs	mm	0.5	0.5
Winding connection type		Y	Y
Winding phase resistance	mΩ	118.8	110.5
Winding factor	%	96.6	95.1
Coil fill factor	%	40.0	44.7
Bare slot area	mm^2	70.0	53.2
Turn length	mm	318	282
Number of turns		12	5
End winding outer diameter	mm	81.7	77.3
End winding height	mm	26.4	21.8
End winding resistance	mΩ	62.0	51.0
End winding inductance	μH	48.2	19.0
Stator core mass	kg	1.84	1.86
Stator winding mass	kg	0.90	0.83
Core material		M-19 29 Ga	
Conductor material		Copper	
Barrier material		Air	
Cooling method		TENV	
Emissivity		0.85	0.85
Housing thickness	mm	4.18	4.18

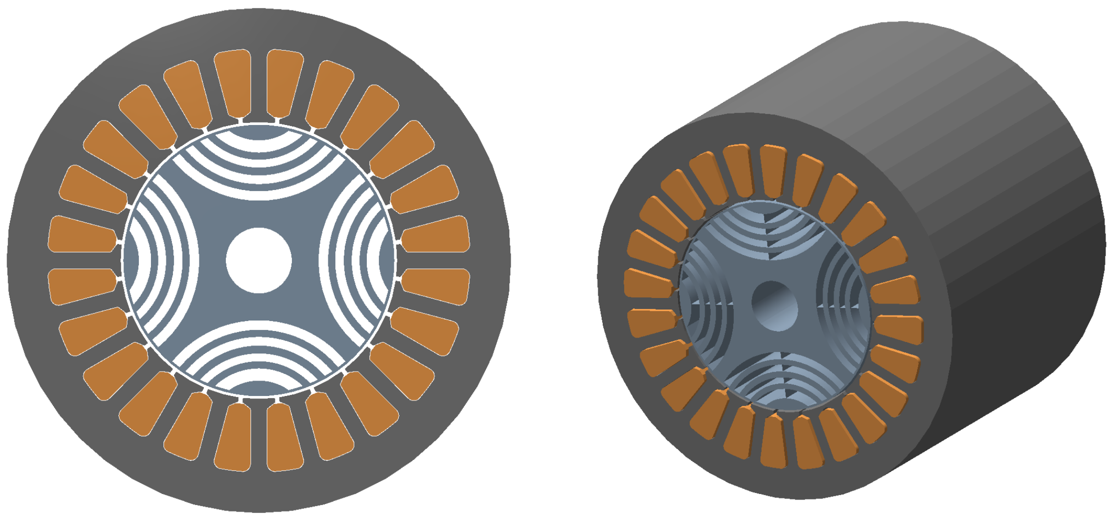

Fig. 2.2 View of the 24-slot SynRM geometry. Color representation: gray for iron, white for air, orange for copper.

In a SynRM rotor, the flux barrier and flux carrier constitute its two main electromagnetic components. As its name suggests, a flux barrier consists of a non-ferromagnetic material enabling a high magnetic reluctance path, while it is the opposite case for a flux carrier. To optimize a SynRM rotor for its multiphysics performances, different numbers of barriers denoted by n_b are considered here ranging from 1 to 4. For a given n_b, the vector of design parameters, $\boldsymbol{x}$, in (2.1) constitute the width of the k^{th} flux carrier, W_{c_k}, the width of the k^{th} flux barrier, W_{b_k}, the inset width of the barrier center, W_f, and the rotor inner radius, R_{ri}. Here, k represents the barrier number with the index starting from the rotor shaft toward the airgap. The tangential rib width, W_t, was kept fixed at 0.5 mm, as it is shown in Chapter 3 that W_{c_k} and W_{b_k} are more nonlinearly correlated with each other than with W_t.

$$\boldsymbol{x} = [W_{c_1}, W_{b_1}, ..., W_{c_{(n_b)}}, W_{b_{(n_b)}}, W_f, R_{ri}] \tag{2.1}$$

In addition, different design metrics are defined in (2.2) as follows: W_c and W_b are the sum of all carrier and barrier widths respectively [Mohammadi et al., 2016], and a is the total flux barrier ratio [Bianchi, 2013]. The linear summation of W_c and W_b is performed to establish a mapping between the multiple- and single-barrier spaces. The simplification is justified by assuming that parallel fluxes flowing through multiple smaller flux carriers can be represented by the flux in a single carrier. These metrics later become useful when comparing different designs. For consistency, the rotor outer radius, R_{ro}, the rotor yoke thickness, W_{ry}, and the stack length, L_{stk}, are kept fixed, whereas R_{ri} depends on (2.3).

$$\begin{aligned} W_c &= \sum_{k=1}^{n_b} W_{c_k} \\ W_b &= \sum_{k=1}^{n_b} W_{b_k} \\ a &= \frac{W_b}{W_c + W_b} \end{aligned} \tag{2.2}$$

$$R_{ri} = R_{ro} - (W_c + W_b) - W_{ry} \tag{2.3}$$

Both W_{c_k} and W_{b_k} are modeled by intersecting different circular radii from a fixed center controlled by W_f and are symmetric about the center of each pole. In order to avoid impractical designs, geometrical constraints discussed in [Mohammadi et al., 2016] are set on $\boldsymbol{x}$ resulting in the feasible set for the entire design space, denoted by $\mathscr{F}_\Delta$. This feasible design set is constrained using (2.4) by lower bounds and a total width limit, W_{lim}, to ensure that two adjacent poles do not intersect. Also, the per-unit widths of W_c and W_b are calculated with respect to W_{lim}. Fig. 2.3 illustrates the corresponding variables for 1, 2, 3 and 4 barriers on a $1/4^{th}$ rotor cross-section. The systematic evaluation of $\boldsymbol{x}$ can yield optimal SynRMs as shown in [Matsuo and Lipo, 1994; Vagati et al., 1998; Pellegrino et al., 2015].

$$\mathscr{F}_\Delta = \left\{ \boldsymbol{x} \;\middle|\; \begin{array}{l} W_{c_k} \geq W_t \quad \forall k \\ W_{b_k} \geq W_t \quad \forall k \\ W_c + W_b \leq W_{\text{lim}} \\ W_t \leq W_f \leq (R_{so} - R_{ro}) \end{array} \right\} \tag{2.4}$$

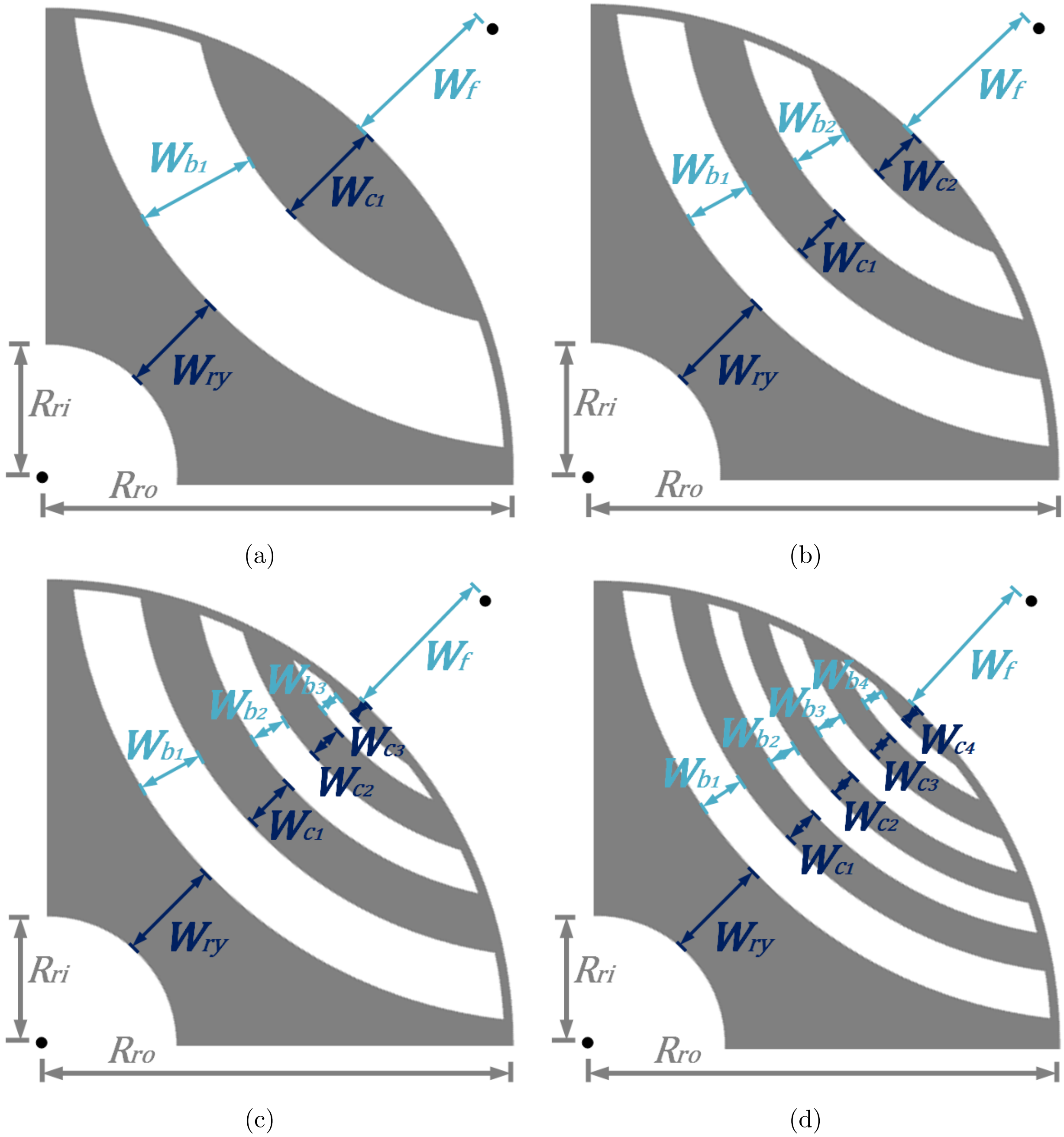

Fig. 2.3 Round-barrier rotor parameterization of a SynRM for different n_b with labeled design variables: (a) 1-barrier, (b) 2-barrier, (c) 3-barrier, (d) 4-barrier. A quarter model is shown due to a pole periodicity. Color representation: gray for iron, white for air. Both R_{ro} and W_{ry} are kept fixed.

Subsequently, the objective priorities must be selected and are generally application-dependent. In most cases, the torque ripple is to be minimized while maximizing the average torque. These two objectives would then be ranked higher than the rest in the MPDP. Next, the user is permitted to select the required analyses (i.e. E, St, A, T). If none are selected, all of them could be performed and presented in later stages to guide the user toward a more realistic design. For the last step of Stage 1, the user is notified about using an HPC system to speed up the total simulation time. In brief, multiple VMs or workstations simulate the different design variations in parallel before reporting all the results. More details on the design space creation and the performance evaluation are discussed below.

2.2 Stage 2: Multiphysics Simulation Process (*internal*)

Stage 2 is handled internally where the MPDP creates and samples the design space based on the parameterization specified in Stage 1. Each sample is then simulated for the chosen analyses, e.g. electromagnetic, as explained below.

2.2.1 Design Space Creation

Prior to calculating the multiphysics objectives, a design of experiments is necessary to sample the rotor design spaces using an appropriate method such as the Latin hypercube [Jurecka, 2007]. Here, the entire design spaces of the 1, 2, 3 and 4-barrier SynRM rotors consisting of 3, 5, 7 and 9 variables according to (2.1) were sampled using the Latin hypercube with the maximin criterion. It was ensured that none of the provided points violate the geometric constraints set by $\mathscr{F}_{\Delta}$. This resulted in 314, 1066, 3242 and 5998 samples used for varying the four rotor geometries across their entire design spaces. Next, close neighbors within a specified distance were removed to ensure uniqueness of designs. In each case, the number of samples was increased incrementally until the entire design space was uniformly covered. The user could also be prompted by the MPDP if more samples are required for a better space representation.

For instance, Fig. 2.4 demonstrates how the design variables (scaled in per-unit) are distributed for the 3-barrier rotor with the help of a *correlation plot*. This plot, which is regularly used throughout this thesis and in [Ghorbanian, 2018], consists of histograms for each variable along the diagonal, pairwise scatter plots between variables on the lower-triangle, and Spearman correlation coefficients for each pair on the upper triangle. Note that the Spearman correlation is preferred to the Pearson, since the former measures the pairwise rank correlation and can handle monotonic nonlinearities (explained using examples in Appendix A). To illustrate the meaning behind the correlation values, a positive coefficient indicates a monotonically increasing relationship, whereas a negative value is for a decreasing case. A coefficient close to 0 suggests no correlation between the variable pair which supports the null hypothesis for a p-value greater than 0.05. Also, Cohen et al. [2014] provide the following guidelines for interpreting correlation strengths: 0.10 for small, 0.30 for medium and 0.50 for high. While W_f is observed to be more uniform in Fig. 2.4, the other widths are skewed below 0.33 due to geometrical constraints. Higher W_{c_k} and W_{b_k} values are removed to ensure there is enough separation between the barriers of two adjacent poles. Also, these variables are more negatively correlated than with W_f due to their summation constraints in (2.4). The correlation values, however, are all small due to the sampling procedure. Similar behaviors are observed for the other barrier datasets, i.e. 1, 2 and 4.

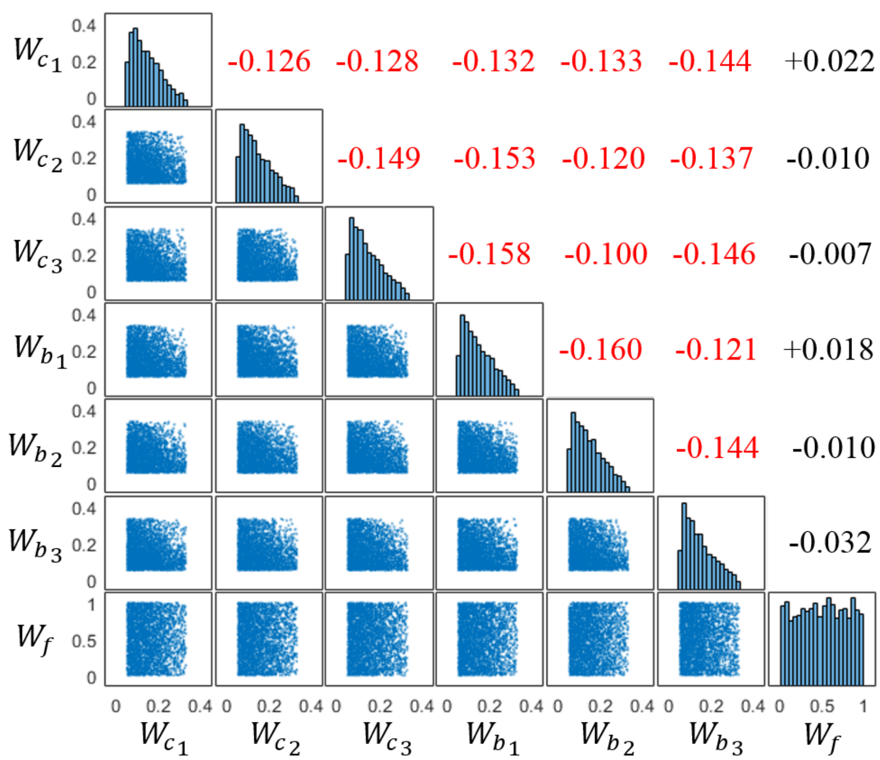

Fig. 2.4 Correlation plot of 3-barrier design variables.

2.2.2 Simulation Coupling

When simulating the performance of an electric machine, its physics can be decoupled depending on the application. For the synchronous reluctance in this thesis, the simulation coupling is summarized in Fig. 2.5 based on the following assumptions:

- Electromagnetic-Thermal: A one-way coupling is used. As in Fig. 1.3 (a), there is a small variation of the magnetic characteristics of silicon steel for different temperatures. This does not significantly affect other electromagnetic performances. Also, no PMs were used for the SynRM design which can be sensitive to a temperature rise.

- Structural-Electromagnetic: There is a small structural effect on BH curves of silicon steel for the rated speed of 2000 RPM, since the maximum von Mises stress on the rotor is less than 10 MPa [Hussain, 2017]. Also, the centrifugal forces dominate the magnetic forces [Barcaro et al., 2014]. Hence, the two physics were decoupled.

- Structural-Acoustic: Only resonances in the stator structure are used. Rotor vibrations can be ignored for speeds below 100 kRPM [Ede et al., 2002].

- Electromagnetic-Acoustic: Only the electromagnetic source is used since the power rating is less than 15 kW, i.e. small-sized machine [Ver and Beranek, 2006].

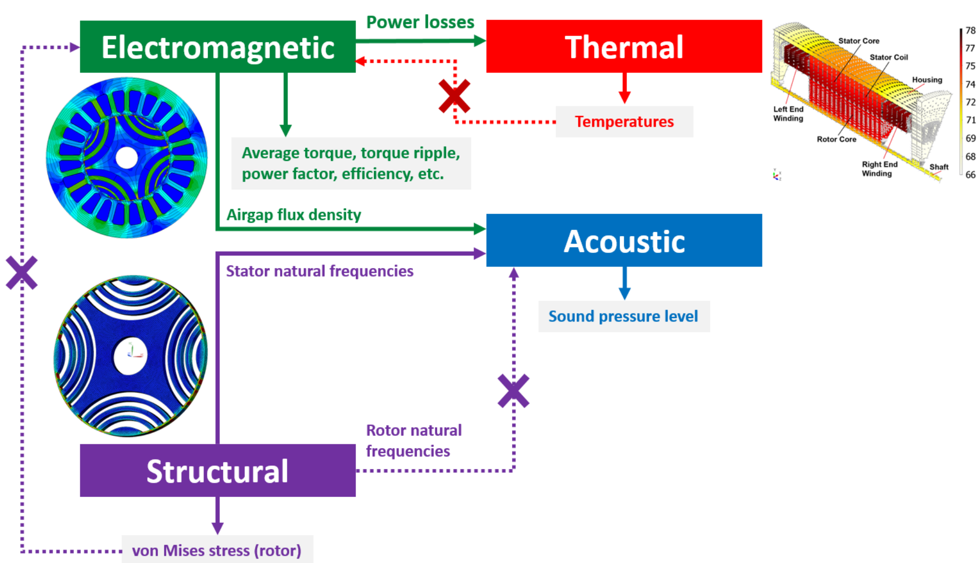

Fig. 2.5 Multiphysics simulation coupling.

2.2.3 Performance Evaluation

After the sampling procedure, a suitable function evaluator must take each design variation to compute the multiphysics performances according to the given application. In an electric machine such as a SynRM, this includes, but is not limited to, electromagnetic, structural, acoustic and thermal analyses. While all the multiphysics performances are computed here, it is up to the user to select which ones are necessary for the later stages. The subsections below describe how each objective is computed for every analysis.

Electromagnetic Analysis

With the help of the electromagnetic FEA tool in [Mentor-Infolytica Corporation, 2018], transient 2-D FEA simulations are used to compute the SynRM's electromagnetic objectives as well as to account for its complex geometry and material nonlinearities. At each time instant, the rotor orientation is synchronized to the excitation frequency to feed the windings with a 3-phase sinusoidal current waveform at rated condition. Through the motor's phase and pole periodicity, only $1/6^{th}$ of an electrical period is used to compute the average torque, T_{avg}, defined in (2.5) and the peak-to-peak torque ripple, T_{rip}, in (2.6). Here, N is the number of rotor positions and $\boldsymbol{T}$ is the instantaneous torque vector.

Other objectives include the power factor, pf, the iron power loss, P_{Fe}, the efficiency, η, the RMS voltage, V_{rms}, the d-axis inductance, L_d, and the saliency ratio, ξ. The normal component of the airgap flux densities, $\boldsymbol{B_n}$, are computed and saved for the acoustic analysis (discussed later). In general, it is desired to maximize T_{avg}, pf, η and ξ, while T_{rip}, P_{Fe}, V_{rms} and L_d are to be minimized. It should be noticed that the winding power loss remains constant across all design samples since the stator winding layout and the current density are kept fixed. Hence, P_{Fe} and η are interchangeable objectives here.

$$T_{avg} = \frac{1}{N}\sum_{i=1}^{N} T_i \tag{2.5}$$

$$T_{rip} = \frac{|\max(\boldsymbol{T}) - \min(\boldsymbol{T})|}{T_{avg}} \tag{2.6}$$

To ensure simulation consistency among all rotor designs, the MTPA strategy is employed using the formulation in (B.1) and the procedure explained in Section 3.2.2. Appendix B includes relevant information on how to incorporate control strategies (e.g. MTPA) within an optimization routine, which also applies to Stage 2 of the MPDP. Briefly speaking, the MTPA strategy maximizes T_{avg} with respect to the current advance angle, γ, for each design variation $\boldsymbol{x}$ at a fixed current magnitude. The result is the optimal MTPA angle, γ^{MTPA}. If other operating points or detailed efficiency maps are required, the computationally-efficient procedure in Appendix C can be used which relies on modeling synchronous AC machines using nonlinear flux linkage maps (accounts for saturation and cross-coupling effects).

Moreover, using the dq model of a SynRM comprised of L_d and ξ for the given current density, the MTPA flux linkage, λ_s^{MTPA}, is calculated using (2.7). Then, the base speed, N_m^{Base}, of each design variation is computed in (2.8) as discussed in [Soong and Miller, 1994] and illustrated in Figs. 1.15 and 1.16. It is assumed that the maximum per-phase voltage, V_s^{Max}, is $2/\pi$ times the DC bus voltage based on the square-wave limit of a 2-level inverter explained in Section 1.2.4. This voltage can be much closer to the DC voltage for the space vector modulation of a 3-level inverter. Basically, N_m^{Base} is computed by intersecting the current-limit circle and the voltage-limit ellipse at the MTPA operating point for V_s^{Max}. It is desired to maximize N_m^{Base} in practice which occurs if the V_{rms} required is not larger than V_s^{Max}. Beyond this base speed, constant torque can no longer be achieved which is a key requirement for pure SynRMs in pump and fan applications [ABB, 2016]. Hence, N_m^{Base} is another electromagnetic objective which is to be maximized for increasing the output power.

$$\lambda_s^{\text{MTPA}} = L_d I_s^{Max} \sqrt{\sin^2 \gamma^{\text{MTPA}} + \xi^2 \cos^2 \gamma^{\text{MTPA}}} \tag{2.7}$$

$$\begin{aligned} \omega_e^{Base} &= \frac{V_s^{Max}}{\lambda_s^{\text{MTPA}}} = \frac{2}{\pi} \frac{V_{dc}}{\lambda_s^{\text{MTPA}}} \\ N_m^{Base} &= \frac{30}{\pi} \frac{\omega_e^{Base}}{n_p/2} \end{aligned} \tag{2.8}$$

Structural Analysis

Once the electromagnetic objectives have been obtained, it is necessary to analyze a SynRM's structural performance. The tangential ribs of a SynRM closest to the rotor outer diameter must be sized accordingly to reduce their mechanical stress during high operating speeds. This is particularly important in industrial applications that require high reliability and long service life. In addition, a SynRM's rotor must not be run at speeds higher than the maximum one as approximated in (2.9). Here, N_m^{Calc} is the calculated mechanical speed (i.e. 2000 RPM in this work), σ is the critical stress computed in the SynRM rotor, and σ_s is the yield strength of electrical steel which is around 300 MPa [Barcaro et al., 2014]. The unknown quantity here is σ which can be computed using a 3-D linear statics solver through a structural FEA package [Siemens PLM Software Inc., 2018] or using an analytical equation in a worst-case approach [Barcaro et al., 2014]. Fig. 2.6 below shows the maximum von Mises stress distribution for a given 4-barrier rotor running at 2000 RPM simulated using a 3-D linear statics solver. As expected, it is observed that the critical stress occurs at the tangential ribs which connect the flux barriers. This stress is primarily caused by the centrifugal forces pushing the ribs outward when running at high speeds. The critical stress using structural FEA, σ_{FEA}, was computed for every design sample.

$$N_m^{Max} = N_m^{Calc}\sqrt{\frac{\sigma_s}{\sigma}} \tag{2.9}$$

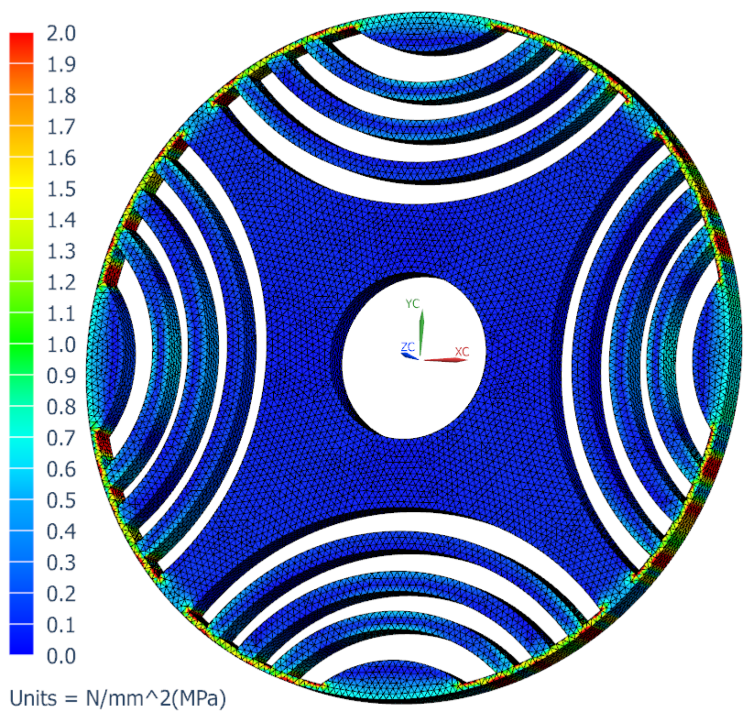

Fig. 2.6 Maximum von Mises stress distribution for a SynRM 4-barrier rotor.

Similarly, the critical stress of the tangential ribs can be analytically computed using static stress analysis in (2.10). The total force, F, is decomposed into the centrifugal force, F_c, and the normal component of the magnetic force, F_m. Here, M_r is the rotor flux carrier mass, R_t is the radius of the tangential rib from the origin, A_g is the circumferential area of the tangential rib, P_n^0 is the constant magnetic pressure wave in the airgap computed through $\boldsymbol{B_n}$. Then, the analytical form of the maximum stress, σ_{Ana}, can be easily found for every design sample $\boldsymbol{x}$ without the need for a structural FEA package. As discussed in [Barcaro et al., 2014], this analytical approach was found to safely overestimate the actual critical stress, σ_{FEA}, which means that N_m^{Max} of the analytical case would be smaller.

$$\begin{aligned} F &= F_c + F_m \approx M_r R_t \omega_m^2 + A_g P_n^0 \\ \sigma_{Ana} &= \frac{F}{W_t L_{stk}} \end{aligned} \tag{2.10}$$

To quantify possible deviations of these mechanical performances, a series of factors are defined below in (2.11). First, k_S is the safety factor which compares the maximum permissible speed to the base condition. While k_S should be a high value from a mechanical perspective, this approach does not utilize N_m^{Base} well. Since a SynRM is mostly operated below base speed using the MTPA strategy, N_m^{Max} is almost never reached. If k_S is already beyond 1.5, the structural integrity is already guaranteed for speeds exceeding N_m^{Base} by 50%. The second one is the stress correction factor, k_C, defined as the ratio between the analytical- and FEA-based stress (or inverse of max speeds). A motor designer can empirically use k_C to correct for the σ_{Ana} calculated. Third, k_F is the ratio of the centrifugal force to the total force on the tangential ribs. If this ratio is close to 1, this ensures that the structural and electromagnetic simulations are loosely related in terms of the critical stress in the tangential ribs and can be safely decoupled in a multiphysics analysis. Hence, k_S and k_F are to be maximized, while k_C is to be minimized.

$$\begin{aligned} k_S &= \frac{N_m^{Max}}{N_m^{Base}} \\ k_C &= \sqrt{\frac{\sigma_{Ana}}{\sigma_{FEA}}} = \frac{N_{m,FEA}^{Max}}{N_{m,Ana}^{Max}} \\ k_F &= \frac{F_c}{F_c + F_m} \end{aligned} \tag{2.11}$$

Acoustic Analysis

After the structural simulation, an acoustic analysis is performed to compute the SynRM's sound pressure level, P_{SL}, using the analytical/FEA-based approach discussed in [Gieras et al., 2005; Islam et al., 2014]. A detailed explanation is provided in the same section of the flowchart shown in Fig. 1.27 for the noise computation.

In summary, the sound pressure level due to electromagnetic sources is calculated using $\boldsymbol{B_n}$ from the electromagnetic analysis and using the stator natural frequencies, $\boldsymbol{f_s}$, computed via modal analysis from a structural FEA package [Siemens PLM Software Inc., 2018]. Table 2.2 provides $\boldsymbol{f_s}$ for both SynRM stators. As the harmonics of the normal airgap magnetic pressure wave, $\boldsymbol{P_n}$, and normal force, $\boldsymbol{F_n}$, computed in (2.12) get closer to $\boldsymbol{f_s}$, then the stator teeth are subjected to larger radial displacements, A_{mr}, as shown in (2.13), thereby resonating and causing sound pressure, P_S, in the surrounding air based on (2.14). This pressure value is then compared to a sound reference in order to finally calculate P_{SL} in dB using (2.15). Therefore, the P_{SL} objective is to be minimized. Here, w_{st} is the tooth width, L_{stk} is the stack length, μ_0 is the permeability of free space, F_{n_r} is the r^{th} amplitude of the normal force, f_{e_r} is the r^{th} harmonic frequency, f_{s_m} is the m^{th} mode of the stator's natural vibration, M_s is the stator mass (iron core and winding), ζ_m is the m^{th} harmonic of the damping factor, ρ_0 is the air density, c_0 is the speed of sound, and n_p is the number of poles.

Table 2.2 Stator Natural Frequencies $\boldsymbol{f_s}$ in Hz (first 10 modes)

Mode	1	2	3	4	5	6	7	8	9	10
24-slot	2177	5522	8673	10380	11092	11423	11581	11722	11777	11821
30-slot	2459	6227	9551	10994	11567	11788	11909	12015	12132	12160

$$\boldsymbol{P_n} \approx \frac{\boldsymbol{B_n}^2}{2\mu_0} = \frac{\boldsymbol{F_n}}{w_{st} L_{stk}} \tag{2.12}$$

$$A_{mr} = \frac{F_{n_r} / [(2\pi f_{s_m})^2 M_s]}{\sqrt{[1 - (f_{s_m}/f_{e_r})^2]^2 + [2\zeta_m (f_{s_m}/f_{e_r})]^2}} \tag{2.13}$$

$$P_S = 2\pi \rho_0 c_0 n_p \sum_m \sum_r A_{mr} \tag{2.14}$$

$$P_{SL} = 10 \log_{10} \left(\frac{P_S}{2 \times 10^{-5}} \right) \tag{2.15}$$

Thermal Analysis

Finally, the thermal results are computed using transient 3-D FE simulations for a totally enclosed non-ventilated cooling system [Mentor-Infolytica Corporation, 2018]. Different components, such as the housing, cores, and windings, were included. At every transient iteration, the total losses from the electromagnetic simulations are used to find the corresponding temperature distribution across all components at rated operation. Given the computational expense of running many simulations on a single workstation, the steady-state temperatures were not used to perform an additional electromagnetic analysis (HPC services were unavailable for thermal analysis). Also, results were only collected for the 24-slot SynRM.

Fig. 2.7 (a)-(b) show the transient response and the temperature distribution for a sample design. It is observed that the steady-state was reached in 20 iterations and that the winding and rotor core are among the hottest components. Appendix D displays the histograms of the component steady-state temperatures for the minimum, average and maximum cases. Since more than 15 thermal performances were calculated, it is imperative to check whether the thermal problem can be reduced. The correlation plot shown in Fig. 2.8 indicates that the average temperatures of all components have strong positive correlations (above +0.7). This means that only a few performances can be used to represent the thermal results. Therefore, two objectives, namely the average winding temperature, T_W, and the average rotor core temperature, T_R, are used. Here, T_W is averaged by the coil and end windings temperatures as in (2.16). It is desired to minimize both T_W and T_R.

$$T_W = \frac{T_{end}^{left} + T_{coil} + T_{end}^{right}}{3} \tag{2.16}$$

For all designs, the histograms of steady-state average component temperatures in Fig. 2.9 indicate that the hottest component is the stator winding due to copper loss, running below 80°C. This permits a higher current rating given that copper insulation can withstand up to around 150°C [Jiang, 2014]. After re-running the thermal simulations for peak transient operation, i.e. RMS current density of 9 A/mm^2 at twice the rated condition, it is observed in Fig. 2.10 (a) that there is a strong linear relationship between the rated and peak operations (correlation above +0.98) for both T_W and T_R across all designs. This means that the rated temperatures can be used to predict the peak temperatures.

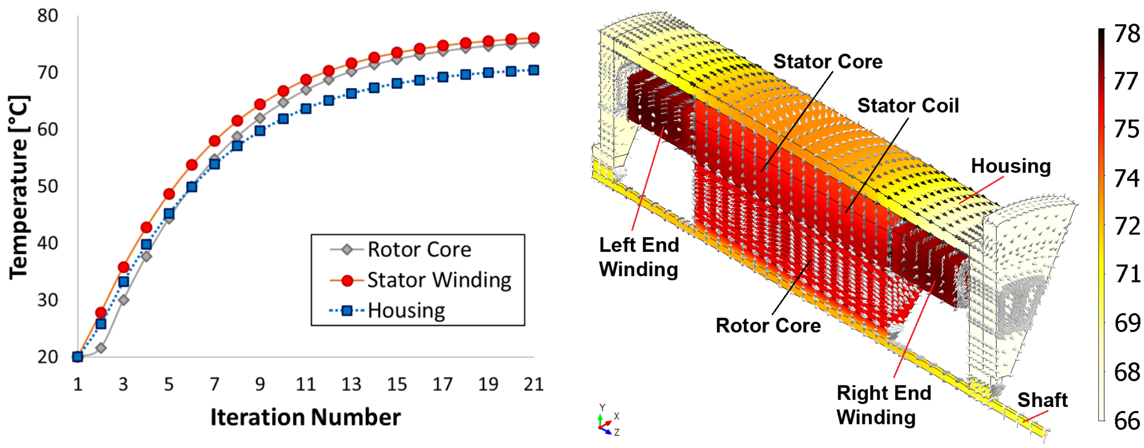

(a) (b)

Fig. 2.7 3-D thermal analysis results for an example SynRM: (a) transient temperature response, (b) steady-state temperature distribution [°C]. Note that a single slot is modeled using the stator's periodicity.

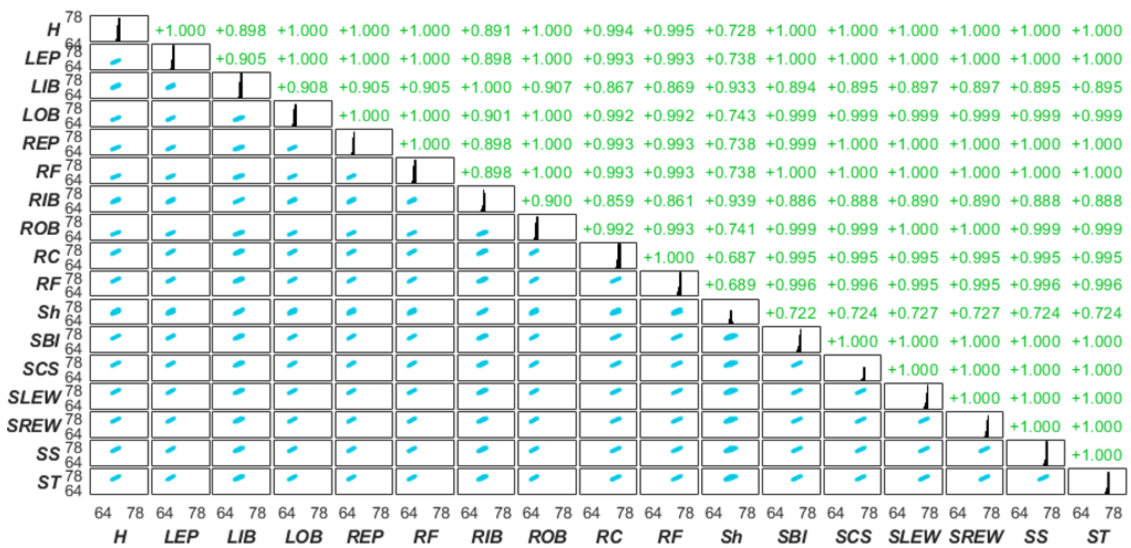

Fig. 2.8 Correlation of average component temperatures for 24-slot 3-barrier: housing (H), left end plate (LEP), left inner bearing (LIB), left outer bearing (LOB), right end plate (REP), right flange (RF), right inner bearing (RIB), right outer bearing (ROB), rotor core (RC), rotor filler (RF), shaft (Sh), stator back iron (SBI), stator coil side (SCS), stator left end winding (SLEW), stator right end winding (SREW), stator slot (SS), stator tooth (ST).

Also, the results indicate that the winding temperatures heat to around 180°C due to natural cooling. As seen in Fig. 2.10 (b), a current density of 8 A/mm^2 is recommended for transient peak operation to keep the winding insulation below its thermal limit. Similar results were observed for the other barrier datasets.

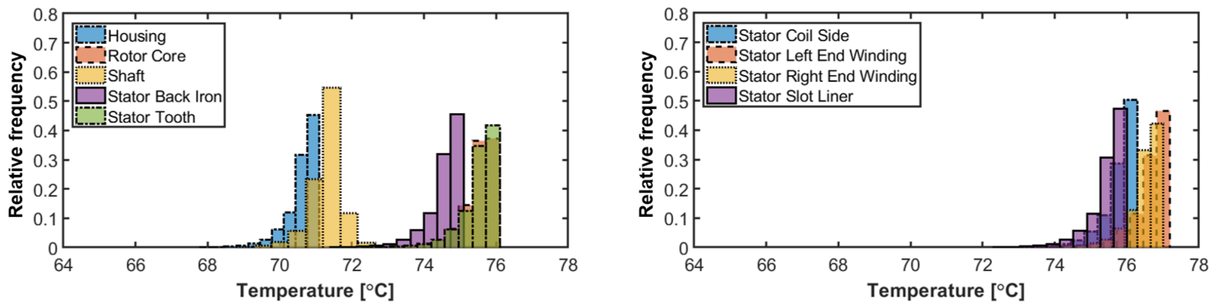

Fig. 2.9 Histograms of average component steady-state temperatures from 3-D thermal analysis: 24-slot 3-barrier.

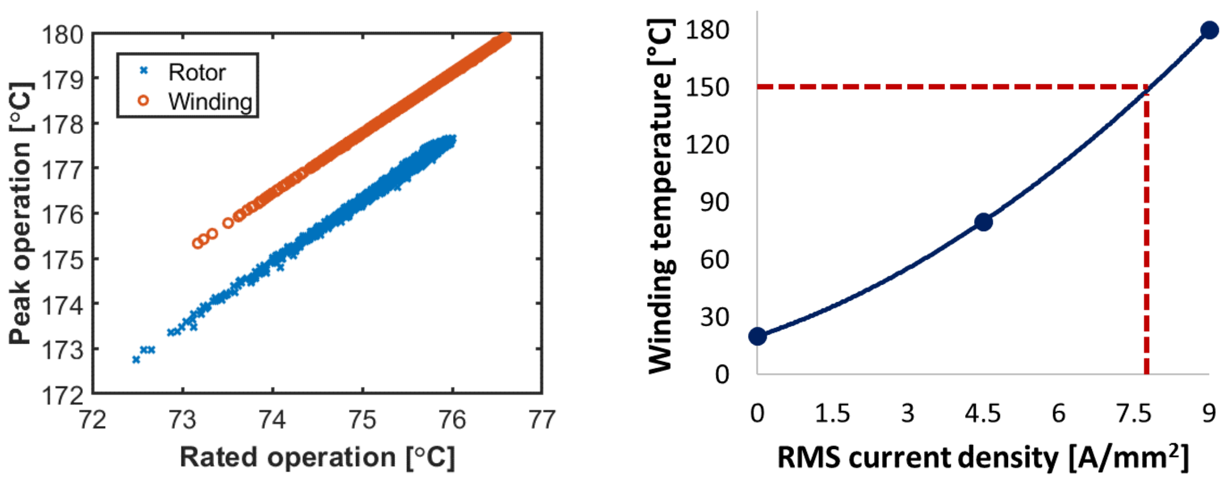

(a) (b)

Fig. 2.10 (a) Average rotor and winding temperatures at rated and peak operations. (b) Average winding temperature against RMS current density.

Multiphysics Objectives

In summary, electromagnetic (E), structural (St), acoustic (A) and thermal (T) analyses are performed to compute different multiphysics performances. These objectives are collectively shown within (2.17) in the form of 12 independent objectives with respect to the design variable vector, $\boldsymbol{x}$ and the MTPA advance angle, γ^{MTPA}. Note that the structural objectives do not depend on γ^{MTPA}, since the simulation only relied on centrifugal forces as explained in Section 2.2.2.

$$
\begin{array}{lll}
\text{E} & 1. & \text{max.} \quad T_{avg}\big(\boldsymbol{x}, \gamma^{\mathrm{MTPA}}\big) \\
\text{E} & 2. & \text{min.} \quad T_{rip}\big(\boldsymbol{x}, \gamma^{\mathrm{MTPA}}\big) \\
\text{E} & 3. & \text{max.} \quad pf\big(\boldsymbol{x}, \gamma^{\mathrm{MTPA}}\big) \\
\text{E} & 4. & \text{min.} \quad P_{Fe}\big(\boldsymbol{x}, \gamma^{\mathrm{MTPA}}\big) \\
 & & \quad \textit{or} \\
 & & \text{max.} \quad \eta\big(\boldsymbol{x}, \gamma^{\mathrm{MTPA}}\big) \\
\text{E} & 5. & \text{min.} \quad V_{rms}\big(\boldsymbol{x}, \gamma^{\mathrm{MTPA}}\big) \\
\text{E} & 6. & \text{max.} \quad \xi\big(\boldsymbol{x}, \gamma^{\mathrm{MTPA}}\big) \\
\text{E} & 7. & \text{min.} \quad L_d\big(\boldsymbol{x}, \gamma^{\mathrm{MTPA}}\big) \\
\text{E} & 8. & \text{max.} \quad N_m^{Base}\big(\boldsymbol{x}, \gamma^{\mathrm{MTPA}}\big) \\
\text{St} & 9. & \text{max.} \quad k_S\big(\boldsymbol{x}\big) \\
 & & \quad \textit{or} \\
 & & \text{max.} \quad N_m^{Max}\big(\boldsymbol{x}\big) \\
\text{A} & 10. & \text{min.} \quad P_{SL}\big(\boldsymbol{x}, \gamma^{\mathrm{MTPA}}\big) \\
\text{T} & 11. & \text{min.} \quad T_W\big(\boldsymbol{x}, \gamma^{\mathrm{MTPA}}\big) \\
\text{T} & 12. & \text{min.} \quad T_R\big(\boldsymbol{x}, \gamma^{\mathrm{MTPA}}\big)
\end{array}
\tag{2.17}
$$

2.2.4 High-Performance Computing

For each SynRM stator, i.e. 24-slot and 30-slot, there are 10,620 samples across the four barrier datasets (314+1066+3242+5998). This resulted in 21,240 samples in total, which poses computational problems during the performance evaluation stage, especially the electromagnetic analysis. In addition, more than 1 transient electromagnetic simulation is required for all design variations to find γ^{MTPA} for use in (2.17) due to the MTPA control strategy. For instance, in this thesis, an electromagnetic FE model discretizes its 2-D geometry using around 25,000 triangle mesh elements and simulates for approximately 4 minutes on a single workstation. Considering the total sample size of 21,240 variations and 3 runs per model for the MTPA strategy on a single workstation, the total simulation time would take around 177 days (6 months) to complete, that is for only one operating point!

To speed up the time-consuming electromagnetic simulations, a distributed computing approach is employed by simulating multiple models in parallel as shown in Fig. 2.11 through an HPC platform [Microsoft Azure, 2018]. Parallel VMs of size A1v2 (specs: 1 core, 2.1 GB RAM, 10.7 GB SSD storage) for a *Price* of CA$ 0.065 per hour per VM are used. The total duration, denoted by *Time*, includes the time required to set up a cluster of virtual machines (CC: *cluster creation*), deploy and run the required tasks as well as download all the results (DR: *deploy and run*), and remove the cluster (CR: *cluster removal*). As shown in (2.18), *Time* represents the total simulation time per dataset, *Unit* is the unit time per sample and VM, and *Cost* is the total cost to run the HPC in the cloud platform. Here, n_{Sample} is the number of samples in the dataset and n_{VM} is the number of virtual machines used. *Cost* adds 1 to n_{VM} since a master VM is required to coordinate the other VMs responsible for running the simulations. The flowchart of Fig. 2.12 describes the steps followed for running the electromagnetic simulation in the HPC system.

$$\begin{aligned} Time &= Time_{CC} + Time_{DR} + Time_{CR} \\ Unit &= \frac{Time}{(n_{Sample})(n_{VM})} \\ Cost &= (Price)(n_{VM}+1)(Time_{DR}) \end{aligned} \tag{2.18}$$

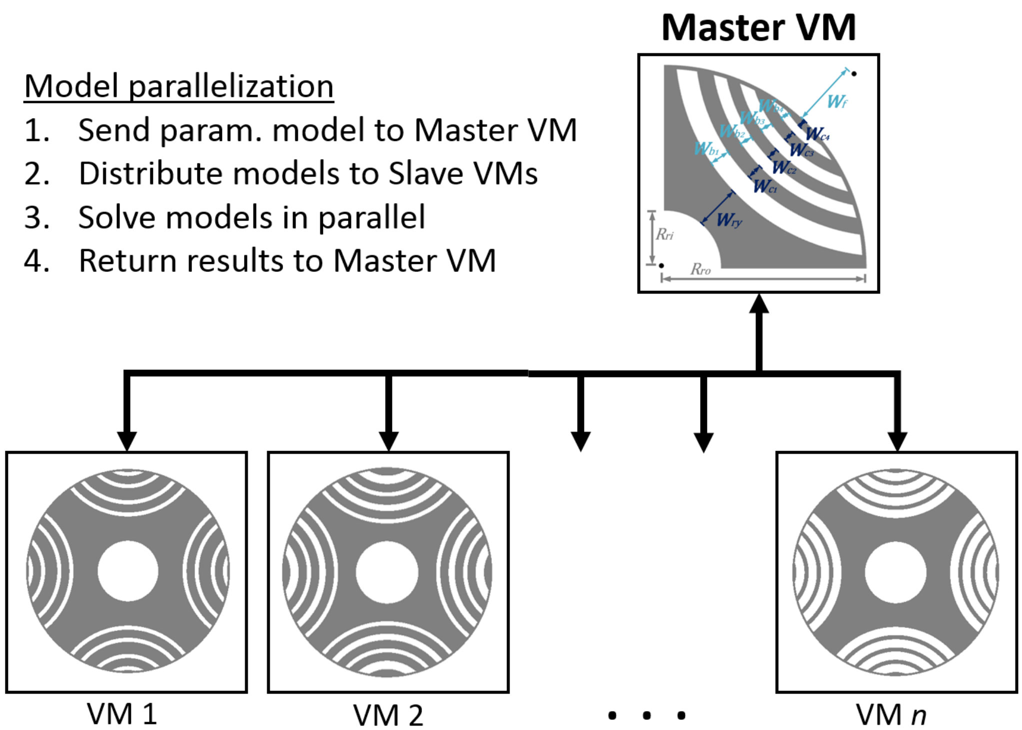

Fig. 2.11 Modeling parallelization through high-performance computing.

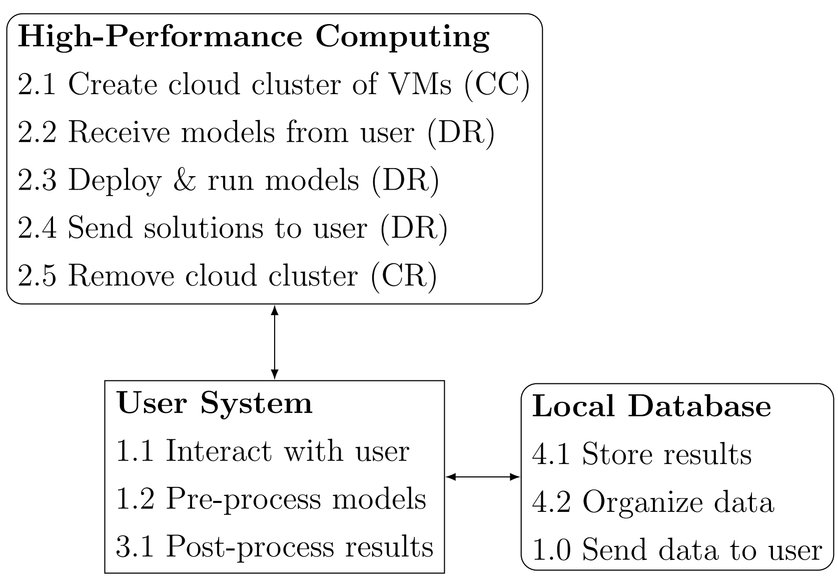

Fig. 2.12 Flowchart for high-performance computing.

A summary of the HPC simulations is shown in Table 2.3, where each dataset is represented by one row. Note that more samples were simulated to study the effect of different numbers of VMs on the simulation times and costs. That is, the datasets listed in the first 5 rows were not used in the MPDP. Also, the *Cost* is computed with respect to the DR time since the cluster of VMs is only available for use during that period.

Table 2.3 Summary of HPC Simulations for Electromagnetic Analysis

n_s	n_b	n_{Sample}	n_{VM}	$Time_{CC}$ [hours]	$Time_{DR}$ [hours]	$Time_{CR}$ [hours]	$Time$ [hours]	$Unit$ [sec]	$Cost$ [\$]
24	4	20	1	0.94	2.78	0.12	3.84	691.35	0.36
24	1	220	10	1.16	2.75	0.12	4.04	6.60	1.97
24	2	840	10	1.31	10.98	0.15	12.44	5.33	7.85
24	3	924	10	1.24	12.43	0.12	13.80	5.38	8.89
24	4	990	20	0.96	6.89	0.13	7.99	1.45	9.41
24	1	314	30	0.84	1.43	0.15	2.42	0.93	2.88
24	2	1066	30	0.84	4.81	0.15	5.80	0.65	9.70
24	3	3242	30	0.84	14.90	0.15	15.89	0.59	30.02
24	4	3000	40	0.93	11.70	0.16	12.79	0.38	31.17
24	4	2998	40	0.93	11.50	0.16	12.60	0.38	30.65
30	1	314	20	0.94	2.17	0.13	3.23	1.85	2.96
30	2	1066	20	0.94	7.63	0.13	8.69	1.47	10.41
30	3	3242	40	0.91	11.15	0.16	12.21	0.34	29.71
30	4	3000	40	0.91	10.43	0.16	11.50	0.34	27.81
30	4	2998	30	0.89	14.30	0.15	15.34	0.61	28.81

For the 24-slot case study, the total HPC times took approximately 3, 6, 16 and 26 hours (CA\$ 3, CA\$ 10, CA\$ 30 and CA\$ 62 of *Cost*) for the four datasets respectively. Also, the *Time* and *Cost* of the 30-slot case study are observed to be slightly higher due to the increased stator and winding complexity. A few more observations can be made from Table 2.3. First, $Time_{CC}$ and $Time_{CR}$ are approximately constant with averages and standard deviations of 0.97±0.15 and 0.14±0.02 hours respectively. This means that only $Time_{DR}$ varies with respect to n_{Sample} and n_{VM}. Second, the utilization ratio defined in [Ghorbanian, 2018], i.e. $UR = Time_{DR}/Time$ is observed to be higher than 88% meaning that the VMs in the HPC platform are used well for this application. A computational bottleneck, reported in [Ghorbanian, 2018], was the download of electromagnetic solutions (results and fields) during DR. In this work, only the results were saved which practically reduces the download portion. Third, the *Cost* of running both case studies is around CA$ 204 which is a reasonable tradeoff for reducing the total time to 4.2 days.

Moreover, Figs. 2.13 and 2.14 show the *Unit* and speedup respectively against the number of VMs. An inverse relationship is observed which corresponds to a time-versus-cost tradeoff. The number of VMs can be chosen when the incremental benefit of increasing the number of VMs does not significantly change the simulation time. This helps to reduce *Cost* which was performed by choosing mostly 30 or 40 VMs for the datasets. Due to the negligible download time, i.e. each solved result for a design sample was in the order of kilobytes, the speedup is almost linear with respect to the number of VMs. However, the speedup did not scale linearly for the case study in [Ghorbanian, 2018] since the downloaded files consisted of solved FEA models that are megabytes large. There are fewer communication overheads in the employed HPC system when simulating the considered electromagnetic FE models.

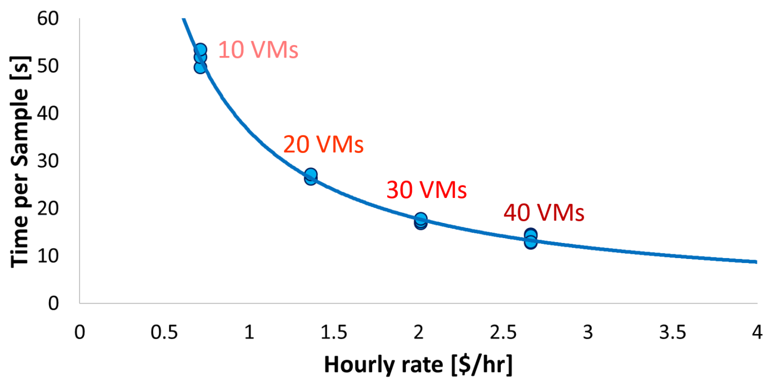

Fig. 2.13 HPC simulation report: time-vs-cost.

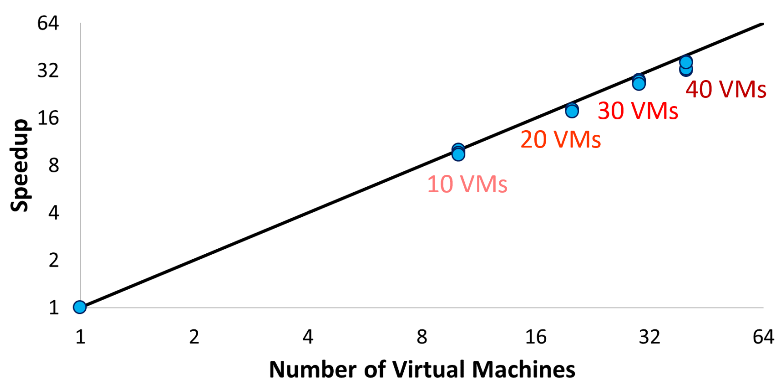

Fig. 2.14 HPC simulation report: speedup against number of VMs.

Since the HPC platform was unavailable for the structural and thermal analyses, they were run on individual workstations for the following specifications: Intel Xeon E5-1650 (6 cores, 3.50 GHz) with 32 GB of RAM. Each 3-D structural FEA evaluation with around 30,000 tetrahedral elements took about 40 seconds on average resulting in a total simulation time of 5 days for 10,620 samples (same rotor variations for both stators). The axial or stack size was fixed at 8 laminations since it was observed that increasing the number did not significantly change the maximum von Mises stress. Therefore, 8 laminations were chosen based on a computational tradeoff for the structural analysis.

For the 3-D thermal transient analysis, each model required 1.5 minutes to run the electromagnetic analysis before running the transient thermal simulation for 2.5 minutes. This resulted in a total of around 4 minutes per sample using the same workstation, i.e. Intel Xeon E5-1650 (6 cores, 3.50 GHz) with 32 GB of RAM. The simulation times correspondingly took 1, 3, 9 and 17 days for the four barrier datasets. Similar times are reported for the 30-slot case study. Note that only 1 coupled iteration was used for reducing total computational times, i.e. the electromagnetic analysis fed into the thermal one without another feedback loop. While this assumption may impact the accuracy of results, all the samples are affected and the MPDP compares their trends.

Since the acoustic analysis relied on the electromagnetic results along with the stator natural frequencies using the semi-analytical procedure described in Fig. 1.27, the sound pressure level values were calculated without any computational issues. All the acoustic results for both cases were obtained on the order of minutes.

2.3 Stage 3: Filtering Undesirable Solutions (*interact*)

Once the multiphysics performances of all design samples are evaluated, various constraints must be set in Stage 3. This ensures practical designs are used in subsequent stages [Ghorbanian and Lowther, 2017]. While certain limits can be preset within the MPDP, such as the maximum operating temperature, other thresholds could be based on the knowledge of an experienced user. For example, the rotor design widths, W_{c_k} and W_{b_k}, can be checked as to whether they are within manufacturing tolerances. Otherwise, the MPDP can continue to the knowledge extraction stage explained in Chapter 4.

2.4 Summary

The first three stages of the MPDP displayed in Fig. 1.30 were discussed and explained in this chapter. These stages include: (1) setting the initial specifications by the user (i.e. classical, sizing and simulation settings), (2) running the multiphysics simulation process internally (electromagnetic, structural, acoustic, thermal), and (3) filtering undesirable solutions based on a user's constraints. Specifically, the parameterization, the design metrics and the geometric constraints of a SynRM rotor with round-shaped barriers were demonstrated. Two different stators, i.e. the 24- and the 30-slot, were also introduced for comparing results in subsequent chapters. For each of the four rotor datasets considered in this chapter (i.e. 1, 2, 3 and 4 barriers), Latin hypercube sampling with the maximin criterion was used to sample and cover the corresponding design space. Next, different multiphysics performances were simulated, which included electromagnetic (average torque, torque ripple, power factor, iron loss or efficiency, RMS voltage, saliency ratio, d-axis inductance, base speed), structural (safety factor or maximum mechanical speed), acoustic (sound pressure level), and thermal analyses (average winding temperature, average rotor temperature). Also, the use and benefit of an HPC system were discussed in the context of generating electromagnetic results. Due to the distributed nature of simulating many models in parallel, the computational time was significantly reduced from months to days when compared to simply running on a single or few workstations. A linear speedup was reported due to negligible communication overheads in the HPC system for the considered finite element models.

Chapter 3

Restricting the Design Space of Multiple-Barrier Rotors

With a deviation from the MPDP, which continues in Chapter 4, this chapter introduces the concept of *barrier mapping*, useful in the design process. This numerical methodology, proposed in Section 3.1, reduces the number of computations required to optimally design the rotor of SynRMs with multiple barriers. Optimal geometrical constraints of a multiple-barrier SynRM rotor can be found to restrict its corresponding design space. This approach can handle the curse of dimensionality when the number of geometric parameters increases and can reduce the number of initial samples required prior to a multi-objective optimization.

In Section 3.2, *barrier mapping* is applied to two electromagnetic objectives, i.e. average torque and torque ripple. Different numbers of rotor flux barriers are statistically analyzed to find their respective design correlation for high average torque solutions. From this information, optimal geometrical constraints are then found to restrict the design space of multiple-barrier rotors. Statistical analysis of the considered SynRMs demonstrates a design similarity between the different numbers of flux barriers.

Next, *barrier mapping* is extended to acoustic analysis in Section 3.3. The two electromagnetic objectives and the sound pressure level are considered using a surrogate-based multi-objective approach to extract optimal design regions. Similar to Section 3.2, these regions or constraints help decrease the computational time required during the sampling procedure of a multiple-barrier design. Adding the sound pressure level objective is found to affect the previous results by spreading the Pareto front solutions across the design space.

3.1 Barrier Mapping Methodology

Compared to a single-barrier rotor, more variables are needed to accurately model a multiple-barrier rotor's geometry as in (2.1) and seen in Fig. 2.3. Additional parameters introduce the curse of dimensionality since more computational effort is required to sample the design space prior to starting an optimization process. To tackle this issue, a generalized methodology called *barrier mapping* is proposed as illustrated in Fig. 3.1. Instead of directly sampling the entire design space of an M-barrier rotor with k variables per barrier using N_D samples, a 1-barrier rotor is initially explored using N_1 samples. After statistically analyzing the different performances (e.g. average torque, torque ripple), the M-barrier rotor is sampled in its optimal region derived from the 1-barrier's optimal space using N_M samples only. Finding this restricted region of the M-barrier rotor's design space would then require fewer samples, as shown by the inequality in (3.1).

Hence, the sections below use the proposed *barrier mapping* methodology to arrive at optimal SynRM designs for two examples: (1) only electromagnetic objectives in Section 3.2, and (2) a combination of electromagnetic and acoustic objectives in Section 3.3.

$$(N_1 + N_M) \leq N_D \tag{3.1}$$

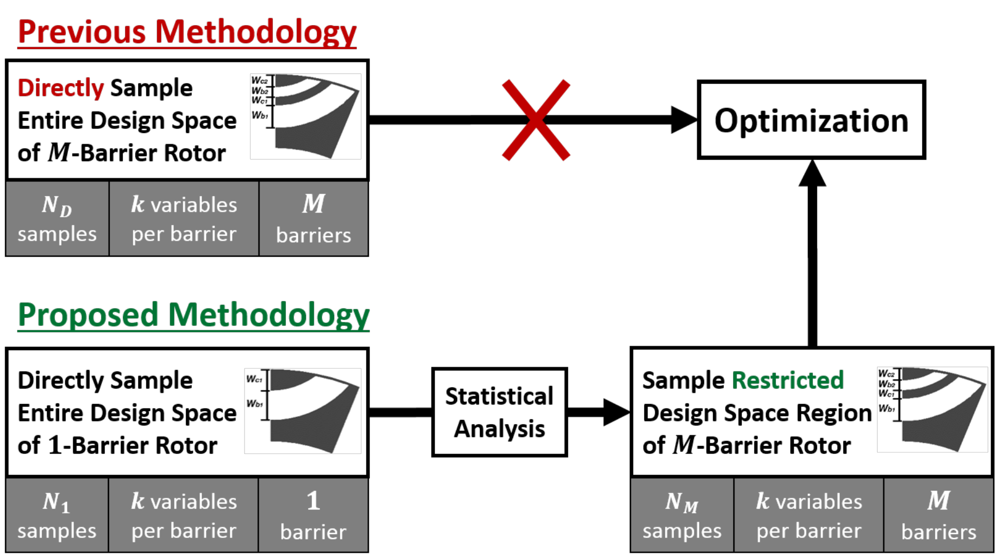

Fig. 3.1 *Barrier mapping* methodology for design space restriction.

3.2 Electromagnetic Example

This section based on [Mohammadi et al., 2017a] applies the *barrier mapping* methodology for two electromagnetic objectives for two SynRM models.

3.2.1 Rotor Geometric Design

Table 3.1 displays the fixed design parameters of two SynRM models. Model A uses liquid cooling and is a relatively large motor sized for a Class IV electric vehicle, while Model B is a smaller motor rated at 250 W. Both models were chosen to compare the effectiveness of the proposed approach for different slot-per-pole combinations and motor sizes. The number of poles is selected based on the method presented in [Mohammadi et al., 2016].

Table 3.1 Fixed SynRM Design Parameters

Parameter	**Model A**	**Model B**
Number of slots/poles	33/8	12/4
Stator's outer diameter	325 mm	75 mm
Rotor's outer diameter	220 mm	40 mm
Stack length	275 mm	34 mm
Airgap thickness	0.75 mm	0.50 mm
RMS current density	20.0 A/mm^2	10.0 A/mm^2
Cooling method	Liquid	Natural Convection

The rotor geometric design follows the one defined in Chapter 2.1.3. The same metrics and constraints specified in (2.2) and (2.4) are used. A difference, however, is that the width of the k^{th} tangential rib, W_{t_k}, is added to $\boldsymbol{x}$ in (2.1) for Model B. The W_{t_k} of Model A is fixed at 1 mm. Also, the flux barrier ratio, a_k, is defined in (3.2) for every k.

$$a_k = \frac{W_{b_k}}{W_{c_k} + W_{b_k}} \tag{3.2}$$

Next, a full factorial approach, explained in [Jurecka, 2007], is used to sample the multiple-barrier designs for both Model A and Model B in $\mathscr{F}_\Delta$. This sampling approach helps later in Section 3.2.5 when a relative measure of the design space restriction is calculated. Table 3.2 lists the sampled parameters for each model, while Table 3.3 displays the number of FEA samples computed per barrier number. Also, these samples include different variations of a_k which was kept constant across every barrier in [Hudák et al., 2006].

Table 3.2 Variable Design Parameters

Parameter	**Symbol**	**Model A**	**Model B**
Current advance angle	γ	Varied	Varied
Width of flux carrier k	W_{c_k}	Varied	Varied
Width of flux barrier k	W_{b_k}	Varied	Varied
Width of tangential rib k	W_{t_k}	Fixed	Varied
Inset width of barriers	W_f	Fixed	Varied

Table 3.3 Number of FEA Samples

k	**Model A**	**Model B**
1 barrier	91	806
2 barrier	1366	21250
3 barrier	5004	6722
4 barrier	6436	-

3.2.2 Simulation Setup

For every design sample, the procedure described in Section 2.2.3 is adopted to compute T_{avg} and T_{rip} as in (2.5) and (2.6) respectively. Next, the MTPA control strategy is used to relatively compare each rotor design. The average reluctance torque T_{avg} (post-processed from 2-D FEA solutions) is maximized for a given current level I_s by varying the current advance angle γ [Matsuo and Lipo, 1994; Soong et al., 1995]. Upon examining the simplified dq representation of T_{avg} in (3.3), the dq rotor inductances, L_d and L_q, depend on the rotor geometry in each design. This implies that a single γ (e.g. 45°) cannot be used for all rotor variations and an alternative sub-optimization model is required to find the maximum T_{avg} with respect to γ at a fixed I_s.

$$T_{avg} = \frac{1}{2}\frac{3}{2}\frac{n_p}{2}\left(L_q - L_d\right) I_s^2 \sin 2\gamma \tag{3.3}$$

3.2.3 Objective Space

Once all the MTPA samples in Table 3.3 are computed, the non-dominated Pareto front solutions for both models are plotted in Fig. 3.2. Here, T_{avg} is maximized, while T_{rip} is minimized. In short, these optimal points in the (T_{avg},T_{rip}) objective space demonstrate a tradeoff relationship.

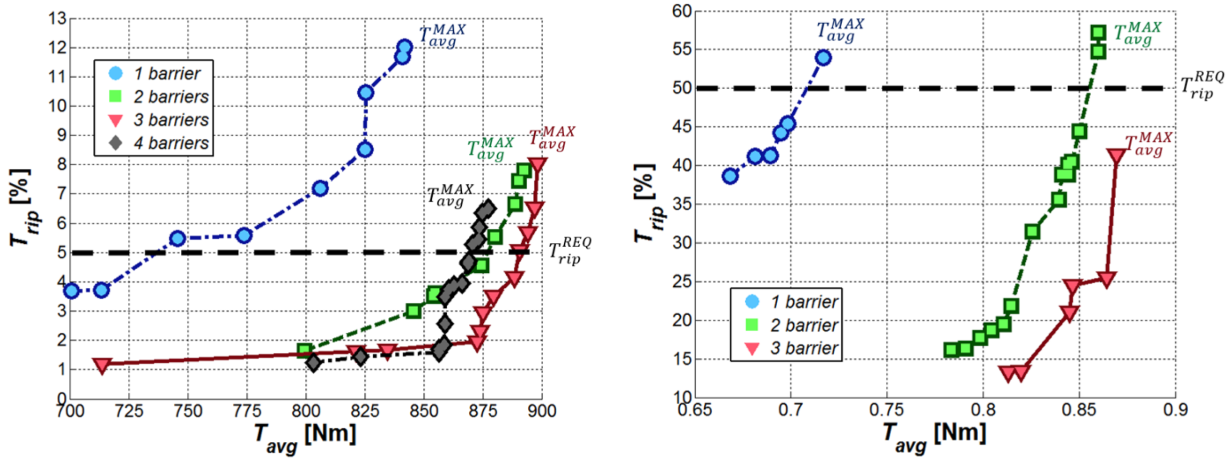

Fig. 3.2 Pareto solutions in the objective space: (a) Model A, (b) Model B.

As the number of rotor barriers increases, the corresponding fronts move toward higher T_{avg} and lower T_{rip} values. For instance, a 3-barrier rotor design of Model A can provide a (T_{avg},T_{rip}) of (875 Nm, 2%) as displayed in Fig. 3.2 (a). Referring to the analytical recommendation presented in [Vagati et al., 1998], a 33-slot, 8-pole SynRM with the lowest torque ripple requires a 3-barrier configuration which correlates well the different Pareto fronts. Interestingly, a 4-barrier configuration does not improve the torque performance which signifies an optimal relationship between the number of stator slots and rotor flux carriers. A similar trend is also observed in Fig. 3.2 (b) for Model B where multiple-barrier rotors have better torque performances.

3.2.4 Design Space

Once the Pareto front solutions are computed, e.g. Fig. 3.2 for Models A and B, it is desired to visualize how these optimal solutions align together and cluster in the design space. Hence, all the high-T_{avg} solutions are constrained using (3.4) for Models A and B. Here, $\mathscr{F}_{\mathrm{HT}}$ represents the set of high-T_{avg} set of designs of each case study. Note that a relative measure using T_{avg}^{MAX} is employed for the constraint since the multiple-barrier Pareto fronts are far away from the 1-barrier's. Then, $\mathscr{F}_{\mathrm{HT}}$ is mapped into the (W_c,W_b) design space using (2.2) as illustrated in Fig. 3.3 (a)-(b) respectively. Different ellipses, ε_k, are computed such that each ε_k encapsulates $\mathscr{F}_{\text{HT}}$ per barrier number k [Mohammadi et al., 2016]. The procedure to analytically capture these high-T_{avg} Pareto solutions is described as follows.

$$\mathscr{F}_{\text{HT}} = \left\{\boldsymbol{x} | T_{avg}(\boldsymbol{x}) \geq 0.90 T_{avg}^{\text{MAX}}\right\} \tag{3.4}$$

First, the convex optimization given in (3.5) is formulated. For a given set of optimal design points such as $\mathscr{F}_{\text{HT}}$, the area of the ellipse ε is minimized such that the interior of ε contains all the given design points [Boyd and Vandenberghe, 2004]. Second, the unknown parameters of ε in (3.5) are computed which include the matrix $\boldsymbol{A}$ and the vector $\boldsymbol{b}$, each of size 2. Here, $\boldsymbol{A}$ and $\boldsymbol{b}$ govern the eccentricity and the center of ellipse ε respectively, and $\boldsymbol{W}$ is the vector of the mapped widths to the single-barrier plane.

$$\begin{aligned} \max. \ & \sqrt{\det \boldsymbol{A}} \\ \text{s.t.} \ & \left\| \boldsymbol{A}\boldsymbol{W} + \boldsymbol{b} \right\|_2 \leq 1 \\ & \boldsymbol{W} = [W_c, W_b]^T \end{aligned} \tag{3.5}$$

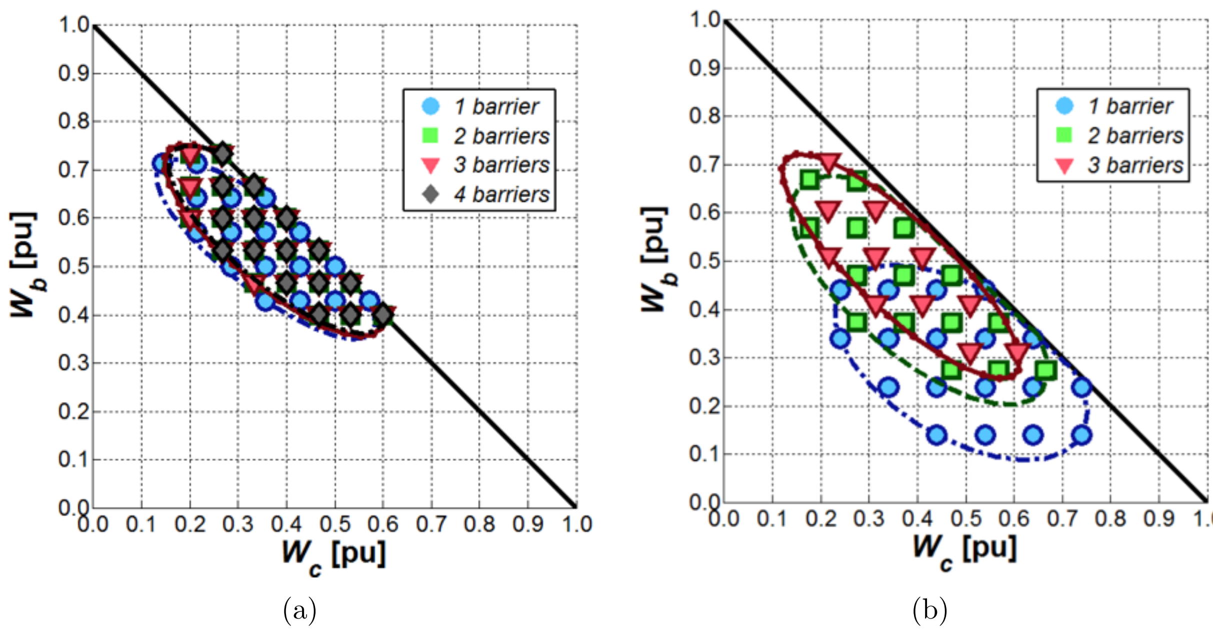

Fig. 3.3 $\mathscr{F}_{\text{HT}}$ solutions in (W_c,W_b) design space: (a) Model A, (b) Model B.

Upon solving (3.5), it is observed that the ε constraints in Fig. 3.3 (a)-(b) are similar to the constant-T_{avg} contour lines in Fig. 1.21 (c). For example, ellipse ε_1 constrains the design region of optimal 1-barrier solutions. Note that the multiple-barrier ellipses (e.g. ε_2, ε_3, ε_4) are affine transformations of ε_1 and visually verify (2.2), by overlapping with ε_1. The location of the high-T_{avg} solutions, $\mathscr{F}_{\mathrm{HT}}$, in the 1-barrier space can then help identify a restricted region in a multiple-barrier space through (2.2) and reduce the number of samples needed to optimize a rotor geometry.

Although the ellipses indicate an optimal region in the (W_c,W_b) plane, useful information about the flux barrier ratios a_k is lost by only using (2.2). To find the optimal a_k values, $\mathscr{F}_{\mathrm{HT}}$ is further constrained for low T_{rip} using (3.6) for both Model A and Model B. Here, $\mathscr{F}_{\mathrm{OPT}}$ represents the set of optimal solutions satisfying the high-T_{avg} and the low-T_{rip} constraints to compute a_k using (3.2). The T_{rip}^{REQ} value for Models A and B are set to be 5% and 50% respectively. This extra condition constrains the multiple-barrier space to an optimal region.

$$\mathscr{F}_{\mathrm{OPT}} = \left\{ \boldsymbol{x} | \mathscr{F}_{\mathrm{HT}} \cap T_{rip}(\boldsymbol{x}) \geq T_{rip}^{\mathrm{REQ}} \right\} \tag{3.6}$$

Subsequently for both case studies, the per-unit ranges of optimal a_k values for each barrier number k are used to compute the total flux barrier ratio, a, using (2.2) as shown in Table 3.4. This table also includes the range for the total width, $W_c + W_b$, imposed by (2.4). Furthermore, it is observed that the set of optimal solutions tends to cluster near the width limit line, $W_c + W_b = W_{\mathrm{lim}}$. This means that optimal rotor designs are inclined to distribute their flux barriers starting from the rotor's outer diameter to the extreme limit near an adjacent pole. The a ratio ranges in Table 3.4 agree well with the suggested range [0.3, 0.5] in [Matsuo and Lipo, 1994] to produce the highest average torque.

Table 3.4 Optimal Parameter Range [Min, Max]

Model	k	a [pu]	$W_c + W_b$ [pu]
A	2	[0.50, 0.79]	[0.87, 1.00]
	3	[0.40, 0.79]	[0.87, 1.00]
	4	[0.40, 0.73]	[0.87, 1.00]
B	2	[0.29, 0.67]	[0.74, 0.94]
	3	[0.34, 0.77]	[0.73, 0.92]

3.2.5 Comparison of Computational Efforts

The previous two subsections verified the benefit of using the proposed methodology as shown in Fig. 3.1 by analyzing the objective and design spaces for both case studies. Upon mapping the multiple-barrier space to a single-barrier one using (2.2), the relative accuracy of optimal solutions remains consistent as visualized in Fig. 3.3. However, a direct comparison of the computational effort required for the two methodologies is still necessary.

Hence, the N_1, N_D and N_M variables in (3.1) are set using the total number of FEA samples listed in Table 3.3. For instance, if a 2-barrier design of Model A is required, the direct methodology using a full factorial sampling sets $N_D = 1366$, while the proposed methodology sets $N_1 = 91$ and $N_2 = 357$. Here, N_2 includes the set of optimal solutions, $\mathscr{F}^A_{\mathrm{OPT}}$, for the 2-barrier dataset of Model A. A similar analysis is performed for all barrier numbers and both models as in Table 3.5. Then, the total reduction percentage, R_k, for each barrier number k is calculated using (3.7). This percentage value represents the sample reduction in the proposed approach with respect to the direct methodology in Fig. 3.1.

$$R_k = \frac{N_D - (N_1 + N_k)}{N_D} \tag{3.7}$$

Table 3.5 Computational Comparison of Methodologies

Model	k	N_D	$N_1 + N_k$	R_k
A	2	1366	91+ 357	67%
	3	5004	91+1792	62%
	4	6436	91+2770	56%
B	2	21250	806+704	93%
	3	6722	806+794	76%

For example, the search space of the multiple-barrier rotor is reduced by around 67% and 62% for the 2-barrier and 3-barrier rotors of Model A respectively. It should be noted that the 3-barrier dataset is not constrained as much as the 2-barrier case because the 3-barrier rotor has a lower torque ripple in general. This will be explained in the next subsection using histograms. Therefore, the computational efforts required to generate the set of optimal solutions in Fig. 3.3 is significantly reduced by using the proposed design methodology.

3.2.6 Statistical Analysis

In addition to the above discussions, statistical analyses of Model B's results are presented below to correlate the design parameters and the objective values. Note that Model A is ignored in this analysis since two of Model A's parameters were fixed as shown in Table 3.2. For the 1-barrier, 2-barrier and 3-barrier datasets, Fig. 3.4 shows the histograms of Model B's average torque and torque ripple. Generally speaking, it is observed that the average torque increases and the torque ripple reduces in the 2- and 3-barrier cases. Also, the two modes of Fig. 3.4 (a) appear as one peak for the 3-barrier case. Similar trends were also observed for Model A. In addition, the normal distribution statistics (mean and standard deviation) of Model B are listed in Table 3.6 using all the FEA samples described in Table 3.3. The improved torque performance validates the key benefit of using multiple-barrier rotors for SynRMs. Also, the flux plots of two optimal designs of Model B in Fig. 3.5 demonstrate how the flux lines are more evenly distributed for the 3-barrier rotor resulting in lower torque ripples as in Fig. 3.2.

Table 3.6 Normal Distribution Statistics of Model B

k	**Statistic**	T_{avg}	$\log_{10}(T_{rip})$
1	Mean	0.489 Nm	2.077%
	Std. Dev.	0.160 Nm	0.222%
	Num. of Samples	806 samples	
2	Mean	0.624 Nm	1.900%
	Std. Dev.	0.121 Nm	0.203%
	Num. of Samples	21250 samples	
3	Mean	0.700 Nm	1.770%
	Std. Dev.	0.087 Nm	0.191%
	Num. of Samples	6722 samples	

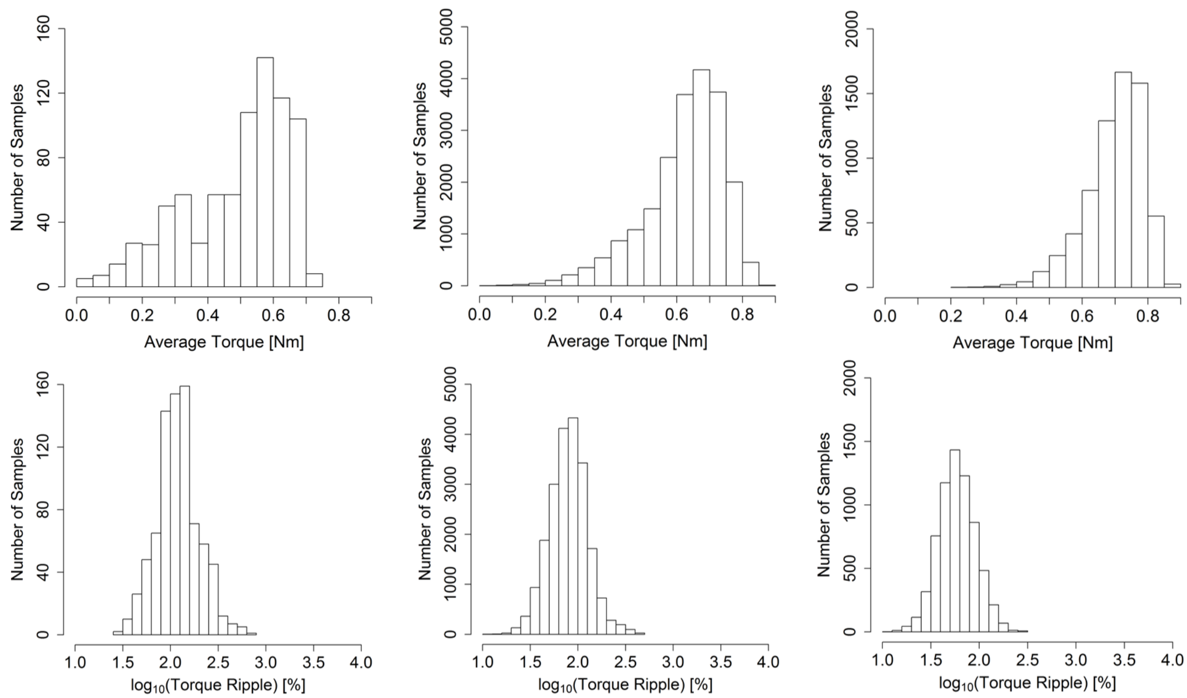

(a) (b) (c)

Fig. 3.4 Performance histograms for Model B. [Top] T_{avg}, [Bottom]: $\log_{10}(T_{rip})$. (a) 1-barrier, (b) 2-barrier, (c) 3-barrier.

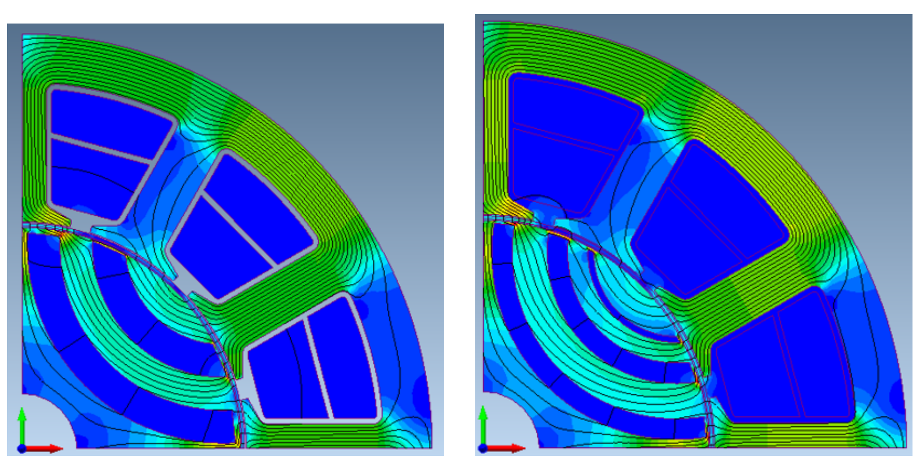

(a) (b)

Fig. 3.5 Flux density distribution at rated condition of Model B's selected designs: (a) 2-barrier, (b) 3-barrier. Only a quarter cross-section is shown.

Furthermore, the Spearman rank correlation coefficients (explained in Appendix A) are computed in terms of the design parameters of the 1-barrier, 2-barrier, and 3-barrier datasets. In short, if the Spearman coefficient of two parameters is greater than zero, then their nonlinear correlation is also positive. Fig. 3.6 (a)-(c) displays the variable clustering dendrograms for the three datasets respectively which help visualize a hierarchy of variable correlations [McIntosh et al., 2016].

For instance, it is observed in Fig. 3.6 (a) that W_c and W_b in a 1-barrier configuration are more nonlinearly correlated to each other than perhaps W_f or even W_t. For the 2-barrier case in Fig. 3.6 (b), W_{t_1} and W_{t_2} are more correlated with each other and with W_f as well. Also, the W_{c_1}, W_{b_1}, W_{c_2} and W_{b_2} parameters are heavily correlated to each other per barrier number k. This suggests that more samples are required to account for these nonlinear design parameters. In addition, the 3-barrier dataset in Fig. 3.6 (c) shows that the W_{t_k} parameters cannot be ignored since they are coupled together with W_f for each k. As expected, each flux barrier and carrier combination W_{c_k} and W_{b_k} are again heavily correlated. The innermost tangential rib controlled by W_{t_2} is also correlated with W_f indicating that adding more design parameters is necessary for accurately modeling multiple-barrier SynRM rotors.

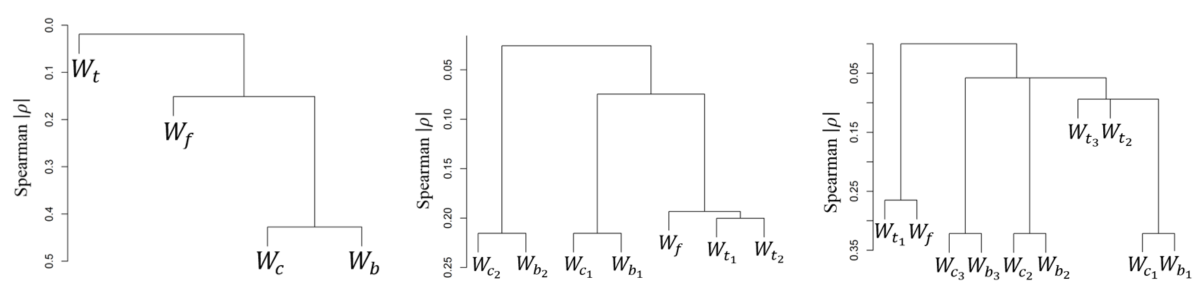

(a) (b) (c)

Fig. 3.6 Variable clustering for Model B: (a) 1-, (b) 2-, (c) 3-barrier.

3.3 Electromagnetic with Acoustic Example

This section based on [Mohammadi et al., 2018b] applies the *barrier mapping* methodology for average torque, torque ripple and sound pressure level for Model A. The structural integrity of the SynRM rotor for fixed speed operation is also analyzed.

3.3.1 Rotor Geometric Design

Similar to Section 3.2.1, the rotor design of Model A (33-slot 8-pole SynRM) follows that defined in Chapter 2.1.3. Its rotor speed was set to 500 RPM for the objective calculation, and its fixed design parameters are shown in Table 3.1.

3.3.2 Objective Calculation

Multi-objective optimization is computationally-intensive especially when FEA simulations are used for the function evaluations. Also, modeling multiple flux barriers requires more variables compared to a single barrier, which increases the computational burden. To overcome this issue, a surrogate-based approach is used where a fixed number of designs are evaluated using FEA before the optimization stage. Three different barrier datasets (1, 2 and 3) are considered and each one is sampled as in Table 3.3. Every objective per dataset is modeled using a surrogate to quickly evaluate solutions during the optimization procedure.

To ensure the rotor's structural integrity during rated operation, static stress analysis discussed in Section 2.2.3 is performed to find the maximum allowable speed, N_m^{Max}. The analytical critical stress, σ_{Ana}, is calculated using centrifugal and electromagnetic forces as in (2.10). Here, N_m is 500 RPM and P_n^0 is set as 0.25 MPa based on average flux density values. This worst-case approach overestimates the stress calculated via structural FEA. Across all the design samples, M_r varied from 14 kg to 46 kg. This implies that N_m^{Max} computed using (3.8) varies from 1200 RPM to 1800 RPM using a safety factor, k_S, of 1.2. Hence, this result confirms that the fixed W_t value for all sampled rotors offers sufficient structural support for this fixed speed application.

$$N_m^{Max} = N_m \sqrt{\frac{\sigma_S}{k_S \sigma_{Ana}}} \tag{3.8}$$

Electromagnetic: average torque and torque ripple

For every design sample, the procedure in Section 2.2.3 is used to compute T_{avg} and T_{rip} as in (2.5) and (2.6) respectively. Both objectives are calculated using the MTPA strategy to fairly compare all rotor designs below base speed. Each FEA evaluation using the MTPA strategy took about 6 minutes on average using an Intel Xeon E5-1650 (6 cores, 3.50 GHz) with 32 GB of RAM.

Acoustic: sound pressure level

Similarly, the sound pressure level, P_{SL}, is calculated using the calculation procedure explained in Section 2.2.3. The harmonics of airgap $\boldsymbol{B_n}$ resonate with the stator structure through $\boldsymbol{f_s}$ causing radial displacements and sound pressure in the surrounding air.

3.3.3 Surrogate Modeling

After sampling the three datasets (i.e. 1, 2, 3-barrier) and calculating all the performances, the surrogate models are fitted to each objective as a function of $\boldsymbol{x}$. As in [Mohammadi et al., 2016], a Bayesian regularization backpropagation neural network with one hidden layer, $2n_b$ inputs, and one output is selected per objective. The training, validation and testing sets are randomly divided into 60%, 10% and 30% per dataset. Also, a standard procedure is used to train each objective network by incrementally varying the number of neurons until convergence is met. This process stops when the coefficient of determination, R^2, of the training, validation and testing sets are all above 0.95. Hence, the number of neurons of (T_{avg},T_{rip},P_{SL}) were then set to be (5,5,5), (10,15,10) and (15,25,15) for the three datasets.

Fig. 3.7 shows the response surfaces of T_{avg}, T_{rip}, P_{SL}, and γ_{MTPA} of the 1-barrier dataset. Similar to [Mohammadi et al., 2016], fewer neurons are needed to fit T_{avg} because its response surface is unimodal. The opposite holds for T_{rip} due to its many peaks and valleys. Also, γ_{MTPA} varies between 35° and 65° within the design space indicating the need of using the MTPA control strategy. Moreover, it is visually observed that P_{SL} conflicts with T_{avg} and T_{rip}. That is, the location of maximum T_{avg} in the (W_c,W_b) design space does not correspond to the minimum P_{SL} location. Thus, the electromagnetic constraint in Section 3.2.4 for restricting the design space does not hold when dealing with the P_{SL} objective.

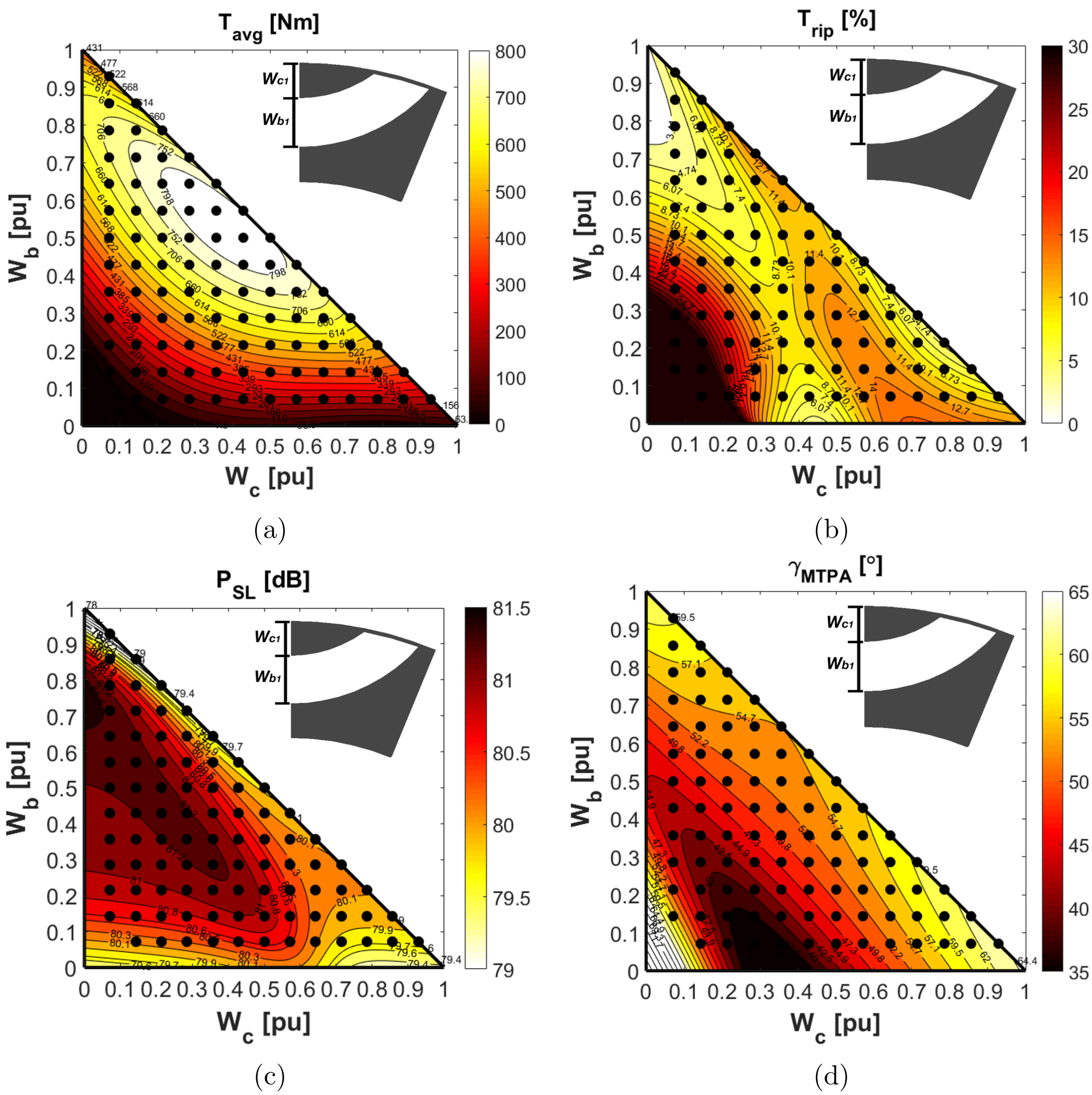

Fig. 3.7 1-barrier response surfaces: (a) T_{avg}, (b) T_{rip}, (c) P_{SL}, (d) γ_{MTPA}. Each dot corresponds to a sampled design evaluated using an FEA simulation.

Moreover, Fig. 3.8 compares all the sampled values of the T_{avg}, T_{rip} and P_{SL} objectives using boxplots. As the number of barriers increases, all three objective values improve due to lower harmonics in the air gap; i.e. T_{avg} increases, T_{rip} decreases, and P_{SL} decreases. Also, their ranges get smaller for higher n_b tending toward optimal designs. Since P_{SL}'s range is around 3 dB, this logarithmic value signifies a scaling factor of 2 for the range of P_S.

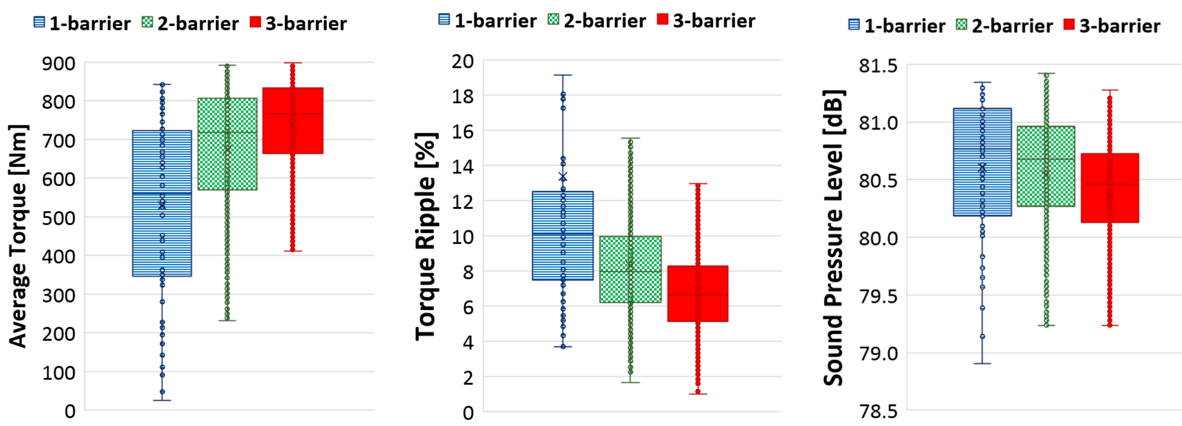

(a) (b) (c)

Fig. 3.8 Objective boxplots for datasets: (a) T_{avg}, (b) T_{rip}, (c) P_{SL}.

3.3.4 Multi-Objective Optimization

When formulating a multi-objective problem, it is important to ensure that the objectives are not redundant. Based on the methodology described in [Freitas et al., 2013], the conflict level between each objective pair was computed using the available FEA samples. A conflict value of 100% means that improving one objective implies that the other deteriorates, while 0% signifies total harmony. The average conflict for (T_{avg}, T_{rip}), (T_{avg},P_{SL}) and (T_{rip},P_{SL}) are computed to be 62.2%, 64.7% and 49.3% respectively.

Therefore, these conflict results indicate that all objectives are needed in the problem formulation. Also, the optimal design region using only the (T_{avg},T_{rip}) pair in [Mohammadi et al., 2016] will probably be affected. Upon fitting all the neural network surrogates, a *multi-objective genetic algorithm* (MOGA) was used to solve (3.9) for ten independent runs per barrier dataset [Kalyanmoy, 2001]. In brief, MOGA follows a natural selection process by searching the design space and keeping good solutions across different populations using different operators. For the three datasets, the number of generations was set to $400n_b$ (i.e. 400, 800, 1200), while the population size was set to $200n_b$ (i.e. 200, 400, 600). Each run took 5, 15 and 45 minutes respectively for the three datasets.

$$\begin{aligned} \min_{\boldsymbol{x}}. \quad & \big(-T_{avg}(\boldsymbol{x}), T_{rip}(\boldsymbol{x}), P_{SL}(\boldsymbol{x})\big) \\ \text{s.t.} \quad & \boldsymbol{x} \in \mathscr{F}_{\Delta} \end{aligned} \tag{3.9}$$

3.3.5 Results and Discussion

After the optimization, the Pareto front solutions with the top 90% of T_{avg} values denoted $\mathscr{F}_{\mathrm{HT}}$ using (3.4) were obtained per dataset. Fig. 3.9 (a)-(c) show their objective projections for the 1-barrier SynRM. For (T_{avg},T_{rip}) in Fig. 3.9 (a), the highest, yet undesirable values of P_{SL} lie along the sub-Pareto front as expected from the high objective conflicts. Similar behaviors are observed in Fig. 3.9 (b)-(c). Moreover, Fig. 3.9 (d)-(f) illustrate all the non-dominated solutions in the (W_c,W_b) design plane. As expected, improving one objective compromised others within the design space. For example, the solutions with smallest P_{SL} are located near the middle as shown in Fig. 3.9 (d) while those with the lowest T_{rip} values are situated along the extremes on Fig. 3.9 (e).

Also, the optimal ellipse region computed in Fig. 3.3 for (T_{avg},T_{rip}) does not completely match with the current points. Adding P_{SL} as an extra objective has spread the Pareto optimal solutions in Fig. 3.9 (d)–(f). Similar outcomes were observed for the 2- and 3-barrier datasets. Hence, the optimal design regions can be constrained by lower and upper bounds of W_c, W_b and W_c+W_b as shown in Table 3.7. Fig. 3.10 displays these constrained regions in the (W_c,W_b) plane, where the multiple-barrier ones are situated within the 1 barrier's. The percentage area occupied A_{OPT} for each region with respect to $\mathscr{F}_{\Delta}$ is computed for each dataset. The presented results indicate that the 1-barrier constraints can reduce the sampling time prior to a multiple-barrier rotor optimization even upon adding the P_{SL} objective. In contrast, the sampling quality of multiple-barrier rotors can be improved by focusing a computational budget within the 1-barrier optimal region as validated below.

Table 3.7 Optimal Per Unit Ranges of Design Variables

n_b	1	2	3
W_c	0.15	0.20	0.23
	0.60	0.47	0.57
W_b	0.39	0.50	0.57
	0.75	0.79	0.73
W_c+W_b	0.83	0.93	0.93
	1.00	1.00	1.00
A_{OPT}	11.7%	3.6%	2.2%

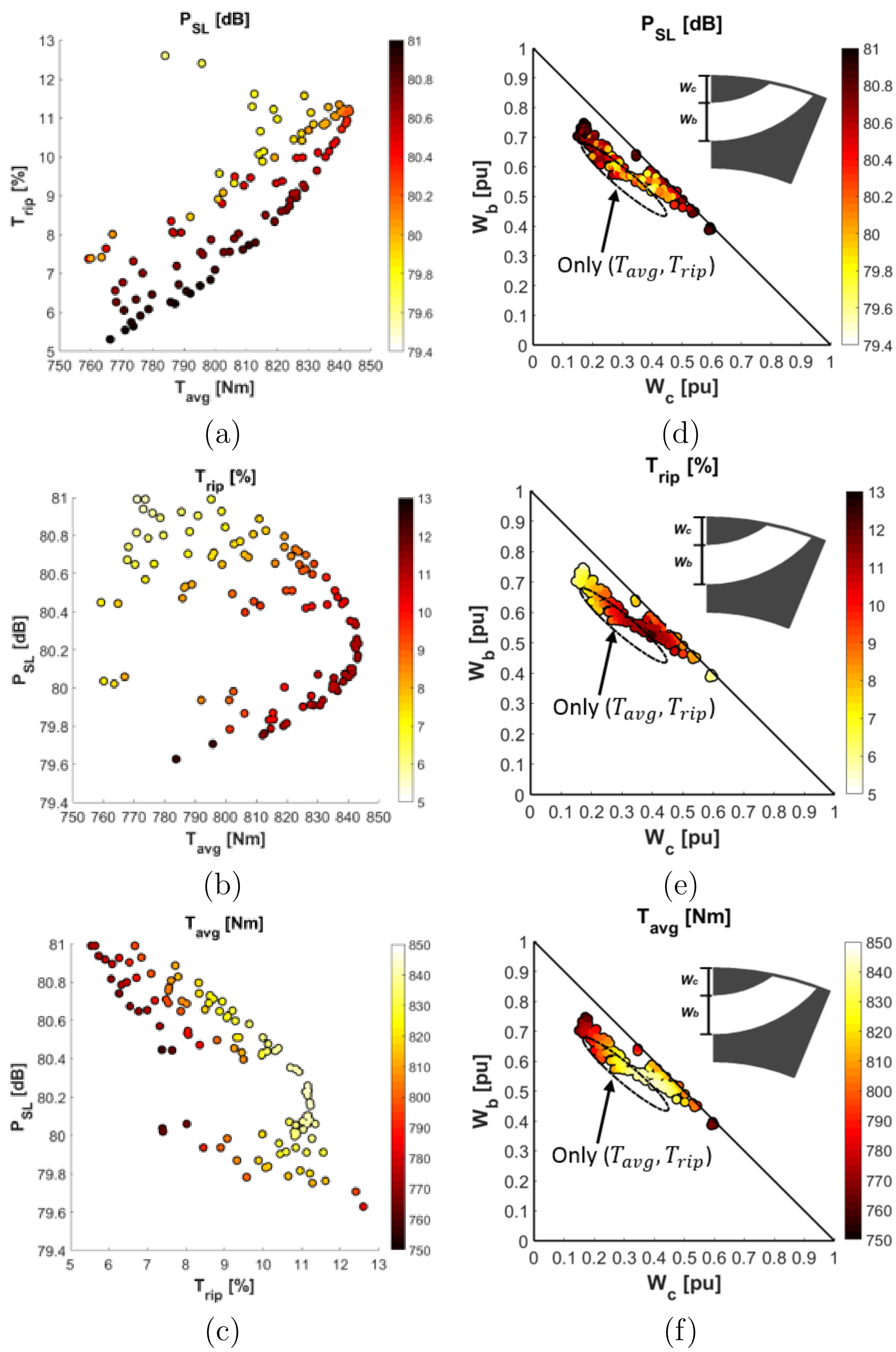

Fig. 3.9 Pareto front solutions of 1-barrier dataset: (left): projections for each objective pair. (Right): solution locations in the (W_c,W_b) design plane. Scatter colors display each objective value's variation. Note: optimal ellipse corresponds to optimizing only (T_{avg},T_{rip}) as shown on the right-hand plots.

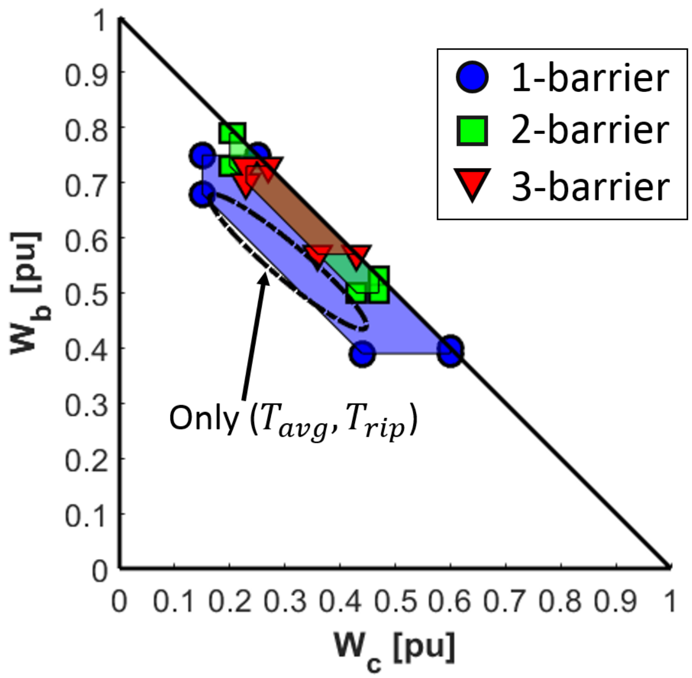

Fig. 3.10 Optimal design regions or constraints for different n_b.

Two methodologies are compared to design a 3-barrier SynRM rotor: *unconstrained* and *constrained*. The *unconstrained* approach sampled a 3-barrier design space using 1950 points. Meanwhile, the *constrained* method explored the 1-barrier space using 90 designs before sampling a *constrained* 3-barrier space using the 1-barrier's optimal region with 1860 points [Mohammadi et al., 2017a]. Then, both approaches followed the procedure shown above to compute their Pareto solutions. Their objective histograms are displayed in Fig. 3.11. Despite the fixed computational budget (1950=90+1860), the *constrained* approach produced more solutions with high T_{avg} while keeping low T_{rip} and P_{SL} values. Hence, the constraints shown in Fig. 3.10 can help improve the optimization quality while designing multiple-barrier SynRM rotors. Also, a selected 3-barrier rotor cross-section is displayed in Fig. 3.11 relative to its objective values. This rotor design can then be refined for manufacturability and typical operation.

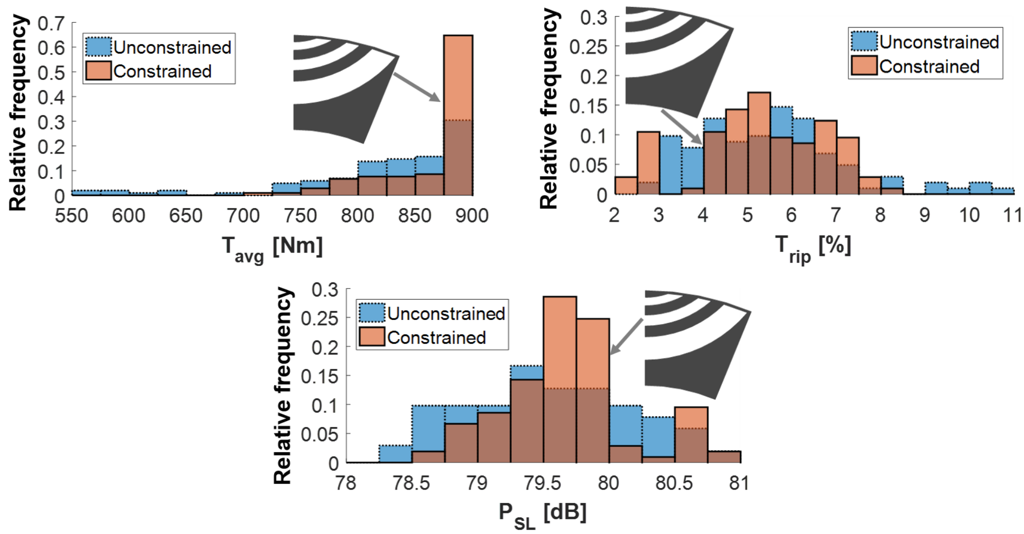

Fig. 3.11 Comparison of objective histograms. Selected 3-barrier rotor: $x^* = [4.4,3.8,2.9,9.0,4.2,3.1]$ mm, $(T^*_{avg},T^*_{rip},P^*_{SL}) = (886$ Nm, 4.2%, 79.9 dB$)$.

3.4 Summary

The proposed *barrier mapping* methodology helped restrict the design space of multiple-barrier rotors through different SynRM models. A single-barrier space was used to find a restricted region of the multiple-barrier space which provides geometrical constraints to a multi-objective optimization. Less computational effort is required to handle the curse of dimensionality when the number of geometric parameters increases. It was demonstrated here that the proposed methodology reduced the number of required FEA samples by more than 56% for the electromagnetic example. Moreover, multiple-barrier rotors were shown to improve the torque performance (i.e. average torque increases and torque ripple decreases) of SynRMs based on the presented statistical analysis. Also, it was observed that adding the sound pressure level did not yield the same non-dominated solutions for a 33-slot 8-pole SynRM rotor as shown in Fig. 3.10. This occurred due to the tradeoff relationships that exist between the electromagnetic and acoustic objectives. Optimal ranges of design variables were found for high average torque solutions. The results indicate that the numerical knowledge gained from a 1-barrier's design space can constrain the design region of a multiple-barrier rotor to reduce the problem's computational burden.

Chapter 4

Multiphysics Knowledge Extraction and Design Selection

The MPDP from Chapter 2 continues here to provide multiphysics guidelines and selection criteria for the design of synchronous reluctance machines. From a sampled design space of various rotor geometries, the self- and mutual-correlations of different physical performances defined in (2.17) are internally evaluated within Stage 4 as will be explained in Section 4.1. Statistical analysis is conducted to extract knowledge for relating the design and objective spaces to each other. The *barrier mapping* technique introduced in Chapter 3 is also used to cluster optimal solutions for different numbers of barriers.

Next in Stage 5 of Section 4.2, it is demonstrated that not all the objectives must be incorporated into the design process since some of them are non-conflicting. Due to the inter-dependency of the computed objectives, only some are used to search the design space and select optimal solutions for different user requirements and tradeoffs. With the help of a software package, a motor designer can evaluate which design variables should be changed and by how much in order to fulfill the design specifications. Lastly in Stage 6 of Section 4.3, multiple designs are internally selected based on the user requirements specified previously. Useful guidelines for selecting the appropriate motor speed and voltage ratings are also proposed while considering structurally-reliable designs. Among the final solutions, an optimal SynRM design is assisted with permanent magnets in Section 4.4 to achieve variable-speed performance beyond base speed. Its demagnetization distribution and efficiency map are computed to validate its performance improvement.

4.1 Stage 4: Multiphysics Knowledge Extraction (*internal*)

4.1.1 Knowledge Extraction

The 24-slot 3-barrier dataset is used to show the correlation plots for important electromagnetic, acoustic and structural performances in Figs. 4.1 and 4.2. To visualize the design tradeoffs through examples, a generalized selection function, g_S, defined in (4.1) is used to choose different designs based on a least sum-square-error. This single-objective function takes in a vector of M performances or objectives in per-unit, $\boldsymbol{f}(\cdot) = [f_1, f_2, ..., f_M]$, and the objective weights, $\boldsymbol{k}$, that specify the relative importance of each objective. For a uniformly distributed $\boldsymbol{k}$, the returned solution is the closest point in the objective space to the utopia point, i.e. best solution of each individual objective.

$$\begin{aligned} g_S\big(\boldsymbol{k}, \boldsymbol{f}(\boldsymbol{x})\big) &= \min_{\mathbf{x}\in\mathscr{F}_\Delta} \sum_{i=1}^{M} k_i \Big(f_i(\boldsymbol{x}) - \min\big(f_i(\boldsymbol{x})\big)\Big)^2 \\ \sum_{i=1}^{M} k_i &= 1 \end{aligned} \tag{4.1}$$

Based on this selection criteria, five multiphysics optimization problems (4.2) were solved to arrive at five different designs. These selected geometries, i.e. D_1, D_2, D_3, D_4 and D_5, are highlighted to provide design guidelines with respect to each other. Designs D_1-D_3 only considered electromagnetic performances, D_4 included both electromagnetic and acoustic, and D_5 was selected based on electromagnetic, acoustic and structural. A similar correlation plot of design metrics defined in Section 2.2.1 is displayed in Fig. 4.3. The flux density distributions of the selected designs are shown below the correlation plots for convenience. A summary of the performances, design metrics and variables are listed in Table 4.1.

$$\begin{aligned} \mathrm{D}_1 : \mathrm{E} \quad &\rightarrow g_S\big([-T_{avg}, T_{rip}]\big) \\ \mathrm{D}_2 : \mathrm{E} \quad &\rightarrow g_S\big([T_{rip}, -pf]\big) \\ \mathrm{D}_3 : \mathrm{E} \quad &\rightarrow g_S\big([-\xi, L_d]\big) \\ \mathrm{D}_4 : \mathrm{E} + \mathrm{A} \quad &\rightarrow g_S\big([-N_m^{Base}, P_{SL}]\big) \\ \mathrm{D}_5 : \mathrm{E} + \mathrm{A} + \mathrm{St} \quad &\rightarrow g_S\big([-T_{avg}, T_{rip}, -pf, P_{Fe}, V_{rms}, -\xi, L_d, -N_m^{Base}, P_{SL}, -k_S, k_C]\big) \end{aligned} \tag{4.2}$$

Table 4.1 Selected Design Performances and Variables (24-slot 3-barrier)

Symbol	**Unit**	**D1 (●)**	**D2 (✖)**	**D3 (★)**	**D4 (○)**	**D5 (✚)**
T_{avg}	Nm	**0.90**	0.77	**0.92**	0.56	0.79
T_{rip}	%	**8.88**	29.58	43.18	61.81	20.83
pf		0.48	**0.59**	**0.55**	0.47	0.41
P_{Fe}	W	3.96	**2.24**	3.17	**2.69**	4.22
V_{rms}	V	27.67	**19.24**	24.27	**18.76**	28.78
ξ		2.68	**3.29**	**3.73**	2.52	2.19
L_d	mH	1.82	**1.21**	**1.14**	**1.27**	2.26
P_{SL}	dB	57.80	56.28	57.04	**55.56**	56.64
N_m^{Base}	RPM	1925	**2415**	**2270**	**2922**	1841
k_S		6.97	7.97	4.69	6.21	6.18
k_C		1.90	2.05	**1.18**	1.97	1.72
k_F		0.99	0.99	0.97	0.98	0.99
W_c	pu	0.58	0.35	0.26	0.45	0.69
W_b	pu	0.29	0.64	0.67	0.55	0.15
$W_c + W_b$	pu	0.88	0.98	0.93	0.99	0.84
a	pu	0.34	0.64	0.72	0.55	0.18
W_{c_3}	mm	3.06	1.10	3.09	0.78	2.92
W_{b_3}	mm	1.49	3.98	0.96	1.91	0.87
W_{c_2}	mm	2.57	2.11	0.88	2.59	1.99
W_{b_2}	mm	2.58	2.44	1.31	2.16	3.92
W_{c_1}	mm	1.26	1.04	4.29	3.04	0.84
W_{b_1}	mm	1.67	3.07	2.29	1.31	0.95
W_f	mm	15.11	12.53	16.06	12.54	14.24
R_{ri}	mm	7.61	6.52	7.43	8.46	8.75

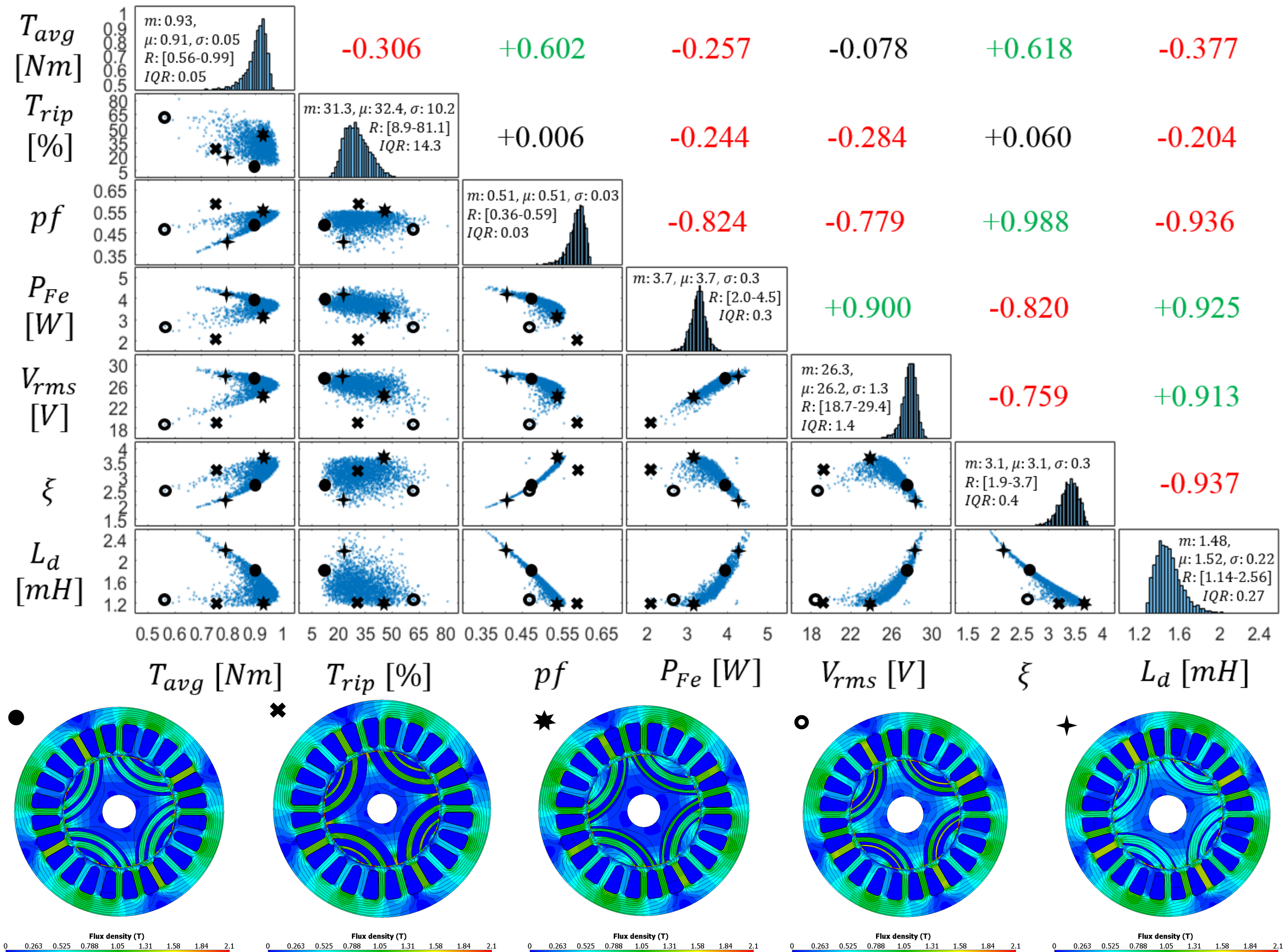

Fig. 4.1 (Top) Correlation plot of 24-slot, 3-barrier electromagnetic performances. (Bottom) Flux density distributions of selected designs: ● for $[-T_{avg},T_{rip}]$, ✖ for $[T_{rip},-pf]$, ★ for $[-\xi,L_d]$, **o** for $[P_{SL},-N_m^{Base}]$, ✚ for all objectives.

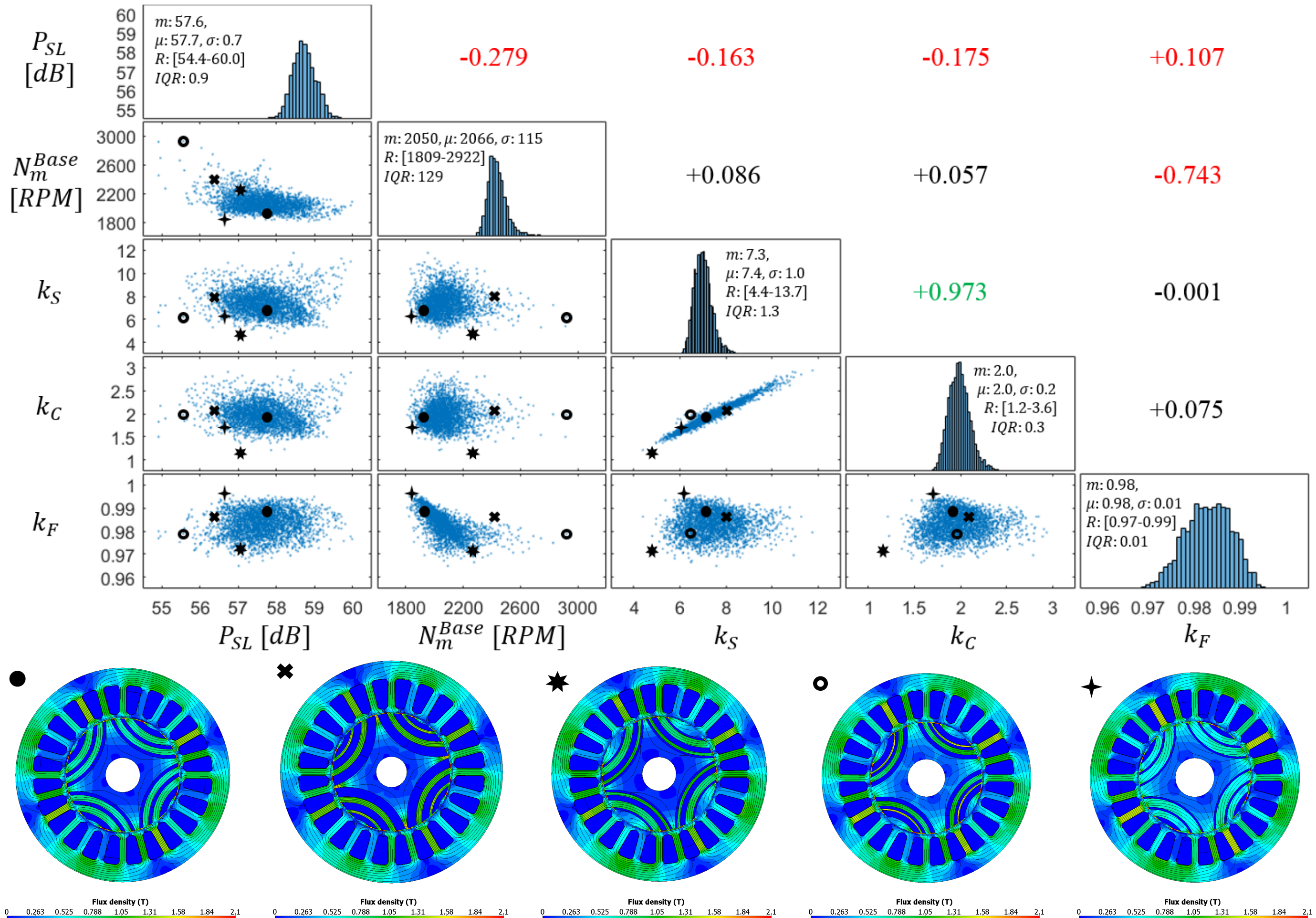

Fig. 4.2 (Top) Correlation plot of 24-slot, 3-barrier acoustic and structural performances. (Bottom) Flux density distributions of selected designs: ● for $[-T_{avg}, T_{rip}]$, ✖ for $[T_{rip}, -pf]$, ★ for $[-\xi, L_d]$, **O** for $[P_{SL}, -N_m^{Base}]$, ✚ for all objectives.

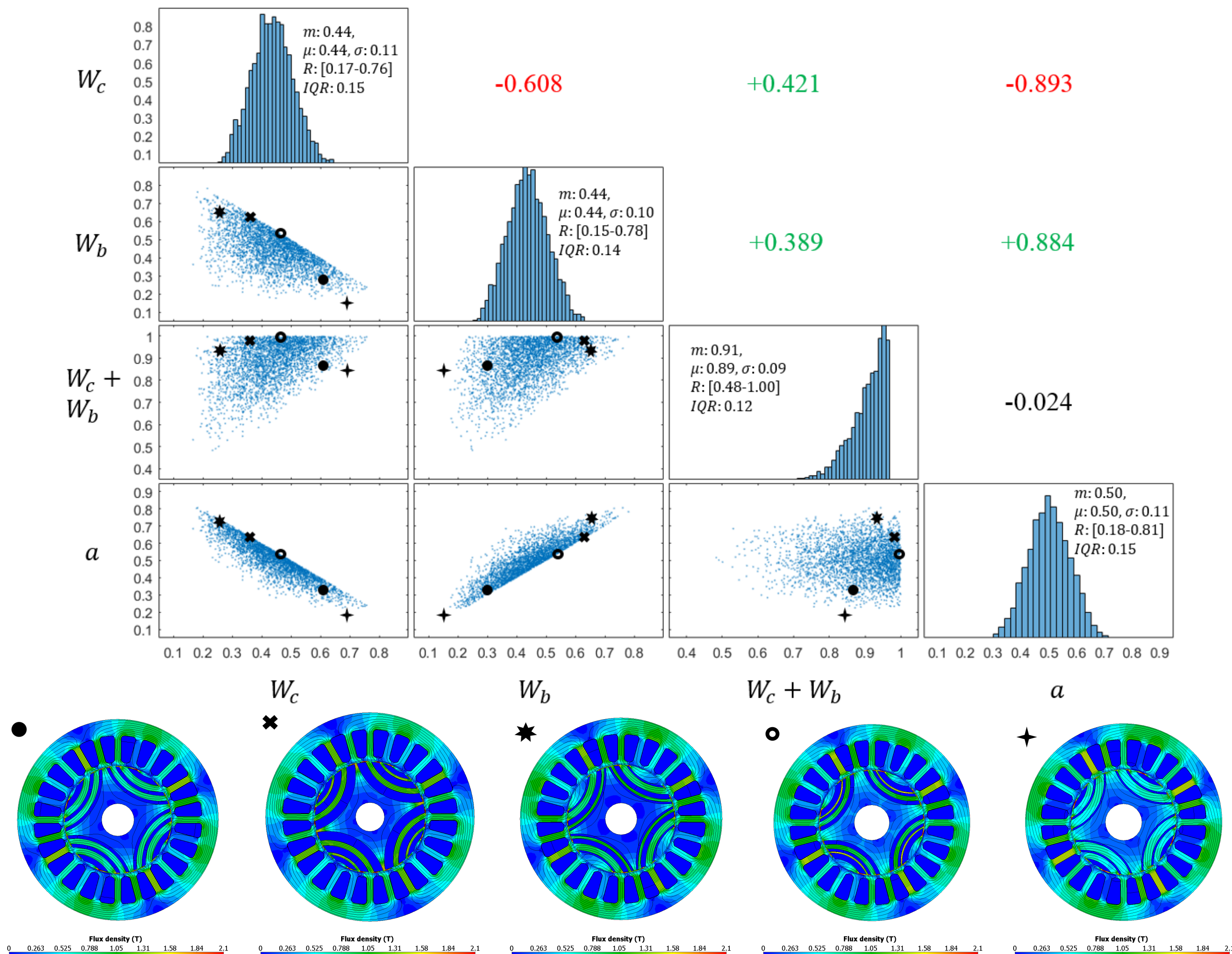

Fig. 4.3 (Top) Correlation plot of 24-slot, 3-barrier design metrics in per-unit. (Bottom) Flux density distributions of selected designs: ● for $[-T_{avg}, T_{rip}]$, ✖ for $[T_{rip}, -pf]$, ★ for $[-\xi, L_d]$, ○ for $[P_{SL}, -N_m^{Base}]$, ✚ for all objectives.

According to Figs. 4.1, 4.2 and 4.3 and Table 4.1, design knowledge and guidelines can be extracted as discussed below:

- Higher power factor levels, pf, can be achieved regardless of the torque ripple, T_{rip}. This is supported by their near-zero correlation coefficient.

- The average torque, T_{avg}, possesses a long left-tailed distribution which means that its outliers consist of sub-optimal designs in terms of itself. However, the iron power loss distribution, P_{Fe}, is closer to a Gaussian one indicating that these outliers may not necessarily correspond to sub-optimal designs.

- Unlike other performances, the torque ripple, T_{rip}, does not reveal any recognizable trend in variation as shown in the second column of Fig. 4.1. This is also observed in the correlation coefficients of itself with respect to other performances where the second row values of Fig. 4.1 are smaller than the rest.

- The largest correlation occurs between the saliency ratio, ξ, and power factor, pf, as supported in [Matsuo and Lipo, 1994]. Maximizing the average torque, T_{avg}, leads to an average level of iron power loss, P_{Fe}.

- Optimizing the saliency ratio, ξ, is in accordance with optimizing the power factor, pf, as well as the d-axis inductance, L_d. They could be considered as non-conflicting performances to quantitively reduce the number of optimization objectives.

- Design 1 with higher T_{avg} and lower T_{rip} requires a larger supply voltage to fulfill the rated current density. This reduces the base speed, N_m^{Base}.

- Either a small or large value of L_d can cause a decrease in the average torque, T_{avg}.

- As per Table 4.1, selecting based on $[T_{rip}, -pf]$ or $[P_{SL}, -N_m^{Base}]$, i.e. Designs 2 and 4, requires a smaller W_f while this does not hold true for other designs.

- Thicker flux barriers, i.e. Designs 2-4, as in Fig. 4.1 and Table 4.1 are needed to achieve an improved power factor and losses, i.e. $[-pf, P_{Fe}]$. This means that the rotor flux is more concentrated in the thinner flux carriers. However, the flux carrier width, W_{c_k}, should be generally higher for $[-T_{avg}, T_{rip}]$, i.e. Design 1.

- Interestingly, Design 5 with an optimal weighted value of all the objectives reveals the largest k_F. This means the contribution of the magnetic flux density, $\boldsymbol{B_n}$, to the total radial force on the tangential ribs is small (or the centrifugal force dominates). Therefore, a weakly coupled magnetic and structural analysis returns a satisfactory optimal design. Large k_F values are also observed for designs with low N_m^{Base}.

- Except for Design 3 with improved [T_{rip},$-pf$], the analytical stress analysis in (2.10) overestimates the FEA results by about 2 times for all selected designs. Hence, the corresponding stress should be corrected using k_C which is in the range [1.2, 3.6].

- Design 4 with the improved [P_{SL},$-N_m^{Base}$] is the quietest motor with the lowest sound pressure level, P_{SL}. All other selected designs are at least 1 dB louder which is more than 1 standard deviation away. On the other hand, its base mechanical speed, N_m^{Base}, is the highest among all selected designs and samples.

- The high correlation between k_C and k_S represents the ratio of the analytical maximum speed (through static stress analysis) and the base speed.

- The safety factor, k_S, of all selected designs is larger than 4.6 which indicates that the widths of tangential ribs, W_{t_k}, can be safely reduced to improve the electromagnetic performance. Otherwise, its value permits high-speed operation through PM-assist.

- Although the base speed, N_m^{Base}, is not included in Design 3 with optimal [-ξ,L_d], it has one of the largest N_m^{Base} among all five designs. This occurs due to a reduced L_d value which impacts (2.7) and (2.8). If a high base speed is required, L_d must be minimized.

- The range of the total barrier ratio, a, for the selected designs supports those suggested in [Matsuo and Lipo, 1994]. Also, the sum of W_c and W_b are higher than 0.8 which can serve as a useful design constraint for optimal solutions.

- The location of Design 1 with optimal [$-T_{avg}$,T_{rip}] in the (W_c,W_b) design plane, i.e. row 2 and column 1 of Fig. 4.3, is almost in the middle and is surrounded by other designs. This suggests that T_{avg} could behave in a unimodal manner with respect to (W_c,W_b) as shown in Fig. 3.7. Once other objectives are considered, the design changes due to tradeoffs.

In summary, the five selected solutions are located in distinct regions of the scatter plots shown in Figs. 4.1, 4.2 and 4.3, revealing that completely different design variables are required to satisfy various goals. For example, if the user's target is to only improve the electromagnetic performance of an electric machine, the selected design would be different from the case when another physical objective, such as sound pressure level, is added. Also, a requirement for extracting the design guidelines listed above was to statistically analyze a given dataset (procedure described in Section 2.2). With the help of a data-driven approach such as the MPDP, this dataset (containing thousands of sample points) can be simulated and analyzed with flexibility even when the motor topology changes (e.g. SynRM, PM-SynRM, IPM). From the perspective of the MPDP, it does not matter what the individual performances mean as long as the designer's prioritized targets in a specific application are addressed. Providing such knowledge can help the user make a more informed choice for a motor design. If different physical disciplines are incorporated into this procedure, other optimal solutions can be extracted, possibly different from those in Fig. 4.1.

4.1.2 Barrier Mapping

Until now, only one of the barrier datasets, i.e. 24-slot 3-barrier, was analyzed to extract design knowledge and guidelines. It may also be required to show the effect of varying the number of barriers, n_b, on the multiphysics performances based on the acquired samples. One way to demonstrate this relationship is through a histogram for each objective as shown in Fig. 4.5. For each histogram plot, the corresponding distribution of the performance is visualized for the 1, 2, 3 and 4 barrier datasets. The results are also compared between the 24 and 30-slot cases as shown in Fig. 4.5 (a)-(b). While there are 10 performances displayed in total, the user can be prompted to view only the histograms of interest. For example, only the electromagnetic and structural distributions could be displayed instead of all. Note that the thermal performances were not included here since they were not obtained for the 30-slot case as mentioned above and cannot be compared for the two stator cases.

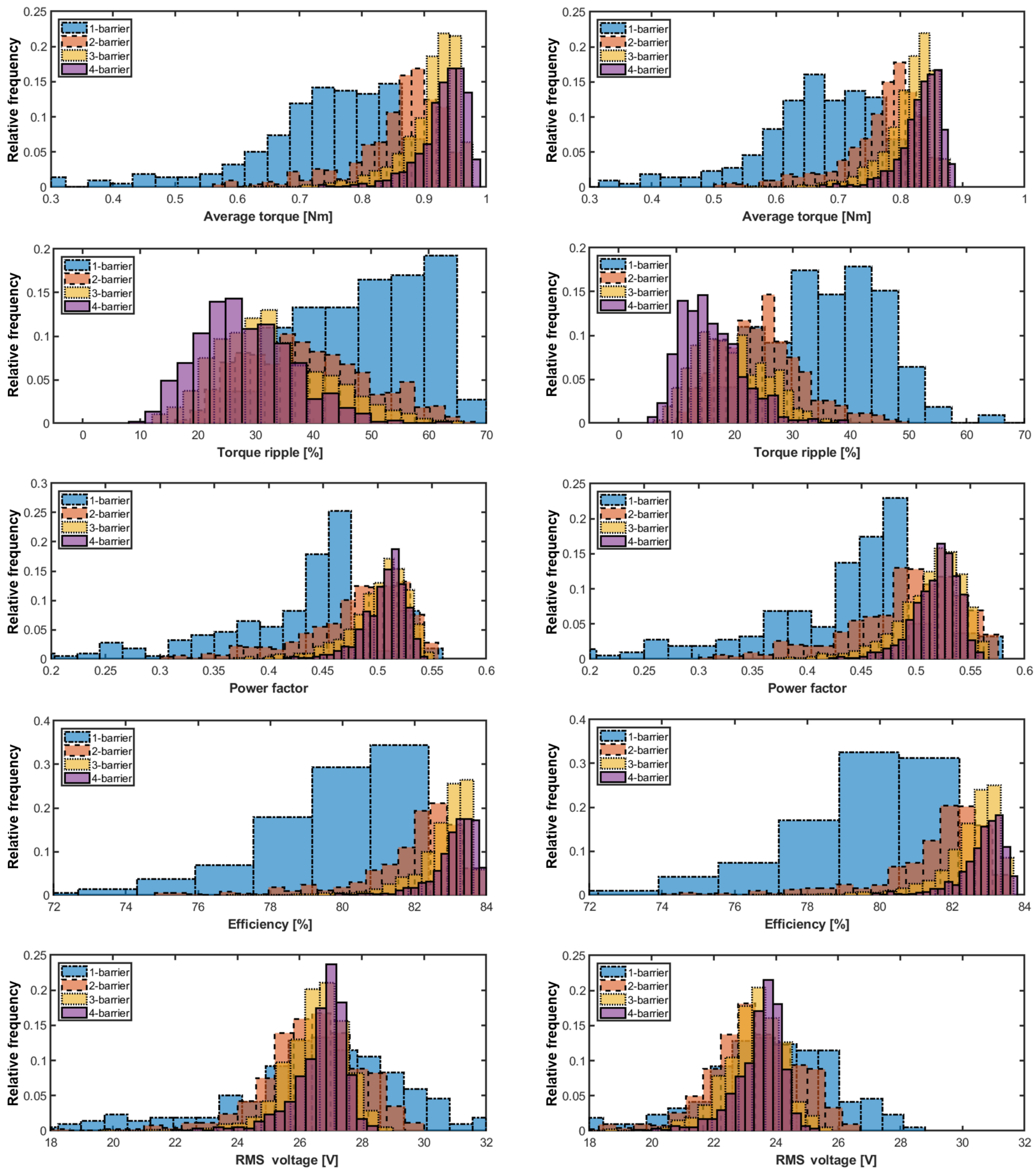

(a) (b)

Continued on next page.

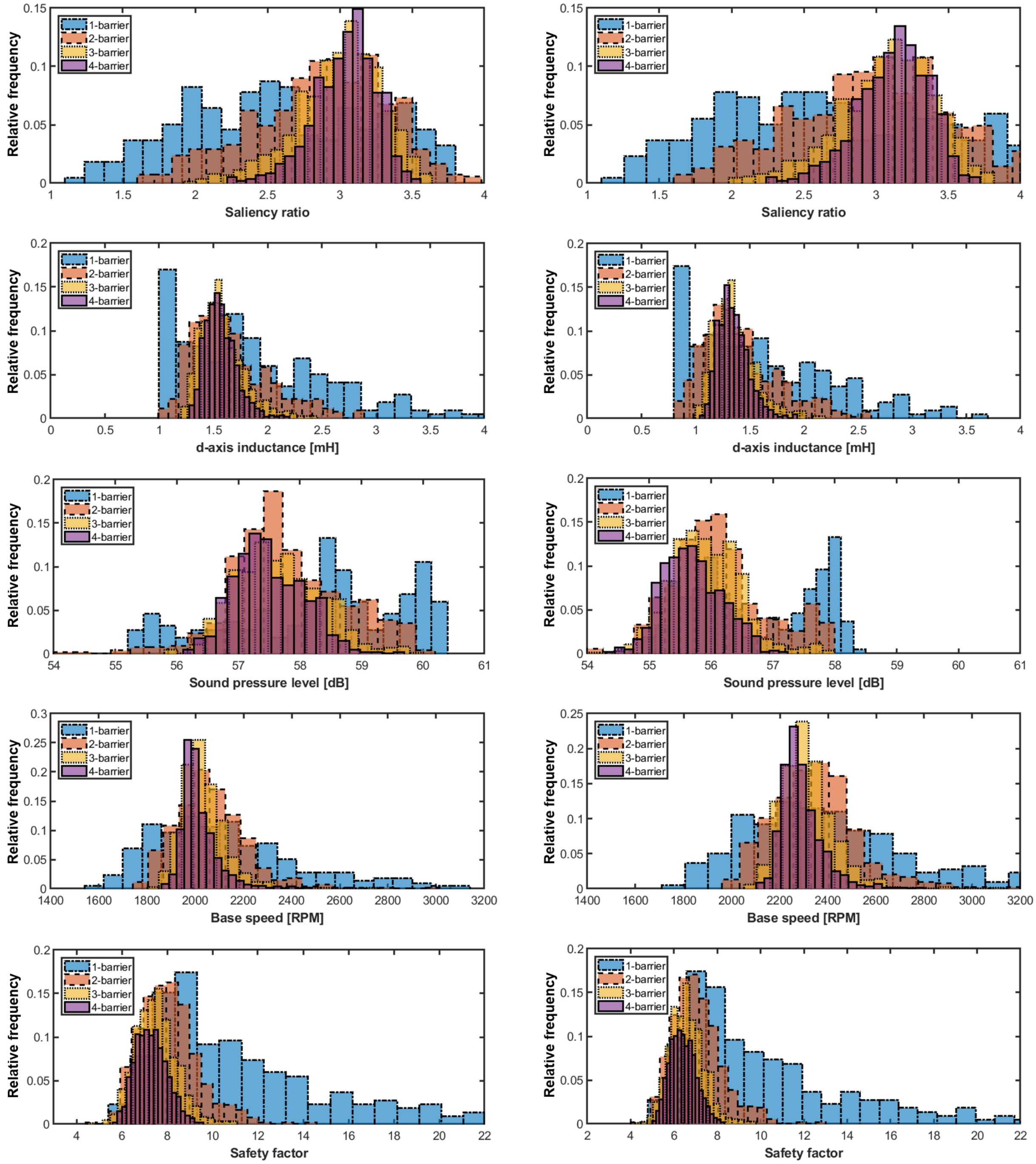

(a) (b)

Fig. 4.5 Performance histograms for different n_b: (a) 24-slot, (b) 30-slot.

Hence, the following points are observed for every objective shown in Fig. 4.5:

- Average torque: as n_b increases from 1 to 4, the T_{avg} distributions converge to high values for both 24 and 30-slot cases, while their variances decrease. The 1-barrier dataset is more spread out indicating that there are many sub-optimal solutions.

- Torque ripple: as n_b increases from 1 to 4, the T_{rip} distributions decrease to lower values for both models. However, their variances do not decrease as much when compared to the T_{avg} distributions. The 1-barrier dataset still includes many sub-optimal solutions which are practically undesirable. The 30-slot values are generally lower due to the stator's fractional slot-pole combination (i.e. $30/4 = 7.5$, while $24/4 = 6.0$). Nevertheless, lower T_{rip} of around 10% can be achieved for more barriers.

- Power factor, efficiency and saliency ratio: behave similar to the T_{avg} distributions.

- RMS voltage: the distributions converge to a median value for both cases as the number of barriers increases. Also, the average V_{rms} values are lower for the 30-slot case due to lower average L_d values.

- d-axis inductance: behaves similar to the T_{avg} distributions (minimization direction).

- Sound pressure level: the 1-barrier dataset does not seem to follow a known distribution for the number of samples used with peaks situated in different locations. This could be due to the higher airgap harmonics affecting $\boldsymbol{B_n}$ and P_{SL}. However, the V_{rms} distributions tend toward lower values for higher n_b with a relatively wide variance indicating that the rotor structure influences the airgap harmonics.

- Base speed: behaves similar to the V_{rms} distributions (maximization direction).

- Safety factor: as n_b increases from 1 to 4, the positively-skewed k_S distributions converge to lower values for both cases, while their variances decrease as well. The 1-barrier dataset includes many optimal solutions with values beyond 12 because the maximum von Mises stress at the tangential rib is lower for the single barrier's larger area. Higher n_b designs subject their tangential ribs to more stress.

Appendix D includes detailed histogram plots of the minimum, average and maximum component temperatures at steady-state for all four barrier datasets of the 24-slot SynRM.

While the component temperatures are within safe limits, comparing Figs. D.1 to D.4 indicates that increasing n_b also increases the component temperature by about 1°C on average. In addition, the ranges of all component temperatures (i.e. minimum to maximum) are almost similar to one another with the exception of the housing. Since the motor is naturally cooled, the surrounding environment permits the external housing structure to dissipate its heat, thereby enabling a variable thermal gradient on its outer surface. This can also be seen in the temperature distribution in Fig. 2.7 (b) where the maximum housing temperatures are concentrated in the middle due to the underlying heated components.

Next, it is desired to find how the different barrier datasets of SynRMs relate to each other for every multiphysics performance in a common design space. Using the procedure described in Chapter 3, the *barrier mapping* technique is performed to visualize the optimal solutions for each objective in the 1-barrier design plane. When different datasets are collected, the linear or nonlinear constraints defining optimal design regions are found so that the MPDP can decrease the simulation time for future designs. Figs. 4.6 and 4.7 show the *barrier mapping* for the 24-slot dataset of the top 5% and 10% percentile solutions for each objective in (W_c,W_b) using (2.2). Appendix D includes similar plots for the 30-slot case.

Previously, Sections 3.2 and 3.3 demonstrated that the computational effort to sample higher n_b rotor designs reduces by using the 1-barrier's optimal region. It is observed from Figs. 4.6 and 4.7 that design clustering occurs for T_{avg}, pf, η, ξ, L_d, N_m^{Base}, T_W and T_R. Varying the top percentile cutoff does not affect the clustered objectives, but instead changes the coverage area of the optimal solutions in the 1-barrier design plane. This means that these objectives are good candidates to constrain higher n_b design spaces for increasing the sampling quality in Stage 2. The choice is left to the user to select an appropriate objective for the *barrier mapping* technique. For example, T_{avg} can be chosen if it is listed as a high priority objective in Stage 1.

Also, the higher n_b solutions, e.g. 4-barrier, tend to be subsets of the lower n_b designs, e.g. 1-barrier, in the (W_c,W_b) plane, thereby ensuring a minimal loss of information by setting the design constraints. Other objectives such as T_{rip} or k_S do not reveal any substantial relationship between the barrier datasets. It is interesting to note that as n_b increases, the location of optimal solutions tends to converge close to the limit line, i.e. $W_c + W_b = 1$, and cluster near $W_c \approx W_b$. This means that the total barrier ratio, a, is almost close to 0.5 for optimal designs as mentioned in [Matsuo and Lipo, 1994; Bianchi, 2013].

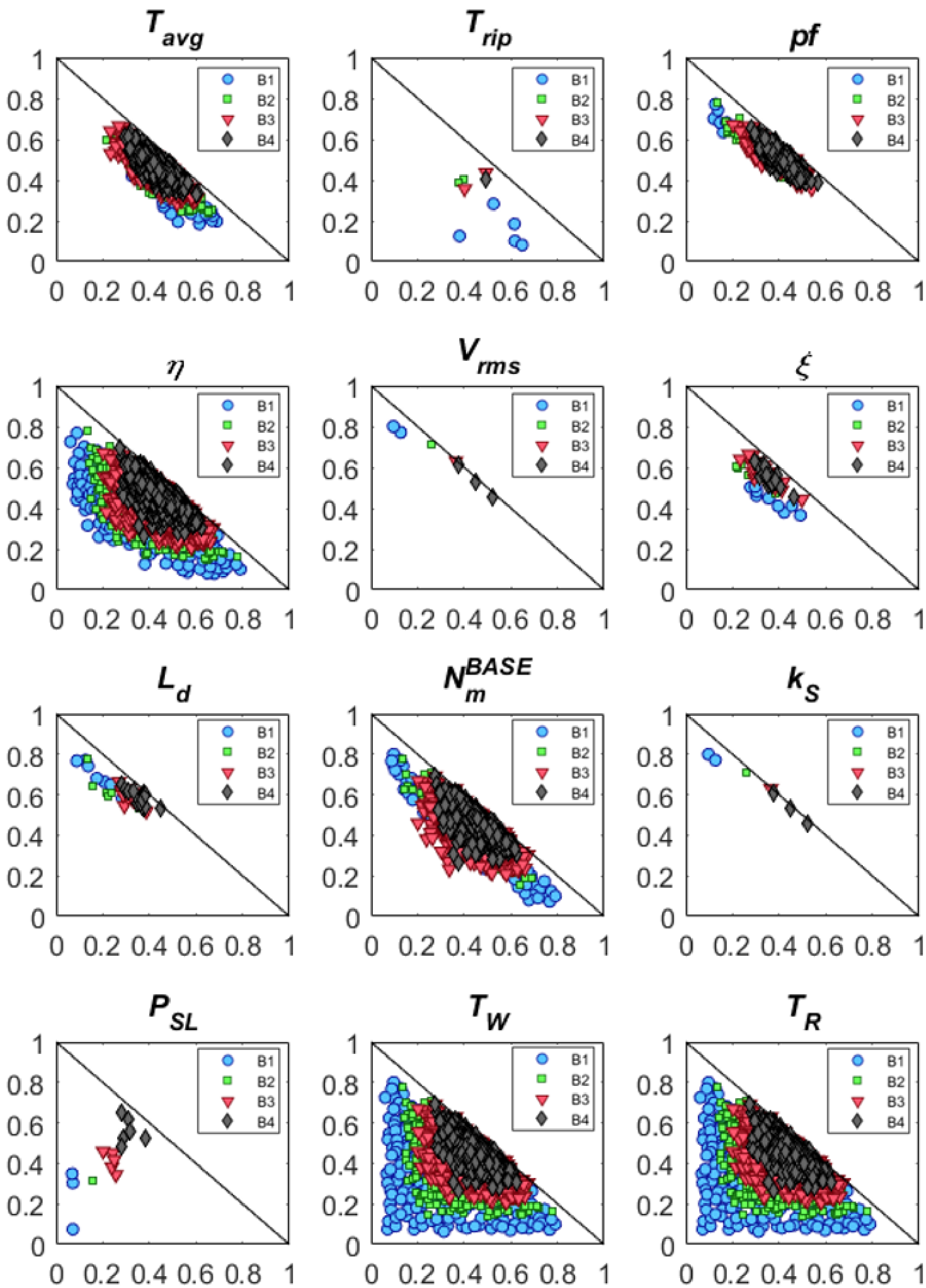

Fig. 4.6 *Barrier mapping* for 24-slot multiphysics performances in (W_c,W_b) plane for top 5% percentile solutions. T_{avg} average torque, T_{rip} torque ripple, pf power factor, η efficiency, V_{rms} RMS voltage, ξ saliency ratio, L_d d-axis inductance, N_m^{Base} base speed, k_S safety factor, P_{SL} sound pressure level, T_W average winding temperature, T_R average rotor temperature.

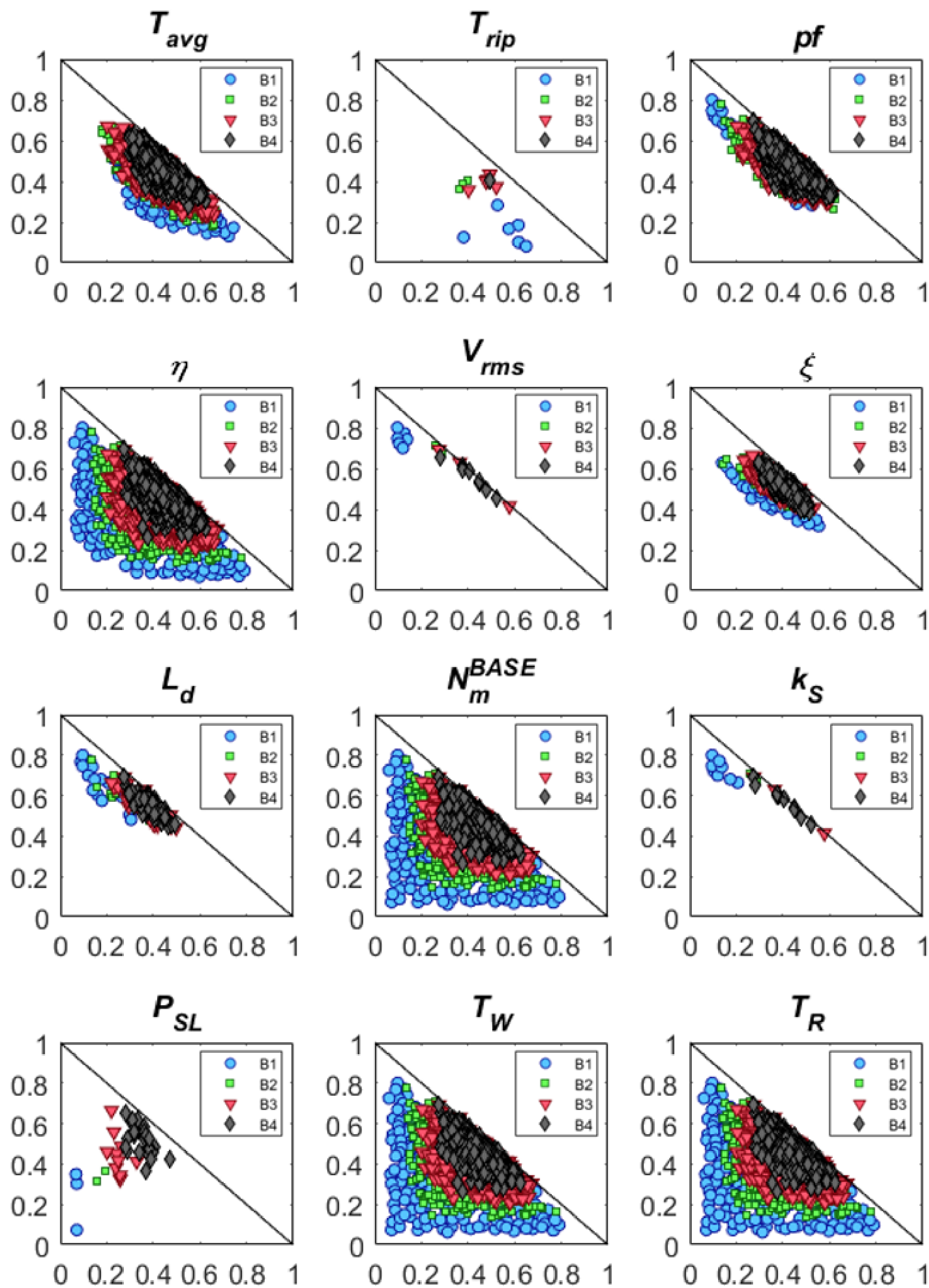

Fig. 4.7 *Barrier mapping* for 24-slot multiphysics performances in (W_c,W_b) plane for top 10% percentile solutions. T_{avg} average torque, T_{rip} torque ripple, pf power factor, η efficiency, V_{rms} RMS voltage, ξ saliency ratio, L_d d-axis inductance, N_m^{Base} base speed, k_S safety factor, P_{SL} sound pressure level, T_W average winding temperature, T_R average rotor temperature.

4.1.3 Global Knowledge Analysis

Before proceeding to the next stage, advanced users can ask the MPDP to perform a global knowledge analysis of the simulated dataset as explained below.

Referring to the histograms of the multiphysics performances in Fig. 4.5, not all of them are symmetric or appear to be normally distributed. For example, the average torque's distribution is asymmetric about its peak and has a left skew. This means that more than half of its samples are concentrated on the left tail. Since the other performances can be similarly analyzed, the mean, μ, the median, $\widetilde{\mu}$, and the standard deviation, σ, are computed for the 24-slot case across all barrier datasets and tabulated in Table 4.2. Similar trends are observed in Table 4.3 for the 30-slot case. Both tables indicate that σ decreases when the number of barriers, n_b, increases for all performances. For larger n_b values, the performances converge to a point with less degree of variation due to the geometric constraint in (2.4) and the increased sample size. With the exception of k_S, the mean values of all performances either improve (e.g. η) or stay relatively the same (e.g. N_m^{Base}) as n_b increases. When more barriers are packed into the rotor, the smaller areas of the tangential ribs increases the critical stress values, thereby reducing k_S and the maximum mechanical speed.

In addition to the normal statistics, the degree of asymmetry for a distribution (i.e. how much it leans to one side of its mean) can be calculated to check whether the distribution favors optimal solutions or not. For example, most average torque values are concentrated toward the high end (i.e. left skew) which directly benefits maximizing this performance. The skewness, defined as S, provides such as a measure and is calculated using (4.3). It relies on the third standarized moment for a given performance labeled as X, where $\mathbf{E}[\cdot]$ is the expected value. Typically, the skewness values of S range from around -4 to +4, similar to the domain of the standard normal curve. When the skewness is negative, the distribution is known to have a left tail (e.g. average torque T_{avg}). On the other hand, a positive value signifies a right tailed distribution (e.g. safety factor k_S). The strength of skewness S can be interpreted from its values; the distribution is highly skewed to one side if $|S| > 1.5$ (e.g. efficiency η), moderately skewed for $0.5 < |S| < 1.5$ (e.g. RMS voltage V_{rms}), and approximately symmetric about its mean when $|S| < 0.5$ (e.g. saliency ratio ξ).

$$S = \mathbf{E}\Big[\Big(\frac{X-\mu}{\sigma}\Big)^3\Big] \tag{4.3}$$

Table 4.2 Performance Statistics for the 24-slot Datasets: $\mu \pm \sigma$ $(\widetilde{\mu})$

Performance		**1-barrier**	**2-barrier**	**3-barrier**	**4-barrier**
T_{avg}	Nm	0.73±0.12 (0.75)	0.86±0.07 (0.88)	0.91±0.05 (0.92)	0.93±0.04 (0.94)
T_{rip}	%	50.7±14.4 (50.6)	38.9±10.5 (37.7)	32.8±9.7 (31.7)	28.2±8.2 (27.2)
pf		0.42±0.08 (0.45)	0.48±0.05 (0.49)	0.50±0.03 (0.51)	0.51±0.02 (0.51)
η	%	78.9±4.1 (79.9)	81.9±1.5 (82.3)	82.8±0.8 (83.0)	83.1±0.6 (83.3)
V_{rms}	V	26.5±2.8 (26.8)	26.4±1.6 (26.4)	26.5±1.0 (26.6)	26.7±0.8 (26.9)
ξ		2.58±0.65 (2.57)	2.87±0.46 (2.91)	2.99±0.29 (3.03)	3.04±0.21 (3.07)
L_d	mH	1.87±0.68 (1.75)	1.66±0.37 (1.57)	1.58±0.21 (1.55)	1.57±0.14 (1.55)
N_m^{Base}	RPM	2124±302 (2084)	2064±152 (2052)	2034±92 (2021)	2015±75 (1997)
P_{SL}	dB	58.3±1.4 (58.5)	57.8±0.9 (57.6)	57.7±0.7 (57.6)	57.5±0.6 (57.4)
k_S		11.3±4.1 (10.1)	8.1±1.3 (8.0)	7.5±0.9 (7.46)	7.3±0.7 (7.2)
T_W	°C	75.7±0.6 (75.9)	76.0±0.4 (76.2)	76.2±0.3 (76.4)	76.3±0.3 (76.5)
k_S	°C	75.1±0.6 (75.3)	75.4±0.4 (75.6)	75.6±0.3 (75.7)	75.7±0.3 (75.9)

Table 4.3 Performance Statistics for the 30-slot Datasets: $\mu \pm \sigma$ $(\widetilde{\mu})$

Performance		**1-barrier**	**2-barrier**	**3-barrier**	**4-barrier**
T_{avg}	Nm	0.65±0.11 (0.67)	0.77±0.06 (0.78)	0.81±0.04 (0.82)	0.83±0.03 (0.84)
T_{rip}	%	37.2±11.6 (37.0)	24.8±7.1 (24.4)	19.4±6.1 (18.7)	15.9±5.3 (15.2)
pf		0.43±0.08 (0.45)	0.49±0.05 (0.50)	0.51±0.03 (0.52)	0.52±0.02 (0.52)
η	%	78.8±4.2 (79.5)	81.6±1.5 (82.0)	82.5±0.9 (82.8)	82.9±0.6 (83.0)
V_{rms}	V	23.5±2.5 (23.7)	23.3±1.5 (23.3)	23.3±1.0 (23.4)	23.5±0.8 (23.6)
ξ		2.71±0.78 (2.64)	2.98±0.56 (3.01)	3.07±0.33 (3.11)	3.12±0.24 (3.15)
L_d	mH	1.61±0.64 (1.50)	1.42±0.36 (1.35)	1.36±0.20 (1.33)	1.35±0.14 (1.33)
N_m^{Base}	RPM	2414±364 (2359)	2346±181 (2338)	2314±111 (2299)	2290±86 (2272)
P_{SL}	dB	56.7±1.0 (56.5)	56.1±0.8 (56.1)	55.9±0.6 (55.9)	55.7±0.5 (55.7)
k_S		10.0±3.7 (8.9)	7.1±1.2 (7.0)	6.6±0.8 (6.6)	6.4±0.6 (6.4)

The skewness values calculated using (4.3) across all datasets are presented in Tables 4.4 and 4.5 for the 24- and 30-slot cases respectively. Generally, the skewness sign or direction is maintained for a given performance when the number of barriers is varied. For example, the average torque T_{avg} distributions are left skewed for the 1, 2, 3 and 4-barrier datasets in both cases. However, only the 1-barrier dataset for ξ and P_{SL} seem to be outliers as they have opposite signs as shown in bold. This may be attributed to the low number of points used for the 1-barrier dataset (i.e. 314 samples).

In addition, the relative strength of S, labeled accordingly as "+" and "-" for positive and negative skewness, is also shown for each performance. It is observed that the following performances are all left-skewed: T_{avg}, pf, η, V_{rms}, ξ, T_W and T_R. This inherent skew benefits their maximization as previously described in (2.17), except for V_{rms}, T_W and T_R which must be minimized. On the other hand, the distributions of T_{rip}, L_d, N_m^{Base}, P_{SL} and k_S are all right-skewed where most of their values tend to lower ends. Apart from N_m^{Base} and k_S, all these right-skewed performances benefit from their respective asymmetry which then favors their minimization. Moreover, the positive/negative skewness benefit, which considers the sign of S and the minimization or maximization direction for a given performance, is displayed as Y/N respectively. Each physics, whether electromagnetic, structural, acoustic or thermal, has at least one performance with a negative skew benefit. This result indicates that these performances or objectives should be prioritized during an optimization or selection process since their distributions work against the desired outcome.

While this information can be shared with an advanced user, the MPDP can use this global knowledge to notify a non-experienced user on the importance of including or prioritizing certain multiphysics performances in a given application. For example, although the left-skewed distribution of efficiency, η, statiscally benefits finding an optimal solution, this result does not hold for the distributions of N_m^{Base} and k_S. Both these performances tend to produce lower values which works against their desired maximization. The strength of S is also useful to emphasize the effect of a distribution's skew on selecting optimal designs. Afer performing the global analysis, the user can decide on filtering undesirable solution subsets (e.g. outliers). It is also possible to present the relationship between objectives and design variables. For example, the user could request to decrease the widths of the tangential ribs in order to improve the electromagnetic performance instead of further increasing N_m^{Max} from k_S as in (2.9), since the rated speed may be sufficient for a given application.

Table 4.4 Skewness S of Multiphysics Performances for the 24-slot Datasets

Performance		Number of barriers 1	2	3	4	Strength Low	Med.	High	Skew Benefit?
T_{avg}	Nm	-1.55	-1.52	-1.79	-1.57			-	Y
T_{rip}	%	+2.06	+0.33	+0.56	+0.50		+		Y
pf		-1.11	-1.14	-1.27	-1.19		-		Y
η	%	-3.38	-2.02	-2.20	-1.80			-	Y
V_{rms}	V	-0.75	-0.78	-1.09	-1.66		-		N
ξ		-0.01	-0.36	-0.60	-0.61	-			Y
L_d	mH	+0.85	+0.95	+1.05	+0.90		+		Y
N_m^{Base}	RPM	+0.81	+1.18	+1.53	+1.88		+		N
P_{SL}	dB	**-0.51**	+0.03	+0.37	+0.35	+			Y
k_S		+1.19	+0.83	+0.49	+0.32	+			N
T_W	°C	-1.24	-2.24	-2.24	-2.36			-	N
k_S	°C	-1.28	-2.25	-2.21	-2.31			-	N

Table 4.5 Skewness S of Multiphysics Performances for the 30-slot Datasets

Performance		Number of barriers 1	2	3	4	Strength Low	Med.	High	Skew Benefit?
T_{avg}	Nm	-1.54	-1.47	-1.71	-1.51			-	Y
T_{rip}	%	+1.57	+0.57	+0.34	+0.88		+		Y
pf		-1.06	-0.95	-1.17	-1.08		-		Y
η	%	-3.36	-1.96	-2.11	-1.72			-	Y
V_{rms}	V	-0.95	-0.72	-0.86	-1.34		-		N
ξ		**+0.12**	-0.05	-0.50	-0.55	-			Y
L_d	mH	+0.82	+0.87	+1.02	+0.86		+		Y
N_m^{Base}	RPM	+0.81	+1.04	+1.28	+1.58		+		N
P_{SL}	dB	+0.00	+0.32	+0.44	+0.27	+			Y
k_S		+1.22	+0.87	+0.51	+0.31	+			N

4.2 Stage 5: Post-Computation Interaction (*interact*)

After extracting design knowledge in the previous stage, Stage 5 initiates a post-computational interaction with the user by providing a general summary and a list of recommendations.

For instance, the correlation plots of the performances and design variables in Figs. 4.1, 4.2 and 4.3 could be presented for a given dataset (e.g. 24-slot 3-barrier). These correlation plots can be coupled with a visual cursor to navigate through different points. If a user selects one point on a scatter plot, e.g. that of (T_{avg},T_{rip}) in Fig. 4.1, the selected design has corresponding points on other scatter plots, e.g. that of (k_S,P_{SL}) in Fig. 4.2, or (W_c,W_b) in Fig. 4.3. Choosing another point shifts the previously selected one to a new location on the scatter plots, thereby demonstrating tradeoff relationships among various performances and metrics. Providing such an option can help the user to arrive at a more informed choice with statistical justification. An example of this cursor tool has been implemented in Section 4.1.1 using the five selected designs. Moreover, the clustering of optimal solutions shown in Figs. 4.6 and 4.7 indicates that the 4-barrier dataset generally improves all performances and can be recommended to the user. A list of important objectives with high priorities can be suggested for applying the *barrier mapping* technique (e.g. T_{avg} is suitable, while T_{rip} is not). In brief, this technique can reduce the computational time required for running multiphysics simulations of multiple-barrier SynRMs (explained in Chapter 3). A summary of the design knowledge and guidelines listed above can also be presented. While a correlation plot is a useful statistical tool for the design process, it may be difficult to use since it requires a user's interaction to understand the relationships of different performances. Another way to systematically illustrate how these multiphysics objectives are related is to use an objective aggregation tree through rank-based conflict [Silva, 2018] which is explained below.

From a given dataset with m multiphysics objectives and n samples, a vector of m-objective values, $\boldsymbol{f_i}(\boldsymbol{x}^{(i)})$, for each sample i is constructed to form the set, $\boldsymbol{F} = \{\boldsymbol{f_1}, ..., \boldsymbol{f_n}\}$. Then, the conflict for each performance pair ($f_{i,a}$,$f_{i,b}$) is estimated by C_{ab}, a conflict measure proposed in [Freitas et al., 2013] and given by (4.4). Here, $R_{i,a}$ and $R_{i,b}$ are the associated ranks of sample $\boldsymbol{x}^{(i)}$ for a performance pair, e.g. (T_{avg},T_{rip}). As an example, $R_a = 1$ for the sample with highest T_{avg}, $R_b = 1$ for the sample with lowest T_{rip}, $R_a = 2$ for the sample with the second highest T_{avg}, and so on. By this C_{ab} measure, a 100% conflict means that one performance improves at the expense of another, while 0% signifies total harmony; i.e., both objectives improve simultaneously. Any midway value implies a non-uniform tradeoff between the two performances over the design space.

$$C_{ab} = \frac{\sum_{i=1}^{n} |R_{i,a} - R_{i,b}|}{\sum_{i=1}^{n} |2i - n - 1|} \tag{4.4}$$

To construct an objective aggregation tree, the conflict between each pair of objectives is computed using (4.4). Pairs with the lowest conflicts are combined as a single objective. Then, the conflict between the new aggregated performance and another objectve is computed. This procedure repeats until the conflicts among all pairs of objectives and their aggregations are found. Finally, the aggregation tree is constructed by placing the lowest conflicting pairs at the bottom, while the total combined objective with the highest conflict is located at the top. If the conflict between a performance pair is low (e.g. $< 10\%$), then one of them can be removed without affecting a many-objective optimization problem [Silva et al., 2018]. Choosing which objectives to aggregate is based on how much loss of information is acceptable for the design process and is quantified through the conflict percentages.

Fig. 4.8 displays the aggregation tree for the 24-slot 4-barrier dataset. Similar trees are observed for the other datasets, such as Fig. 4.9 for the 30-slot 4-barrier case. Objectives located near the bottom are more closely tied to one another than the ones shown above. For example, the 4% conflict between T_W and T_R indicates that considering both objectives is redundant. A similar argument holds for the following objective pairs: (V_{rms},N_m^{Base}), (pf,ξ) and (T_{avg},η). However, k_S, P_{SL} and T_{rip} are situated higher up in the aggregation tree meaning that they are more conflicting with the other performances. For example, the total aggregated objective located at the top has a 90% conflict which cannot be ignored. To address this issue, non-redudant objectives can be selected to reduce the complexity of finding an optimal solution. It can be seen that T_{avg}, T_{rip}, pf, V_{rms}, k_S, P_{SL} and T_W are all independent objectives that cannot be ignored without a loss of information. Therefore, all these objectives highlighted in Fig. 4.8 with boxes are considered for the MPDP while focusing on the 24-slot 4-barrier case. Another dataset could be used for building the aggregation tree, such as that for the 30-slot 4-barrier in Fig. 4.9, as long as the initial specfications set in Stage 1 are met. Now, the user is ready to select optimal designs based on the presented solutions in the next stage.

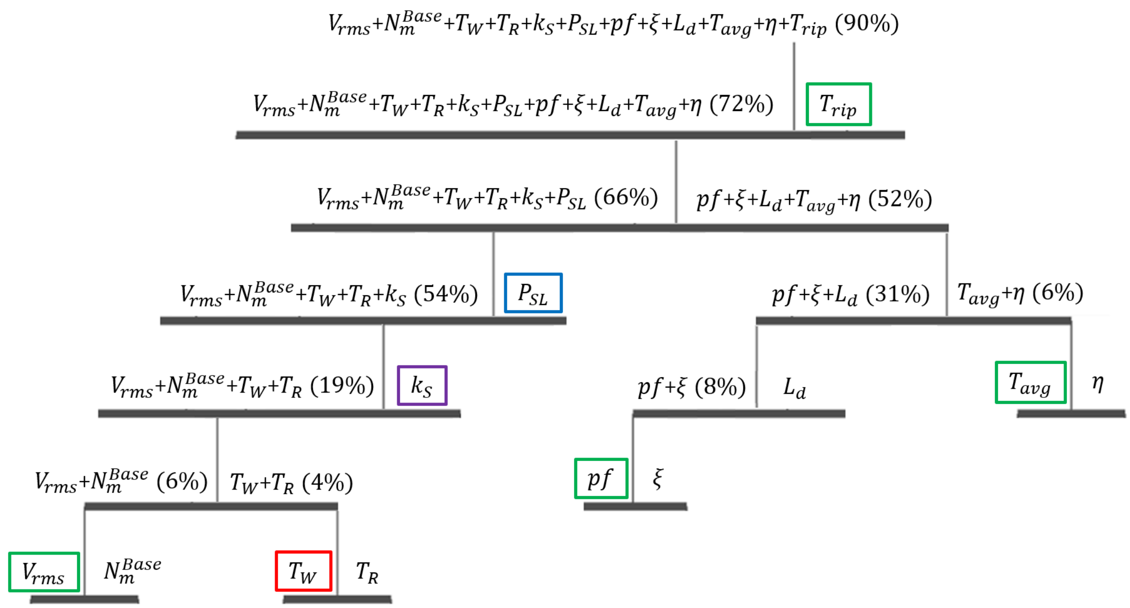

Fig. 4.8 Aggregation tree using rank-based conflict (24-slot, 4-barrier). Selected objectives are boxed corresponding to analysis colors.

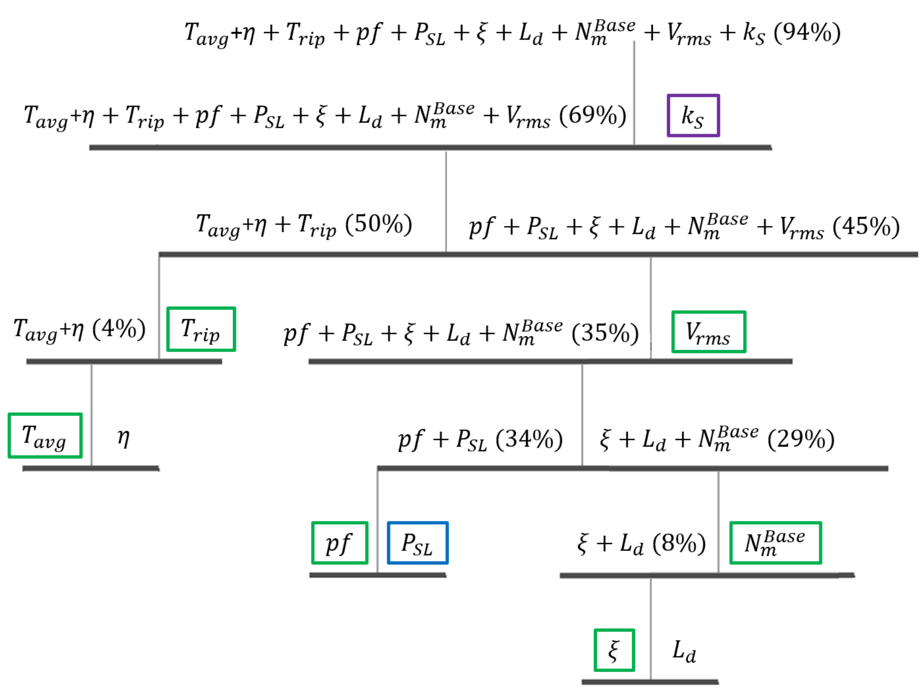

Fig. 4.9 Aggregation tree using rank-based conflict (30-slot, 4-barrier). Selected objectives are boxed corresponding to analysis colors.

4.3 Stage 6: Design Search and Selection (*internal*)

In Stage 6, the MPDP considers the evaluated performances, the user's constraints and priorities, and the acquired knowledge from the previous stage to begin searching the design space. The aim here is to suggest the best possible designs to the user based on the inputs received in the previous stages. To visualize and select optimal designs, the generalized selection function, $g_S(\cdot)$, defined in (4.1) is used to find five different SynRM designs for the 24-slot 4-barrier dataset. A similar selection procedure could be performed for the 30-slot 4-barrier case but is not performed here. The 4-barrier dataset was chosen, since it was previously shown in Sections 3.2, 3.3 and 4.1.2 that increasing the number of barriers generally improves the SynRM's performance, while lower n_b values lead to sub-optimality.

Among the selected designs specified in (4.5), D_1 considers two electromagnetic objectives. D_2-D_4 individually combine electromagnetic with either structural, acoustic or thermal performances. For D_1-D_4, $\boldsymbol{k}$ was set to a uniform objective weighting, while D_5 considers all multiphysics performances from the aggregation tree in Fig. 4.8. However, a heavier T_{rip} weight is set (to avoid high torque ripple designs) with the rest distributed evenly among T_{avg}, pf, V_{rms}, P_{SL}, k_S and T_W. Hence, the chosen objectives weights are shown in (4.6). The flux density distributions of the five selected designs are shown in Fig. 4.10 (a)-(e). A summary of the performances, design metrics and variables are listed in Table 4.6.

$$\begin{aligned}
\mathrm{D}_1 &: \mathrm{E} && \rightarrow g_S\big([-T_{avg}, T_{rip}]\big)\\
\mathrm{D}_2 &: \mathrm{E}+\mathrm{St} && \rightarrow g_S\big([-T_{avg}, T_{rip}, -k_S]\big)\\
\mathrm{D}_3 &: \mathrm{E}+\mathrm{A} && \rightarrow g_S\big([-T_{avg}, T_{rip}, P_{SL}]\big)\\
\mathrm{D}_4 &: \mathrm{E}+\mathrm{T} && \rightarrow g_S\big([-T_{avg}, T_{rip}, T_W]\big)\\
\mathrm{D}_5 &: \mathrm{All} && \rightarrow g_S\big([-T_{avg}, T_{rip}, -pf, V_{rms}, P_{SL}, -k_S, T_W]\big)
\end{aligned} \tag{4.5}$$

$$\begin{aligned}
\mathrm{D}_1 &: \mathrm{E} && \rightarrow \boldsymbol{k} = [0.5, 0.5]\\
\mathrm{D}_2 &: \mathrm{E}+\mathrm{St} && \rightarrow \boldsymbol{k} = [0.33, 0.33, 0.33]\\
\mathrm{D}_3 &: \mathrm{E}+\mathrm{A} && \rightarrow \boldsymbol{k} = [0.33, 0.33, 0.33]\\
\mathrm{D}_4 &: \mathrm{E}+\mathrm{T} && \rightarrow \boldsymbol{k} = [0.33, 0.33, 0.33]\\
\mathrm{D}_5 &: \mathrm{All} && \rightarrow \boldsymbol{k} = [0.1, 0.4, 0.1, 0.1, 0.1, 0.1, 0.1]
\end{aligned} \tag{4.6}$$

From the selected designs in Table 4.6, the multiphysics tradeoffs are clearly observed. In short, D_1 has the lowest T_{rip}, D_2 permits high speed operation (i.e. N_m^{Max} of 15751 RPM) due to the high k_S value, D_3 is the quietest motor at 56.46 dB, and D_4 has the lowest winding and rotor temperatures (i.e. 75.63°C and 75.01°C). It is interesting to note that D_4 has the highest N_m^{Max} at 16630 RPM while it minimized T_W. On the other hand, D_5 generally performs well for all objectives with its T_{rip} being around 11%. For all cases, T_{avg} is relatively high (>0.9 Nm) due to the high saliency ratios (>3.1). If T_{rip} needs to be further minimized, the rotor could be skewed by one slot pitch, i.e. 15°, to result in a T_{rip} of 2.47%, 2.30%, 2.72%, 4.85% and 3.86% for D_1-D_5 respectively with less than 6% deviation in the other performances. Finally, the user is asked whether any of the selected designs satisfy the original targets. If not, the MPDP returns to Stage 5 as shown in Fig. 1.30 to reset the constraints and priorities before searching for new solutions.

The correlation plot of all the 24-slot 4-barrier performances mentioned in (2.17) is displayed in Fig. 4.11. Also, the same plot for the design metrics is shown in Fig. 4.12. Other correlation plots (i.e. performance and design metrics) are shown in Appendix D for the 24 and 30-slot cases and for all four barriers. Note that since the 30-slot dataset does not include thermal results, D_4 and D_5 are set differently as specified in the corresponding figure captions. From the two correlation plots, similar design knowledge to that in Section 4.1.1 can be extracted. For example, there is not enough evidence to suggest that T_{avg} is correlated with V_{rms}, P_{SL}, N_m^{Base}, k_S and T_W. This means that it is important to treat these objectives as independent from each other during the selection process. Another guideline would be that pf and V_{rms} are negatively correlated indicating a harmonious relationship, since pf must be maximized and V_{rms} minimized. Also, the design metrics in Fig. 4.12 correspond well with the cluster of optimal solutions obtained though *barrier mapping* in Figs. 4.6 and 4.7. This means that the 4-barrier design can be arrived at by using fewer FEA samples based on the optimal constraints from the 1-barrier design plane. These constraints can be initially suggested to the user and set in Stage 1 of the MPDP.

Table 4.6 Summary of Selected Designs (24-slot, 4-barrier)

Type	Symbol	Unit	D_1	D_2	D_3	D_4	D_5
E	T_{avg}	Nm	**0.987**	0.972	0.977	0.969	**0.989**
	T_{rip}	%	**9.14**	11.74	16.75	26.16	**11.04**
	pf		0.529	0.524	0.517	**0.545**	0.529
	η	%	**83.92**	83.75	83.75	83.79	83.95
	V_{rms}	V	26.87	26.74	27.22	**25.59**	26.90
	ξ		3.29	3.22	3.15	**3.53**	3.30
	L_d	mH	1.46	1.48	1.54	**1.30**	1.46
	N_m^{Base}	RPM	1993	**2004**	1967	**2105**	1992
St	k_S		7.32	**7.86**	7.43	**7.90**	7.54
	N_m^{Max}	RPM	14589	**15751**	14615	**16630**	15020
A	P_{SL}	dB	57.60	57.75	**56.46**	58.35	57.27
T	T_W	°C	76.53	76.51	76.53	**75.63**	76.47
	T_R	°C	75.95	75.92	75.96	**75.01**	75.86
Metrics	W_c	pu	0.49	0.48	0.50	0.34	0.44
	W_b	pu	0.41	0.45	0.39	0.60	0.45
	W_c+W_b	pu	0.90	0.93	0.89	0.94	0.89
	a	pu	0.45	0.49	0.44	0.64	0.50
Variables	W_{c_4}	mm	3.18	1.66	2.10	1.55	2.89
	W_{b_4}	mm	1.50	1.57	1.76	2.08	2.27
	W_{c_3}	mm	1.66	1.11	2.60	1.42	1.33
	W_{b_3}	mm	1.06	1.75	1.27	1.83	1.46
	W_{c_2}	mm	1.01	3.70	1.69	1.26	1.47
	W_{b_2}	mm	1.91	1.97	1.55	3.52	1.61
	W_{c_1}	mm	1.69	1.32	1.22	1.57	1.33
	W_{b_1}	mm	1.74	2.10	1.31	2.82	1.76
	W_f	mm	8.98	4.98	9.46	3.05	6.74
	R_{ri}	mm	6.51	5.07	6.76	4.20	6.13

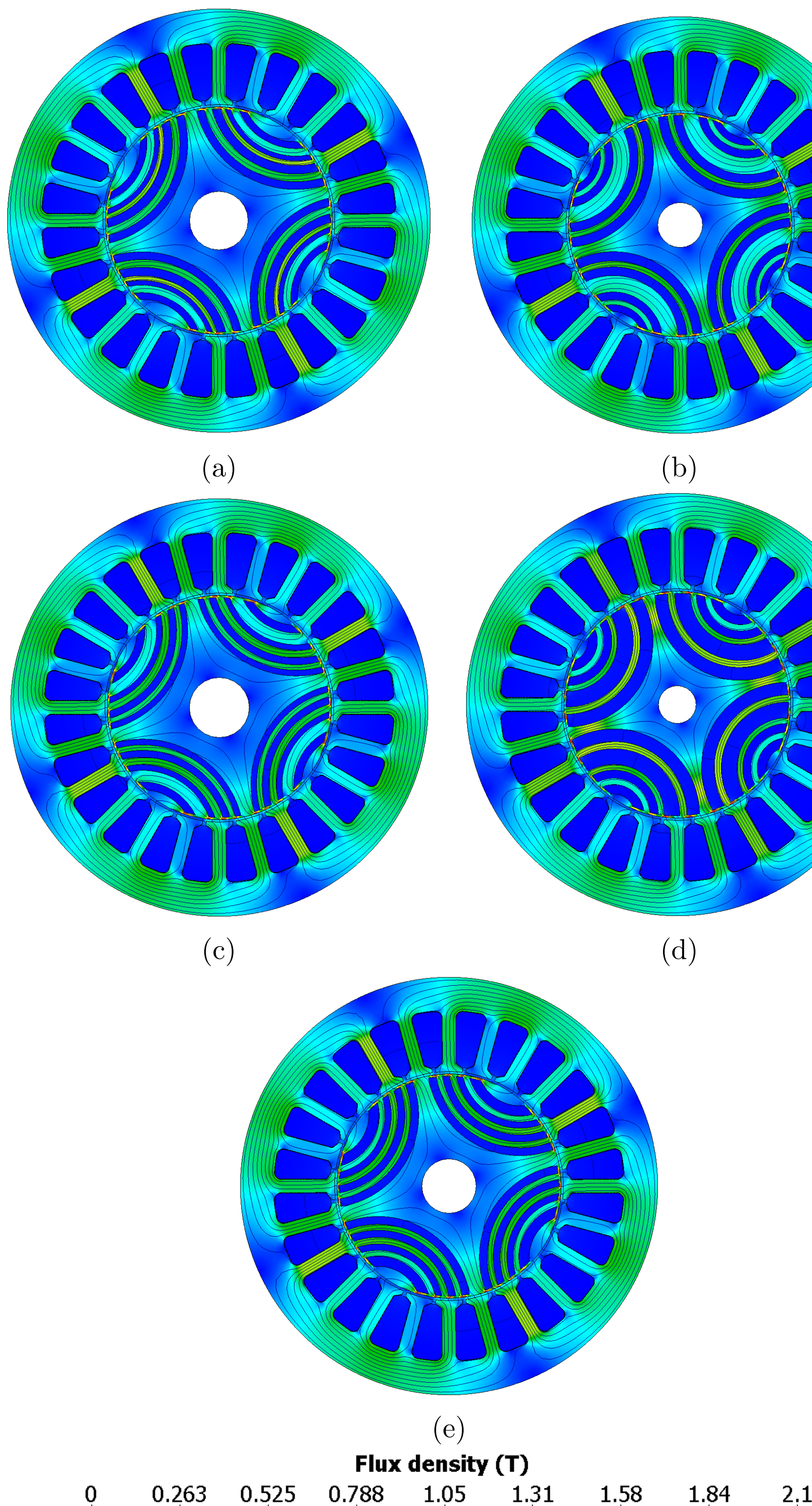

Fig. 4.10 Flux density distributions at rated condition of selected SynRM designs (24-slot, 4-barrier): (a) D_1, (b) D_2, (c) D_3, (d) D_4, (e) D_5.

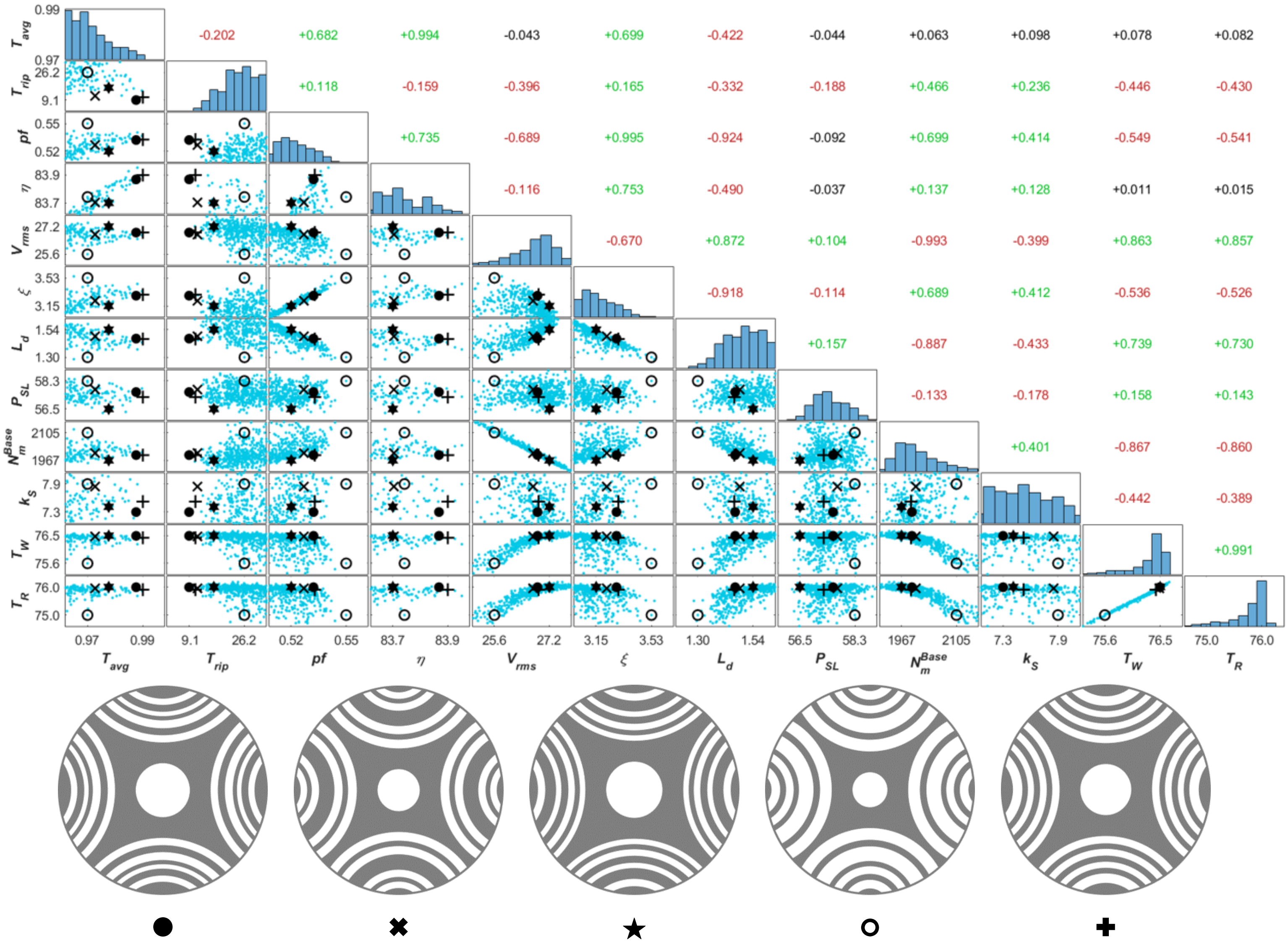

Fig. 4.11 (Top) Correlation plot of 24-slot, 4-barrier performances. (Bottom) Selected designs: ● for [-T_{avg},T_{rip}], ✖ for [-T_{avg},T_{rip},-k_S], ★ for [-T_{avg},T_{rip},P_{SL}], ○ for [-T_{avg},T_{rip},T_W], ✚ for all.

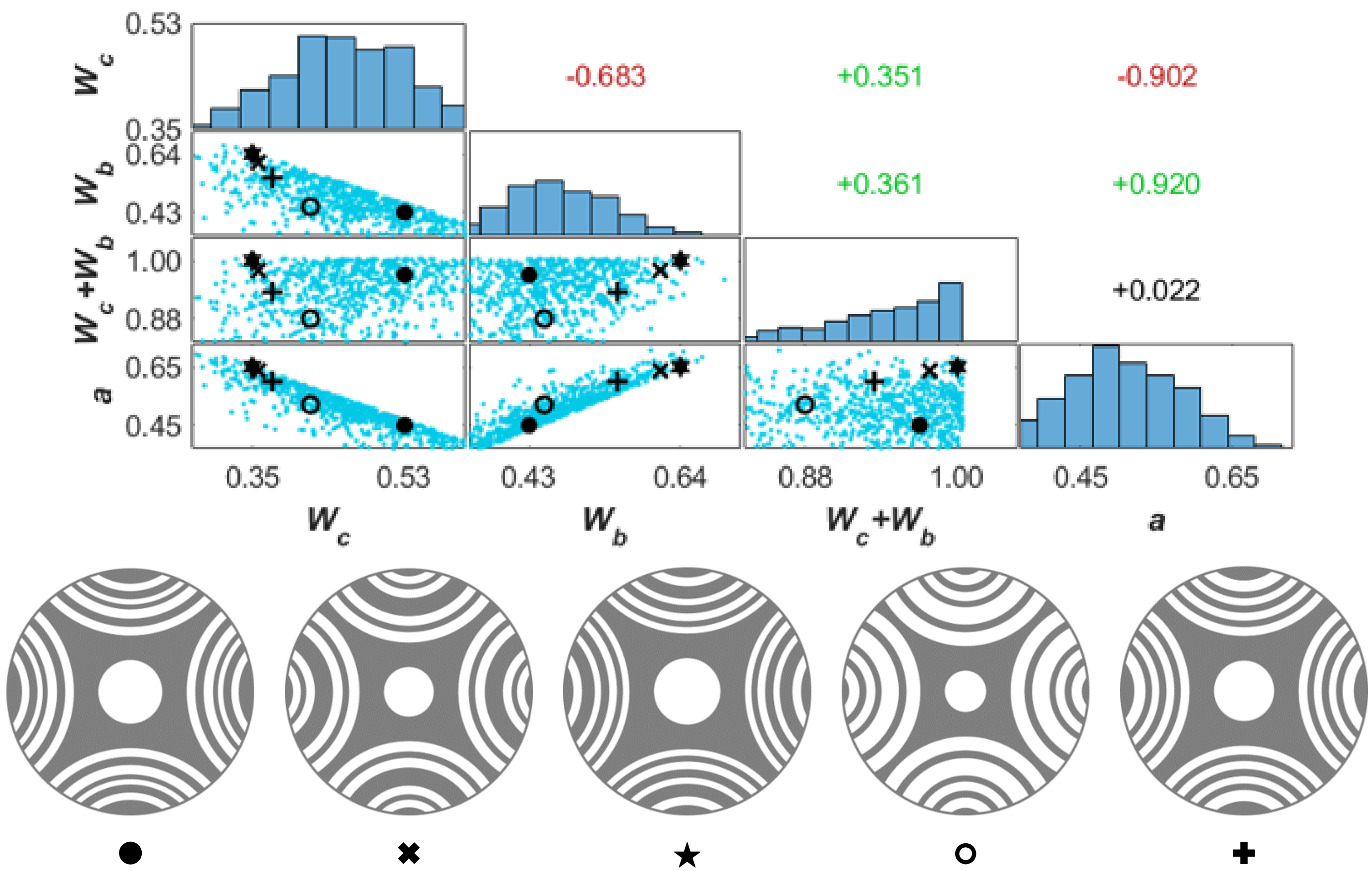

Fig. 4.12 (Top) Correlation plot of 24-slot, 4-barrier design metrics. (Bottom) Selected designs: ● for [-T_{avg},T_{rip}], ✖ for [-T_{avg},T_{rip},-k_S], ★ for [-T_{avg},T_{rip},P_{SL}], ○ for [-T_{avg},T_{rip},T_W], ✚ for all.

Focusing on the correlation plots in Figs. 4.11 and 4.12 and selected design summary of Table 4.6, the following design knowledge and guidelines can be extracted:

- For these following objective pairs, there is a strong positive correlation (above +0.7). Depending on the selected objective, its pair objectives could be ignored when using (4.1). For example, choosing either pf or η would be sufficient.
  - average torque T_{avg} with pf, η and ξ
  - power factor pf with η, ξ and N_m^{Base}
  - efficiency η with ξ
  - RMS voltage V_{rms} with L_d, T_W and T_R
  - saliency ratio ξ with N_m^{Base}
  - d-axis inductance L_d with T_W and T_R
  - average winding temperature T_W with T_R
- A strong negative correlation (below -0.7) exists for these pairs. Similarly, redundant selection objectives can be removed.
  - power factor pf with V_{rms} and L_d
  - RMS voltage V_{rms} with ξ and N_m^{Base}
  - saliency ratio ξ with L_d
  - d-axis inductance L_d with N_m^{Base}
  - base speed N_m^{Base} with T_W and T_R
- There is no pairwise correlation (coefficient near 0) between such pairs. These non-correlated performances cannot be ignored and could be used as objectives.
  - average torque T_{avg} with P_{SL}, k_S, T_W and T_R
  - torque ripple T_{rip} with pf, ξ and k_S
  - efficiency η with k_S
  - sound pressure level P_{SL} with k_S

- The range of temperature values is 1°C, and D_4 has the lowest temperature among all. The values indicate that the selected motors operate within safe thermal limits.

Table 4.7 compares the relative performances of the selected designs with respect to each other using the correlation plot in Fig. 4.11. Each row corresponds to a selected design, while the columns show the multiphysics objectives. The highlighted cells indicate the objectives used for selection as in (4.5). In each cell, one of three markers are used: '+' corresponds to an improvement, '-' is for a worsening, 'o' indicates an average value. For instance, D_1 has improved values in T_{avg} and T_{rip} (selected objectives) as well as in η. However, its V_{rms}, L_d, N_m^{Base}, k_S, P_{SL} and T_W values all are worse compared to other selected designs. This result indicates that using only electromagnetic objectives does not yield an optimal solution for other multiphysics objectives. A similar outcome holds as well for D_2-D_4, where different selection criteria yield different solutions. On the contrary, D_5 has a relatively good performance for all objectives without any worsening. Its T_{avg}, T_{rip}, η and V_{rms} values have improved while other objectives are about average. Therefore, the five selected solutions located at various design regions show that completely different design variables are required to satisfy different design goals. This finding provides a need for a data-driven design process to address a designer's targets in a specific application. Providing such knowledge can help the user make a more informed choice for a motor design. If different physical disciplines are incorporated into this procedure, other optimal solutions can be extracted, possibly different from that in Figs. 4.11 and 4.12.

Table 4.7 Summary of Relative Performances of Selected Designs.

	EM								ST	AC	TH
	T_{avg}	T_{rip}	pf	η	V_{rms}	ξ	L_d	N_m^{Base}	k_S	P_{SL}	T_W
● D_1	++	++	o	+	- -	o	-	- -	- -	- -	- -
✖ D_2	o	-	+	-	+	+	+	+	++	o	-
★ D_3	+	o	- -	o	- -	- -	- -	- -	o	++	- -
○ D_4	- -	- -	++	- -	++	++	++	++	-	++	++
✚ D_5	++	++	o	++	+	o	o	o	o	o	o

With respect to each other: + improvement, - worsening, o average

4.4 Performance Improvement through PM-Assist

After an optimal SynRM design is selected in Stage 6 of the MPDP, the user may ask for PMs to be added into the rotor structure to result in a PM-SynRM. While this motor type relies more on reluctance torque, its additional PM content permits it to run in flux-weakening operation at higher speeds [Morimoto et al., 2001]. This feature becomes especially important in traction applications to maintain a constant power. Lu et al. [2017] suggested a useful procedure summarized in Fig. 1.22 to transform a SynRM design into a PM-assisted one. Design D_5 from the previous section is used as an example in Step 1 of Fig. 1.22 to transform it into a PM-SynRM, named as D_5^* in the discussion below.

In Step 2 of Fig. 1.22, all the rotor barriers are filled with a fictitious PM with remnant flux density, B_r'. Next, the PM flux linkage, λ_m, and L_d are found using electromagnetic FE simulations, and the characteristic current, I_{ch}, is computed using (4.7). In order to have a *constant power speed range* (CPSR) for the rated current, I_{ch} must get close to the rated current (i.e. 10 A) or the d-axis flux linkage, λ_d, must reach near 0. If not, B_r' must be adjusted accordingly to directly vary λ_m assuming that L_d is relatively constant. Fig. 4.13 shows how I_{ch}, λ_d, L_d and λ_m vary for different values of B_r'. Once this condition is achieved, a specific PM such as NdFeB or a ferrite with remnant flux density, B_r, is chosen in Step 3. Then, (4.8) is used to find the PM volume, V_m, based on the equivalent PM volume, V_m'. For the case of D_5^*, B_r' is 0.2 T, V_m' is 54 mL, B_r is 1.2 T, V_m is 9 mL and I_{ch} is 11.4 A for NdFeB 38/23. The flux density distribution of D_5^* is shown in Fig. 4.14, where its PMs are concentrated along the barrier centers. A similar procedure can be used for ferrite magnets.

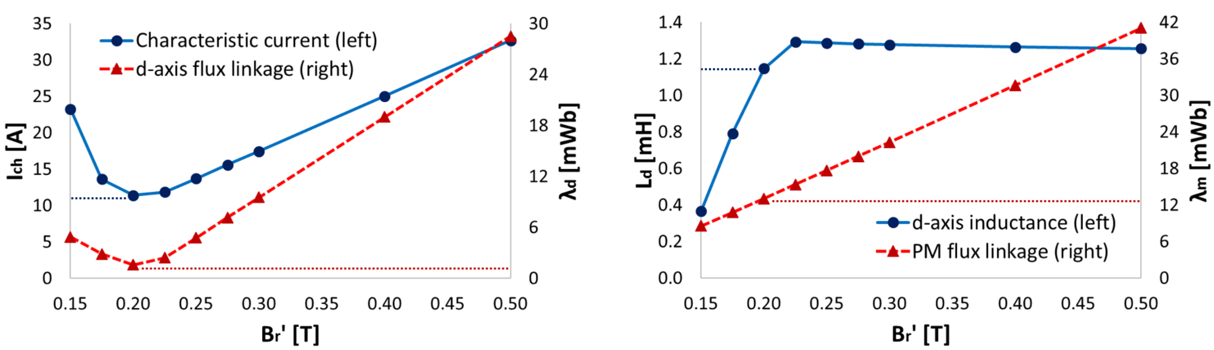

Fig. 4.13 I_{ch}, λ_d, L_d, λ_m vs. equivalent PM remnant flux density.

$$I_{ch} = \frac{\lambda_m}{L_d} \tag{4.7}$$

$$\frac{V_m}{V_m'} = \frac{B_r'}{B_r} \tag{4.8}$$

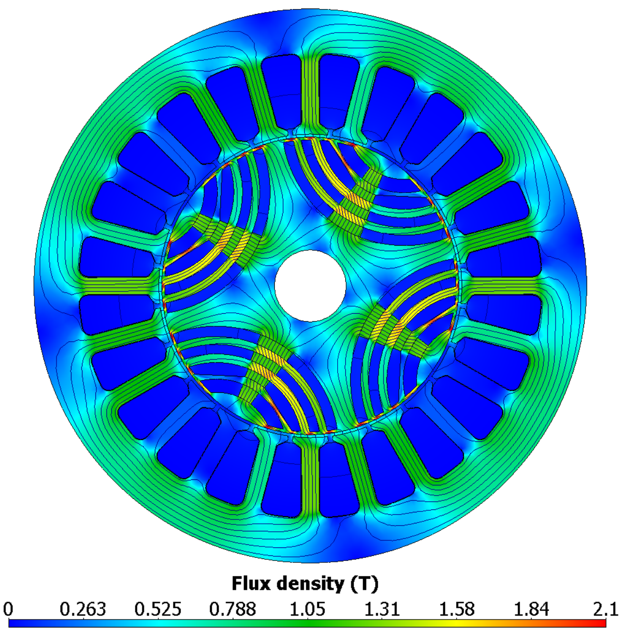

Fig. 4.14 Flux density distribution at rated condition of PM-SynRM D_5^*.

Table 4.8 compares the performances of the PM-SynRM, D_5^*, with its original SynRM D_5. The relative percentage improvement of performances is defined as ΔP. Both T_{avg} and pf significantly improved by adding PMs which enabled a higher ξ and nonzero λ_m, i.e. 13mWb (torque: 61% reluctance + 39% PM). A higher pf means that the inverter size can be reduced. In terms of the structural and thermal analyses, similar behaviors to that of D_5 were noticed. The PMs are mechanically safe since they are inserted inside the barriers.

Table 4.8 Performance Comparison of PM-SynRM.

Perf.	T_{avg}	T_{rip}	pf	η	V_{rms}	ξ
Value	1.627 Nm	12.72%	0.791	89.6%	27.72V	4.76
ΔP	65%	1.68%	50%	7%	3%	44%

In addition, the efficiency map of D_5^* displayed in Fig. 4.15 was calculated using the computationally-efficient procedure described in Appendix C. Two torque-speed envelopes are plotted on top for the continuous (4.5 A/mm^2) and peak (9.0 A/mm^2) conditions. Briefly speaking, the efficiency map was found as follows: first, the nonlinear dq flux linkages were computed for different dq currents using electromagnetic FE analysis. Various control strategies were then applied to find optimal dq currents for every torque and speed value. Next, these points were used to compute the motor losses in order to interpolate and visualize its efficiency map shown in Fig. 4.15. To better compare the variable-speed performance of D_5^* with D_5, their torque-speed and power-speed characteristics are displayed in Fig. 4.16 for the rated condition. Note that D_5 with no PMs has a drooping power beyond base speed, whereas the PM-SynRM design, D_5^*, can operate well up to 14000 RPM for the same constant power. In other words, D_5^* has a high CPSR value of more than 3.5. This maximum speed was selected based on k_S in Table 4.6 which still permits a mechanical safety factor of 1.12. If the provided power is beyond the user requirements, the machine can be downsized to lower its volume and mass.

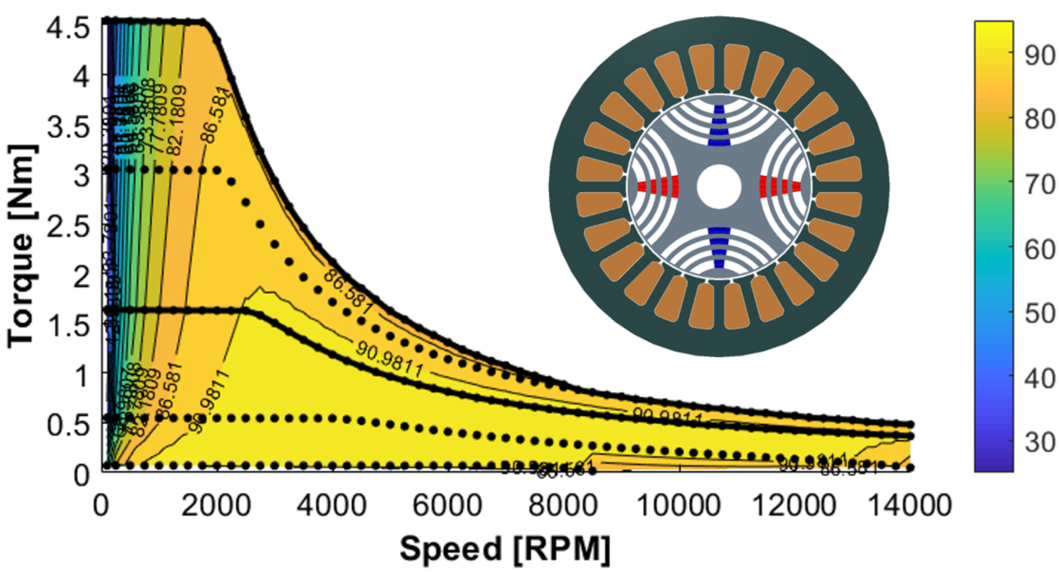

Fig. 4.15 Efficiency map of PM-SynRM D_5^*.

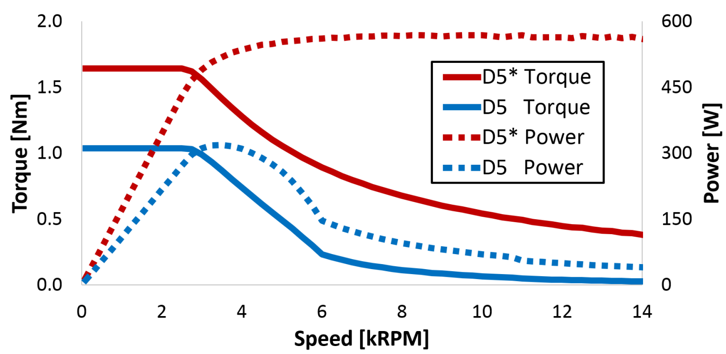

Fig. 4.16 Comparison of torque-speed and power-speed characteristics of PM-less design D_5 and PM-assisted design D_5^*.

For the peak current condition at high speed, it is necessary to check for irreversible demagnetization. The electromagnetic FE solver [Mentor-Infolytica Corporation, 2018] is used to plot the *demagnetization proximity* (DP) and flux density fields as shown in Fig. 4.17. The DP is defined such that negative values are safe, while positive values mean irreversible demagnetization in those PM regions. Fig. 4.17 (a) proves that the inserted PMs are not close to demagnetization and can be safely used.

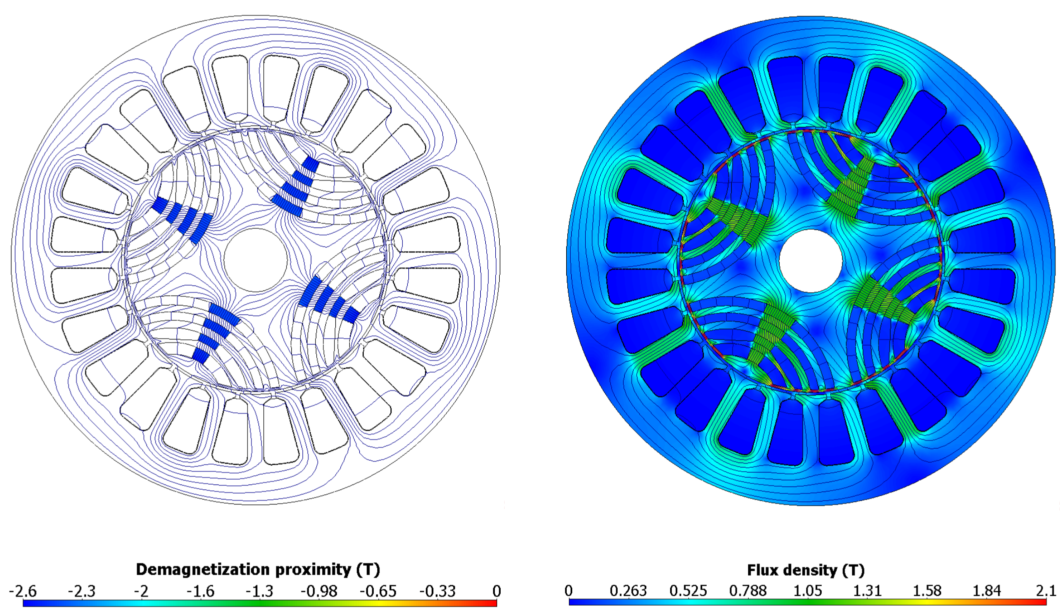

(a) (b)

Fig. 4.17 Field distributions of PM-SynRM D_5^* at (200% 79°) flux-weakening condition: (a) demagnetization proximity, (b) flux density.

From a cost perspective, the prices discussed in [Bianchi, 2013] can be used to evaluate the material expense of producing D_5^* whose total mass is 3.49 kg. For example, rare-earth PMs were quoted at 70 US$/kg in 2013. This corresponds to a total cost of US$ 15.45 for the following: magnet US$ 5.00 (0.07 kg), iron US$ 2.77 (2.52 kg), copper US$ 7.68 (0.90kg). The addition of PM in D_5^* provides many performance benefits at a low material cost.

4.5 Summary

The last 3 stages of the 6-stage MPDP in Fig. 1.30 were discussed and explained in this chapter: (4) extracting design knowledge and guidelines, (5) performing *barrier mapping* for relating different rotor topologies (i.e. 1, 2, 3, and 4 barriers), interacting with the user after computation to show how the solutions are clustered together for different objectives (i.e. average torque, power factor, efficiency, saliency ratio, d-axis inductance, base speed, average winding and rotor temperatures), statistically analyzing the global results, and (6) finally selecting optimal designs based on a user's requirements using a weighted-sum approach.

With the help of correlation plots and the selected designs for different problems (e.g. only electromagnetic, or electromagnetic + acoustic + structural), tradeoff relationships among the multiphysics performances were observed. When the number of barriers was increased, nearly all performances showed statistical improvement for both the 24- and 30-slot case studies. It is interesting to note that not all performances tend toward the same optimization direction (minimization or maximization); some of their distributions were skewed in the opposite direction (e.g. safety factor), suggesting that these performances should be prioritized. Using objective aggregation trees based on a conflict measure, the multiphysics problem was simplified by reducing the number of objectives from 12 to 7. Also, a single SynRM design with optimal multiphysics performances was assisted with PMs to achieve many performance improvements such as wide speed operation, high power factor and low demagnetization proximity at peak conditions. All of these benefits were obtained while maintaining the strengths of a pure SynRM which includes low material cost, robustness, and high torque-to-volume ratio.

Chapter 5

Conclusion

This thesis has described a data-driven, multiphysics design process to statistically analyze and generate design knowledge for synchronous AC machines, e.g. interior or surface permanent magnet types. Specifically, a synchronous reluctance machine with round-shaped rotor barriers for different slot-pole combinations has been investigated under a single operating condition. Finite element analysis was used to simulate thousands of different motor designs by varying geometrical parameters in order to acquire their multiphysics performances. These 12 objectives include: average torque, torque ripple, power factor, iron power loss or efficiency, RMS phase voltage, saliency ratio, d-axis inductance and base speed for the electromagnetic analysis, safety factor or maximum mechanical speed for the structural analysis, sound pressure level for the acoustic analysis, and average winding and rotor temperatures for the thermal analysis. Multivariate design spaces corresponding to multiple-barrier rotors consisting of both optimal and suboptimal possibilities were created and statistically analyzed to address various design targets, including those defined in electrified transportation.

From the multiphysics analysis, it was proven that several very different final design choices can be produced, depending on the user's choice and application requirements. For instance, considering only electromagnetic objectives compromised other performances, which necessitates incorporating the different physics during the design process in order to arrive at optimal multiphysics solutions. Also, the skewness of some performance distributions was observed to be statistically opposite to the optimization direction, such as the safety factor. By relying on a data-driven approach, the proposed design process can arrive at final designs which can satisfy a user's specifications and priorities.

All these results arose from the comprehensive knowledge gained from the design process and its different stages which can be transferred to software packages for future design and optimization purposes. For example, it was found that the centrifugal force contributes to at least 95% of the total force (electromagnetic and structural combined) for all design variations. This means that the critical mechanical stress on the tangential ribs can be optimized with a loosely coupled electromagnetic-structural analysis. In addition, general guidelines that relate the design variables to the selected objectives have been proposed. These can help motor designers to systematically define design constraints for optimization. Specifically, it was observed that simultaneously increasing the power factor and reducing the iron power loss (or maximizing the motor efficiency) was possible by using thicker flux barriers for the analyzed case study. Another knowledge is that the voltage rating was related to other objectives from which an appropriate DC bus voltage limit can be determined.

While the proposed multiphysics design process was only applied to a synchronous reluctance machine as a case study, the design process is expected to be generalizable for other machine topologies (e.g. interior or surface permanent magnet types) and possibly other physical devices; the design process focuses on statistically analyzing performances and variables irrespective of a device's behavior. It was also demonstrated that the electromagnetic simulation time was significantly reduced from months to days with the help of a high-performance computing system. Given the tradeoff relationship of computational time and the number of virtual machines, the latter quantity was chosen near the knee point to avoid a high financial cost of renting virtual machines in the employed cloud platform. Suggestions on how to choose this HPC parameter have been discussed.

Other stages of the design process included: analyzing the conflicts among objectives for simplifying the problem's complexity (dimensionality reduction), handling of multiphysics design constraints, tradeoff analysis of performances or objectives, introducing and using the *barrier mapping* technique for relating different design spaces in order to effectively reduce the computational effort, and selecting optimal designs based on a user's specifications and priorities. Finally, an optimal machine design was further improved by adding permanent magnet material within its rotor structure to fulfill the requirements of recent technologies such as electric vehicles. This magnet assist was found to be suitable for variable-speed drives with a wide range of operating speeds. Lastly, a computationally efficient algorithm for generating detailed efficiency maps was developed and used for evaluating the final design.

5.1 Future Work

Since the work presented in this thesis is a fundamental step toward defining a multiphysics design process based on a data-driven approach, the extracted knowledge and guidelines were mostly visualized in order to show how they work as a proof of concept. Future works can extend the demonstrated ideas by automating the knowledge extraction stage within a software package by using artificial intelligence or an advanced expert system. For example, with the help of the computed correlation coefficients, the software can suggest to the user on which objectives to prioritize based on the underlying application. Some examples include high-speed applications which prioritize the structural integrity of an electric machine, while small-sized machines with tight cooling constraints concentrate on the thermal aspects.

Despite the use of a high-performance computing system for the electromagnetic analysis (helped reduce computational time), other physical analyses were simulated on lab workstations which limited the possibility of coupling the different physical phenomena. For example, electromagnetic and thermal analyses must be coupled especially when permanent magnets are involved. In brief, the magnet power loss is computed using an electromagnetic simulation which in turn causes its temperature rise after a thermal analysis. This temperature change would then affect the magnetic properties of the permanent magnets, which requires re-running the electromagnetic simulation for the updated performances. In this thesis, a one-way coupling was assumed (only electromagnetic, then thermal), whereas a fully-coupled simulation could modify or add to the suggested design guidelines. This outcome can especially occur for other motor types such as the interior permanent magnet.

Also, future studies can expand the presented case study by including the stator structure within the multi-physics design process or using alternative rotor topologies such as the angled or fluid barrier shapes. The challenge, however, lies in defining additional geometric parameters for different topologies that can be used for performing *barrier mapping* in order to transform a multiple-barrier design to single-barrier one. Lastly, the electromagnetic analysis only included a single operating condition, i.e. Maximum Torque Per Ampere, for the simulation process. Other conditions for balanced or faulty cases could be considered given the means presented here to visualize and relate many objectives, such as the correlation plot or the aggregation tree. If a distributed computing approach is maintained, different points on the efficiency map could be used to design an optimal motor for a given drive cycle.

References

ABB (2012). SynRM motor and drive package, Motor Summit 2012.

ABB (2016). Low Voltage IE4 Synchronous Reluctance Motors.

Audet, C. and Dennis Jr, J. E. (2002). Analysis of generalized pattern searches. *SIAM Journal on Optimization*, 13(3):889–903.

Baranyai, M., Mosavi, A., Vajda, I., and Varkonyi-Koczy, A. R. (2017). Optimal design of electrical machines: State of the art survey. In *International Conference on Global Research and Education*, pages 209–216. Springer.

Barcaro, M., Meneghetti, G., and Bianchi, N. (2014). Structural analysis of the interior PM rotor considering both static and fatigue loading. *IEEE Transactions on Industry Applications*, 50(1):253–260.

Bianchi, N. (2013). Synchronous reluctance and interior permanent magnet motors. In *IEEE Workshop on Electrical Machines Design Control and Diagnosis (WEMDCD)*, pages 75–84. IEEE.

Bianchi, N., Fornasiero, E., Ferrari, M., and Castiello, M. (2014). Experimental comparison of PM assisted synchronous reluctance motors. In *IEEE Energy Conversion Congress and Exposition (ECCE)*, pages 4499–4506. IEEE.

Boglietti, A., Cavagnino, A., Pastorelli, M., and Vagati, A. (2005). Experimental comparison of induction and synchronous reluctance motors performance. In *40th IEEE Industry Applications Annual Meeting*, pages 474–479. IEEE.

Boglietti, A., Cavagnino, A., Staton, D., Shanel, M., Mueller, M., and Mejuto, C. (2009). Evolution and modern approaches for thermal analysis of electrical machines. *IEEE Transactions on industrial electronics*, 56(3):871–882.

Boglietti, A., El-Refaie, A. M., Drubel, O., Omekanda, A. M., Bianchi, N., Agamloh, E. B., Popescu, M., Di Gerlando, A., and Bartolo, J. B. (2014). Electrical machine topologies: Hottest topics in the electrical machine research community. *IEEE Industrial Electronics Magazine*, 8(2):18–30.

Boldea, I., Tutelea, L. N., Parsa, L., and Dorrell, D. (2014). Automotive electric propulsion systems with reduced or no permanent magnets: An overview. *IEEE Transactions on Industrial Electronics*, 61(10):5696–5711.

Boyd, S. and Vandenberghe, L. (2004). *Convex Optimization*. Cambridge University Press.

Bracikowski, N., Hecquet, M., Brochet, P., and Shirinskii, S. V. (2012). Multiphysics modeling of a permanent magnet synchronous machine by using lumped models. *IEEE Transactions on Industrial Electronics*, 59(6):2426–2437.

Bramerdorfer, G., Zăvoianu, A.-C., Silber, S., Lughofer, E., and Amrhein, W. (2016). Possibilities for Speeding Up the FE-Based Optimization of Electrical Machines—A Case Study. *IEEE Transactions on Industry Applications*, 52(6):4668–4677.

Brent, R. P. (2013). *Algorithms for minimization without derivatives*. Courier Corporation.

Cai, S., Jin, M.-J., Hao, H., and Shen, J.-X. (2016). Comparative study on synchronous reluctance and PM machines. *International Journal for Computation and Mathemathics and Electrical and Electronic Engineering*, 35(2):607–623.

Chan, C. and Chau, K. (1991). Design of electrical machines by the finite element method using distributed computing. *Computers in industry*, 17(4):367–374.

Chapman, S. J. (2005). *Electric Machinery Fundamentals*. McGraw-Hill, 4th edition.

Chauvicourt, F. (2018). *Vibro-acoustics of rotating electric machines*. PhD thesis, Université Libre de Bruxelles.

Cohen, P., West, S. G., and Aiken, L. S. (2014). *Applied multiple regression/correlation analysis for the behavioral sciences*. Psychology Press.

Degano, M., DiNardo, M., Galea, M., Gerada, C., and Gerada, D. (2016). Global design optimization strategy of a synchronous reluctance machine for light electric vehicles. In *8th IET International Conference on Power Electronics, Machines and Drives (PEMD)*, pages 1–5. IET.

Dlala, E., Solveson, M., Stanton, S., Tang, Z., Christini, M., Ong, R., and Peaslee, B. (2013). Efficiency map simulations for an interior PM motor with experimental comparison and investigation of magnet size reduction. In *IEEE International Electric Machines & Drives Conference (IEMDC)*, pages 23–29. IEEE.

Dorrell, D. G. (2014). A review of the methods for improving the efficiency of drive motors to meet IE4 efficiency standards. *Journal of Power Electronics*, 14(5):842–851.

Dziechciarz, A., Oprea, C., and Martis, C. (2016). Multi-physics design of synchronous reluctance machine for high speed applications. In *42nd Annual Conference of the IEEE Industrial Electronics Society (IECON)*, pages 1704–1709. IEEE.

Ede, J. D., Zhu, Z., and Howe, D. (2002). Rotor resonances of high-speed permanent-magnet brushless machines. *IEEE Transactions on Industry Applications*, 38(6):1542–1548.

Ehsani, M., Gao, Y., and Emadi, A. (2009). *Modern electric, hybrid electric, and fuel cell vehicles: fundamentals, theory, and design*. CRC press, 2nd edition.

Fatemi, A., Demerdash, N. A., Nehl, T. W., and Ionel, D. M. (2016a). Large-scale design optimization of pm machines over a target operating cycle. *IEEE Transactions on Industry Applications*, 52(5):3772–3782.

Fatemi, A., Ionel, D. M., Demerdash, N. A., and Nehl, T. W. (2016b). Optimal Design of IPM Motors With Different Cooling Systems and Winding Configurations. *IEEE Transactions on Industry Applications*, 52(4):3041–3049.

Freitas, A. R., Fleming, P. J., and Guimaraes, F. G. (2013). A non-parametric harmony-based objective reduction method for many-objective optimization. In *IEEE International Conference on Systems, Man, and Cybernetics (SMC)*, pages 651–656. IEEE.

Fukami, T., Momiyama, M., Shima, K., Hanaoka, R., and Takata, S. (2008). Steady-state analysis of a dual-winding reluctance generator with a multiple-barrier rotor. *IEEE Transactions on Energy Conversion*, 23(2):492–498.

Gai, K. and Li, S. (2012). Towards cloud computing: a literature review on cloud computing and its development trends. In *4th International Conference on Multimedia Information Networking and Security (MINES)*, pages 142–146. IEEE.

Ghorbanian, V. (2018). *An HPC-based Data-driven Approach to System-level Design Process for Integrated Motor-Drive Systems*. PhD thesis, McGill University, Department of Electrical and Computer Engineering, Canada.

Ghorbanian, V., Hussain, S., Hamidzadeh, S., Chromik, R., and Lowther, D. (2018a). The role of temperature-dependent material properties in optimizing the design of permanent magnet motors. *IEEE Transactions on Magnetics*, 54(3):1–4.

Ghorbanian, V. and Lowther, D. (2017). A statistical solution to efficiently optimize the design of an inverter-fed permanent-magnet motor. *IEEE Transactions on Industry Applications*, 53(6):5315–5326.

Ghorbanian, V., Salimi, A., and Lowther, D. (2018b). A computer-aided design process for optimizing the size of inverter-fed permanent magnet motors. *IEEE Transactions on Industrial Electronics*, 65(2):1819–1827.

Giancoli, D. C. (2004). *Physics: Principles with applications*. Pearson, 6th edition.

Gieras, J. F., Wang, C., Joseph, C. L., and Ertugrul, N. (2007). Analytical prediction of noise of magnetic origin produced by permanent magnet brushless motors. In *IEEE International Electric Machines & Drives Conference (IEMDC)*, pages 148–152. IEEE.

Gieras, J. F., Wang, C., and Lai, J. C. (2005). *Noise of polyphase electric motors*. CRC press.

Giurgea, S., Zire, H., and Miraoui, A. (2007). Two-stage surrogate model for finite-element-based optimization of permanent-magnet synchronous motor. *IEEE Transactions on Magnetics*, 43(9):3607–3613.

Gope, D., Jandhyala, V., Wang, X., Macmillen, D., Camposano, R., Chakraborty, S., Pingenot, J., and Williams, D. (2011). Towards system-level electromagnetic field simulation on computing clouds. In *20th IEEE Conference on Electrical Performance of Electronic Packaging and Systems (EPEPS)*, pages 167–170. IEEE.

Goss, J., Wrobel, R., Mellor, P., and Staton, D. (2013). The design of AC permanent magnet motors for electric vehicles: A design methodology. In *IEEE International Electric Machines Drives Conference (IEMDC)*, pages 871–878. IEEE.

Haataja, J. (2003). *A comparative performance study of four-pole induction motors and synchronous reluctance motors in variable speed drives*. PhD thesis, Lappeenranta University of Technology, Finland.

Hamidizadeh, S. (2016). Study of magnetic properties and demagnetization models of permanent magnets for electric vehicles application. Master's thesis, McGill University, Department of Mining and Materials, Canada.

Hendershot, J. R. and Miller, T. J. E. (2010). *Design of brushless permanent-magnet machines*. Motor Design Books, 2nd edition.

Howard, E. and Kamper, M. J. (2016). Weighted Factor Multiobjective Design Optimization of a Reluctance Synchronous Machine. *IEEE Transactions on Industry Applications*, 52(3):2269–2279.

Howard, E., Kamper, M. J., and Gerber, S. (2015). Asymmetric flux barrier and skew design optimization of reluctance synchronous machines. *IEEE Transactions on Industry Applications*, 51(5):3751–3760.

Hudák, P., Hrabovcová, V., and Rafajdus, P. (2006). Geometrical dimension influence of multi-barrier rotor on reluctance synchronous motor performances. In *International Symposium on Power Electronics, Electrical Drives, Automation and Motion (SPEEDAM)*, pages 346–351. IEEE.

Hussain, S. (2017). *Development of Advanced Material Models for the Simulation of Low Frequency Electromagnetic Devices*. PhD thesis, McGill University, Department of Electrical and Computer Engineering, Canada.

Hussain, S., Mohammadi, M. H., Sidhu, K. S., and Lowther, D. A. (2017). Effects of PWM Excitations on Iron Loss in Electrical Steels and Machines. In *IEEE Industry Applications Annual Meeting*. IEEE.

International Efficiency Commission (2016). Efficiency classes of variable speed AC motors (IE-code). Standard, International Organization for Standardization.

International Energy Agency (2016). *World Energy Outlook 2016*. International Energy Agency.

Islam, M. S., Islam, R., and Sebastian, T. (2014). Noise and vibration characteristics of permanent-magnet synchronous motors using electromagnetic and structural analyses. *IEEE Transactions on Industry Applications*, 50(5):3214–3222.

Islam, R. and Husain, I. (2009). Analytical model for predicting noise and vibration in permanent magnet synchronous motors. In *IEEE Energy Conversion Congress and Exposition (ECCE)*, pages 3461–3468. IEEE.

Jahns, T. M. (1987). Flux-weakening regime operation of an interior permanent-magnet synchronous motor drive. *IEEE Transactions on Industry Applications*, 23(4):681–689.

Jiang, W. (2014). *Coupled Electromagnetic/Thermal Machine Design Optimization Based on Finite Element Analysis Using High-Throughput Computing*. PhD thesis, University of Wisconsin-Madison.

Jiang, W. and Jahns, T. (2013). Development of efficient electromagnetic-thermal coupled model of electric machines based on finite element analysis. In *IEEE International Electric Machines & Drives Conference (IEMDC)*, pages 816–823. IEEE.

Jiang, W. and Jahns, T. (2014). Coupled electromagnetic/thermal machine design optimization based on finite element analysis with application of artificial neural network. In *IEEE Energy Conversion Congress and Exposition (ECCE)*, pages 5160–5167. IEEE.

Jiang, W., Jahns, T., Lipo, T., Taylor, W., and Suzuki, Y. (2012). Machine design optimization based on finite element analysis in a high-throughput computing environment. In *IEEE Energy Conversion Congress and Exposition (ECCE)*, pages 869–876. IEEE.

Jin, J.-M. (2015). *The finite element method in electromagnetics*. John Wiley & Sons, 3rd edition.

Jurecka, F. (2007). *Robust design optimization based on metamodeling techniques*. PhD thesis, Technische Universität München, Germany.

Jurkovic, S., Rahman, K., Bae, B., Patel, N., and Savagian, P. (2015). Next generation Chevy Volt electric machines; design, optimization and control for performance and rare-earth mitigation. In *IEEE Energy Conversion Congress and Exposition (ECCE)*, pages 5219–5226. IEEE.

Kalyanmoy, D. (2001). *Multi objective optimization using evolutionary algorithms*. John Wiley and Sons.

Keyes, D. E., McInnes, L. C., Woodward, C., Gropp, W., Myra, E., Pernice, M., Bell, J., Brown, J., Clo, A., Connors, J., et al. (2013). Multiphysics simulations: Challenges and opportunities. *The International Journal of High Performance Computing Applications*, 27(1):4–83.

Kolehmainen, J. (2010). Synchronous reluctance motor with form blocked rotor. *IEEE Transactions on Energy Conversion*, 25(2):450–456.

Kostko, J. (1923). Polyphase reaction synchronous motors. *Journal of the American Institute of Electrical Engineers*, 42(11):1162–1168.

Krause, P. C., Wasynczuk, O., and Pekarek, S. D. (2012). *Electromechanical motion devices*. John Wiley & Sons, 2nd edition.

Le Besnerais, J. (2016). Fast prediction of variable-speed acoustic noise due to magnetic forces in electrical machines. In *XXII International Conference Electrical Machines (ICEM)*, pages 2259–2265. IEEE.

Li, M., Mohammadi, M. H., Rahman, T., and Lowther, D. A. (2017). Analysis and design of electrical machines with material uncertainties in iron and permanent magnet. *International Journal for Computation and Mathemathics and Electrical and Electronic Engineering*, 36(5):1326–1337.

Lipo, T. A. (1991). Synchronous reluctance machines-a viable alternative for AC drives? *Electric Machines and Power Systems*, 19(6):659–671.

Lowther, D. A. and Silvester, P. P. (1986). *Computer-aided design in magnetics*. Springer-Verlag.

Lu, C., Ferrari, S., and Pellegrino, G. (2017). Two Design Procedures for PM Synchronous Machines for Electric Powertrains. *IEEE Transactions on Transportation Electrification*, 3(1):98–107.

Mahmoudi, A., Soong, W. L., Pellegrino, G., and Armando, E. (2015). Efficiency maps of electrical machines. In *IEEE Energy Conversion Congress and Exposition (ECCE)*, pages 2791–2799. IEEE.

Matsuo, T. and Lipo, T. A. (1994). Rotor design optimization of synchronous reluctance machine. *IEEE Transactions on Energy Conversion*, 9(2):359–365.

Maxwell, J. C. (1881). *A treatise on electricity and magnetism*, volume 1. Clarendon press.

McCoy, G. and Douglass, J. (2014). Premium Efficiency Motor Selection and Application Guide. *US Department of Energy's Office of Energy Efficiency and Renewable Energy*.

McIntosh, S., Kamei, Y., Adams, B., and Hassan, A. E. (2016). An empirical study of the impact of modern code review practices on software quality. *Empirical Software Engineering*, 21(5):2146–2189.

Mellor, P., Roberts, D., and Turner, D. (1991). Lumped parameter thermal model for electrical machines of tefc design. *IEE Proceedings B (Electric Power Applications)*, 138(5):205–218.

Mentor-Infolytica Corporation (2018). *MotorSolve BLDC: 2D/3D Electromagnetic Field Simulation Software*. Mentor-Infolytica Corporation, Montréal, Canada.

Miao, Y., Preindl, M., Ge, H., Cheng, B., and Emadi, A. (2016). MTPA fitting and torque estimation technique based on a new flux-linkage model for interior permanent magnet synchronous machines. In *IEEE Transportation Electrification Conference and Expo (ITEC)*, pages 1–6. IEEE.

Microsoft Azure (2018). *Sizes for Windows Virtual Machines in Azure*. Microsoft Corporation.

Moghaddam, R. R. (2007). Synchronous reluctance machine (SynRM) design. Master's thesis, Royal Institute of Technology, Department of Electrical Engineering, Electrical Machines and Power electronics, Stockholm.

Mohammadi, M. H. (2015). Rotor Design Optimization of Permanent Magnet–Assisted Synchronous Reluctance Machines for Traction Applications. Master's thesis, McGill University, Department of Electrical and Computer Engineering, Canada.

Mohammadi, M. H., Ghorbanian, V., and Lowther, D. A. (2018a). A Data-Driven Approach for Design Knowledge Extraction of Synchronous Reluctance Machines using Multi-Physical Analysis. In *XXIII International Conference Electrical Machines (ICEM)*, pages 479–485. IEEE.

Mohammadi, M. H. and Lowther, D. A. (2017). A Computational Study of Efficiency Map Calculation for Synchronous AC Motor Drives including Cross-Coupling and Saturation Effects. *IEEE Transactions on Magnetics*, 53(6).

Mohammadi, M. H., Rahman, T., and Lowther, D. A. (2017a). Restricting the Design Space of Multiple-Barrier Rotors of Synchronous Reluctance Machines. *International Journal for Computation and Mathemathics and Electrical and Electronic Engineering*, 36(5):1338–1350.

Mohammadi, M. H., Rahman, T., Silva, R., Li, M., and Lowther, D. A. (2016). A Computationally Efficient Algorithm for Rotor Design Optimization of Synchronous Reluctance Machines. *IEEE Transactions on Magnetics*, 52(3).

Mohammadi, M. H., Rahman, T., Silva, R. C. P., Wang, B., Chang, K., and Lowther, D. A. (2018b). Effect of Acoustic Noise on Optimal SynRM Design Regions. *IEEE Transactions on Magnetics*, 54(3).

Mohammadi, M. H., Silva, R. C. P., and Lowther, D. A. (2017b). Finding Optimal Performance Indices of Synchronous AC Motors. *IEEE Transactions on Magnetics*, 53(6).

Mohammadi, M. H., Silva, R. C. P., and Lowther, D. A. (2018c). Incorporating Control Strategies Into the Optimization of Synchronous AC Machines: A Comparison of Methodologies. *IEEE Transactions on Magnetics*, 54(3).

Mohan, N. and Undeland, T. M. (2007). *Power electronics: converters, applications, and design*. John Wiley & Sons, 3rd edition.

Morimoto, S., Sanada, M., and Takeda, Y. (2001). Performance of PM-assisted synchronous reluctance motor for high-efficiency and wide constant-power operation. *IEEE Transactions on Industry Applications*, 37(5):1234–1240.

Motorsolver (2015). *IPM PM-AC Synchronous Motor*. Motorsolver, USA.

Niazi, P. (2006). *Permanent magnet assisted synchronous reluctance motor, design and performance improvement*. PhD thesis, Texas A&M University.

Olszewski, M. et al. (2011). Evaluation of the 2010 Toyota Prius hybrid synergy drive system. *Oak Ridge Nat. Lab., US Dept. Energy*.

Ooi, S., Morimoto, S., Sanada, M., and Inoue, Y. (2013). Performance evaluation of a high-power-density PMa-SynRM with ferrite magnets. *IEEE Transactions on Industry Applications*, 49(3):1308–1315.

Park, J. M., Kim, S. I., Hong, J. P., and Lee, J. H. (2006). Rotor design on torque ripple reduction for a synchronous reluctance motor with concentrated winding using response surface methodology. *IEEE Transactions on Magnetics*, 42(10):3479–3481.

Park, J.-S. (1994). Optimal latin-hypercube designs for computer experiments. *Journal of statistical planning and inference*, 39(1):95–111.

Park, R. H. (1929). Two-reaction theory of synchronous machines generalized method of analysis-Part I. *Transactions of the American Institute of Electrical Engineers*, 48(3):716–727.

Pearson, K. (1896). Mathematical contributions to the theory of evolution. iii. regression, heredity, and panmixia. *Philosophical Transactions of the Royal Society of London. Series A, containing papers of a mathematical or physical character*, 187:253–318.

Pellegrino, G., Cupertino, F., and Gerada, C. (2013). Barriers shapes and minimum set of rotor parameters in the automated design of synchronous reluctance machines. In *IEEE International Electric Machines & Drives Conference (IEMDC)*, pages 1204–1210. IEEE.

Pellegrino, G., Cupertino, F., and Gerada, C. (2015). Automatic design of synchronous reluctance motors focusing on barrier shape optimization. *IEEE Transactions on Industry Applications*, 51(2):1465–1474.

Pyrhonen, J., Jokinen, T., and Hrabovcova, V. (2009). *Design of rotating electrical machines*. John Wiley & Sons.

Rahman, T., Mohammadi, M. H., Humphries, K., and Lowther, D. A. (2017). Comparison of Fractional Slot Concentrated Winding and PM Assisted Synchronous Reluctance Motors for Class IV Electric Vehicles. In *IEEE International Electric Machines and Drives Conference (IEMDC)*. IEEE.

Rahman, T., Silva, R. C. P., Humphries, K., Mohammadi, M. H., and Lowther, D. A. (2016). Design and optimization of fractional slot concentrated winding permanent magnet machines for class IV electric vehicles. In *IEEE Transportation Electrification Conference and Expo (ITEC)*.

Risticevic, M., Iles, D., and Moeckel, A. (2016). Design of an interior permanent magnet synchronous motor supported by the topology optimization algorithm. In *International Symposium on Power Electronics, Electrical Drives, Automation and Motion (SPEEDAM)*, pages 221–225. IEEE.

Rosu, M., Zhou, P., Lin, D., Ionel, D. M., Popescu, M., Blaabjerg, F., Rallabandi, V., and Staton, D. (2017). *Multiphysics Simulation by Design for Electrical Machines, Power Electronics and Drives*, volume 66. John Wiley & Sons.

Saleem, A. (2018). *Effect of manufacturing on microstructure and magnetic properties of non-oriented electrical steel*. PhD thesis, McGill University, Department of Mining and Materials, Canada.

Salimi, A. (2018). *Computer-aided design of electrical machines: the role of robustness and application of statistical analysis techniques in multi-objective design optimization*. PhD thesis, McGill University, Department of Electrical and Computer Engineering, Canada.

Sanada, M., Hiramoto, K., Morimoto, S., and Takeda, Y. (2004). Torque ripple improvement for synchronous reluctance motor using asymmetric flux barrier arrangement. *IEEE Transactions on Industry Applications*, 40(4):1076–1082.

Sarikhani, A. and Mohammed, O. (2014). A multi-physics multi-objective optimal design approach of PM synchronous machines. In *International Conference on Electrical Machines (ICEM)*, pages 968–974. IEEE.

Siemens PLM Software Inc. (2018). *NX Nastran*. Siemens PLM Software Inc.

Silva, R. C. P. (2018). *Surrogate problem evaluation and selection for optimization with expensive function evaluations*. PhD thesis, McGill University, Department of Electrical and Computer Engineering, Canada.

Silva, R. C. P., Rahman, T., Mohammadi, M. H., and Lowther, D. A. (2018). Multiple operating points based optimization: Application to fractional slot concentrated winding electric motors. *IEEE Transactions on Industrial Electronics*, 65(2):1719–1727.

Silvester, P. P. and Ferrari, R. L. (1996). *Finite elements for electrical engineers*. Cambridge University Press, 3rd edition.

Simpson, N. and Mellor, P. (2015). Exploiting cloud computing in the multi-physics design and optimisation of electromagnetic devices. In *16th IEEE Workshop on Control and Modeling for Power Electronics (COMPEL)*. IEEE.

Sizov, G. Y., Zhang, P., Ionel, D. M., Demerdash, N. A., and Rosu, M. (2013). Automated multi-objective design optimization of PM AC machines using computationally efficient FEA and differential evolution. *IEEE Transactions on Industry Applications*, 49(5):2086–2096.

Smith, B. (2012a). 16x Speedup in ANSYS Maxwell DSO on 32-core High-Performance Compute Farm Doubles Traction Motor Design Productivity at General Motors. *ANSYS White Paper*.

Smith, B. (2012b). Charging Simulation with HPC. *ANSYS Advantage*, VI(3).

Soong, W. L. and Miller, T. (1994). Field-weakening performance of brushless synchronous AC motor drives. *IEE Proceedings-Electric Power Applications*, 141(6):331–340.

Soong, W. L., Staton, D. A., and Miller, T. J. (1995). Design of a new axially-laminated interior permanent magnet motor. *IEEE Transactions on Industry Applications*, 31(2):358–367.

Spearman, C. (1904). The proof and measurement of association between two things. *The American journal of psychology*, 15(1):72–101.

Specht, D. F. (1991). A general regression neural network. *IEEE Transactions on Neural Networks*, 2(6):568–576.

Staton, D. (2005). Motor-CAD V2. *Motor Design Ltd*.

Staton, D. A. and Cavagnino, A. (2008). Convection heat transfer and flow calculations suitable for electric machines thermal models. *IEEE Transactions on Industrial Electronics*, 55(10):3509–3516.

Staton, D. A., Miller, T. J. E., and Wood, S. E. (1993). Maximising the saliency ratio of the synchronous reluctance motor. *IEE Proceedings B-Electric Power Applications*, 140(4):249–259.

Stipetic, S. and Goss, J. (2016). Calculation of efficiency maps using scalable saturated flux-linkage and loss model of a synchronous motor. In *XXII International Conference on Electrical Machines (ICEM)*, pages 1380–1386. IEEE.

Taghavi, S. and Pillay, P. (2014). A sizing methodology of the synchronous reluctance motor for traction applications. *IEEE Journal of Emerging and Selected Topics in Power Electronics*, 2(2):329–340.

Taghavi, S. and Pillay, P. (2015). A mechanically robust rotor with transverse laminations for a wide-speed-range synchronous reluctance traction motor. *IEEE Transactions on Industry Applications*, 51(6):4404–4414.

Tariq, A. R., Nino-Baron, C. E., and Strangas, E. G. (2010). Iron and magnet losses and torque calculation of interior permanent magnet synchronous machines using magnetic equivalent circuit. *IEEE Transactions on Magnetics*, 46(12):4073–4080.

Torregrossa, D., Peyraut, F., Fahimi, B., M'Boua, J., and Miraoui, A. (2011). Multiphysics finite-element modeling for vibration and acoustic analysis of permanent magnet synchronous machine. *IEEE Transactions on Energy Conversion*, 26(2):490–500.

US Department of Energy (2010). Multi-Year Program Plan 2011 - 2015.

US Department of Energy (2011). Annual energy review. *Energy Information Administration, US Department of Energy: Washington, DC.*

Vagati, A., Boazzo, B., Guglielmi, P., and Pellegrino, G. (2014). Design of ferrite-assisted synchronous reluctance machines robust toward demagnetization. *IEEE Transactions on Industry Applications*, 50(3):1768–1779.

Vagati, A., Pastorelli, M., Francheschini, G., and Petrache, S. C. (1998). Design of low-torque-ripple synchronous reluctance motors. *IEEE Transactions on Industry Applications*, 34(4):758–765.

Vartanian, R. and Toliyat, H. A. (2009). Design and comparison of an optimized permanent magnet-assisted synchronous reluctance motor (PMa-SynRM) with an induction motor with identical NEMA Frame stators. In *IEEE Electric Ship Technologies Symposium (ESTS)*, pages 107–112. IEEE.

Ver, I. L. and Beranek, L. L. (2006). *Noise and Vibration Control Engineering: Principles and Applications*. John Wiley and Sons.

Vijayraghavan, P. and Krishnan, R. (1998). Noise in electric machines: A review. In *33rd IEEE Industry Applications Society Annual Meeting*, pages 251–258. IEEE.

Wang, B. (2017). A neural network based analytical model for predicting acoustic noise in synchronous reluctance motors. Master's thesis, McGill University, Department of Electrical and Computer Engineering, Canada.

Wang, Y., Ionel, D. M., Rallabandi, V., Jiang, M., and Stretz, S. J. (2016). Large-Scale Optimization of Synchronous Reluctance Machines Using CE-FEA and Differential Evolution. *IEEE Transactions on Industry Applications*, 52(6):4699–4709.

Wang, Y., Ionel, D. M., and Staton, D. (2015). Ultrafast steady-state multi-physics model for PM and synchronous reluctance machines. *IEEE Transactions on Industry Applications*, 51(5):3639–3646.

Yang, S. (1981). *Low-noise electrical motors*. Oxford University Press, USA.

Yang, Z., Shang, F., Brown, I. P., and Krishnamurthy, M. (2015). Comparative study of interior permanent magnet, induction, and switched reluctance motor drives for EV and HEV applications. *IEEE Transactions on Transportation Electrification*, 1(3):245–254.

Appendix A

Correlation Coefficients

Correlation coefficients are useful measures to show the correlation or statistical dependence between two variables X and Y which could be design parameters or performances. For example, if X and Y are positively correlated, an increased X value leads to an increase in Y, and vice versa. The same argument holds for decreasing values. For negative correlation, a decrease in X generally results in an increased Y value, and vice versa.

Hence, this appendix briefly defines two useful correlation coefficients, namely the Pearson and Spearman, and describes their similarities and differences with the help of examples. Other correlation coefficients such as the Kendall exist, but are not used in this thesis.

A.1 Pearson Correlation Coefficient

The Pearson correlation coefficient, denoted by ρ^P_{XY}, of two variables X and Y provides a measure of their linear correlation [Pearson, 1896]. Its values range from -1 to $+1$. A ρ^P_{XY} value of $+1$ indicates that X and Y have a strong positive linear correlation. On the other hand, a coefficient value of -1 signifies a strong negative linear correlation. The value of ρ^P_{XY} can be calculated using (A.1), where $\mathrm{cov}(X, Y)$ is the covariance of X and Y, and σ_X, σ_Y are the standard deviations of the two variables respectively. The covariance $\mathrm{cov}(X, Y)$ is computed using the expectation in (A.1), where μ_X, μ_Y are the means of X and Y.

$$\begin{aligned} \rho^P_{XY} &= \frac{\mathrm{cov}(X, Y)}{\sigma_X \sigma_Y} \\ \mathrm{cov}(X, Y) &= E\big[(X - \mu_X)(Y - \mu_Y)\big] \end{aligned} \tag{A.1}$$

A main assumption for using the Pearson coefficient is the linear relationship between X and Y. If the two variables are not linearly correlated, then ρ^P_{XY} does not offer a good correlation measure. Instead, the Spearman coefficient can be used as explained below.

A.2 Spearman Correlation Coefficient

For two variables X and Y, the Spearman correlation coefficient, ρ^S_{XY}, measures their rank correlation which effectively shows their monotonic relationship [Spearman, 1904]. This means that the Pearson requirement for linearity is not required for the Spearman. To calculate ρ^S_{XY}, the values of X and Y must first be individually ranked from smallest to largest resulting in their ranks r_X and r_Y respectively. Then, the Spearman coefficient is calculated using (A.2) which is similar to Pearson's formula in (A.1) with the exception of using ranks r_X and r_Y instead of X and Y.

$$\rho^S_{XY} = \frac{\mathrm{cov}(r_X, r_Y)}{\sigma_{r_X}\sigma_{r_Y}} \tag{A.2}$$

A.3 Comparison and Examples

The following examples demonstrate the similarities and differences of the Pearson ρ^P_{XY} and Spearman ρ^S_{XY}. For linear functions (whether positive or negative), both coefficients are observed to be the same in Fig. A.1, since the ranking of variables is preserved.

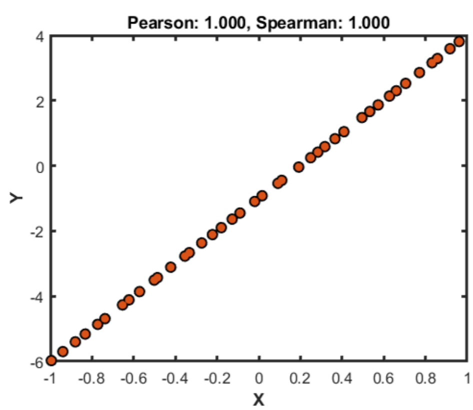

(a) $Y = 5X - 1$

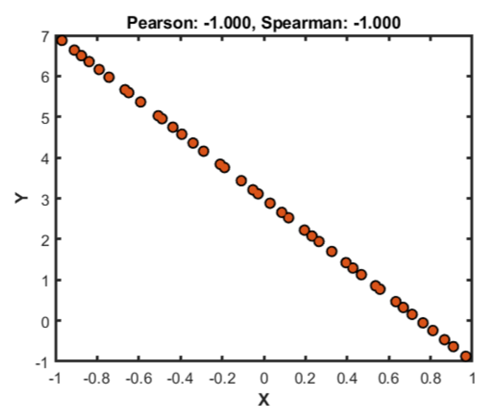

(b) $Y = -4X + 3$

Fig. A.1 Strong linear correlations between variables X and Y.

However, when the relationship between X and Y is not linear yet monotonic, then the Pearson ρ^P_{XY} suffers and produces values different from $+1$ and -1. This effect is more prominent when there are outliers in the studied dataset (i.e. Pearson ρ^P_{XY} is more sensitive to outliers). As shown in Fig. A.2, the Spearman ρ^S_{XY} are maintained at $+1$ and -1, since Y is monotonically increasing or decreasing with respect to X.

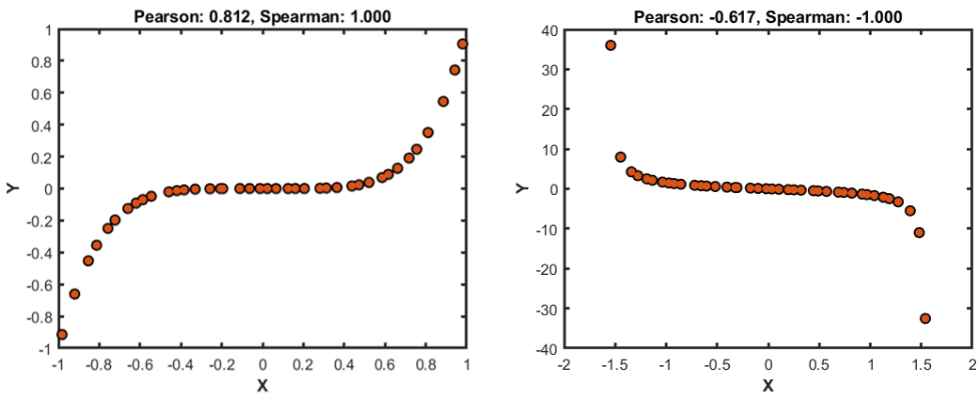

(a) $Y = X^5$ (b) $Y = \tan(X)$

Fig. A.2 Strong correlations between variables X and Y.

In Fig. A.3, both the Pearson ρ^P_{XY} and the Spearman ρ^S_{XY} are close to zero. This could mean that the relationship X and Y is random or non-existent as in Fig. A.3 (a). Otherwise, there could be a strong correlation as in Fig. A.3 (b) which neither coefficients can capture.

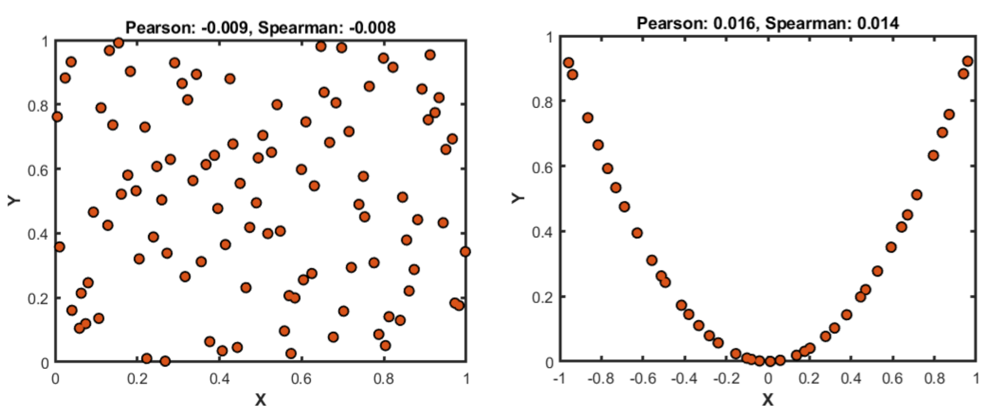

(a) Random independent sampling (b) $Y = X^2$

Fig. A.3 Weak correlations between variables X and Y.

Appendix B

Incorporating Control Strategies within Design Optimization

This appendix based on [Mohammadi et al., 2018c] presents a comparison of methodologies to incorporate control parameters into the design optimization of synchronous AC machines. A metric is used to quantify the conflict level between the average torque and torque ripple for an interior permanent magnet machine and a synchronous reluctance machine. Using 2-D finite element analysis simulations, the results demonstrate that the traditional approach of lumping the control and design variables together can lead to poor designs, especially when the conflict is high.

B.1 Introduction

In recent years, the design of synchronous AC machines, like synchronous reluctance and interior permanent magnet motors, has undergone significant improvement through optimization research. As discussed in previous works [Pellegrino et al., 2015; Freitas et al., 2013; Mohammadi et al., 2016], both discrete (e.g. number of slots or poles) or continuous (e.g. the width of tooth/flux barrier) variables are considered in a machine's initial sizing.

However, various performance indices (e.g. average torque, torque ripple) are required during an optimization procedure and, generally evaluated using FEA. Often, each index depends on control variables (e.g. for an applied control strategy) which adds more complexity to the existing optimization formulation. For instance, the Maximum-Torque-Per-Ampere control strategy of a synchronous AC machine defined by (B.1) finds the advance angle, γ, which maximizes the average torque, T_{avg}, for a fixed current magnitude below base speed.

$$\begin{aligned} \max_{\gamma}. \quad & T_{avg}(\gamma) \\ \text{s.t.} \quad & \gamma_l \leq \gamma \leq \gamma_u \end{aligned} \tag{B.1}$$

A general methodology was proposed in [Mohammadi et al., 2017b] to incorporate a motor control strategy, e.g. MTPA in (B.1), as a subproblem within an optimization framework. Using one γ value for all rotor designs may not yield accurate results due to the variation of dq inductances [Mohammadi et al., 2016]. Furthermore, the torque ripple, T_{rip}, as well as T_{avg} were improved when the MTPA strategy was used for a V-shaped IPM motor. Despite this positive outcome, it was noticed that the direct approach (i.e. simpler optimization without a control strategy but with γ added as an additional design variable) was superior to the proposed methodology for the 3-barrier SynRM.

To explain these results, it was hypothesized that T_{avg} and T_{rip} were not conflicting near the SynRM's initial design; i.e. minimizing T_{rip} implies maximizing T_{avg}. Hence, the outcome of SynRM shows that minimizing T_{rip} in terms of γ would incorporate the MTPA control strategy automatically. It also suggests that the two performances can be in harmony for some design regions which may permit using a computationally cheaper methodology instead. Moreover, using a direct approach as followed in [Pellegrino et al., 2015] and [Wang et al., 2016] may not always yield optimal designs for synchronous AC machines when motor control strategies are considered in the design optimization.

Therefore, this work extends the analysis presented in [Mohammadi et al., 2017b] by quantitatively measuring the conflict between T_{avg} and T_{rip} using the method presented in [Freitas et al., 2013] and testing the proposed methodology for different initial designs. The goal is to explain why and when the direct methodology works, which, in turn, would help to save computational time. Also, results in both IPM and SynRM optimization-related problems indicate that by using conflict analysis, the optimization's performance can be predicted within a local design region.

B.2 Methodology

Typically, the design optimization of any electrical machine involves two sets of variables; design variables, $\boldsymbol{x}$, that are set by the designer, and control variables, $\boldsymbol{c}$, which depend on the employed control strategy. In a direct optimization framework, both $\boldsymbol{x}$ and $\boldsymbol{c}$ are treated together as lumped variables to the global optimization as shown in Fig. B.1 (a). Conversely, in Fig. B.1 (b), a *control strategy emulator* (CSE) computes the optimal control parameters by solving a unidimensional problem such as (B.1). This becomes important during normal operation, because $\boldsymbol{c}$ may assume values which are completely different from the ones found by the optimization method. In this work, the *Golden search method with parabolic interpolation* (GSM), described in [Brent, 2013] is used as the CSE. This method showed superior performance over other deterministic ones in [Mohammadi et al., 2017b].

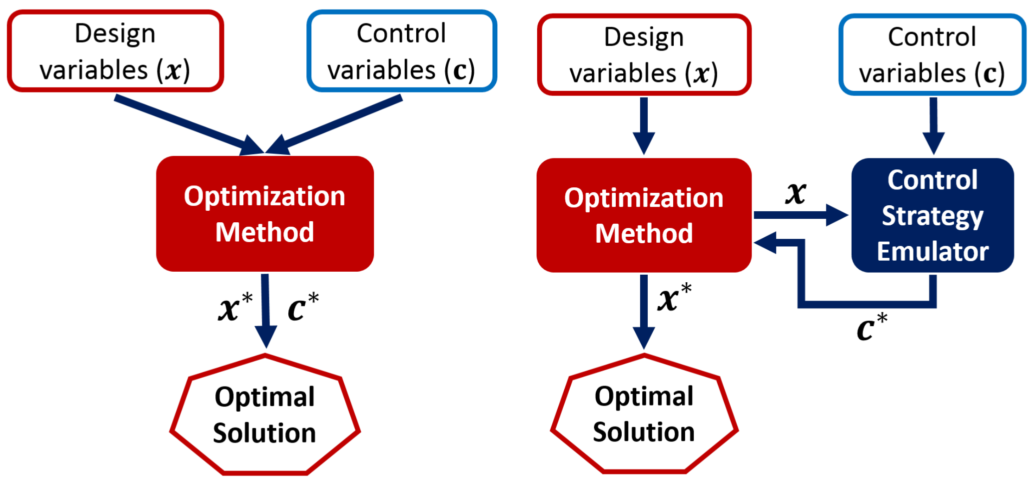

(a) (b)

Fig. B.1 Motor optimization methodology [Mohammadi et al., 2017b]. (a) Direct. (b) CSE-based.

Next, the procedure for computing the conflict level between T_{avg} and T_{rip} is described for an initial design, $\boldsymbol{x_0}$, of d dimensions. Within its neighborhood, $\boldsymbol{\Delta_0}$, a Latin hypercube sampling is performed to obtain its set of local samples, $\boldsymbol{X_0}$, as in (B.2). Here, n is the total number of local samples and $\Delta_{0_i} = x_{0_i} \times \Delta$. In this work, 300 local samples were used per initial design and the percentage deviation, Δ, is 20%. Fig. B.2 displays the procedure for a design with 2 variables, x_{0_1} and x_{0_2}.

$$\boldsymbol{X_0} = \{\boldsymbol{x_0}^{(1)}, ..., \boldsymbol{x_0}^{(n)}\} \tag{B.2}$$

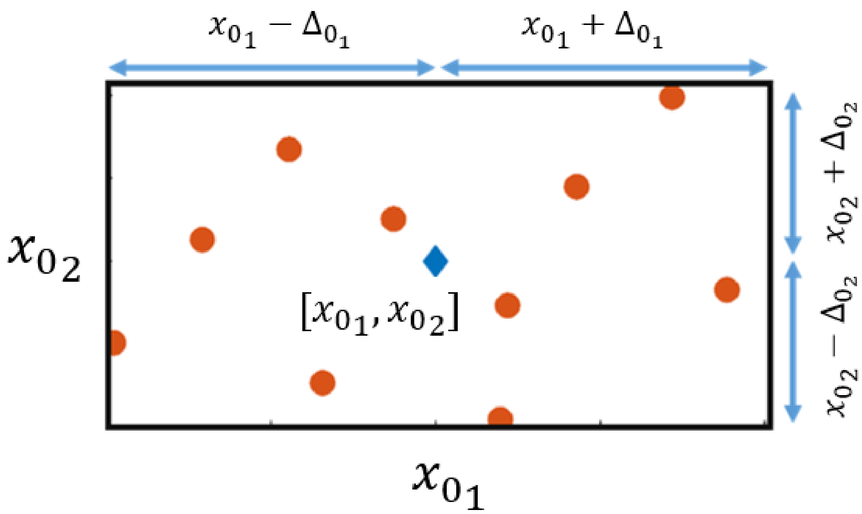

Fig. B.2 Local samples (●) about an initial point (♦) for conflict assessment.

After the local samples are chosen, a vector of performance values, $\boldsymbol{f_i}(\boldsymbol{x_0}^{(i)})$ comprised of (T_{avg},T_{rip}) for each local sample i, is constructed to form the set, $\boldsymbol{F} = \{\boldsymbol{f_1}, ..., \boldsymbol{f_n}\}$. The conflict between T_{avg} and T_{rip} is then estimated by the conflict measure, C_{ab}, proposed in [Freitas et al., 2013] and described by (B.3). Here, $R_{i,a}$ and $R_{i,b}$ are the associated ranks of sample $\boldsymbol{x_0}^{(i)}$ for T_{avg} and T_{rip} respectively. For example, $R_a = 1$ for the sample with highest T_{avg}, $R_b = 1$ for the sample with lowest T_{rip}, $R_a = 2$ for the sample with the second highest T_{avg}, and so on. By this measure, a 100% conflict means that one performance improves at the expense of another, while 0% signifies total harmony; i.e., an improvement in T_{avg} implies an improvement in T_{rip}. Any midway value implies a non-uniform tradeoff between the two performances over the design space.

$$C_{ab} = \frac{\sum_{i=1}^{n} |R_{i,a} - R_{i,b}|}{\sum_{i=1}^{n} |2i - n - 1|} \tag{B.3}$$

B.3 Problem Statement

Equations (B.4) and (B.5) define the optimization problems to be solved by the direct and CSE-based (i.e., MTPA in this chapter) methods, respectively. Here, T_{rip} is to be minimized and the vector of design variables $\boldsymbol{x}$ is restricted within the $\boldsymbol{\Delta_0}$ neighborhood about $\boldsymbol{x_0}$. This neighborhood constraint ensures physical feasibility as well as consistency between the optimization's design space and that used by the conflict measure.

Since optimal solutions may no longer achieve improved T_{avg} over the initial design, especially in regions of high conflict, the inequality constraint for T_{avg} guarantees non-negative values, i.e., motoring operation. Note that there is a significant difference among both formulations. For the direct approach in (B.4), γ is added as an extra design variable. On the other hand, the MTPA-based approach in (B.5) emulates the control strategy by finding its optimal γ_{MTPA} to maximize T_{avg} for a given current magnitude and $\boldsymbol{x}$. Other control strategies could be tackled in a similar manner.

$$\begin{aligned} \min_{\boldsymbol{x},\gamma}.\quad & T_{rip}(\boldsymbol{x},\gamma) \\ \text{s.t.}\quad & T_{avg}(\boldsymbol{x},\gamma) \geq 0 \\ & (\boldsymbol{x}-\boldsymbol{\Delta_0}) \leq \boldsymbol{x} \leq (\boldsymbol{x}+\boldsymbol{\Delta_0}) \end{aligned} \tag{B.4}$$

$$\begin{aligned} \min_{\boldsymbol{x}}.\quad & T_{rip}(\boldsymbol{x},\gamma) \\ \text{s.t.}\quad & \gamma_{\text{MTPA}} = \underset{\gamma_{\text{MTPA}}}{\operatorname{argmax}}(T_{avg}(\boldsymbol{x},\gamma)) \\ & T_{avg}(\boldsymbol{x},\gamma_{\text{MTPA}}) \geq 0 \\ & (\boldsymbol{x}-\boldsymbol{\Delta_0}) \leq \boldsymbol{x} \leq (\boldsymbol{x}+\boldsymbol{\Delta_0}) \end{aligned} \tag{B.5}$$

The V-shaped IPM motor described in [Motorsolver, 2015] and a 3-barrier SynRM (round-shaped barrier) are used as test cases. While both motors have a similar stator geometry and configuration shown in Table B.1, their rotors are geometrically different. Fig. B.3 show the rotor design variables. To ensure feasibility, the IPM's V-shaped layer and the SynRM's flux barriers are both constrained inside the rotor. The instantaneous torque waveform, $\boldsymbol{T}$, is computed for a fixed sinusoidal current excitation using transient 2-D FEA, which benefit from 4-pole and 3-phase periodicities to reduce computation time. Then, T_{rip} and T_{avg} are post-processed from $\boldsymbol{T}$ similar to that described in [Mohammadi et al., 2016].

Table B.1 Fixed Design Parameters of IPM and SynRM

Parameter	Value	Parameter	Value
Number of slots/poles	12/4	Airgap thickness	0.5 mm
Stator outer diameter	75 mm	RMS current density	10.0 A/mm^2
Rotor outer diameter	40 mm	Core material	M-19 29 Ga
Rotor inner diameter	11 mm	Magnet material	NdFeB 32/16
Stack length	34 mm	Barrier material	Air

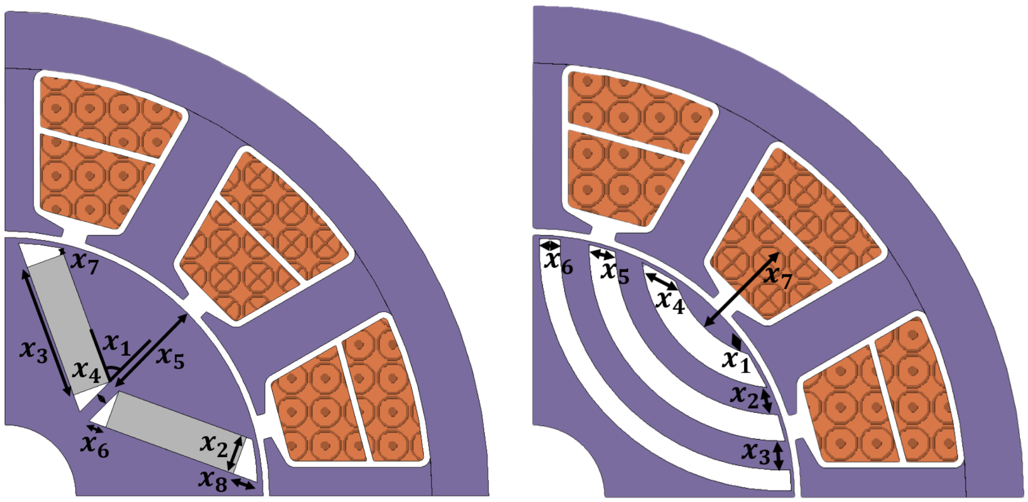

(a) (b)

Fig. B.3 Motor model cross sections. (a) IPM. (b) SynRM

B.4 Optimization Results

To assess the connection between the conflict and the performance of the two optimization methods, it was necessary to compare both methodologies for different initial points with various conflict levels. Hence, more than 15 initial base designs that are physically feasible were randomly chosen for the IPM and SynRM. Next, every design was optimized for T_{rip} based on the problems defined in (B.4) and (B.5) to compare the results of the direct and MTPA methodologies. Similar to [Mohammadi et al., 2017b], the pattern search method [Audet and Dennis Jr, 2002] was used as the main optimizer. Each design evaluation using a 2-D FEA simulation took about 10s on average for an Intel Core i7-3517U (quad core, 1.90 GHz) with 8 GB of RAM. Every MTPA calculation required around six FEA evaluations.

Table B.2 presents the final solution values of each motor in ascending order of the initial point's conflict level. Every row corresponds to one initial design, while the columns list the final values of T_{rip}, T_{avg}, and γ_{MTPA} of the two approaches. The base values of the initial samples are shown for comparison with the methods. The total number of FEA evaluations for the two methods are displayed as well. Hence, certain observations can be made based on the presented results. As expected, T_{avg} was forced to be compromised for high-conflict designs since T_{rip} is minimized. Interestingly, the MTPA converged to better solutions in 32 out of the 33 instances (∼97% success, shown by highlighted cells). Even when the levels of conflict are relatively low, the direct method is unable to converge to the true optimal solution (i.e., under MTPA control). Furthermore, the use of the direct approach can lead to solutions that are worse than the initial design when the conflict level is very high (shown in bold). This is especially noticeable for the SynRM example. In contrast, the MTPA approach is generally more robust to the level of conflict than the direct method.

Table B.2 Optimization Results for Each Design Sample (Direct, CSE PoV).

			T_{rip} [%]			T_{avg} [Nm]			γ_{MTPA} [°]		#FE Evaluations		Spearman ρ
	ID	Conflict	Base	MTPA	Direct	Base	MTPA	Direct	MTPA	Direct	MTPA	Direct	Direct
IPM	1	18.26%	81.264	59.181	75.111	0.391	0.673	0.343	47.10	51.07	5972	602	**-0.02**
	2	31.45%	80.115	63.069	68.908	1.394	1.470	1.753	37.36	35.02	6435	702	0.90
	3	33.94%	108.280	86.912	**111.817**	0.517	0.547	0.298	50.42	53.79	4543	720	**-0.74**
	4	44.29%	101.124	49.142	49.720	0.686	0.648	0.627	49.04	48.43	5660	674	0.94
	5	61.03%	61.986	44.871	56.821	0.966	1.182	1.446	40.75	39.75	5257	709	0.57
	6	68.11%	67.856	38.268	51.662	0.634	0.525	0.412	46.45	48.61	5630	718	0.36
	7	68.93%	86.975	28.213	66.440	1.103	0.626	1.440	48.62	42.71	4289	631	0.84
	8	69.18%	73.071	41.029	73.006	1.085	1.141	1.085	43.41	44.47	5751	3	N/A
	9	73.97%	79.371	21.756	69.876	0.159	0.174	0.026	56.04	61.30	3630	706	**-0.45**
	10	78.32%	68.606	52.222	**86.778**	0.568	0.523	0.423	46.37	44.62	5838	721	**-0.48**
	11	79.47%	93.377	34.937	52.167	0.754	0.393	0.836	53.05	46.43	4569	554	0.97
	12	79.87%	53.581	18.817	19.523	0.882	0.985	0.982	42.04	41.93	4461	350	0.59
	13	86.64%	85.942	14.353	35.867	0.705	0.590	0.641	51.74	47.91	3441	691	0.81
	14	88.70%	70.565	48.301	**99.024**	0.942	0.781	1.111	45.85	43.18	6077	723	**-0.72**
	15	89.12%	71.536	43.682	48.410	0.922	0.855	0.839	45.95	45.91	4788	669	0.24
	16	90.43%	81.269	24.907	33.329	0.781	0.464	0.765	49.60	45.96	4435	500	0.93
SynRM	1	13.04%	48.806	25.925	35.333	0.510	0.551	0.530	53.50	53.66	3941	678	0.79
	2	25.44%	46.687	34.021	55.457	0.430	0.463	0.393	54.41	53.25	4830	679	**-0.90**
	3	26.72%	46.232	18.796	32.354	0.817	0.837	0.835	55.62	55.62	4312	694	0.06
	4	28.29%	50.699	35.111	53.526	0.388	0.426	0.378	54.12	53.05	4816	684	0.24
	5	32.33%	113.182	73.443	93.951	0.667	0.695	0.613	50.07	48.18	4716	488	0.91
	6	45.34%	63.994	26.883	30.399	0.812	0.851	0.849	55.03	55.02	3171	698	0.64
	7	58.08%	38.949	13.001	19.206	0.487	0.523	0.507	55.62	55.29	4158	711	**-0.39**
	8	58.94%	29.089	14.248	26.189	0.484	0.487	0.493	55.28	55.62	4170	673	0.35
	9	67.02%	59.546	31.940	57.053	0.805	0.845	0.792	55.29	56.01	6883	699	0.76
	10	73.55%	27.920	15.899	27.856	0.491	0.487	0.458	55.62	55.20	6756	690	**-0.52**
	11	81.70%	60.737	53.380	**63.374**	0.757	0.742	0.746	55.99	56.29	5488	702	**-0.26**
	12	90.00%	39.336	34.031	38.350	0.444	0.442	0.425	54.29	54.00	2156	702	**-0.16**
	13	90.30%	43.419	35.034	38.794	0.447	0.432	0.424	54.07	53.91	2891	558	0.29
	14	91.98%	93.945	70.252	65.573	0.673	0.653	0.649	49.17	49.15	9718	512	0.98
	15	98.04%	34.211	25.777	**38.536**	0.578	0.555	0.575	53.59	54.03	11284	707	**-0.43**
	16	98.35%	39.467	27.307	**47.244**	0.577	0.553	0.579	53.64	54.05	4298	685	**-0.14**
	17	98.47%	37.183	25.158	**42.744**	0.572	0.553	0.572	53.41	53.78	9534	694	0.20

Fig. B.4 (a) and (b) shows the torque ripple convergence curves for one IPM and one SynRM design, respectively. The displayed trajectories include the MTPA, the direct from its own *point-of-view* (PoV) and the direct from the CSE's perspective. The CSE's perspective is generated by calculating the MTPA advance angle γ_{MTPA} using (B.1) to recompute T_{rip} for each solution generated by the direct method. This analysis shows that while the direct methodology "thinks" it reaches a lower T_{rip} solution, its CSE PoV could obtain worse results indicating that the direct method does not actually optimize for T_{rip}. However, this is not surprising since the CSE was not incorporated in the optimization formulation of (B.4). Moreover, the MTPA methodology performed better than its direct counterpart by improving T_{rip} in both examples and quickly arrives near the final solutions. In terms of the number of FEA evaluations, the MTPA methodology takes longer to reach its final solution. However, as observed from the convergence curves in Fig. B.4, the MTPA's trajectory settles near the final solution within 800 evaluations. Beyond this point, there is a minimal improvement in T_{rip}. Also, the Spearman rank coefficient ρ was calculated for each design between the two direct trajectories to show their level of association. For example, a -0.48 value for Fig. B.4 (a) demonstrates that the self PoV and CSE PoV trajectories of the direct methodology are negatively correlated since they affect T_{rip} in the opposite directions. Similarly, the Spearman ρ of each design was calculated in Table B.2 to determine how the direct methodology's path is affected by suboptimal advance angles (negative values shown in bold). From here onward and in Table B.2, the direct results only refer to the CSE PoV since the advance angle needs to be optimized for a given design.

To visually compare the MTPA and direct methodologies, Fig. B.5 displays two polar plots of the Trip improvement for the IPM and SynRM examples with every initial design's cross section shown. Each angle represents one sample design and a radial value signifies the Trip improvement of each approach from the base value. Since the improvement is to be maximized, the larger polar plot of the MTPA approach demonstrates its superiority over its direct counterpart, regardless of the initial design or conflict level.

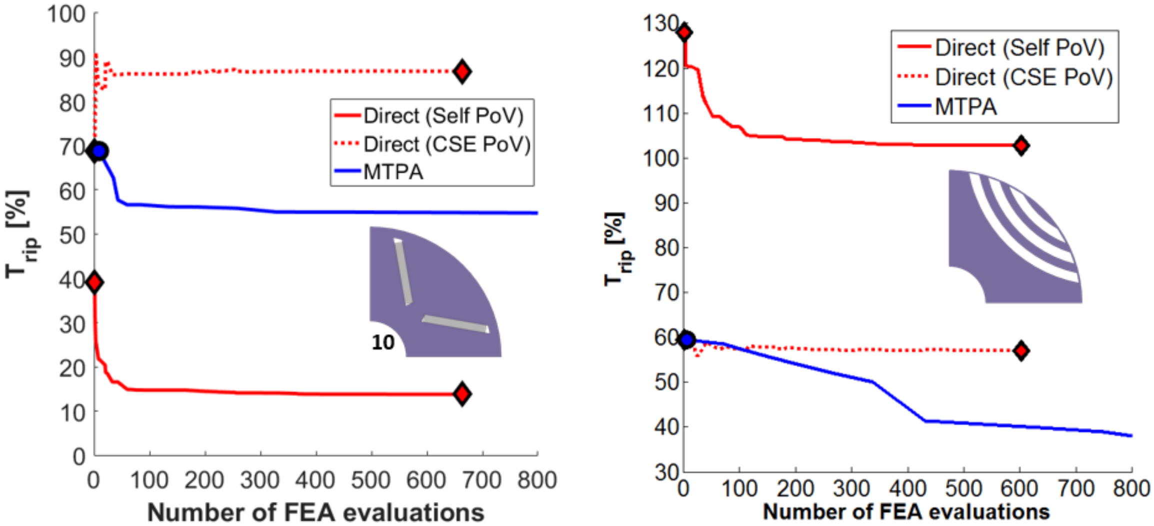

(a) (b)

Fig. B.4 Convergence curves for torque ripple [%]. (a) IPM (ID of 10, C_{ab} = 78.32%, ρ = -0.48). (b) SynRM (ID of 9, C_{ab} = 67.02%, ρ = +0.76). Refer to Table B.2 for ID number of each motor example.

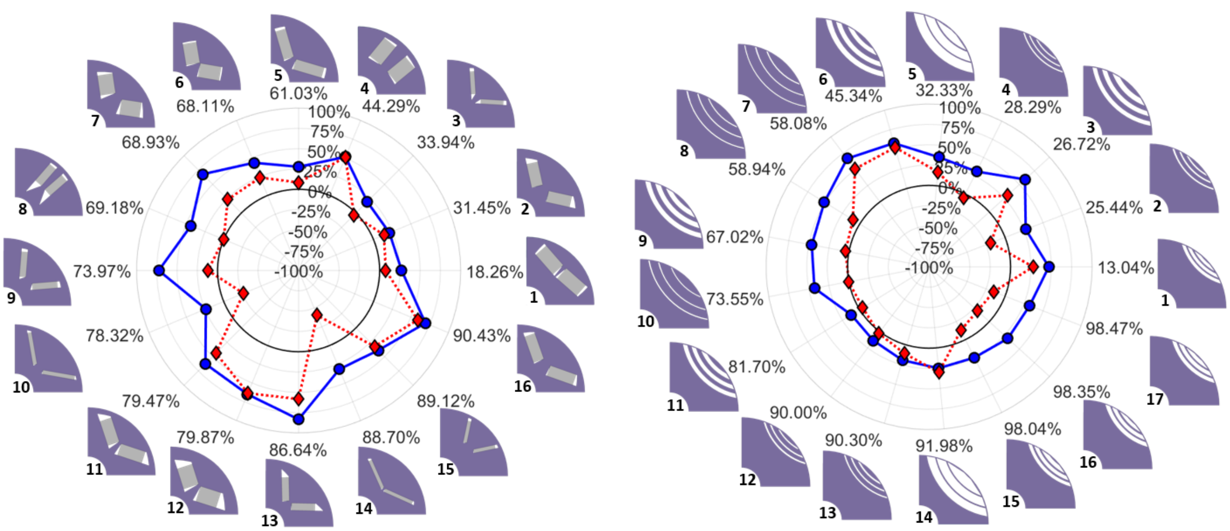

(a) (b)

Fig. B.5 Polar plots of the torque ripple improvement over the base values in ascending order of conflict. (a) IPM. (b) SynRM. Each initial design's cross section and ID is shown. The solid line (•) represents the MTPA methodology, while the dotted line (♦) represents the direct methodology (CSE PoV).

B.5 Conclusion

This appendix presented a detailed comparison of two different optimization methodologies using a quantitative measure of conflict. The torque ripple was minimized subject to a positive average torque constraint. Two different case studies were considered, namely, a V-shaped IPM motor and a three-barrier SynRM, where their rotor geometries were optimized while their stators were kept fixed. In total, more than 30 initial designs were used for testing. It was demonstrated that the CSE-based methodology, which incorporates the MTPA control strategy, generally performs better than a direct approach regardless of the conflict level, initial design, or motor case study. Also, the CSE-based approach can help users include the control variables, such as the current advance angle, in the main optimization procedure through an inner optimization loop. The displayed convergence curves of torque ripple indicate that the actual path taken by the direct methodology from the CSE PoV (normal operation) can be significantly different from what is expected. Therefore, the direct approach cannot be relied upon for the design optimization of synchronous ac motors due to its poor performance.

Appendix C

Efficiency Map Calculation for Synchronous AC Motors

After designing and optimizing an electric machine, efficiency maps are needed to predict a vehicle's performance in a dynamic simulation. Calculating efficiencies at various torque and speed points, however, requires prior knowledge of the input excitation conditions, such as the current magnitude and advance angle, in an electromagnetic finite-element analysis simulation. Hence, this appendix chapter based on [Mohammadi and Lowther, 2017] derives and uses nonlinear motor control equations (MTPA, FW, MTPV) in the study of efficiency map calculation while accounting for both saturation and cross-coupling effects. Two synchronous AC motors are considered in this work, including the 2010 Prius IPM and a PM-assisted synchronous reluctance machine, with all procedure steps outlined in detail. This procedure has been used to calculate the efficiency maps of PM machines and PM-assisted SynRMs ranging from 50 kW to 100 kW ratings in [Rahman et al., 2016, 2017].

C.1 Procedure

In this work, the computation of a motor's efficiency map follows the detailed procedure outlined in Algorithm 1. The employed variables are described below in Section C.2, while the described steps are illustrated in Section C.5 through an example.

Algorithm 1 Efficiency map calculation

Result: Efficiency map $\boldsymbol{\eta}^{\mathrm{FEA}}$ as a function of ($\boldsymbol{N}^{*}$,$\boldsymbol{T}_{em}^{\mathrm{FEA}}$)

1 **FEA Sampling**: compute ($\boldsymbol{\lambda}_{d}^{\mathrm{FEA}}$,$\boldsymbol{\lambda}_{q}^{\mathrm{FEA}}$) given ($\boldsymbol{I}_{s}^{\mathrm{FEA}}$,$\boldsymbol{\gamma}^{\mathrm{FEA}}$)

2 **Motor Characterization**: nonlinear least-squares curve fitting
Find $\lambda_{d/q}^{\mathrm{NL}}(\boldsymbol{I}_s)$ using ($\boldsymbol{\lambda}_{d/q}^{\mathrm{FEA}}$,$\boldsymbol{I}_{d}^{\mathrm{FEA}}$,$\boldsymbol{I}_{q}^{\mathrm{FEA}}$)
Find $I_{d/q}^{\mathrm{NL}}(\boldsymbol{\lambda}_s)$ using ($\boldsymbol{I}_{d/q}^{\mathrm{FEA}}$,$\boldsymbol{\lambda}_{d}^{\mathrm{FEA}}$,$\boldsymbol{\lambda}_{q}^{\mathrm{FEA}}$)

3 **Control Strategies**: for a given I_{s}^{MAX}
MTPA: calculate (I_{s}^{MTPA},γ^{MTPA}) & N_{Base}
FW: calculate ($\boldsymbol{N}^{\mathrm{FW}}$,$\boldsymbol{I}_{s}^{\mathrm{FW}}$,$\boldsymbol{\gamma}^{\mathrm{FW}}$)
MTPV: calculate ($\boldsymbol{N}^{\mathrm{MTPV}}$,$\boldsymbol{I}_{s}^{\mathrm{MTPV}}$,$\boldsymbol{\gamma}^{\mathrm{MTPV}}$)
Post-process ($\boldsymbol{N}^{*}$,$\boldsymbol{I}_{s}^{*}$,$\boldsymbol{\gamma}^{*}$) using **MTPA**, **FW**, **MTPV** values

4 **Efficiency Map**: compute ($\boldsymbol{\eta}^{\mathrm{FEA}}$,$\boldsymbol{T}_{em}^{\mathrm{FEA}}$) given ($\boldsymbol{N}^{*}$,$\boldsymbol{I}_{s}^{*}$,$\boldsymbol{\gamma}^{*}$) & interpolate

C.2 Nonlinear Motor Control

Before deriving the nonlinear motor control equations for the three strategies, the main parameters need to be introduced. The dq convention used here follows that in [Soong and Miller, 1994]. First, the stator current vector, $\boldsymbol{I}_s$, is represented by (C.1) in the Cartesian coordinate system using the d-axis current, I_d, and the q-axis current, I_q. An alternative representation utilizes Polar coordinates, where I_s is the current magnitude and γ is the current advance angle. The reference point of γ is taken from the q-axis with a counterclockwise positive rotation.

$$\boldsymbol{I}_s = \begin{bmatrix} I_d \\ I_q \end{bmatrix} = \begin{bmatrix} -I_s \sin\gamma \\ +I_s \cos\gamma \end{bmatrix} \tag{C.1}$$

Similarly, the stator flux linkage vector, $\boldsymbol{\lambda}_s$, is represented by (C.2). Here, λ_d and λ_q are the dq-axis flux linkages, and λ_s and δ are the flux linkage magnitude and load angle. To account for saturation and cross-coupling effects of $\boldsymbol{\lambda}_s$ as a function of I_s, the nonlinear dq-axis flux linkages, λ_d^{NL} and λ_q^{NL}, are also denoted. Note that either coordinate system could be used. As described later in Section C.3, λ_d^{NL} and λ_q^{NL} are individually characterized by a nonlinear curve for different (I_s,γ) points at a fixed motor speed. Furthermore, both λ_s and I_s contribute to the electromagnetic torque, T_{em}, in a 3-phase synchronous AC motor as shown in (C.3), where n_p is the number of poles.

$$\boldsymbol{\lambda}_s = \begin{bmatrix} \lambda_d(I_s, \gamma) \\ \lambda_q(I_s, \gamma) \end{bmatrix} = \begin{bmatrix} -\lambda_s \sin\delta \\ +\lambda_s \cos\delta \end{bmatrix} = \begin{bmatrix} \boldsymbol{\lambda_d^{\mathrm{NL}}} \\ \boldsymbol{\lambda_q^{\mathrm{NL}}} \end{bmatrix} \tag{C.2}$$

$$T_{em} = \frac{3}{2}\frac{n_p}{2}\boldsymbol{\lambda}_s \times \boldsymbol{I}_s = \frac{3}{2}\frac{n_p}{2}\left(\lambda_d I_q - \lambda_q I_d\right) \tag{C.3}$$

C.2.1 Maximum-Torque-Per-Ampere (MTPA)

Below base speed operation, the motor's back EMF has not matched the terminal winding voltage which means that the input voltage has not yet been constrained [Soong and Miller, 1994]. The MTPA control strategy is then applied to minimize the motor's copper losses. For a given I_s, T_{em} is maximized to find an optimal γ^{MTPA} using (C.4). This condition leads to a nonlinear equation which requires the first-order derivatives of λ_d^{NL} and λ_q^{NL} to solve for γ^{MTPA}. From zero to base speed, commonly known as the Constant Torque region, the corresponding T_{em} values are computed at every speed using a fixed (I_s,γ^{MTPA}).

$$\frac{dT_{em}}{d\gamma} = 0 \rightarrow \tan\gamma = \frac{+\lambda_q^{\mathrm{NL}} + d\lambda_d^{\mathrm{NL}}/d\gamma}{+\lambda_d^{\mathrm{NL}} - d\lambda_q^{\mathrm{NL}}/d\gamma} \tag{C.4}$$

Moreover, the electrical base speed, $\omega_{e_{\mathrm{Base}}}$, is calculated using (C.5). Here, V_{dc} is the DC bus voltage. It is assumed that the 2-level inverter is operating at its square-wave limit and the MTPA flux linkage magnitude, $\lambda_s^{\mathrm{MTPA}}$, is computed using (C.2).

$$\omega_{e_{\mathrm{Base}}} = \frac{2}{\pi}\frac{V_{dc}}{\lambda_s^{\mathrm{MTPA}}} \tag{C.5}$$

C.2.2 Flux Weakening (FW)

Above base speed operation, the motor's back EMF has exceeded the maximum terminal winding voltage so the MTPA strategy cannot be employed anymore [Soong and Miller, 1994]. Thus, the FW strategy ensures that I_s is maintained while the voltage limit ellipse in (C.6) is satisfied. The machine's flux is weakened by reducing I_d or varying γ for different speeds. In practice, injecting large amounts of negative I_d could increase the risk of demagnetization. Here, V_s is the stator phase voltage, and V_d and V_q are the dq-axis voltages. In vector form, $\boldsymbol{V}_s$ is a function of $\boldsymbol{\lambda}_s$ using the electrical speed, ω_e, as shown in (C.7). The stator winding's resistive losses are ignored, due to their small effect on the control compared to $\omega_e\boldsymbol{\lambda}_s$. Substituting (C.7) in (C.6) yields (C.8) which consists of λ_d^{NL} and λ_q^{NL}. From base to max speed operation, known as the Constant Power range, this nonlinear FW equation is solved for every ω_e to find γ^{FW}.

$$V_s^2 = V_d^2 + V_q^2 \tag{C.6}$$

$$\boldsymbol{V}_s = \begin{bmatrix} V_d \\ V_q \end{bmatrix} = j\omega_e\boldsymbol{\lambda}_s = \omega_e \begin{bmatrix} -\lambda_d^{\mathrm{NL}} \\ +\lambda_q^{\mathrm{NL}} \end{bmatrix} \tag{C.7}$$

$$\left(\frac{2}{\pi}\frac{V_{dc}}{\omega_{e_{\mathrm{Base}}}}\right)^2 = \left(\lambda_d^{\mathrm{NL}}\right)^2 + \left(\lambda_q^{\mathrm{NL}}\right)^2 \tag{C.8}$$

C.2.3 Maximum-Torque-Per-Volt (MTPV)

Beyond a certain speed in the Constant Power region, the FW strategy can no longer produce a nonzero T_{em}. For an infinite-speed machine, the center of the voltage limit ellipse is located inside the current limit circle which suggests that both I_s and γ must be varied [5]. Hence, the MTPV strategy maximizes T_{em} for a given V_{dc} or λ_s to find an optimal δ^{MTPV} through (C.9). This equation requires the nonlinear dq-axis currents, I_d^{NL} and I_q^{NL}, as a function of λ_s and δ as shown in (C.10). Once δ^{MTPV} is found at a given speed, I_s^{MTPV} is then computed using (C.10) and (C.1).

$$\frac{dT_{em}}{d\delta} = 0 \rightarrow \tan\delta = \frac{+I_q^{\mathrm{NL}} + dI_d^{\mathrm{NL}}/d\delta}{-I_d^{\mathrm{NL}} + dI_q^{\mathrm{NL}}/d\delta} \tag{C.9}$$

$$\boldsymbol{I}_s = \begin{bmatrix} I_d(\lambda_d, \lambda_q) \\ I_q(\lambda_d, \lambda_q) \end{bmatrix} = \begin{bmatrix} I_d(\lambda_s, \delta) \\ I_q(\lambda_s, \delta) \end{bmatrix} = \begin{bmatrix} I_d^{\mathrm{NL}} \\ I_q^{\mathrm{NL}} \end{bmatrix} \tag{C.10}$$

C.3 Curve Fitting Functions

The three equations presented above for the MTPA (C.4), FW (C.8) and MTPV (C.9) control strategies depend on the evaluation of the nonlinear functions, λ_d^{NL}, λ_q^{NL}, I_d^{NL} and I_q^{NL}, as well as their first-order derivatives which is discussed below. Fitting a Nth-order polynomial to the nonlinear function $\lambda_d^{\mathrm{NL}}(\boldsymbol{I}_s)$ for 2 variables can be represented via (C.11). Here, $\boldsymbol{a}$ denotes the vector of unknown coefficients and $\boldsymbol{X}$ denotes the vector of self and cross terms of $\boldsymbol{I}_s$. Similarly, the first-order derivative of $\lambda_d^{\mathrm{NL}}(I_s)$ with respect to γ is shown in (C.12), where $\boldsymbol{X}_D$ is the derivative vector of $\boldsymbol{X}$.

$$\lambda_d^{\mathrm{NL}}(I_s) = \boldsymbol{a}^T \boldsymbol{X} \tag{C.11}$$

$$\frac{d\lambda_d^{\mathrm{NL}}(I_s)}{d\gamma} = \boldsymbol{a}^T \boldsymbol{X}_D \tag{C.12}$$

For instance, a 2^{nd}-order polynomial and its derivative form are shown in (C.13) and (C.14). Given a set of points ($\boldsymbol{I}_s^{\mathrm{FEA}}$,$\boldsymbol{\gamma}^{\mathrm{FEA}}$), λ_d^{NL} is fitted using nonlinear least-squares regression to find $\boldsymbol{a}$. A similar analysis is expected for other nonlinear functions. Moreover, alternative fitting functions could be used provided the accuracy is not affected.

$$\lambda_d^{\mathrm{NL}}(I_s) = +a_1 I_d^2 + a_2 I_d + a_3 I_q^2 + a_4 I_q + a_5 I_d I_q + a_6 \tag{C.13}$$

$$\frac{d\lambda_d^{\mathrm{NL}}(I_s)}{d\gamma} = -2a_1 I_d I_q - a_2 I_q + 2a_3 I_d I_q + a_4 I_d + a_5 (I_d^2 - I_q^2) \tag{C.14}$$

C.4 Model Specifications

In order to test the nonlinear control equations presented above, two different motors were studied. First, the 2010 Toyota Prius IPM motor has been considered since its design details and performances have been published in [Olszewski et al., 2011]. Second, a PM-SynRM rated at a higher power was chosen due to its lower PM torque contribution. It was originally designed in [Rahman et al., 2016] as an alternative to a rare-earth PM machine for a Class IV step van electric vehicle. Fig. C.1 displays the cross-sectional geometries of the Prius IPM and PM-SynRM, and Table C.1 below provides a summary of their design specifications.

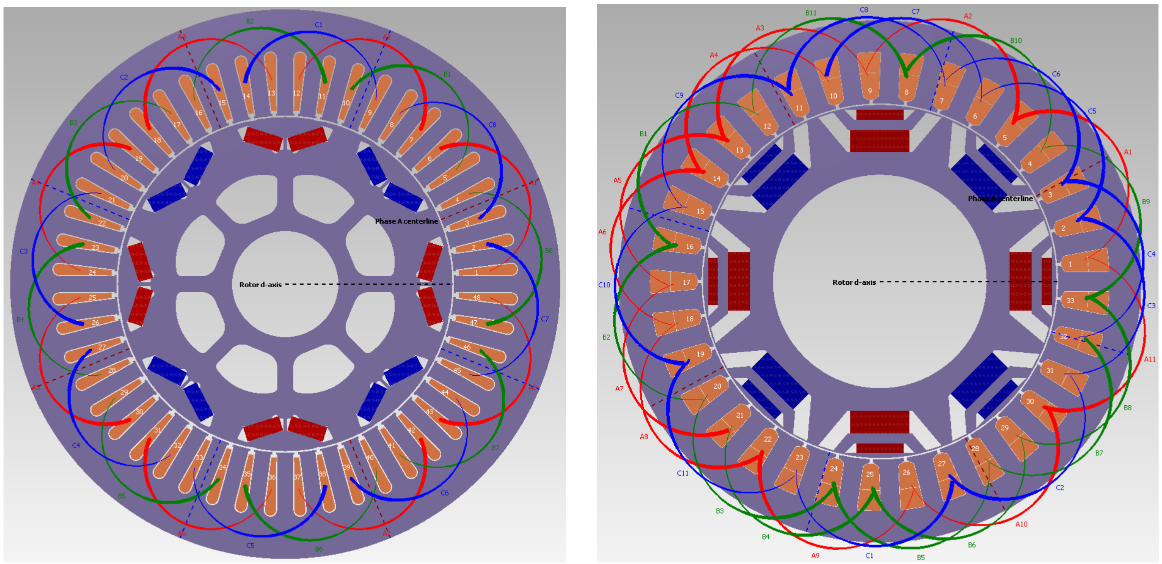

(a) (b)

Fig. C.1 Motor cross-sectional geometry: (a) Prius IPM, (b) PM-SynRM.

Table C.1 Model Design Specifications

Parameter/Dimension	Prius IPM	PM-SynRM
Number of poles/slots	8/48	8/33
DC bus voltage	650 V	650 V
Maximum speed	13500 RPM	6000 RPM
Peak power	60 kW	200 kW
Stator's outer diameter	264 mm	355 mm
Rotor's outer diameter	160 mm	240 mm
Active stack length	51 mm	125 mm
Air gap thickness	0.75 mm	1.00 mm
Rated RMS line current	80 Arms	375 Arms
Number of turns	11 turns	3 turns
Rated current density	13 A/mm^2	10 A/mm^2
Peak current density	26 A/mm^2	27 A/mm^2
Total mass	20.4 kg	75.8 kg
Magnet material	NdFeB 44/15	MQP-B+ 897/780
Core material	M-19 29 Ga	M-19 29 Ga
Cooling method	Liquid	Liquid

C.5 Results and Discussion

Relying on the procedure described in Algorithm 1, the specified steps are performed to compute the motor efficiency maps.

In Step 1, the dataset ($\boldsymbol{\lambda}_d^{\text{FEA}}$,$\boldsymbol{\lambda}_q^{\text{FEA}}$) was computed for a given input ($\boldsymbol{I}_s^{\text{FEA}}$,$\boldsymbol{\gamma}^{\text{FEA}}$) using 2-D FEA simulations. The motor speed was kept fixed and the winding was excited using a sinusoidal current. Both $\boldsymbol{\lambda}_d^{\text{FEA}}$ and $\boldsymbol{\lambda}_q^{\text{FEA}}$ were computed using only the fundamental component of the flux linkage waveforms. Here, $\boldsymbol{I}_s^{\text{FEA}}$ was varied for 0%, 100% and 200% of the rated condition to capture the saturation effects. Also, $\boldsymbol{\gamma}^{\text{FEA}}$ was varied in steps of 10° from 0° to 90° to account for the cross-coupling.

In Step 2, the motors are characterized by individually fitting their flux linkage datasets to 2^{nd}-order polynomial curves using (C.13). Once the unknown coefficients, $\boldsymbol{a}$ were computed, the two interpolated maps of the PM-SynRM were calculated using (C.11) and (C.13) as illustrated below in Fig. C.2. The Prius IPM's flux linkage maps are similar, so were not reproduced here.

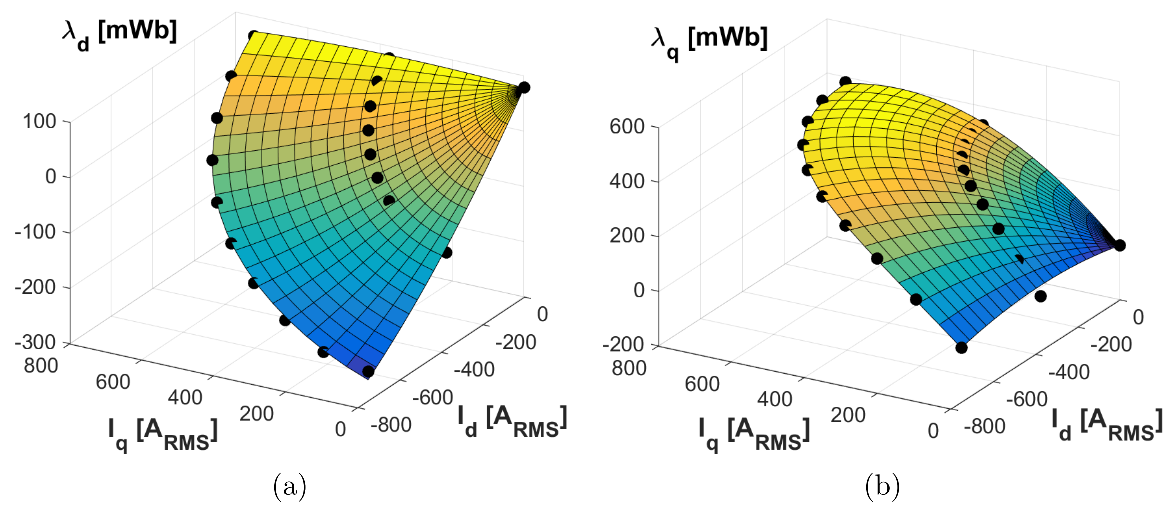

Fig. C.2 Nonlinear flux linkage maps for PM-SynRM: (a) λ_d^{NL}, (b) λ_q^{NL}.

Furthermore, Table C.2 shows the individual values of $\boldsymbol{a}$ for the Prius IPM and PM-SynRM. As expected from typical synchronous AC motors and Fig. C.2, $\lambda_d^{\text{NL}}(\boldsymbol{I}_s)$ depends more on I_d, I_q and 1 than the other inputs. This result also indicates that cross-coupling effects cannot be ignored when the entire (I_d,I_q) plane is considered for motor control. In fact, a_6 represents the PM flux linkage in a constant parameter model. In contrast, $\lambda_q^{\mathrm{NL}}(\boldsymbol{I}_s)$ seems to be dependent on I_d, I_q^2 and I_q as seen from Fig. C.2, where a_3 signifies the prominent saturation effect. The squared norm of the residuals, σ^2, are low compared to the range of flux linkage values which indicate a good fit. Also, I_d^{NL} and I_q^{NL} were similarly calculated using a 4^{th}-order polynomial.

Table C.2 Flux Linkage Characterization

$\lambda_d^{\mathrm{NL}}(\boldsymbol{I}_s)$		**Prius IPM**		$\lambda_q^{\mathrm{NL}}(\boldsymbol{I}_s)$			
a_1	+5.813e-7	a_4	+4.827e-5	a_1	−1.797e-6	a_4	+3.706e-3
a_2	+1.546e-3	a_5	−2.067e-6	a_2	−3.792e-4	a_5	+1.373e-6
a_3	−7.026e-7	a_6	+1.432e-1	a_3	−9.753e-6	a_6	−9.203e-4
σ^2 = 3.894e-4				σ^2 = 1.169e-3			
$\lambda_d^{\mathrm{NL}}(\boldsymbol{I}_s)$		**PM-SynRM**		$\lambda_q^{\mathrm{NL}}(\boldsymbol{I}_s)$			
a_1	+9.068e-8	a_4	+2.547e-5	a_1	−1.457e-7	a_4	+9.405e-4
a_2	+4.168e-4	a_5	−1.271e-7	a_2	−1.545e-4	a_5	+1.443e-7
a_3	−2.949e-8	a_6	+7.777e-2	a_3	−5.513e-7	a_6	−1.300e-3
σ^2 = 8.218e-4				σ^2 = 3.633e-3			

Once the motors were characterized, Step 3 was executed at different values of I_s^{MAX}, for instance, 50%, 100%, 150% and 200% of the rated current. For each current magnitude, the MTPA, FW, and MTPV operation points were computed for speeds ranging from zero to a maximum limit as specified in Table C.1. As a first test, the MTPA torque curves were computed as a function of γ using (C.3) and (C.11) for both motors. There was a good agreement between the maximum torque trajectory and the one obtained through FEA.

As explained in [Soong and Miller, 1994], mode diagrams in the dq current plane allow control engineers to visualize the maximum torque trajectory as the motor speed, N, is increased. Fig. C.3 (a) and (b) show the corresponding diagrams for both motors. Due to the low PM content of the PM-SynRM, the MTPV control plays an important role at higher speeds at different currents. Conversely, the FW control dominates for the Toyota IPM.

Moreover, both mode diagrams can be converted to a more familiar form as in Fig. C.3 (c) and (d) which displays the torque, current magnitude and advance angle as a function of speed for different I_s^{MAX}. Although the predicted torque values are not necessarily accurate due to the fundamental assumption of the dq flux linkages (since higher order harmonics are ignored), the control operation points are nevertheless the same.

In Step 4, the efficiency, η, and torque values are computed using 2-D FEA simulations given the ($\boldsymbol{N}^*$,$\boldsymbol{I}_s^*$,$\boldsymbol{\gamma}^*$) values found in Step 3. Then, an artificial neural network similar to the one described in [Mohammadi et al., 2016] was used to interpolate and create an efficiency map for less computational effort as opposed to direct FEA evaluations. A 2-input network with 1 hidden layer of 5 neurons was used. Also, the *root-mean-square-error* (RMSE) between FEA and interpolated values of η was calculated. To balance between accuracy and over-fitting, the training set's division was varied while the validation set was fixed and the remaining samples were included in the testing set. Referring to Fig. C.4 below, a training set division of 60% was chosen to compute the efficiency maps in Fig. C.5. Table C.3 specifies the neural networks' performances for both case studies. Moreover, the efficiency map of the Prius IPM in Fig. C.5 seems relatively close to the one reported in [Olszewski et al., 2011], while the inverter losses are ignored.

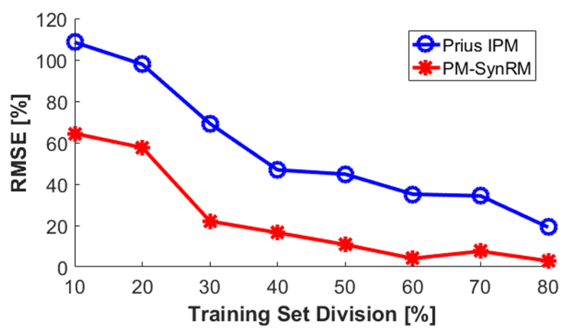

Fig. C.4 Root-mean-square-error curves for varying training set ratios.

Table C.3 Neural Network Performances for Two Efficiency Maps

Motor	#Samples	Train.	Valid.	Test.	RMSE
Prius IPM	90	0.9971	0.9796	0.9526	26.45%
PM-SynRM	44	0.9999	0.9960	0.9992	2.84%

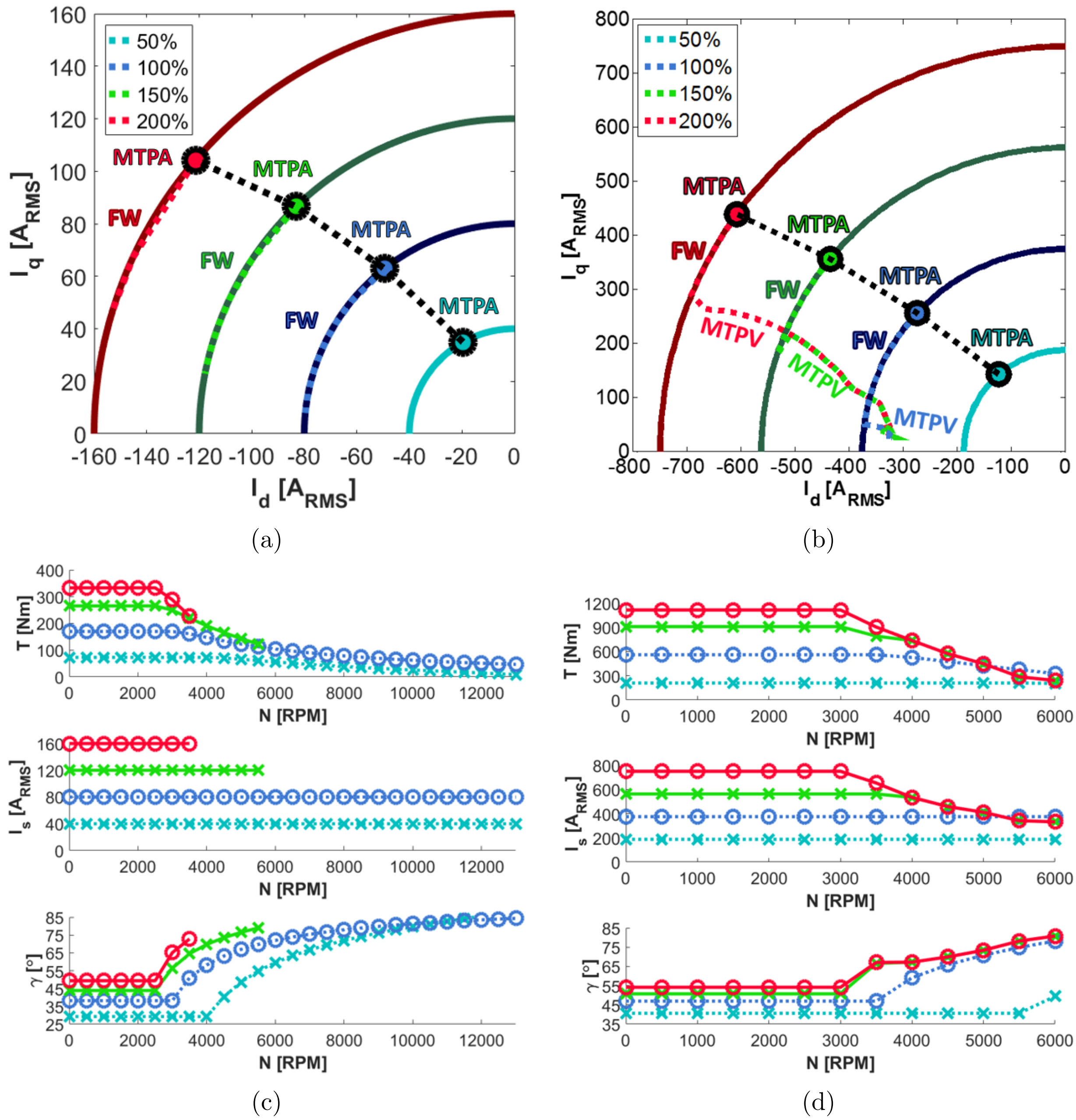

Fig. C.3 [Top] Mode diagram for different current magnitudes with dotted maximum torque trajectory: (a) Prius IPM, (b) PM-SynRM.
[Bottom] Performances vs. speed curves: (c) Prius IPM, (d) PM-SynRM.

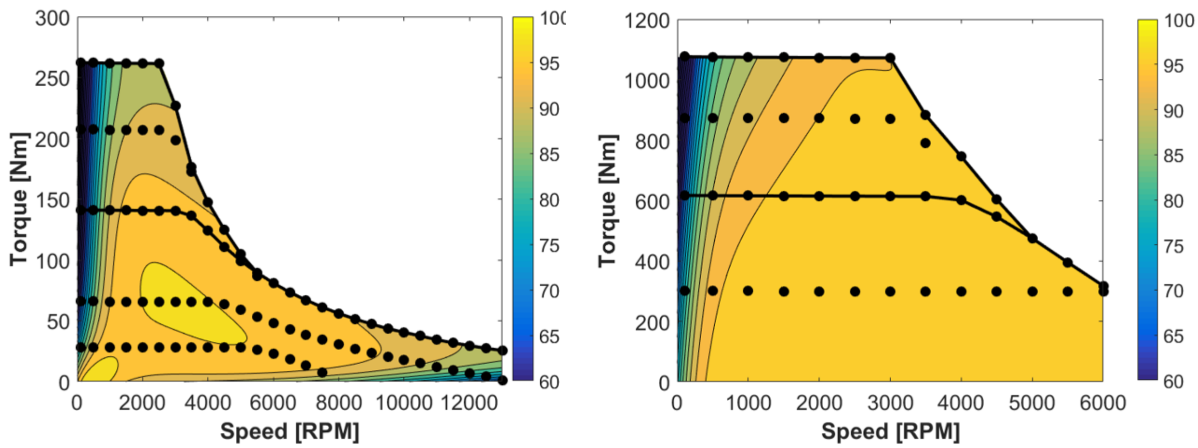

(a) (b)

Fig. C.5 Motor efficiency map: (a) Prius IPM, (b) PM-SynRM.

C.6 Conclusion

In brief, this work derived nonlinear motor control equations general for any synchronous AC motor which account for saturation and cross-coupling effects of the dq flux linkages. Upon characterizing the 2010 Prius IPM and a PM-SynRM, the current magnitudes and advance angles at different speeds were calculated to compute the corresponding efficiency and torque values using 2-D FEA simulations. The two efficiency maps were then interpolated with the help of a simple neural network.

For the nonlinear least-squares curve fitting, a 2^{nd} and a 4^{th}-order polynomial worked best for the flux linkages and currents respectively. Moreover, higher-order polynomials, sigmoid and arc tangent fitting functions all yielded erroneous results while computing the maximum torque trajectory in the mode diagram. Furthermore, a reduced-order model of the efficiency map could possibly be used instead of FEA simulations to reduce computational time at the expense of solution accuracy.

Appendix D

Additional Results

This appendix includes additional results computed for the two synchronous reluctance machine case studies as part of the *multiphysics design process* (MPDP). Captions include relevant information for the selected designs. For example, "● for [-T_{avg},T_{rip}]" represents the marker used on scatter plots for the optimal design of average torque and torque ripple based on the selection function defined in (4.1). For an explanation on how to interpret correlation plots, please refer to Section 2.2.1.

- Fig. D.1: Histograms of component temperatures for 24-slot 1-barrier
- Fig. D.2: Histograms of component temperatures for 24-slot 2-barrier
- Fig. D.3: Histograms of component temperatures for 24-slot 3-barrier
- Fig. D.4: Histograms of component temperatures for 24-slot 4-barrier
- Fig. D.5: Correlation plot of multiphysics performances for 24-slot 1-barrier
- Fig. D.6: Correlation plot of multiphysics performances for 24-slot 2-barrier
- Fig. D.7: Correlation plot of multiphysics performances for 24-slot 3-barrier
- Fig. D.8: Correlation plot of multiphysics performances for 24-slot 4-barrier
- Fig. D.9: Correlation plot of multiphysics performances for 30-slot 1-barrier
- Fig. D.10: Correlation plot of multiphysics performances for 30-slot 1-barrier

- Fig. D.11: Correlation plot of multiphysics performances for 30-slot 1-barrier
- Fig. D.12: Correlation plot of multiphysics performances for 30-slot 1-barrier
- Fig. D.13: Correlation plots of 24-slot design metrics (1/2/3/4-barrier)
- Fig. D.14: Correlation plots of 30-slot design metrics (1/2/3/4-barrier)
- Fig. D.15: Barrier mapping of multiphysics performances for 30-slot (top 5%)
- Fig. D.16: Barrier mapping of multiphysics performances for 30-slot (top 10%)

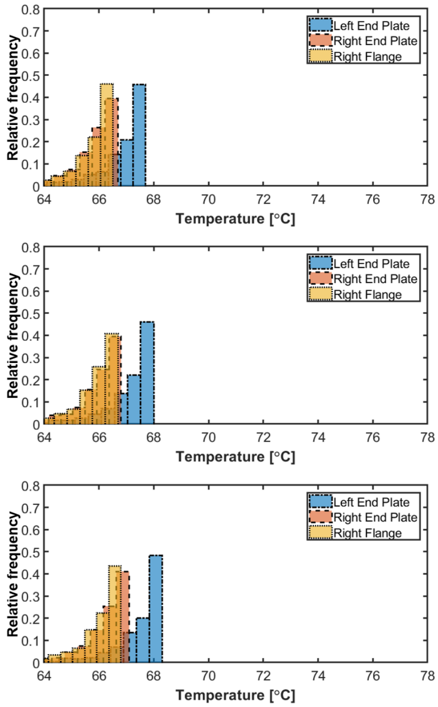

(a) Minimum, Average, Maximum

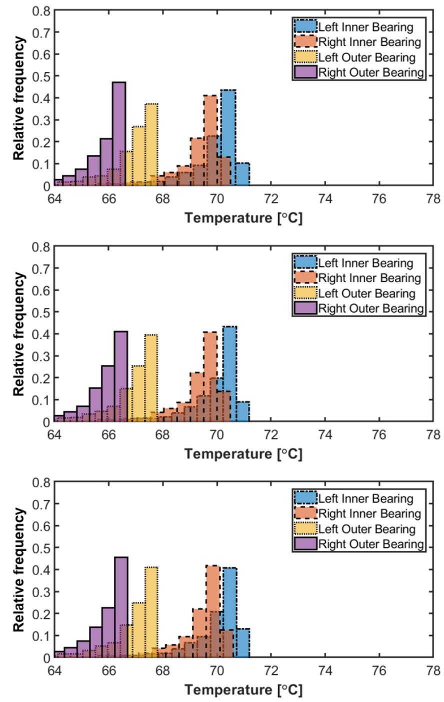

(b) Minimum, Average, Maximum

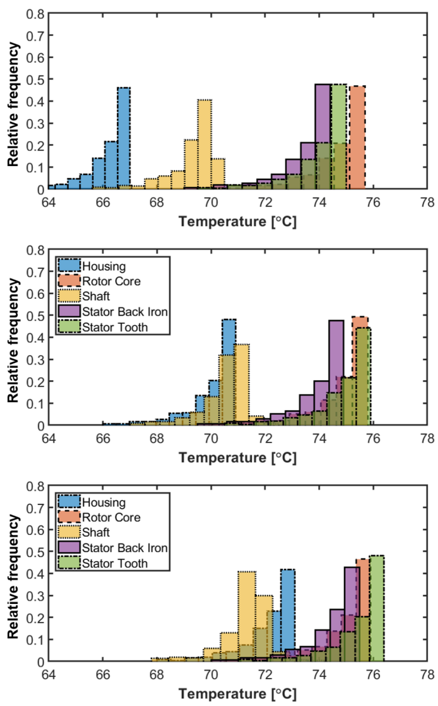

(c) Minimum, Average, Maximum

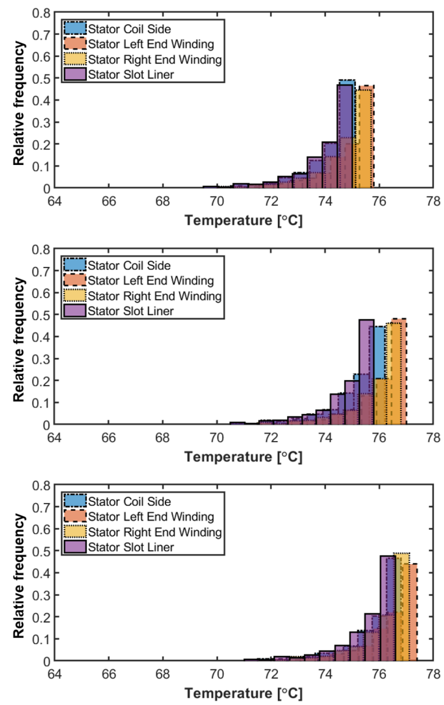

(d) Minimum, Average, Maximum

Fig. D.1 Histograms of component steady-state temperatures from 3-D thermal analysis: 24-slot 1-barrier.

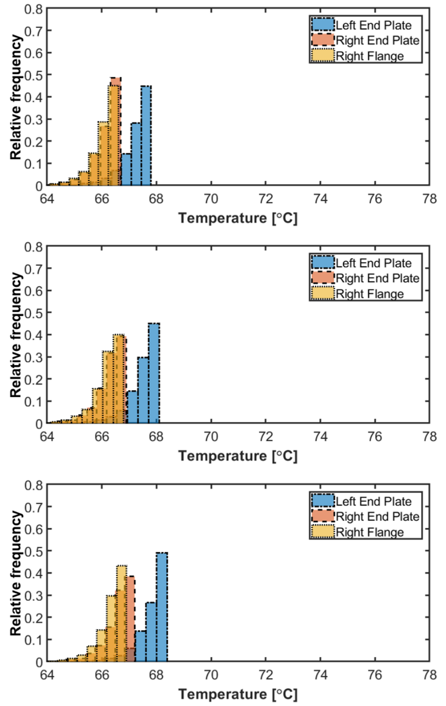

(a) Minimum, Average, Maximum

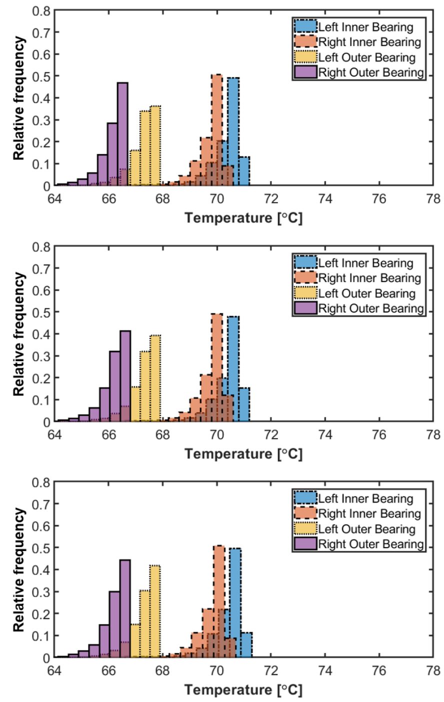

(b) Minimum, Average, Maximum

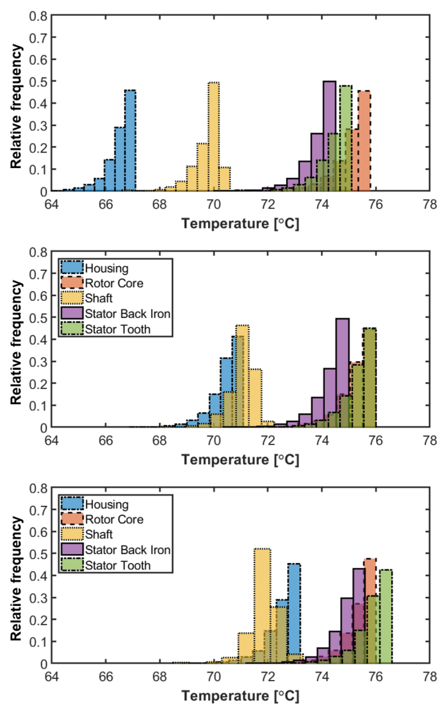

(c) Minimum, Average, Maximum

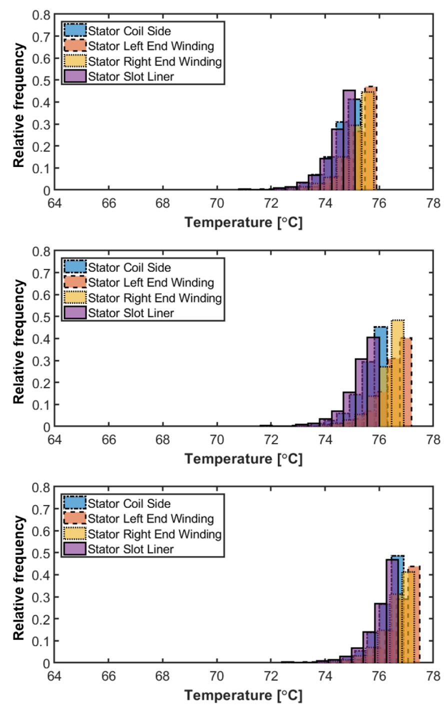

(d) Minimum, Average, Maximum

Fig. D.2 Histograms of component steady-state temperatures from 3-D thermal analysis: 24-slot 2-barrier.

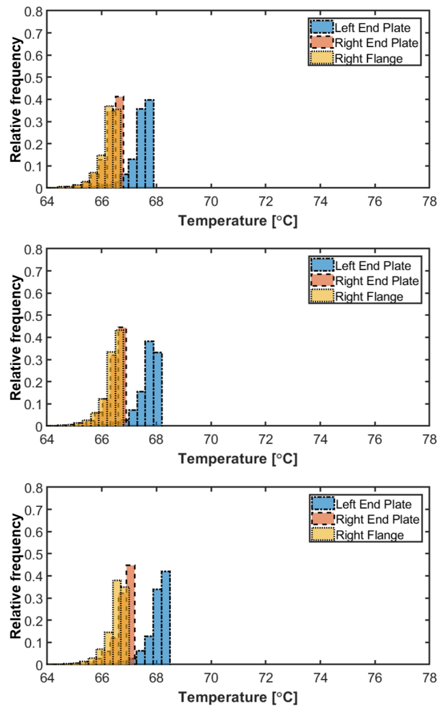

(a) Minimum, Average, Maximum

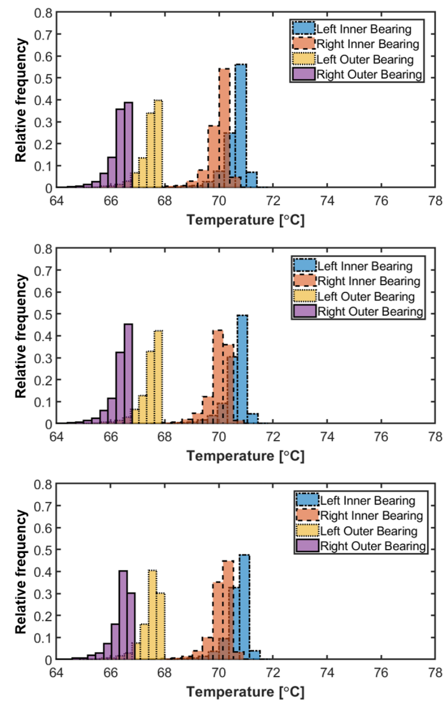

(b) Minimum, Average, Maximum

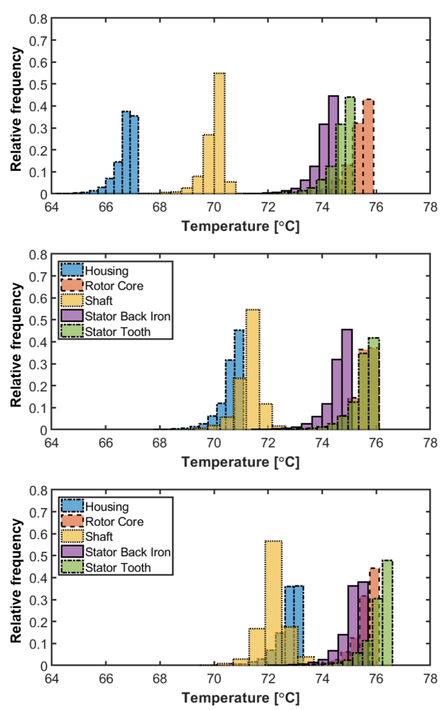

(c) Minimum, Average, Maximum

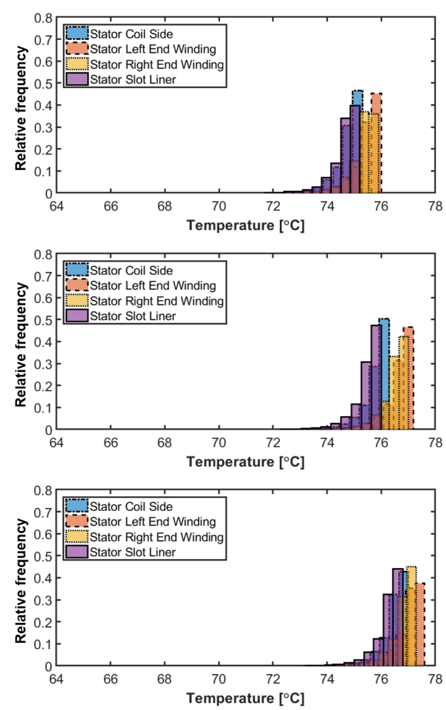

(d) Minimum, Average, Maximum

Fig. D.3 Histograms of component steady-state temperatures from 3-D thermal analysis: 24-slot 3-barrier.

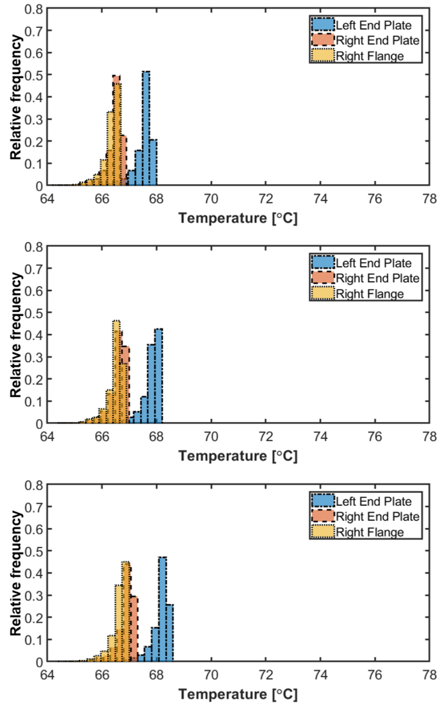

(a) Minimum, Average, Maximum

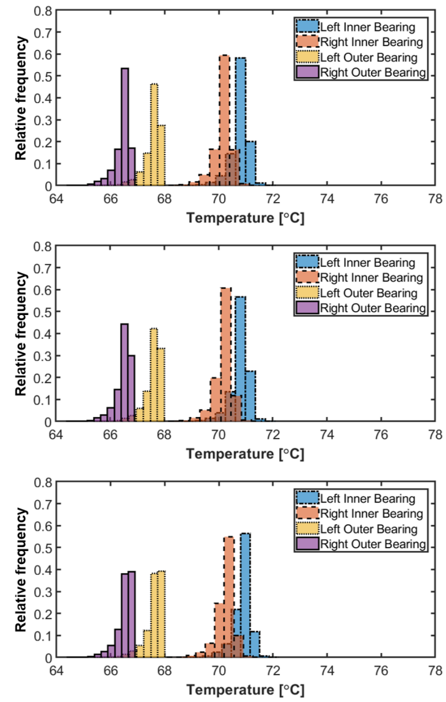

(b) Minimum, Average, Maximum

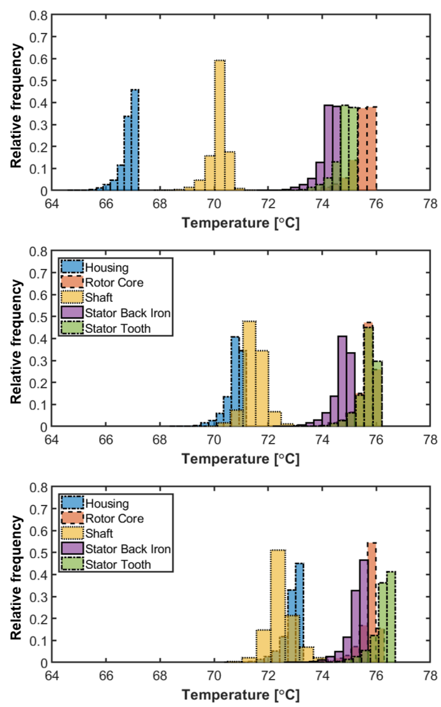

(c) Minimum, Average, Maximum

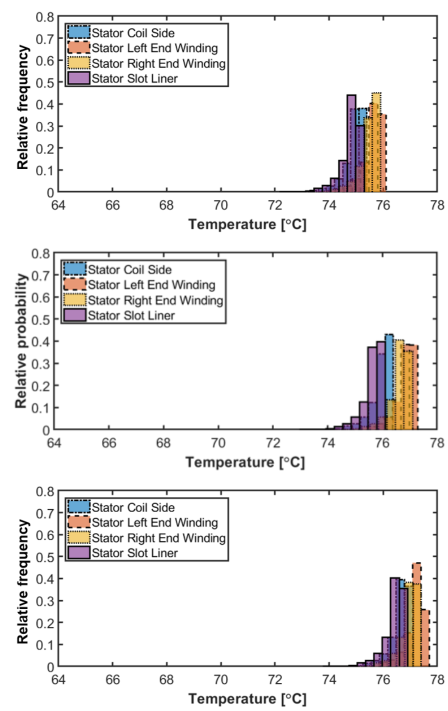

(d) Minimum, Average, Maximum

Fig. D.4 Histograms of component steady-state temperatures from 3-D thermal analysis: 24-slot 4-barrier.

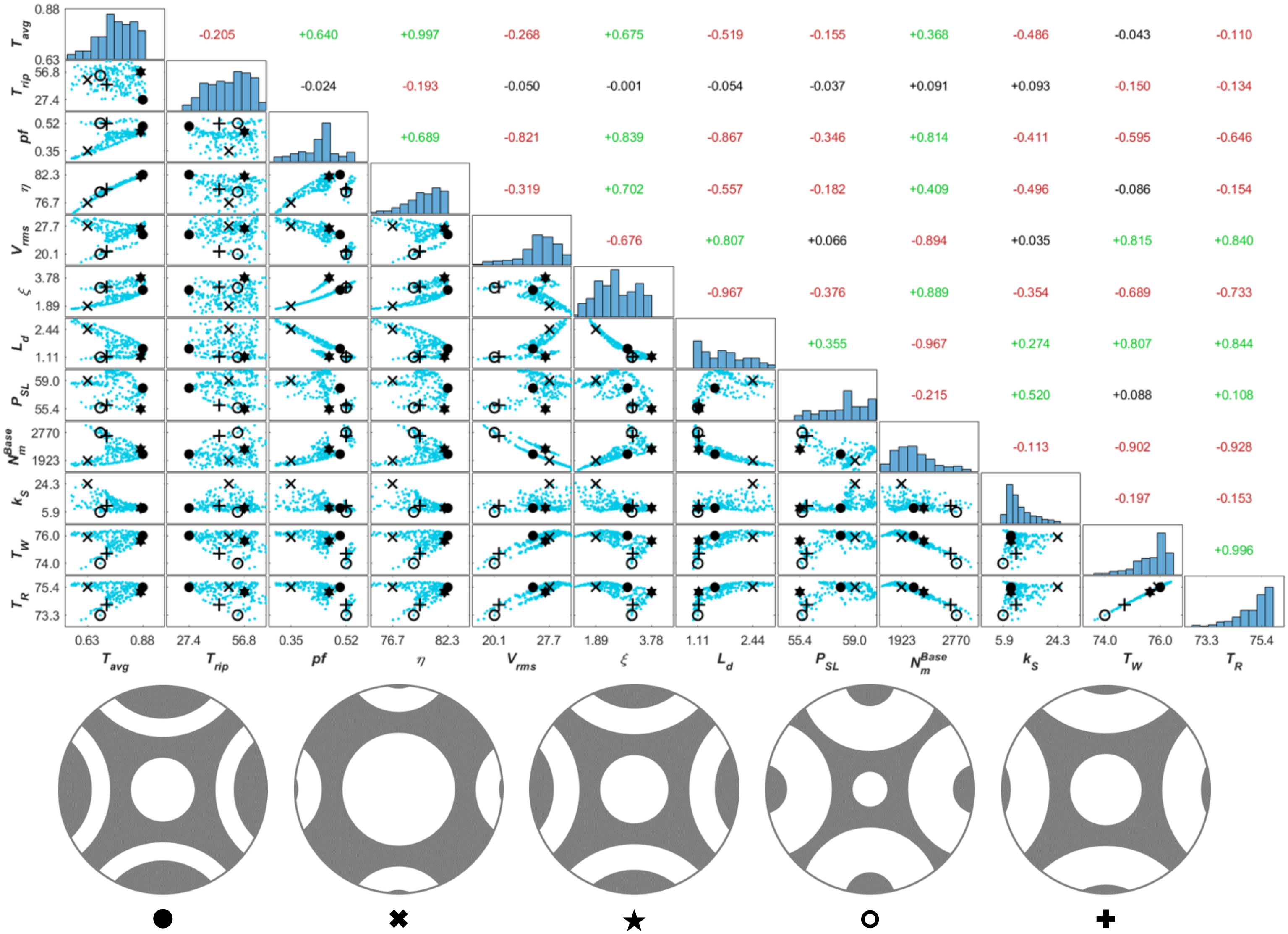

Fig. D.5 (Top) Correlation plot of 24-slot, 1-barrier performances. (Bottom) Selected designs: ● for [-T_{avg},T_{rip}], ✖ for [-T_{avg},T_{rip},-k_S], ★ for [-T_{avg},T_{rip},P_{SL}], ○ for [-T_{avg},T_{rip},T_W], ✚ for all.

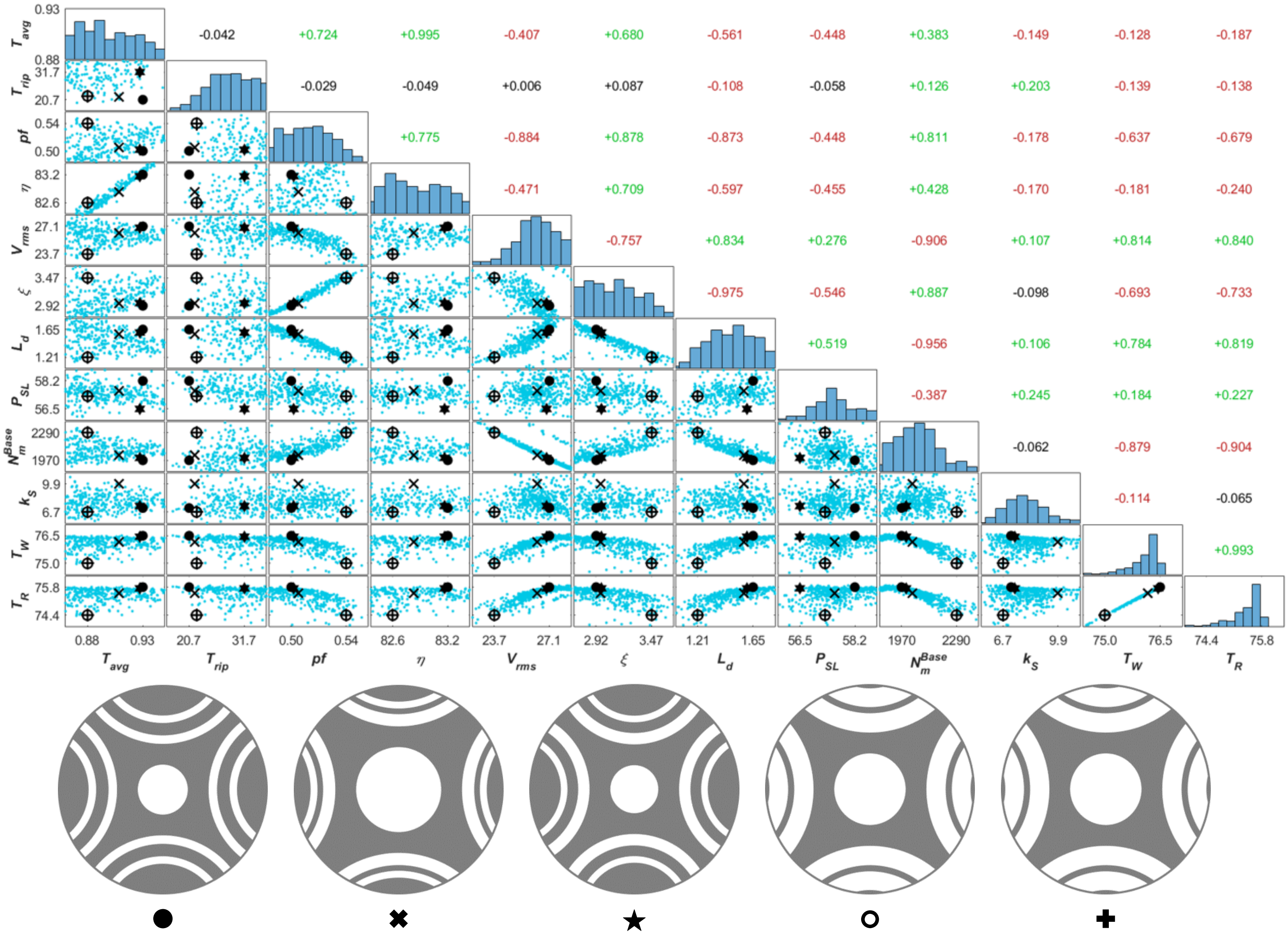

Fig. D.6 (Top) Correlation plot of 24-slot, 2-barrier performances. (Bottom) Selected designs: ● for [-T_{avg},T_{rip}], ✖ for [-T_{avg},T_{rip},-k_S], ★ for [-T_{avg},T_{rip},P_{SL}], ○ for [-T_{avg},T_{rip},T_W], ✚ for all.

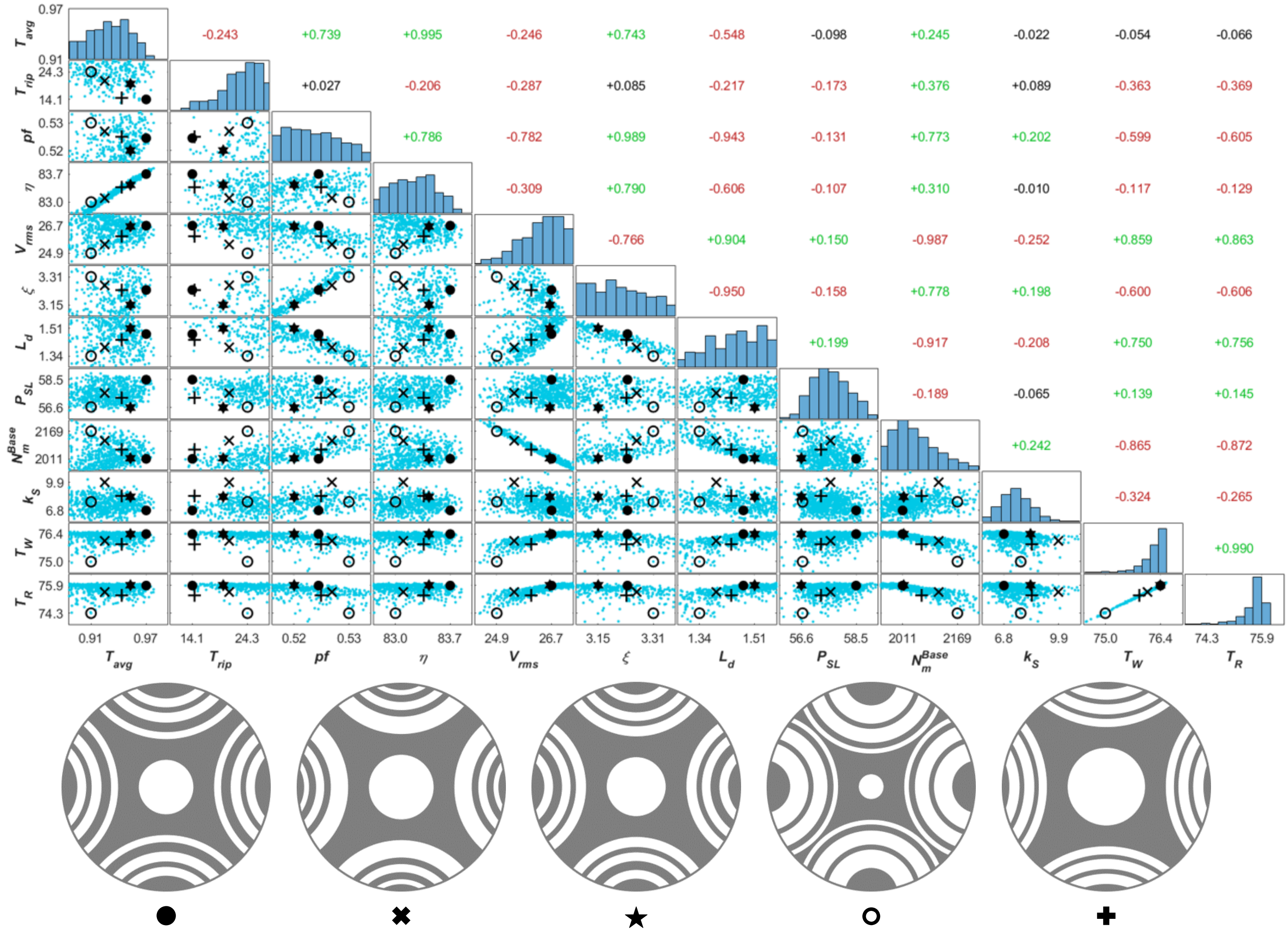

Fig. D.7 (Top) Correlation plot of 24-slot, 3-barrier performances. (Bottom) Selected designs: ● for [-T_{avg},T_{rip}], ✖ for [-T_{avg},T_{rip},-k_S], ★ for [-T_{avg},T_{rip},P_{SL}], ○ for [-T_{avg},T_{rip},T_W], ✚ for all.

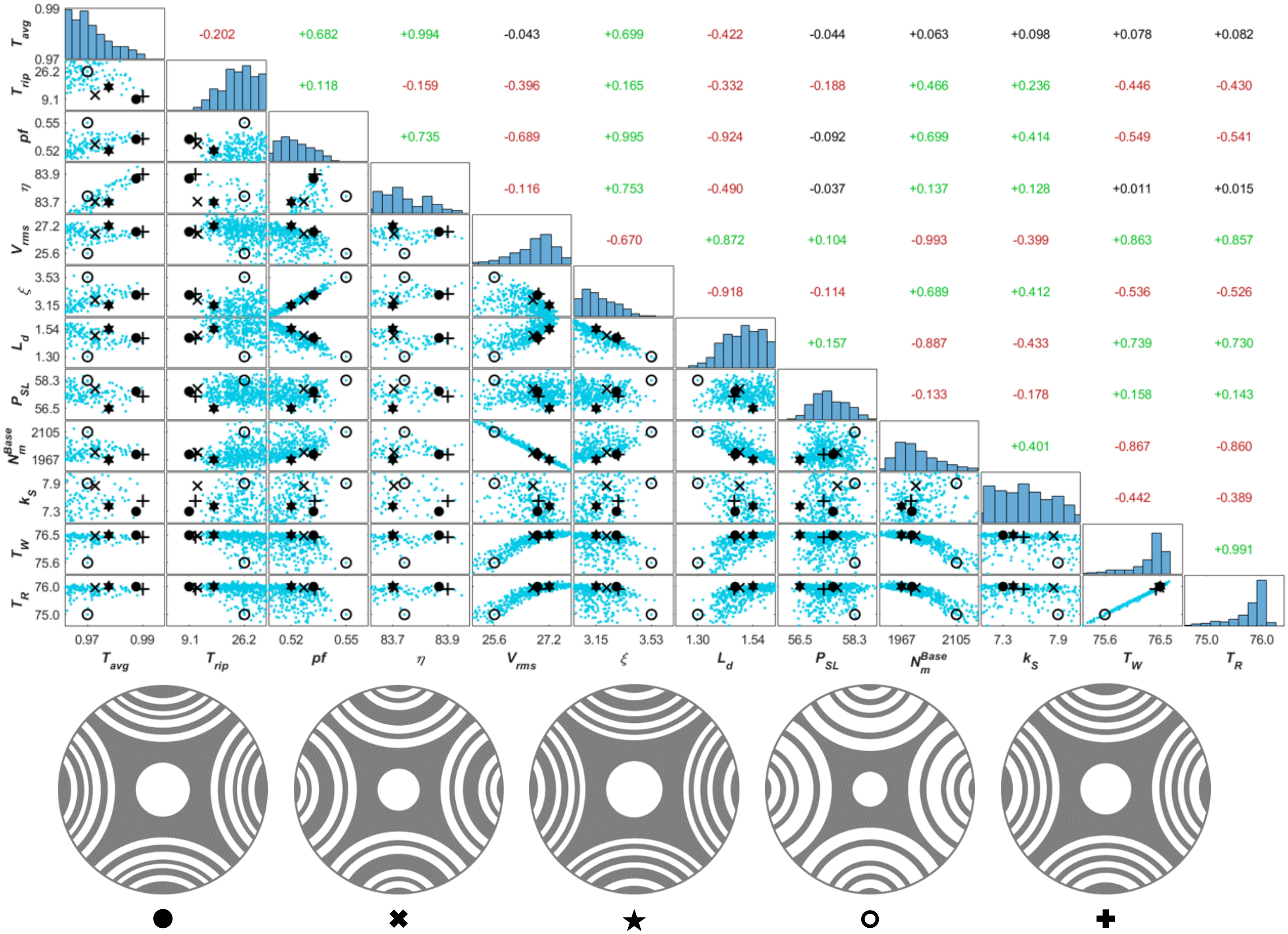

Fig. D.8 (Top) Correlation plot of 24-slot, 4-barrier performances. (Bottom) Selected designs: ● for [-T_{avg},T_{rip}], ✖ for [-T_{avg},T_{rip},-k_S], ★ for [-T_{avg},T_{rip},P_{SL}], ○ for [-T_{avg},T_{rip},T_W], ✚ for all.

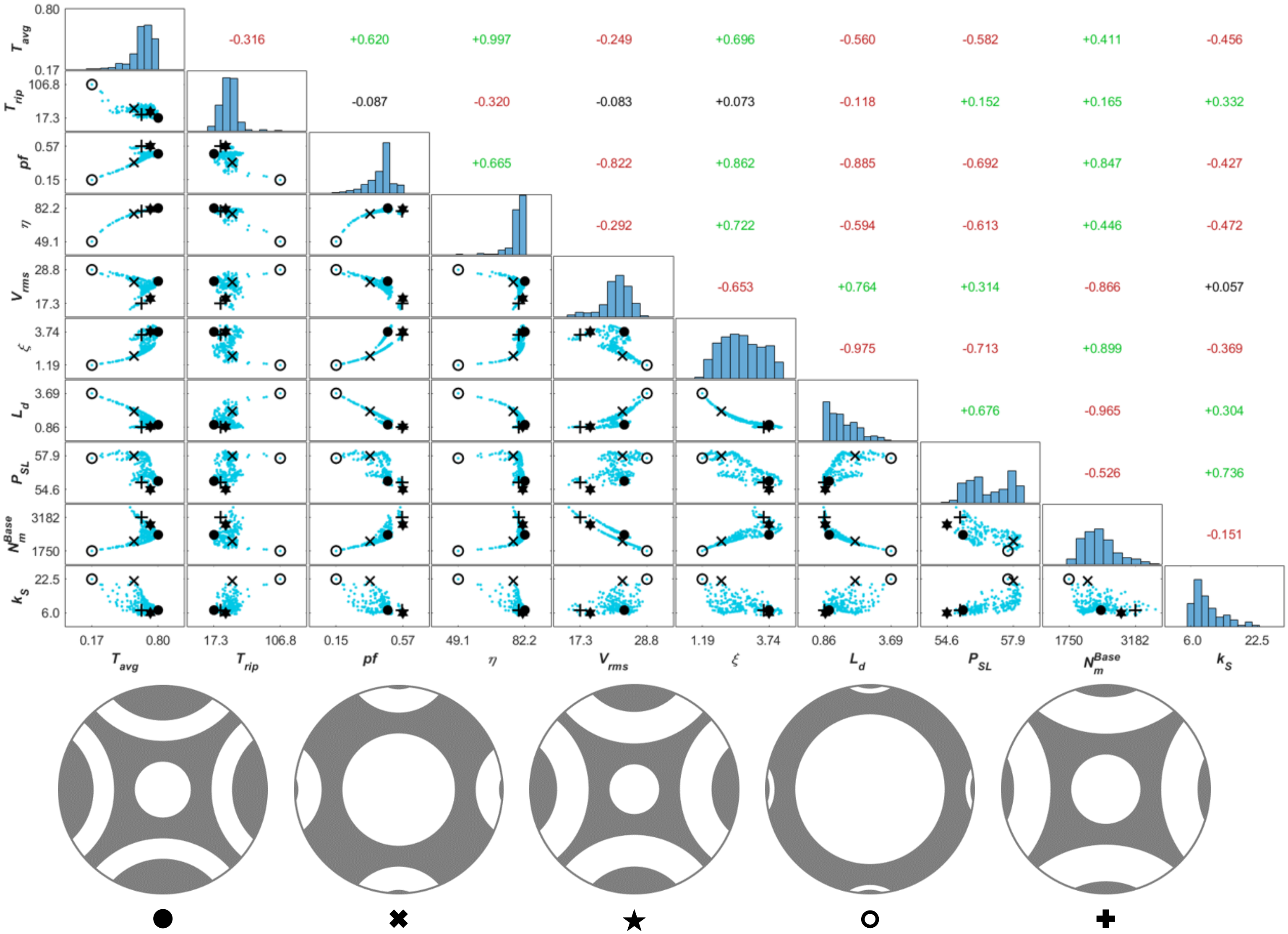

Fig. D.9 (Top) Correlation plot of 30-slot, 1-barrier performances. (Bottom) Selected designs: ● for [-T_{avg},T_{rip}], ✖ for [-T_{avg},T_{rip},-k_S], ★ for [-T_{avg},T_{rip},P_{SL}], ○ for [P_{SL},-k_S], ✚ for all.

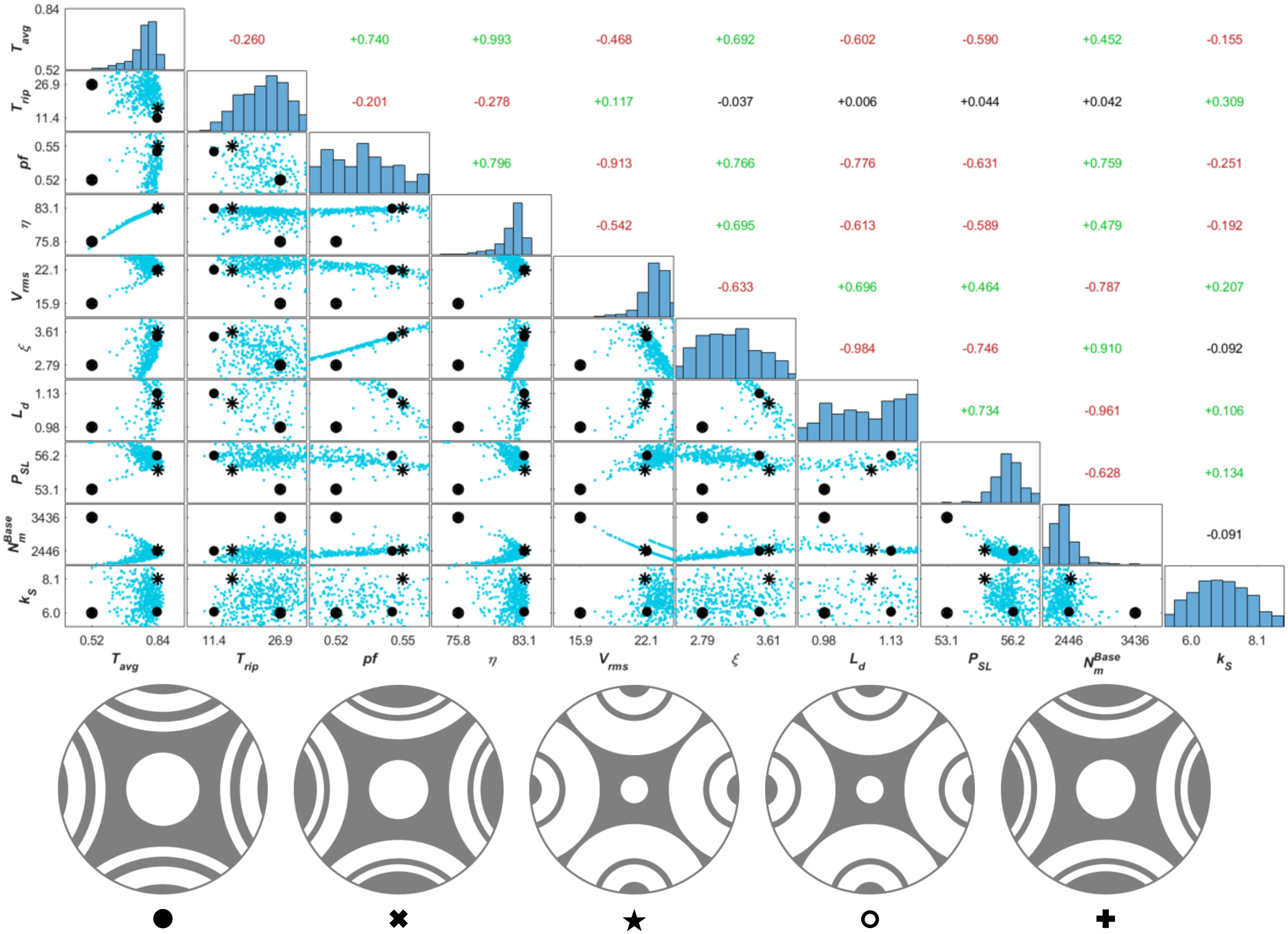

Fig. D.10 (Top) Correlation plot of 30-slot, 2-barrier performances. (Bottom) Selected designs: ● for [-T_{avg},T_{rip}], ✖ for [-T_{avg},T_{rip},-k_S], ★ for [-T_{avg},T_{rip},P_{SL}], ○ for [P_{SL},-k_S], ✚ for all.

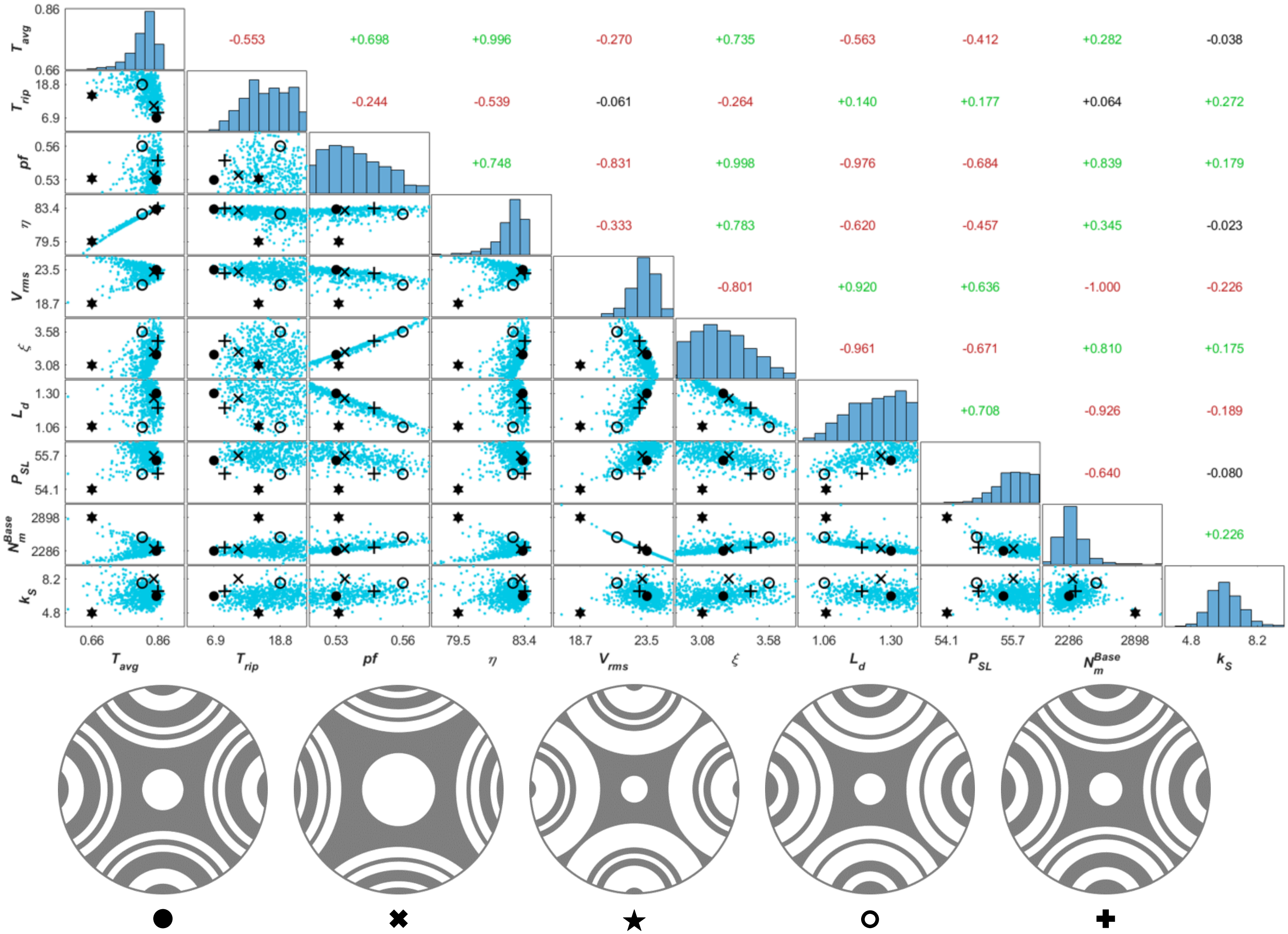

Fig. D.11 (Top) Correlation plot of 30-slot, 3-barrier performances. (Bottom) Selected designs: ● for [-T_{avg},T_{rip}], ✖ for [-T_{avg},T_{rip},-k_S], ★ for [-T_{avg},T_{rip},P_{SL}], **O** for [P_{SL},-k_S], ✚ for all.

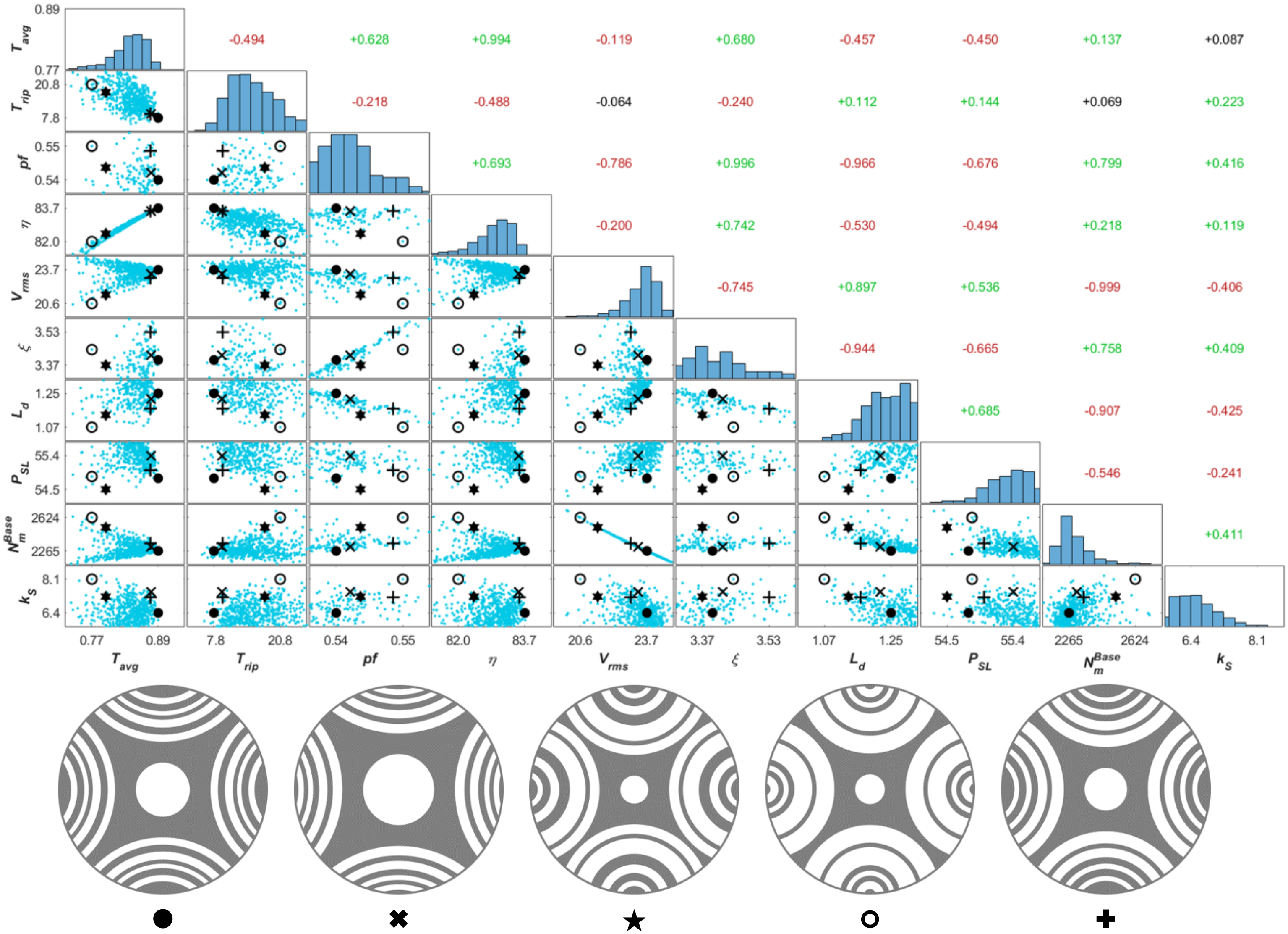

Fig. D.12 (Top) Correlation plot of 30-slot, 4-barrier performances. (Bottom) Selected designs: ● for [-T_{avg},T_{rip}], ✖ for [-T_{avg},T_{rip},-k_S], ★ for [-T_{avg},T_{rip},P_{SL}], ○ for [P_{SL},-k_S], ✚ for all.

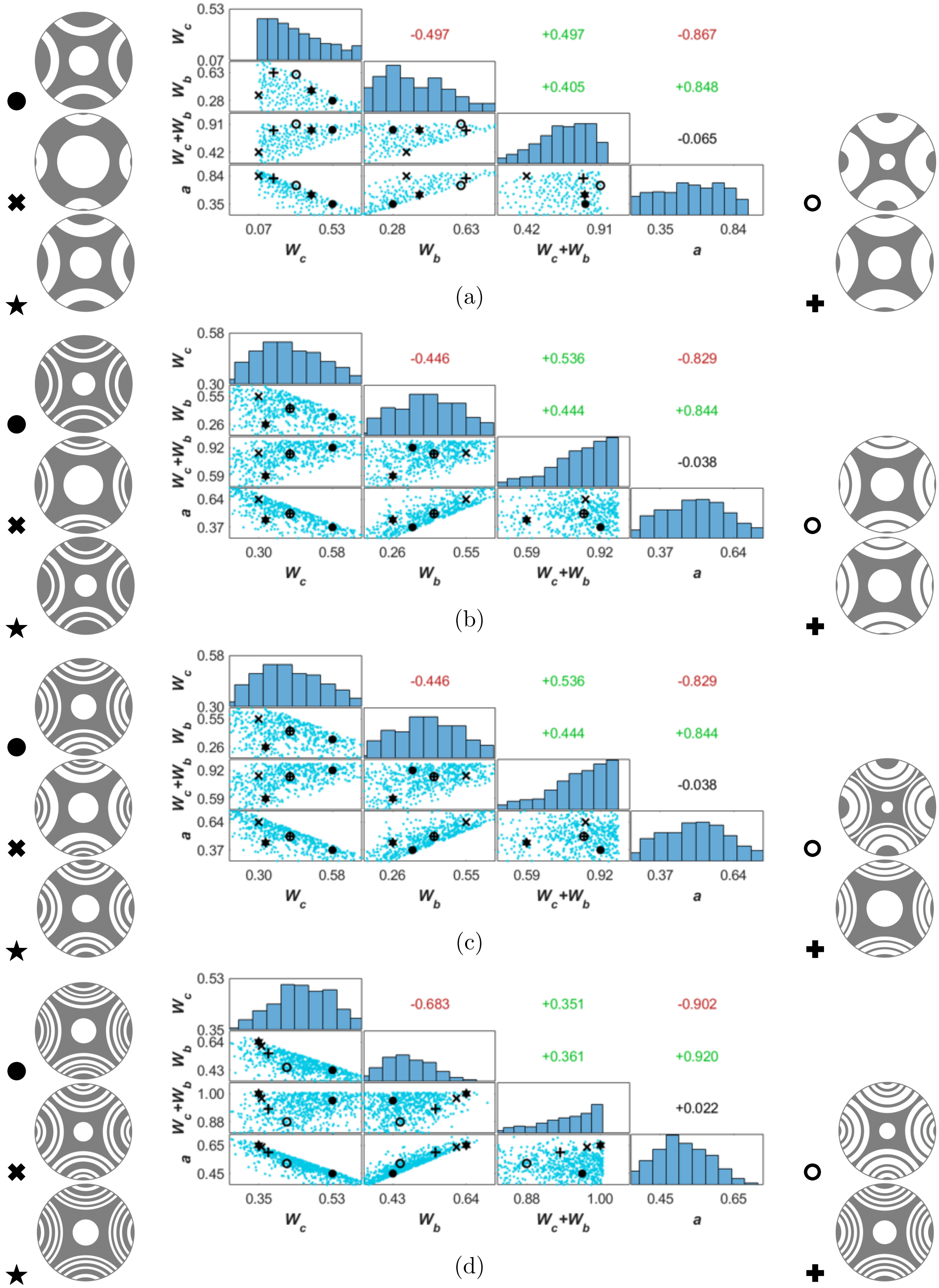

Fig. D.13 Correlation plots of 24-slot design metrics: (a) 1-barrier, (b) 2-barrier, (c) 3-barrier, (d) 4-barrier. Selected designs: ● for [-T_{avg},T_{rip}], ✖ for [-T_{avg},T_{rip},-k_S], ★ for [-T_{avg},T_{rip},P_{SL}], **O** for [-T_{avg},T_{rip},T_W], ✚ for all.

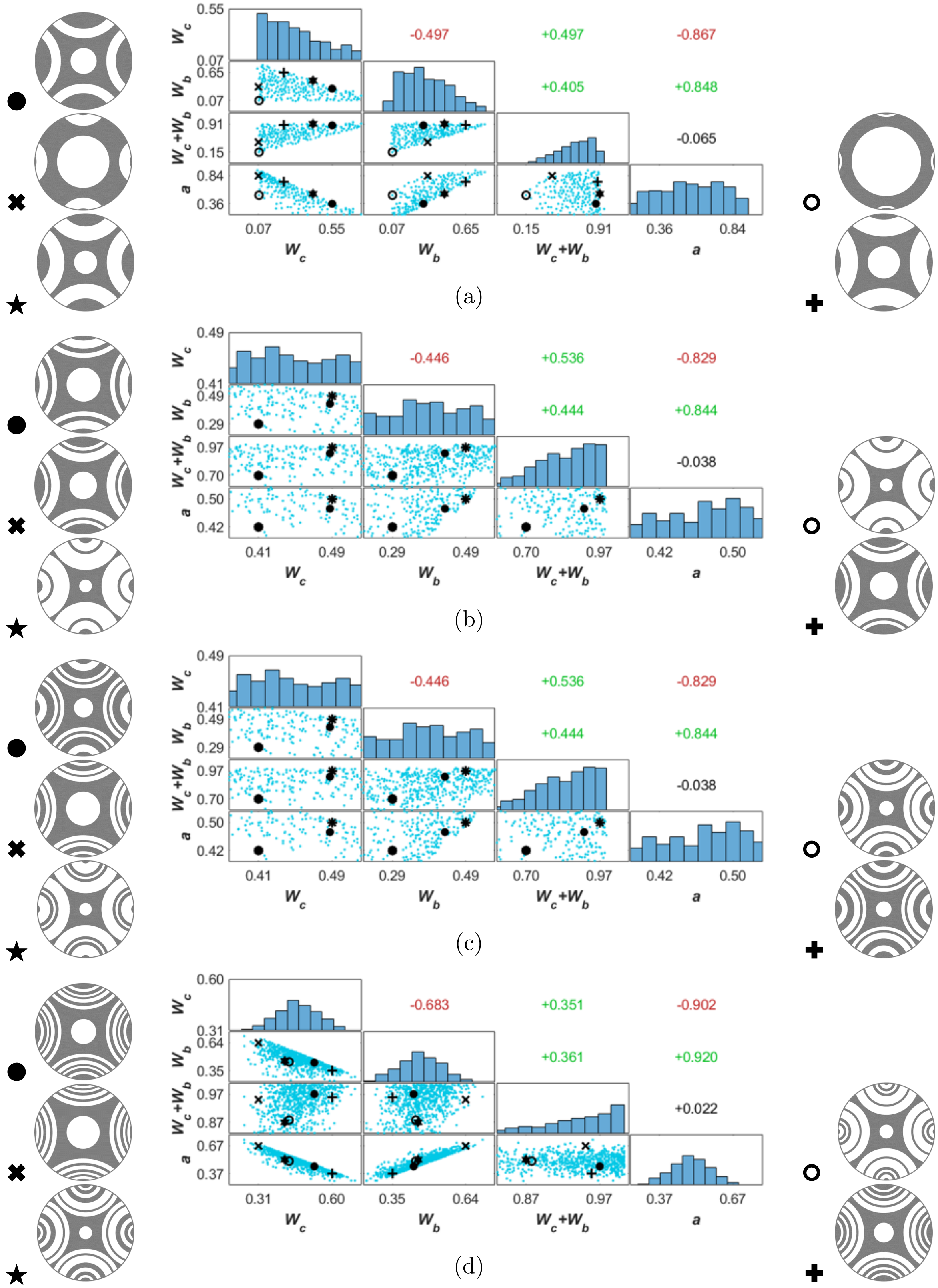

Fig. D.14 Correlation plots of 30-slot design metrics: (a) 1-barrier, (b) 2-barrier, (c) 3-barrier, (d) 4-barrier. Selected designs: ● for [-T_{avg},T_{rip}], ✖ for [-T_{avg},T_{rip},-k_S], ★ for [-T_{avg},T_{rip},P_{SL}], **O** for [P_{SL},-k_S], ✚ for all.

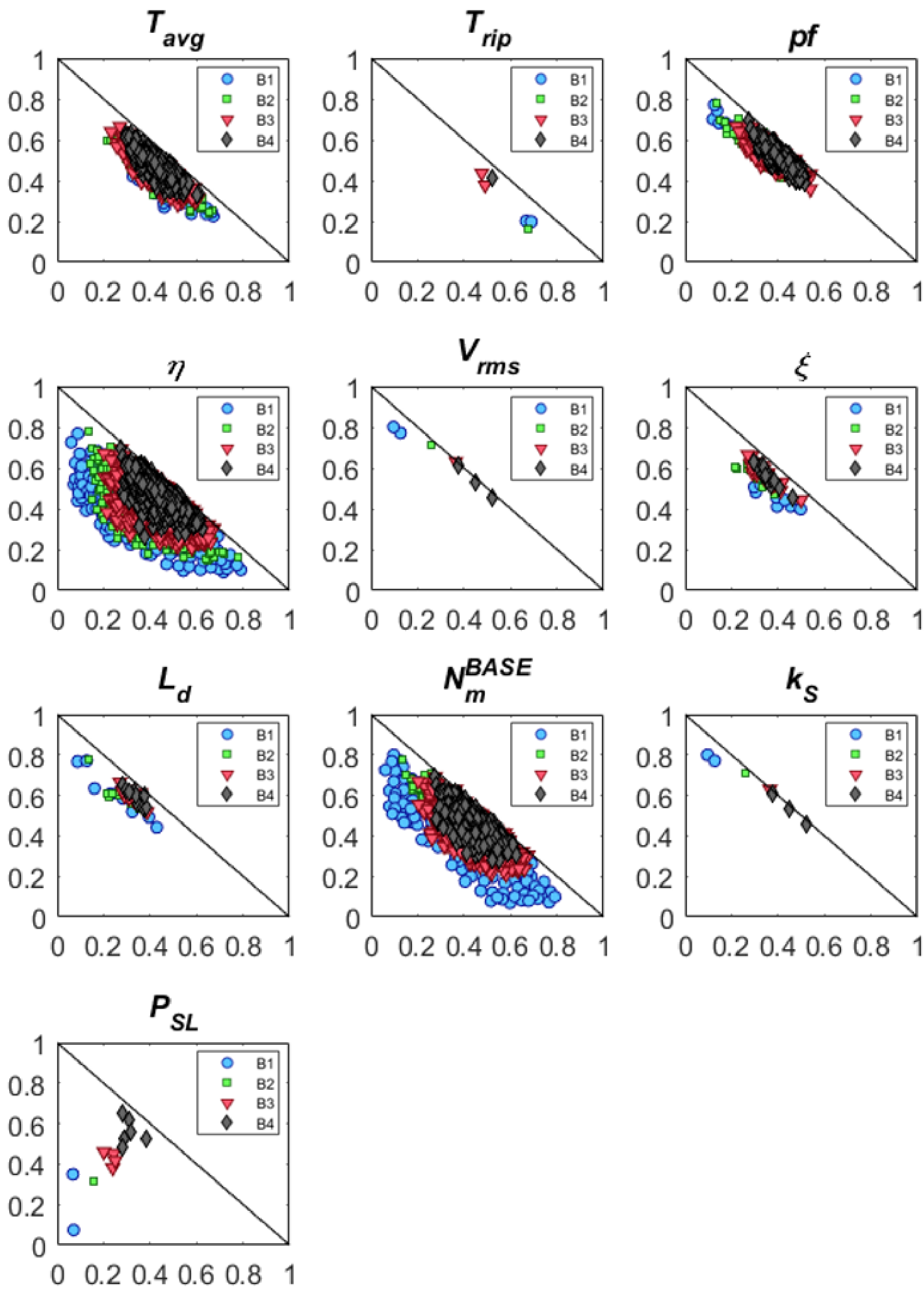

Fig. D.15 *Barrier mapping* for 24-slot multiphysics performances in (W_c,W_b) plane for top 5% percentile solutions. T_{avg} average torque, T_{rip} torque ripple, pf power factor, η efficiency, V_{rms} RMS voltage, ξ saliency ratio, L_d d-axis inductance, N_m^{Base} base speed, k_S safety factor, P_{SL} sound pressure level, T_W average winding temperature, T_R average rotor temperature.

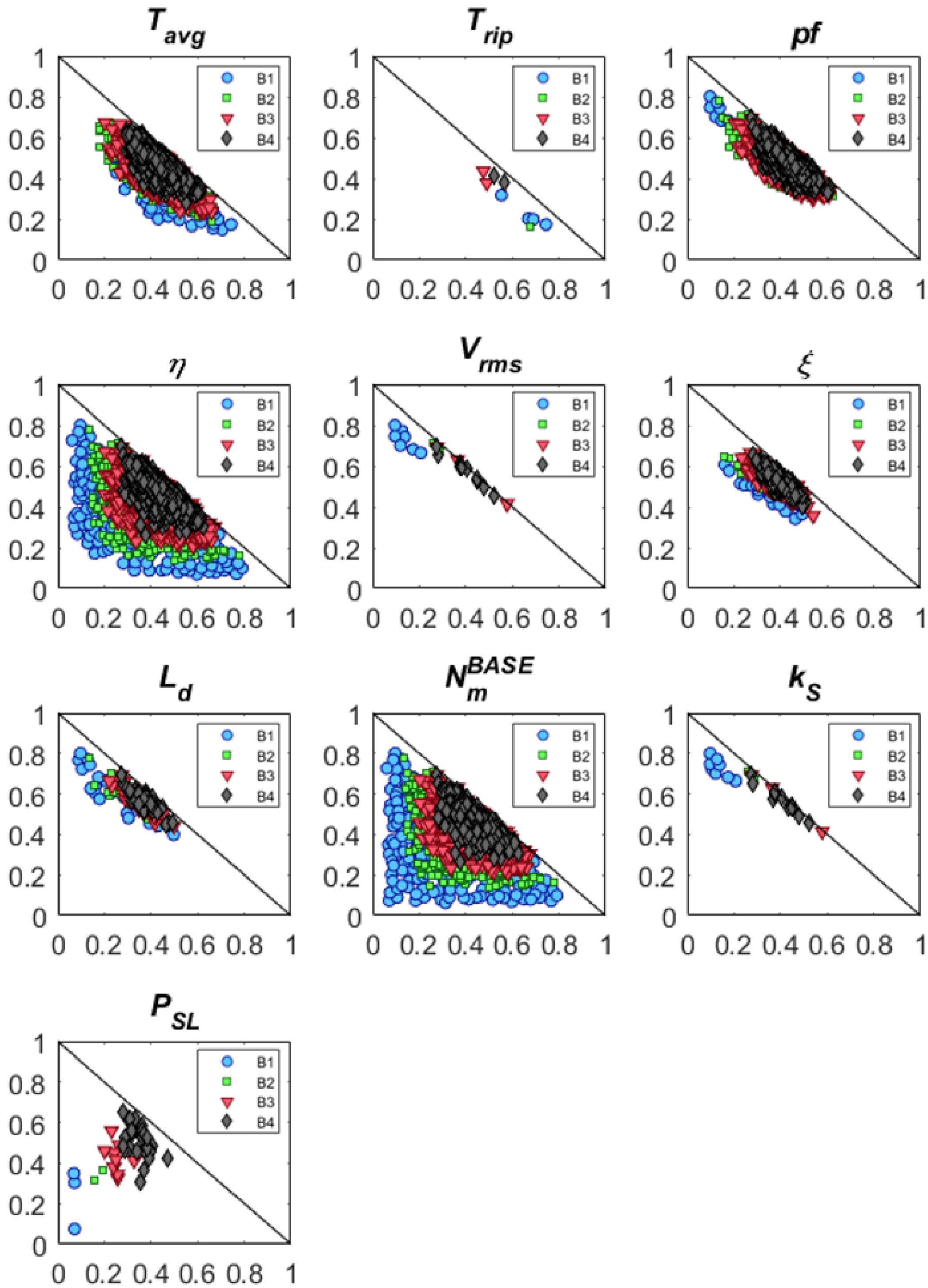

Fig. D.16 *Barrier mapping* for 30-slot multiphysics performances in (W_c,W_b) plane for top 10% percentile solutions. T_{avg} average torque, T_{rip} torque ripple, pf power factor, η efficiency, V_{rms} RMS voltage, ξ saliency ratio, L_d d-axis inductance, N_m^{Base} base speed, k_S safety factor, P_{SL} sound pressure level.